REPORT DOCUMENTATION PAGE

Form Approved
OMB No. 0704-0188

1. REPORT DATE *(DD-MM-YYYY)*	2. REPORT TYPE	3. DATES COVERED *(From - To)*
17-03-2016	Final Technical Report	01-APRIL-12 through 31-DEC-15

4. TITLE AND SUBTITLE
A Novel Method to Predict Circulation Control Noise

5a. CONTRACT NUMBER

5b. GRANT NUMBER
N00014-12-1-0544

5c. PROGRAM ELEMENT NUMBER

6. AUTHOR(S)
Robert Reger, Adam Nickels, Lawrence Ukeiley, and Louis Cattafesta

5d. PROJECT NUMBER

5e. TASK NUMBER

5f. WORK UNIT NUMBER

7. PERFORMING ORGANIZATION NAME(S) AND ADDRESS(ES)
Florida State University
874 Traditions Way, Third Floor
Tallahassee, Florida 32306-4166

8. PERFORMING ORGANIZATION REPORT NUMBER

9. SPONSORING/MONITORING AGENCY NAME(S) AND ADDRESS(ES)
ONR Reg Admin Atlanta - N66020
100 Alabama Street SW Suite 4R15
Atlanta, GA 30303-3104

10. SPONSOR/MONITOR'S ACRONYM(S)

11. SPONSOR/MONITOR'S REPORT NUMBER(S)

12. DISTRIBUTION/AVAILABILITY STATEMENT
Approved for public release

13. SUPPLEMENTARY NOTES

14. ABSTRACT
Underwater vehicles suffer from reduced maneuverability with conventional lifting appendages. Circulation control (CC) offers a method to increase maneuverability. However, with CC comes additional noise sources. A method involving estimation of the velocity, surface pressure, and far-field acoustic fields is developed. In the absence of added noise, the prediction performs well on simulated, low Reynolds number flow over a cylinder. The method also performs reasonably well on a high Reynolds number circulation control airfoil with no blowing but under-performs with the jet active. Delay-and-sum and DAMAS beamforming are used to acquire accurate far-field acoustic levels. A scaling analysis is also performed.

15. SUBJECT TERMS

16. SECURITY CLASSIFICATION OF:			17. LIMITATION OF ABSTRACT	18. NUMBER OF PAGES	19a. NAME OF RESPONSIBLE PERSON
a. REPORT	b. ABSTRACT	c. THIS PAGE			Louis Cattafesta
U	U	U	UU		19b. TELEPHONE NUMBER *(Include area code)*

GRANT N00014-12-1-0544

ONR FINAL REPORT

A Novel Method to Predict Circulation Control Noise

Robert Reger, Adam Nickels, Lawrence Ukeiley, and Louis Cattafesta

March 17, 2016

TABLE OF CONTENTS

LIST OF TABLES

LIST OF FIGURES

ABSTRACT

Underwater vehicles suffer from reduced maneuverability with conventional lifting appendages due to the low velocity of operation. Circulation control offers a method to increase maneuverability independent of vehicle speed. However, with circulation control comes additional noise sources, which are not well understood. To better understand these noise sources, a modal-based prediction method is developed, potentially offering a quantitative connection between flow structures and far-field noise. This method involves estimation of the velocity field, surface pressure field, and far-field noise, using only non-time-resolved velocity fields and time-resolved probe measurements. Proper orthogonal decomposition, linear stochastic estimation and Kalman smoothing are employed to estimate time-resolved velocity fields. Poisson's equation is used to calculate time-resolved pressure fields from velocity. Curle's analogy is then used to propagate the surface pressure forces to the far field.

This method is developed first for a direct numerical simulation of a two-dimensional cylinder at a low Reynolds number (150). Since each of the fields to be estimated are also known from the simulation, a means of obtaining the error from using the methodology is provided. The velocity estimation and the simulated velocity match well when the simulated additive measurement noise is low. The pressure field suffers due to a small domain size; however, the surface pressures estimates fare much better. The far-field estimation contains similar frequency content with reduced magnitudes, attributed to the exclusion of the viscous forces in Curle's analogy. In the absence of added noise, the estimation procedure performs quite nicely for this model problem.

A turbulent wall jet with a rectangular nozzle (possessing an aspect ratio of 8) is studied

with respect to the proposed method, providing an experimental test bed before addressing more complex flow geometries. Synchronized, two-component particle image velocimetry and unsteady surface pressure measurements are obtained at the centerline of the nozzle, oriented in the streamwise flow direction. POD of the velocity fields highlights a number of flow features, corresponding to the shear layer instability, that correlate well with the surface pressure measurements. Resulting velocity field spectrum estimates match well with measured velocity spectra obtained using hotwire anemometry, however low correlations between higher order, small-scale POD modes and surface pressure limits the estimation of frequencies higher than a certain cutoff. Due to the effects of only retaining a limited subset of the velocity field decomposition, far-field acoustic estimates are lower in magnitude than microphone measurements.

The method is tested experimentally on a 650,000 chord-Reynolds-number flow over a 2-D, 20% thick, elliptic circulation control airfoil. Slot jet momentum coefficients of 0 and 0.10 are investigated. Particle image velocimetry, unsteady pressure and phased-acoustic-array data are acquired simultaneously in an aeroacoustic wind-tunnel facility. The velocity field estimation suffers due to poor correlation with the unsteady pressure data, especially in the 0.10 momentum coefficient case. The prediction without slot jet blowing matches single microphone measurements within 0-10 dB over the frequency range of interest while the prediction with the jet active is quite poor and differ from measurements by as much as 35 dB. Suggestions for improvement of the proposed method are offered.

Data from the acoustic array are then investigated. Single microphone spectra are obtained, and it is shown that background noise is significant. In order to circumvent this problem, beamforming is employed. The primary sources of background noise are from the tunnel collector and jet/sidewall interaction. DAMAS (Brooks & Humphreys, 2006) is employed to remove the effects of the array point spread function. Spectra are acquired by integrating the DAMAS result over the source region. The resulting DAMAS spectral levels are significantly below single microphone levels. A scaling analysis is performed on the processed array data. With a constant free-stream velocity and a varying jet velocity

the data scale as M^6. If momentum coefficient is held constant and free-stream velocity is varied the data scale as M^7.

CHAPTER 1

INTRODUCTION

Circulation control via blowing over a Coanda surface has long been known as a method of generating lift without the use of control surfaces (Coanda, 1938). By removing mechanical complexities that come along with conventional control surfaces, the weight and cost of air- and hydro-craft can be significantly reduced. Circulation control has the added benefit of requiring little to no freestream velocity (i.e. forward motion) to allow for maneuverability, unlike traditional lifting mechanisms. This is especially important in underwater vehicles which traditionally maneuver at much lower speeds. Unfortunately, adverse effects associated with circulation control limit its use for a variety of reasons.

Recently, Joslin (2005) reviewed these limitations, one of which is additional noise produced by circulation control. Noise production from circulation control must be significantly reduced before it can be effectively employed aboard sea-based vehicles as their sonar systems can be limited by self noise. In addition, stealth is vital to missions of many underwater craft and, as such, increased noise levels decrease the overall survivability of the vehicle. To understand and control these added noise sources Howe (2002) created a mathematical model to predict levels; however, recent experimental research by Wetzel (2011,2012) have shown significant disagreement with Howe's model. Therefore, we must rely on experiments for circulation control noise prediction. These experiments are currently viable only in either open-jet wind tunnels or flight testing which makes noise prediction for underwater vehicles especially difficult.

In this document, a method by which sound can be predicted using only unsteady pressure probes and a non-time-resolved particle image velocimetry (PIV) system is proposed. By obtaining time-resolved unsteady pressure on the surface synchronously (but not at a 1:1 ratio) with non-time-resolved PIV one can estimate a low-order time-resolved velocity field by a combination of proper orthogonal decomposition, stochastic estimation, and a Kalman filter and smoother. From the time-resolved velocity fields, Poisson's equation can be employed to obtain an estimate of the time-resolved pressure field. Using the surface pressures predicted by Poisson's equation, Curle's (or some other) acoustic analogy can then be employed to estimate the acoustic far-field.

This document provides the details for each of the methodologies applied first to a simple computational problem of flow over a cylinder, next to a canonical experimental study of a turbulent wall jet flow, and finally to the considerably more complex flow over a circulation control airfoil. Analyzing the proposed methodologies in this manner provides a systematic means of separating issues arising from the various complexities introduced at each stage. The computational setup demonstrates the performance of the methodologies in an ideal situation where all information about the flow is known, the flow is at a low Reynolds number, and the data are noiseless. The experimental study of the turbulent wall jet allows for the study of a turbulent flow without the geometric complexity inherent to the circulation control airfoil, but with the added difficulty of larger three-dimensional motion of the flow at a moderate Reynolds number. Then, a high Reynolds number flow over a circulation control airfoil is investigated. This will show both the potential applications of the current methods, as well as show any limitations that may arise in more complex flow. Finally, the acoustics of circulation control will be investigated and discussed.

1.1 Previous Research

This section provides a review of research that has been done on relevant topics. It begins by discussing the topic of circulation control acoustics. Then it examines the relevant

methodology used in the estimation, starting with the velocity estimation, moving on to the pressure field and force estimation, and concluding with acoustic analogies. Each of these sections contains relevant historical milestones for each method as well as some discussion of their previous uses.

1.1.1 Circulation Control Acoustics

While circulation control has been widely investigated for the better part of the 1900's when Coanda (1938) first patented the design for his propeller device, the study of the acoustics of such circulation control devices has been quite limited. A sample circulation control airfoil is shown in 1.1.

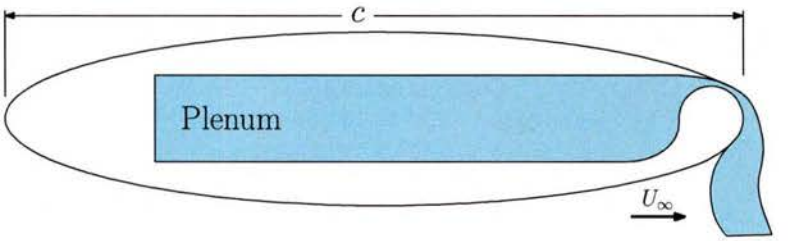

Figure 1.1: A sample circulation control airfoil.

The first major investigation of circulation control acoustics was performed by Williams & Cheeseman (1978). In their work, they suggest ten theoretical sources of circulation control noise for the three-dimensional rotor, five of which correspond to two-dimensional circulation control airfoil noise. He classified these sources as "classical trailing edge noise," "laminar boundary layer instability noise," "jet noise," "incidence turbulence noise," and "radiation from separating surface boundary layer," all of which he proposed as broadband sources. They then describe the generation mechanisms for each of the noise sources. They define "classical trailing edge noise" as the noise generated by turbulence of the wake interacting with the trailing edge of the airfoil. Next, "laminar boundary layer instability noise" is created from an acoustic feedback between pressure disturbances in the wake and the "instability point of the lower surface laminar boundary layer." "Jet noise" is broken

into three distinct categories based on the generation mechanisms: (1) "mixing noise," (2) "excess noise" from the interaction with the round trailing edge, and (3) "wall jet noise." The "incident turbulence noise" comes from the interaction of the rotor with turbulence from the previous rotor due to rotation. Finally, "radiation from the separating surface boundary layer" is self explanatory.

Several years later, Mosher (1983) performed an experimental study on the effect of circulation control on rotor acoustics. Testing of two circulation control rotors ("X-Wing" and circulation control rotors) and a conventional rotor was conducted in the 40 by 80 foot wind tunnel at Ames Research Center. The X-Wing rotor had both leading and trailing edge blowing slots, while the circulation control rotor had only a trailing edge slot. During testing they matched the lift coefficients and either the forward speed or tip advancing Mach number. The tests showed that the circulation control rotor produced the most noise for all three cases due to higher broadband noise levels attributed to jet flow from the trailing edge slot.

After this, Salikuddin *et al.* (1987) investigated the noise generated from upper surface blowing over a circulation control wing. They tested four configurations, one with no blowing, another with just circulation control, one with only upper surface blowing and the last with both; the focus here will be on the circulation control only case. These tests were performed in Lockheed's anechoic free-jet wind tunnel where microphones were placed in a circular arc underneath the wing from 40° to 120°. They showed that at a constant circulation control jet velocity, slot height, and tunnel speed, the low frequency noise was nearly identical for all angles but at high frequencies, the shallower angles saw higher sound pressure levels (SPL). When jet velocity was allowed to vary at a constant tunnel speed, it was shown that the broadband noise levels increased with jet velocity and that this rise was much more significant in the high frequency regions. Finally, they varied the slot height and showed that SPL also increased with slot height.

Munro *et al.* (2001) made a series of noise comparisons between a conventional airfoil and a circulation control airfoil. They initially set the flap angle of the circulation control

airfoil to 90° which was shown to maximize lift. They showed that, in the absence of freestream flow, noise levels increased with increasing jet velocity. When they added a freestream component, they noticed a large peak in the spectrum which they attributed to shedding off of the trailing edge lip. The magnitude of this peak was reduced by increasing the jet velocity, but they were unable to eliminate it completely. In order to remove this peak they changed the flap angle to 30°. At 30° they noticed the peak remained with no jet velocity, but was eliminated with a relatively small amount of blowing. At low frequencies (below about 5 kHz) the noise generated from the circulation control jet was constant, but at higher velocities, the broadband noise levels increased with increasing jet velocity. In order to compare the circulation control airfoil to the conventional one, they held tunnel speed and lift coefficient constant. In order to understand the effect of slot height on the noise production they held the coefficient of momentum constant and varied the slot height. They showed that the noise generated decreased with increasing slot height (and, by extension, decreasing jet velocity) until $h = 0.0012$ inches when it began to increase. It was proposed that this increase was due to internal noise and could be eliminated with careful internal design. In comparing the circulation control airfoil to the conventional wing they find that the circulation control wing showed lower noise level at 90° and 60° angles from the freestream at frequencies below 40 kHz with a significant reduction at frequencies below 10 kHz.

Howe (2002) developed an analytical theory in order to predict the acoustic radiation from circulation control devices at low speeds and small angles of attack. In this work, Howe employed a two-dimensional, elliptical circulation control hydrofoil at zero angle of attack with a rounded trailing edge. He used this hydrofoil in a uniform flow with a very low Mach number but kept the Reynolds number large. In this work, he identifies four primary (external) noise sources which he identifies as (1) "separation noise," (2) "curvature noise," (3) "passive-slot noise," and (4) "jet-slot noise." "Separation noise" is defined as the noise produced when the vortex separates from the hydrofoil while "curvature noise" is the noise created by the freestream boundary layer turbulence interacting with the rounded trailing

edge. "Passive slot noise" is noise generated by the freestream boundary layer turbulence interacting with the sharp upper slot lip. Finally, "jet-slot noise" is the noise created by the circulation control jet interacting with the sharp upper lip and the rounded lower lip; however, the interaction with the lower lip is negligible compared to the other sources. The work then goes on to provide an analytical definition of each of these sources which only depend on jet velocity, local flow speed, friction velocity, displacement thickness, and hydrofoil geometry. Howe then determines the dominant frequency range of each of the noise sources by using experimental data from Novak & Cornelius (1986, 1987) and finds that "separation noise" occurs at such a low frequency and amplitude that it can be ignored. "Curvature noise" is shown to dominate at low frequencies, "passive slot noise" dominates at mid-frequencies, and "slot-jet noise" dominates the upper frequency range.

Recently, a number of papers have been published regarding circulation control acoustics. Shannon & Morris (2008) showed that when just the slot-jet flow and external flow were used independently from one another, the noise scaled like velocity to the 4th and 5th power, respectively. They could not conclude a velocity scaling when both flows were included. They also noticed "distinct spectral tones" were generated when only the slot-jet flow was used and proposed this was from either turbulence or the "Green's function associated with propagation."

Slomski (2009) attempted to determine the source of the discrete frequency tones observed in Rogers & Donnelly (2004) which scaled with the jet velocity. He performs large eddy simulations of three different circulation control slot lip geometries. First, he uses a baseline, blunt lip, then he contours the inside of the lip and, finally, he applied serrations to the lip. In the blunt lip creates spanwise vorticies which are the source of the tone heard during the experiments. By contouring the bottom of the lip, he is able to significantly reduce the amplitude of not only the tones, but also the broadband spectra. Lastly, he shows that the serrated edge reduces the amplitude of the tones and broadband even further, even without the interior contouring.

More recently, Wetzel *et al.* (2012) performed a series of experiments to test the semi-

empirical model from Howe (2002). Wetzel *et al.* (2012) performed experiments on a 2-D, elliptical circulation control airfoil. They acquire near field flow data from particle image velocimetry (PIV) and far field data from a 60 microphone phased acoustic array. By using the acoustic array they are able to remove extraneous noise sources such as sidewall scrubbing. PIV provides some of the relevant flow parameters required by the model developed by Howe (2002), as discussed previously, with the notable exception of friction velocity. They use both the Chase (1980) and the Goody (2004) models to derive the analytical noise source models. They showed that, for both models, the predicted levels were considerably lower than the measured levels for all frequencies. They also show that the dominant source of noise for most frequencies considered was "passive slot noise" while at very high frequencies "slot jet noise" dominated. In order to compare the spectra qualitatively, they normalized the individual spectrum by its level at 80 kHz and showed that the Goody model seemed to perform better than the Chase-Howe model. Finally, they showed that a better agreement between the model and the experiments was obtained by increasing the friction velocity five fold (to 13 meters per second).

Based on the results of Wetzel *et al.* (2012), it seems that Howe's model is not sufficiently accurate. While the phased array can isolate the trailing edge region of the airfoil from extraneous sources, it cannot isolate potential individual noise sources (outlined in 1.2). The ideal solution would provide an experimental means to obtain temporally- and spatially-resolved surface pressure measurements to be used in an acoustic analogy. The next section will discuss a method by which the temporally- and spatially-resolved velocity field can be estimated from which the pressure field can be estimated.

1.1.2 Time-Resolved Velocity Estimation

Stochastic estimation is a statistical means by which a conditional variable can be estimated by an unconditional variable and is commonly used in fluid mechanics to estimate a time-resolved velocity field. Recently, it has also been used in tandem with the proper orthogonal decomposition (POD), which breaks a velocity field into modes based on energy

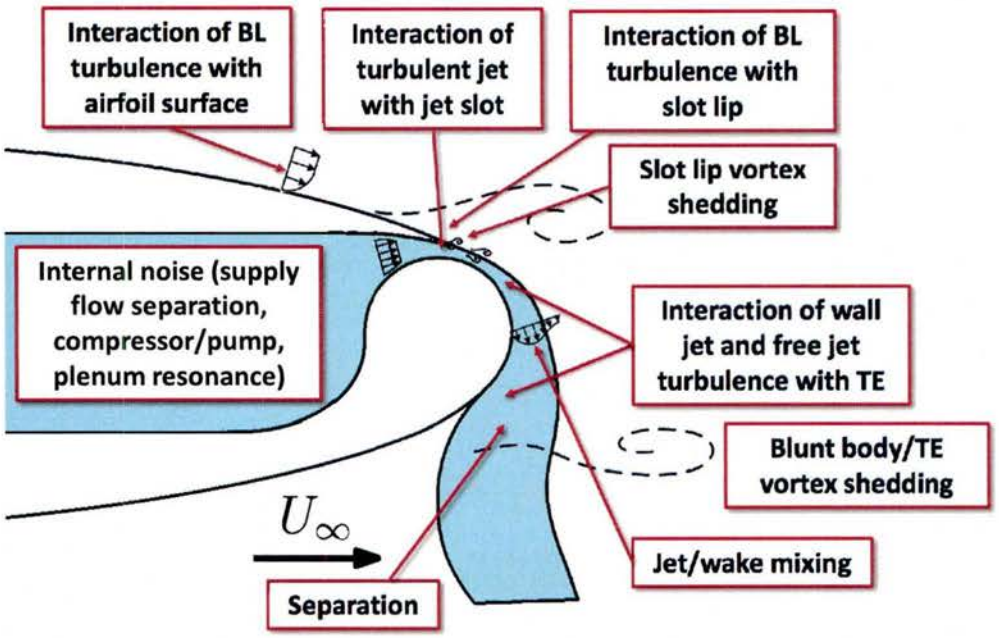

Figure 1.2: An overview of circulation control noise sources as proposed by Williams & Cheeseman (1978); Howe (2002) (adapted from Wetzel (2011)

content, in order to reduce computation time. This section will provide an overview of the history of these methods, while their theory is discussed in chapter 2.

Adrian (1977) developed the idea of stochastic estimation to estimate the conventional conditional averaging techniques used in the study of turbulence. In this work, he focuses on the first term of the Taylor series and investigates linear stochastic estimation. He shows that the solution of the estimation can be made optimal by solving the equation for the minimum mean squared error and using that value for the unknown. After this, he shows that the Reynolds stress tensor can be used as a quadratic term. Finally, he considers the problem of isotropic turbulence by the linear stochastic estimation and finds that the result is quite similar to standard conditional averaging.

Later, Adrian (1979) studied eddies in isotropic turbulence and the effect of the second (quadratic) term in the stochastic estimation. He found that the second-order term is quite small and had "minor effect" and thus concluded that the Taylor series converged rapidly for

"all but the rarest, most intense velocity fluctuations." Adrian also concluded that for most applications the "linear estimate is often sufficient and much of its quantitative behavior, as well," while noting that one of the most attractive features of the linear estimation is its ease of implementation. After this, Tung & Adrian (1980) explored the same problem but retained up to the fourth order term in the Taylor series. They show that the quadratic, cubic, and quartic terms make very little difference in the estimation of the flow. However, as we will discuss later in this section, under certain circumstances, the higher-order terms may provide some improvement (Murray & Ukeiley, 2003; Naguib *et al.*, 2001).

Guezennec (1989) extended the estimation to account for time delays between the measurement and estimated structures. By accounting for some time-delay, Guezennec showed that two-dimensional, two-point correlations outperformed the single time version used by Adrian (1977, 1979) because it allowed for observation of events at different time and length scales instead of viewing events isolated in time. This extension provided a significant increase in the accuracy in the estimation.

Cole *et al.* (1992) extended the use slightly from using two-point correlations to "multi-point correlations" and saw additional improvements. They also hypothesized that the stochastic estimation depends highly on the number and location of the probes. They showed that an instantaneous velocity field could be used instead of the arbitrary definition of a "conditional eddy."

More recently, POD has begun to be used with stochastic estimation. The procedure followed by POD has been independently discovered many times, used in many different disciplines, and goes by many different names (see Gordeyev (1999), Berkooz *et al.* (1993)). It was originally proposed for use in fluid dynamics by Lumley (1967) based on the Karhunen-Loeve expansion (Loeve, 1955). Even within the field of fluid dynamics, POD has been used in too many different manners to be covered here, including, but not limited to, turbulence (Sirovich, 1987; Berkooz *et al.*, 1993; Delville *et al.*, 1999), dynamic model estimation (Aubry *et al.*, 1988; Ukeiley *et al.*, 2001), and stochastic estimation (Adrian, 1979; Adrian & Moin, 1988), the last of which will be the focus of this section.

Bonnet *et al.* (1994) suggested and investigated the use of a "complementary technique" coupling POD and stochastic estimation (specifically linear stochastic estimation). They developed a three step process to obtain a low-order estimation of the velocity field from a very limited data set. (1) Apply POD and determine the eigenfunctions and eigenvalues, (2) apply linear stochastic estimation to the cross-correlation tensor and multi-point estimates, and finally, (3) project the stochastic estimation onto the eigenfunctions obtained in (1). For the paper they investigated two experimental setups. First, they used data from Glauser & George (1987), which consisted of just eight "X" wires in an axisymmetric jet. In the second test, they used data from Delville *et al.* (1989), in which they used 12 "X" wires in a mixing layer. They compared their "complementary technique" to the full (measured) velocity field result, by projecting them onto a single POD mode. They found that the estimation and measured field, when projected onto one mode, were "remarkably similar." They also found that the RMS fields showed their technique to be effective.

Ewing & Citriniti (1999) made use of the Fourier transform (Bendat & Piersol, 2010) in order to remove the time dependency by moving the problem to the frequency domain. In the paper, they first compute a linear stochastic estimation using only a single-time-delay. After that they transform the data to the frequency domain and compute the linear stochastic estimation, effectively using all time data in the estimate. This is the first example of multi-time-delay stochastic estimation. Once they obtained the estimated velocity field, they performed the POD on it to look at the large scale structures. Using an experimental database from Citriniti (2012) the authors compare their single-time-delay linear stochastic estimation and the spectral linear stochastic estimation to a known velocity field. They find that the single-time and spectral estimations do quite well at estimating the bulk features, while only the spectral estimation adequately estimates the "amplitude of the fluctuating velocity component." Finally, the authors pointed out that this method significantly reduced the number of probe measurements required for the experiments.

Naguib *et al.* (2001) perform single-time-delay stochastic estimation with both the linear and quadratic terms included. In these experiments, they studied flow over a flat plate

at Reynolds numbers from 1437 to 5670; they simultaneously sampled a single streamwise hot-wire probe along with the wall unsteady pressure from Knowles EM-3068 microphones. They show that using only the linear term in the estimation is not "satisfactory" for the estimation of so-called "wall-pressure events" and that the quadratic term provides important contribution to the estimation. The authors believe that this is due to the coupling of pressure and velocity from Poisson's equation. Murray & Ukeiley (2003) show a similar result for a simulation of flow over cavity, with the majority of the flow estimated by the linear portion and some significant details appearing from the inclusion of the quadratic term.

Modified stochastic estimation is developed by Taylor & Glauser (2004). To the author's knowledge, this is the first documented use of this method. This method combines POD and stochastic estimation. In their paper, they use modified stochastic estimation with POD and single-time-delay linear stochastic estimation on the problem of a backward facing ramp. They used PIV to capture the velocity field which was decomposed into spatial POD modes and temporal POD coefficients. Then, they used the POD coefficients along with surface pressure data and linear stochastic estimation to estimate a temporally resolved set of POD coefficients. These were then used to estimate a low-order velocity field estimation. They find that the method is "capable of estimating the first three POD modes" and that "increased sensitivity and frequency response of the pressure instrumentation will likely extend the usable range of this tool to higher POD modes." This is a methodology which will be used throughout this document.

Murray & Ukeiley (2007) expanded upon the work by Taylor & Glauser (2004) by including the quadratic term of the Taylor series. The authors study both the velocity and density fields in and around a cavity model. They used PIV to obtain the velocity field and Schlieren to obtain the density field and fourteen Kulite sensors along the centerline of the model to capture the fluctuating pressure. They showed that the modified quadratic stochastic estimation method worked well on the cavity problem for both velocity and density estimation. In the density estimation, it was able to estimate the downstream

motion of the vorticies and the upstream propagation of the acoustics. The authors also show that, if this modified estimation is used along with global POD, it could potentially be used for predictive purposes such as closed loop control.

Ukeiley *et al.* (2008) used a similar idea to that proposed by Ewing & Citriniti (1999) and Tinney *et al.* (2006) except they used it in the time domain, instead of the frequency domain, and in a causal manner. By using multiple-time-delay linear stochastic estimation, the authors hoped to estimate future pressure signals from a time series of past pressure signals. They used a cavity model and compared the "Auto-Regressive Moving Average" filter to the causal, multi-time-delay, linear stochastic estimation. They found that in some cases, the models were nearly identical and both models worked well for low frequency oscillations, but that the "Auto-Regressive Moving Average" model worked better to determine the amplitudes of the fluctuations.

Durgesh & Naughton (2010) performed the complementary LSE-POD technique with a non-causal version of the multi-time-delay formulation in the time domain. Using a "wedge model" with an elliptical leading edge and a truncated trailing edge, the authors gathered 1000 uncorrelated PIV images and 3000 time-resolved samples from the pressure probes both before and after each of the PIV snapshots. In the paper, they compared the LSE-POD results using a single time delay and multiple time delays. They first showed that a single-time-delay with no time offset had significant error in the estimation, they attributed this result to a ninety degree phase difference between the correlated shedding phenomenon and the pressure data. When they moved on to the multi-time-delay version, they found that it performed much better but that when too large a range of time delays was employed, they saw a significant reduction of accuracy, indicating that there was some optimal time delay range which should be used.

Tu *et al.* (2012) used a model-based technique on an experiment using a similar model to that used by Durgesh & Naughton (2010) with the addition of a Kalman smoother. In this experiment set the authors took time-resolved PIV data in ten sets. By taking time-resolved PIV, they had the "known" answer for comparison. The data sets were downsampled

such that the data was no longer time-resolved, and the estimation procedure was used employing the downsampled data as spatially but not temporally resolved snapshots. For the probe location, they used a single point of velocity data in the flow . They found that the stochastic estimation provided an accurate answer when noise was neglected. For the Kalman smoother, they used the LSE-POD results as a linear model of the flow physics. When they looked at the results from the Kalman smoother they found that, for the case which was studied, the smoother provided a slight increase in accuracy and was more robust to the effects of noise.

1.1.3 Force/Pressure Estimation from PIV

The ability to estimate the pressure field of a flow was first studied by Schwabe (1935), but due to limitations of measurements and processing capabilities, it was not widely explored until the advent of PIV. Using PIV data coupled with the Navier-Stokes equations, many have begun to estimate the pressure field. All the methods of pressure field estimation originate from the Navier-Stokes equations, but many practical issues arise in implementation, which has led to a number of different methods to determine the terms within the equations (van Oudheusden, 2013). This section will discuss many of the different ways which have been used to evaluate those terms as well as studies which explore the viability of these different methods. Specifically, we will focus on the incompressible, two-dimensional versions of the equations, with brief forays into three-dimensions. As in previous sections, we will move through the literature in chronological order.

Before discussing the pressure field estimation, brief mention should be made of a method which estimates only the aerodynamic forces on a body, instead of the full pressure field. There have been several efforts which allow one to obtain the time-resolved forces over a body from PIV (Sridhar & Katz, 1995; Lin & Rockwell, 1996; Unal *et al.*, 1997; Berton *et al.*, 2004; van Oudheusden *et al.*, 2006). However, these require knowledge of some part of the pressure field. In Noca *et al.* (1997, 1999) a method is developed which only requires velocity and its derivatives. While this method seems attractive, it requires a "region enclosing the

body," such that we could no longer break the problem into pieces and determine their individual contributions (based on the noise sources suggested by Howe (2002)). Therefore, our focus will be on estimating the unsteady pressure field to extract the forces.

Two important terms to consider in each of these methods are the velocity and the acceleration. While velocity is obtained in the same manner, (via standard PIV) several different methods to obtain acceleration are employed. Sridhar & Katz (1995) studied the forces acting on bubbles. They made use of "triple exposure images" in order to measure the velocity and acceleration in a Lagrangian frame. By using two of the images, they compared the location of the bubble and found a displacement vector (velocity). In order to find the acceleration, they used the difference in the two displacement vectors.

Jakobsen *et al.* (1997) used a four-exposure PIV setup with four cameras to measure the acceleration and forces from surface waves. They investigated both the Lagrangian and Eulerian methods for determining acceleration in gravity waves. The four-exposures were set such that the time between exposures 1 and 2 was minimized; the same time delay was used between exposures 3 and 4. Between exposures 2 and 3 a longer delay was required to reduce error in the acceleration measurement. The Eulerian method simply took the velocity vectors from 1-2 and 3-4 and performed a finite difference in order to determine acceleration. For the Lagrangian method they used the velocity vectors from 1-2 and 2-3 to perform the finite difference. The authors showed that the Eulerian method consistently outperforms the Lagrangian method with 2-3 percent versus 3-7 percent errors, respectively. They also suggest a method in which the correlation between frames 2 and 3 are used to identify the original fluid volume and then use frames 1-2 and 3-4 along with that information but they do not attempt that method.

To the author's knowledge, the first use of PIV for the computation of the pressure field was conducted by Gurka *et al.* (1999). They determined the pressure field by solving the pressure Poisson equation with boundary conditions derived from conservation of momentum (Gresho & Sani, 1987). By using the Poisson equation, they remove the need to solve for the acceleration term. They obtained their Neumann boundary conditions by "solv-

ing inversely the Navier-Stokes equations." In their study, they only looked at the steady (mean) component of pressure.

Christensen & Adrian (2002) employed an Eulerian approach to solving for the acceleration term. In this case, the authors studied turbulence in a high Reynolds number channel flow. They use two double-exposure CCD cameras along with four lasers. In order to observe the same measurement plane with both cameras, they are set up orthogonally to each other and a polarizing beam splitter is placed such that each camera only acquires light from its coupled lasers. They used a similar (Eulerian) method as in Jakobsen *et al.* (1997). The authors then developed a method in which they minimized the error in the acceleration by using "zero-time-delay velocity measurements."

Jensen & Pedersen (2004) explore a set of experiments on gravity waves similar to that in Jakobsen *et al.* (1997) with a comparison between a Lagrangian and Eulerian method for solving for acceleration. In these experiments, the authors extended the Eulerian method to include a linear least-squares regression to determine which velocity vectors are coupled from one velocity snapshot to the next. They found that the methods were quite similar with the regression technique being more susceptible to random error. They also discuss the drawbacks for each method. The regression technique "loses" particles in the presence of a free-surface moving rapidly while the Lagrangian technique had issues near the boundaries where particles moved out of the field of view. Finally, they suggest that some optimal time delay between velocity vectors would provide a minimization of error.

Liu & Katz (2004) employed a setup similar to that used in Christensen & Adrian (2002) to study the unsteady pressure field in a cavity flow. Unlike Gurka *et al.* (1999), the authors use the momentum equation solved for the pressure gradient instead of the pressure Poisson equation. They used one camera to record images 1 and 3 and the other camera to record 2 and 4, in this way they were able to better follow the particle groups by reducing the time delay between velocity vectors. They showed that the results of the pressure solution have a standard deviation within about two percent of the theoretically expected values.

Fujisawa *et al.* (2005) uses the pressure Poisson equation in the form of Gurka *et al.*

(1999) to examine flow over a cylinder at a Reynolds number of 2000. For their formulation, they used the Neumann boundary condition around the cylinder and a homogeneous Dirichlet condition for the outer boundary. They also extended upon the result from Gurka *et al.* (1999) by using this method in both an instantaneous sense as well as the time averaged result. From the pressure field they calculated the forces and showed that they match quite well with previous results.

A new spatial integration technique to solve for the pressure field from the pressure gradient field was developed by Liu & Katz (2006). Their first attempt involved integrating the acceleration terms for each internal node from each boundary node along the shortest path to the node of interest, as shown in figure 1.3(a). However, this method was extremely computationally expensive. In order to reduce the time for computation, the authors used only the boundary locations in their integration. Instead of solving pressure at each internal node, they used the boundary points and integrated from "each of the boundary node to all other boundary nodes" and stored the data as it passed through the internal nodes (figure 1.3(b)). This alteration reduced the computation time, but also increased the bias error due to improper weighting near the boundaries. Finally, they decided to incorporate a set of virtual boundaries (figure 1.3(c)) outside of the image boundary and solved from those boundary points. They called their method the "omni-directional virtual boundary integration scheme." According to the authors, this technique helps to "minimize the effect of local random error."

Murai *et al.* (2007) performs a study using particle tracking velocimetry (PTV) in which they compare the pressure field estimation based on the Navier-Stokes equation to the pressure Poisson formulation for flow over a Savonius turbine. In their work they start by taking the PTV data and interpolate it onto a grid (such that it now resembles PIV data). In their formulation, the estimation based on the Navier-Stokes equations use the homogeneous Neumann boundary conditions while the estimation employing the Poisson formulation uses either uniform Dirichlet or Neumann conditions. The authors state that the Poisson equation can be based on an instantaneous field while the Navier-Stokes approach requires

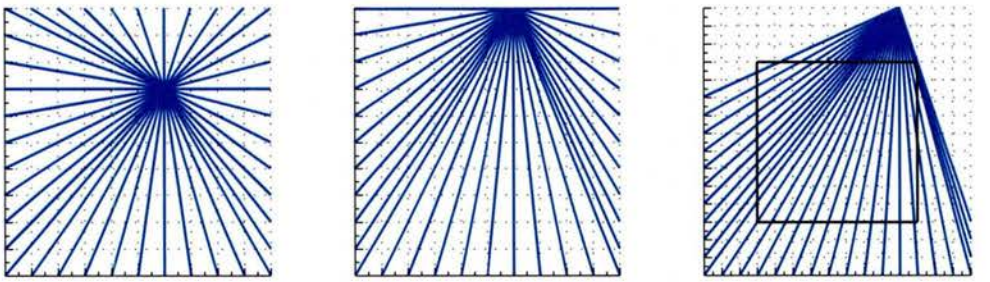

(a) "Shortest path omni-directional integration"

(b) "Omni-directional integration originating at boundaries"

(c) "Virtual boundary omni-directional integration"

Figure 1.3: Spatial pressure integration algorithms (adapted from Liu & Katz (2006))

a time series of velocity fields. They also showed that the pressure Poisson formulation is much less sensitive to random noise than the Navier-Stokes equations, but that the Poisson version relied more heavily on boundary conditions.

Charonko *et al.* (2010) compared a number of different, previously proposed, methods of solving for the pressure field from PIV. They compared several different direct spatial integration methods (multi-lines and the omni-directional method from Liu & Katz (2006)) and different versions of the Poisson equation, all from an Eulerian viewpoint. They studied both internal and external flows, and found that the direct spatial integration was preferable for internal flows and the Poisson formulation excelled for external flows. The authors also found that the error in all of the methods was highly influenced by velocity measurement error, with results becoming "unusable" when velocity error levels grew to even one to two percent. Then they studied the effect of temporal and spatial resolution. They discovered that some optimal spatial resolution existed, but that over-sampling in space was much preferred to undersampling while temporal resolution did not effect the results significantly. Finally, the authors studied the effect of misalignment of the PIV field and showed that for angles as great as thirty degrees, two-dimensional schemes worked well. The authors concluded by stating that there is "no optimum method for estimating the pressure field

and the resulting error will depend highly on the type of flow."

Shortly afterwards, de Kat & van Oudheusden (2010) performed a comparative study which used both simulated PIV data on a convecting Gaussian vortex and experimental data from flow over a square cylinder. In this paper, they studied both Lagrangian and Eulerian frames, both the direct spatial integration and the Poisson formulation and also considered three-dimensional effects by the use of both time-resolved stereo- and tomographic-PIV. For the direct spatial integration they used the method from Baur & Kongeter (1999). When they studied the analytic case, they found that the Poisson formulation was vastly outperforming the direct spatial integration and decided to only consider the Poisson method. After this they studied the influence of the Lagrangian versus the Eulerian method. They found that the Eulerian method is quite accurate while the Lagrangian version has errors near the peak of approximately 5 percent. Then, they studied the impact of noise and showed that it affected both the Lagrangian and Eulerian methods, but seemed to have a slightly greater impact on the Eulerian formulation. After looking at each individual error source for the analytic case, the authors suggest that, in general, the accuracy is increased by decreasing noise or increasing temporal and/or spatial resolution. In the experiments, they confirmed what they saw in the analytic tests. They also noted that three-dimensional flow effects cause especially large inaccuracies in the two-dimensional Lagrangian result.

Violato *et al.* (2011) also studied the differences in Lagrangian and Eulerian methods for a set of rod-airfoil experiments. They show that the maximum time-step allowed for the Eulerian method is even larger than the minimum separation for the Lagrangian method. They also show that the error in the material acceleration term is approximately 1.5 times higher for the Eulerian than the Lagrangian method. They also showed that both of the methods were quite resistant to three-dimensional effects as long as the data plane was well aligned with the flow; if the plane was significantly skewed then the out-of-plane components dominate and the results are poor.

Most recently, in de Kat & van Oudheusden (2012), a comprehensive comparison of the PIV requirements for the Eulerian and Lagrangian forms is performed for both an

analytic and an experimental case. The authors start by pointing out that the viscous term is neglected because van Oudheusden (2008) shows that for a similar Reynolds number (Re = 9500) the viscous forces are more than two orders of magnitude smaller than the remaining terms. When looking at the analytical problem of a convecting Gaussian vortex, they find that the window size (or spatial resolution) should be at least 4 times smaller than the smallest structure of interest while the separation time (or temporal resolution) should be at least 10 times smaller than that of the highest frequency of interest. The authors also show that as overlap increase, the results generally improve, but as the spatial resolution increases the gains from overlap factor shrink. These results are confirmed by their experiments.

While many methods exist to solve the pressure field from velocity, several clearly stand out for the current problem, outlined in figure 1.4. PIV data lends itself nicely to Eulerian methods for determining the pressure gradient field and performs comparably to the Lagrangian method (de Kat & van Oudheusden, 2010; Violato *et al.*, 2011). In order to obtain the pressure field from the gradient field, the method employing the Poisson equation and momentum boundary conditions has performed better than direct spatial integration techniques throughout the comparative studies in the literature (Charonko *et al.*, 2010; de Kat & van Oudheusden, 2010, 2012). Therefore, these methods will be employed in the current estimation.

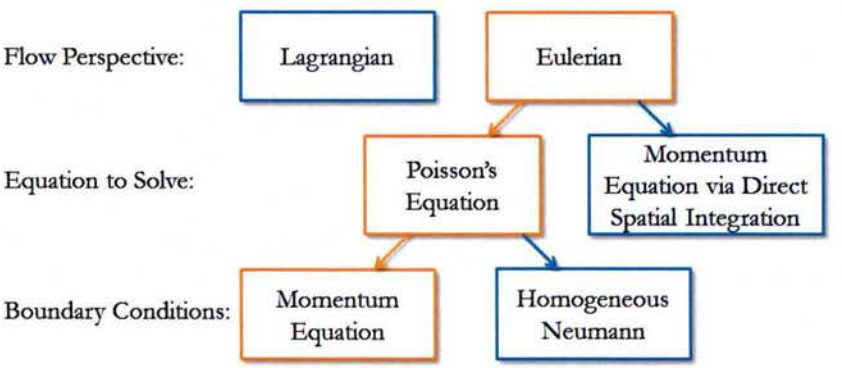

Figure 1.4: An overview of the Poisson solver choices shown in previous literature.

1.1.4 Acoustic Analogies in PIV

Aeroacoustic analogies allow for the near-field sources of sound to be modeled as acoustic sources to better understand their effect on the far-field. The first well-known acoustic analogy was developed by Lighthill (1952). In his landmark paper, Lighthill attempts to solve the problem of sound radiated from a subsonic fluctuating jet flow in a quiescent free-field. Lighthill develops the force terms of the Navier-Stokes momentum equation in a form that is suitable to the aforementioned problem which has since been denoted as the Lighthill stress tensor and applies it to the Navier-Stokes equations and the wave equation to obtain

$$\nabla^2 p(\mathbf{x},t) - \frac{1}{c^2}\frac{\partial^2 p(\mathbf{x},t)}{\partial t^2} = -\frac{1}{c^2}\frac{\partial^2 T_{ij}}{\partial x_i \partial x_j}. \tag{1.1.1}$$

By assuming a low Mach number solution, the Lighthill stress tensor becomes a function of only the Reynolds stresses. He goes on to shows that the solution is simply a "volume distribution of quadrupoles." He then describes the three ways that kinetic energy is converted to acoustic energy as: (1) "Forcing a mass in a fixed region of space to fluctuate," (2) "forcing the momentum in a fixed region of space to fluctuate," and (3) "forcing the rates of momentum flux across a fixed surface to vary," which describe mono-, di-, and quadru-poles, respectively. Applying the Lighthill form of the wave equation, he goes on to show the contribution to the density field of each source type mathematically, as a function of space and time. A scaling analysis is performed, and Lighthill shows that a distribution of quadrupoles scales like the eighth power of velocity.

Several years later, Curle (1955) extended the analogy of Lighthill (1952) by adding a solid boundary. Beginning with the solution to the inhomogeneous wave equation derived by Stratton (1941), Curle shows that in the presence of a solid boundary, an additional term is added on to the Lighthill solution. This term involves integration of fluctuating pressure over the surface area and Curle points out that this term is simply a "surface distribution of dipoles." Curle then goes on to perform a scaling analysis and shows that the surface dipoles scale like the sixth power of velocity.

Mention should be made of another analogy commonly used in the literature. The vortex sound analogy was developed by Powell (1964). This theory proposed that sound is generated by vortices moving through unsteadiness in flow. Howe (1975) showed that this theory was identical to Lighthill's by converting the source terms from Lighthill to terms representing vorticity transfer and formation of turbulent eddies. The four term representation developed by Howe reduces to a single important term at low Mach numbers where Lighthill's stress tensor is replaced by the divergence of the Lamb vector which gives,

$$\nabla^2 p(\mathbf{x},t) - \frac{1}{c^2}\frac{\partial^2 p(\mathbf{x},t)}{\partial t^2} = \frac{\partial}{\partial x_k}(\omega \times v)_k \tag{1.1.2}$$

However, the form of the analogy suggested by Howe requires the knowledge of a tailored Green's function representing the solid surface being studied. This is relatively straightforward for simple geometries (i.e. cylinders, flat plates) but requires a numerical computation for more complex geometries (i.e. airfoils) and therefore is not used in the present study.

Seiner & Ponton (1999) used PIV to study the noise sources in a free jet. The authors made the connection to Lighthill's analogy and proposed that the areas of largest Reynolds stress in the two-dimensional PIV are the dominant noise sources. The authors also mention that in order to fully understand the noise source field, they would need three-dimensional and time-resolved PIV.

Although our discussion will be primarily focused on experimental techniques involving PIV and analogies, a number of numerical simulations employing Curle's analogy have been performed and should be noted. For several examples of uses of Curle's analogy with CFD, see Inoue & Hatakeyama (2002); Larsson *et al.* (2004).

The first attempt at acoustic noise estimation by the use of PIV was made by Schroder *et al.* (2006). In this study, the authors looked at the trailing edge of a flat plate model using time-resolved PIV simultaneously with a directional microphone. In their method, they used the velocity and vorticity fields from PIV in a computational aeroacoustics (CAA) solver which employed the analogy in the form of Howe (1975). From the CAA solver, they

obtained the far field pressure.

In an attempt to distinguish the acoustically important noise sources in the near-field Henning *et al.* (2008) employed PIV along with microphone measurements. They studied two cases, flow over a cylinder and noise generated by a leading-edge slat-cove. Their method of identifying noise sources involved attempting to find a correlation between the microphone measurements and the fluctuating Lamb vector as determined from the PIV data. For each case, they took 5000 PIV snapshots at a rate of 10 Hz and synchronously took microphone data at 102.4 kHz. They found that, for the slat-cove case, the signal-to-noise ratio was too low and could not deduce any relevant noise structures. However, for the simpler cylinder case, they found that the locations of maximum shed vorticity contained the largest correlation. They also tried to correlate the microphone measurements to the POD modes, which they found gave no better results than the direct near-field quantities.

A method involving time-resolved PIV, Poisson's equation, and Curle's analogy is developed by Lorenzoni *et al.* (2009). In this study, the authors used a time-resolved PIV system to study noise produced by a rod-airfoil flow at a Reynolds number (based on cylinder diameter) of 3500 and their results were compared to microphone data taken simultaneously. The authors showed that the estimated spectra agreed well with the microphone measurements at frequencies at and below the shedding frequency. At higher frequencies the estimation was not as good, and the authors suggested that this was due to "the choice of a single spanwise coherence length for all scales." They were also able to determine the main source of noise and found that "the sources of the acoustic emission is concentrated in the first 20 percent of the airfoil surface where vortex-surface interaction produces the strongest unsteady pressure fluctuations." Their results showed that this method is suitable to estimate the far-field noise.

Around the same time Haigermoser (2009) used a similar method as described in Lorenzoni *et al.* (2009). Haigermoser studied flow over a two-dimensional cavity in a water tunnel by the use of a time-resolved planar PIV system. They did not mention their Reynolds number, but did specify a maximum freestream velocity of 0.36 meters per second over a cavity

with 10 millimeter depth. In order to determine the pressure field and surface forces required by Curle's analogy, Haigermoser used the method suggested by Liu & Katz (2006). They found that the spectra matched the literature quite nicely, but that the directivity pattern had produced slightly different results. The authors also mention that, because Curle's analogy depends highly upon surface pressures, "it would be of strong interest to improve PIV algorithms such that velocity data close to the wall becomes more reliable and better resolved." It should also be noted that while both Lorenzoni *et al.* (2009) and this study examined two-dimensional flows, they use the three-dimensional free-field Green's function in Curle's analogy.

Violato *et al.* (2010) studied a water jet at a Reynolds number of 5000 (based on jet diameter) employing time-resolved planar and tomographic PIV. Using the Lamb vector, they first determine the main sources of sound from both PIV methodologies. They show that the main noise source is from the vortex pairing. After this, they use the full analogy proposed by Howe (1975) to determine an estimate for the noise. The authors assume that the flow is axisymmetric and find that the prediction based on planar PIV matches well with the literature.

The method of Lorenzoni *et al.* (2009) was extended into three-dimensions by use of time-resolved tomographic PIV by Lorenzoni *et al.* (2010). The same experiment was studied and the authors showed that the two- and three-dimensional spectra had "minimal differences distributed along the whole bandwidth." They also noted that the small differences present in the three-dimensional version were mostly distributed at high frequencies. This agrees with the findings of Lorenzoni *et al.* (2009). The authors suggested that the main source of error was solving for the surface pressure and, in the future, they planned on solving for the Green's function numerically in order to use the analogy suggested by Howe (1975) instead of Curle's analogy to bypass this step.

Some recent studies using PIV and acoustic analogies include: (1) Liu & Katz (2011) used Curle's analogy to study flow over a cavity in a water tunnel at a Reynolds number of 40000 based on cavity length. (2) Koschatzky *et al.* (2011a) also used Curle's formula to

flow over a cavity in a wind tunnel at a Reynolds number of approximately 30000 based on cavity length. (3) Uda *et al.* (2011) used Powell's analogy to study a rod-airfoil configuration at a maximum Reynolds number of 2000 based on rod diameter.

There have also been several recent comparison studies. In Moore *et al.* (2011), the authors compare Curle's analogy in the time and frequency domains. They studied the results from Lorenzoni *et al.* (2009). They show that the results from both methods are similar at low frequencies and both overestimate the noise at high frequency, with the time version being closer to reality than the Fourier version. At the peak frequency, they showed that the Fourier formulation matches the microphone almost identically, while the time version is approximately 2 dB down.

Koschatzky *et al.* (2011b) used results from Koschatzky *et al.* (2011a) but also compare the Curle's analogy to the Vortex Sound Theory analogy results. They show that, while both match quite nicely to each other and microphone data, the Vortex Sound Theory tends to overestimate the effects of high frequency noise due to "difficulties in reducing the noise error." They also note that a slight difference from the microphone data at low frequency is seen and expected because their facility is not acoustically treated. They conclude by pointing out that Curle's analogy is more affected by temporal resolution, while the Vortex Sound Theory is heavily influenced by noise and has difficulty estimating at sharp corners because the Green's function is difficult to obtain there.

Again studying a cavity, but at a lower Reynolds number (12000), Koschatzky *et al.* (2012) compare results from two-dimensions to three-dimensions both taken with tomographic PIV. In this study, they find that for both Curle's and the Vortex Sound Theory analogies, the two- and three-dimensional flows show nearly identical spectral and directive content. They also showed the areas of "damaged or missing data" can have a large negative effect on the estimation.

Finally, Lorenzoni *et al.* (2012) studied the rod-airfoil configuration at a Reynolds number of 6000 based on rod diameter again to investigate the effects of spanwise coherence on the two-dimensional estimation. They began by showing that the estimated high frequency

component was overestimated when "full span coherence" was assumed. The authors then obtained PIV over the surface of the airfoil and found relative coherence lengths. After applying the correction for the coherence based on frequency, they showed that the levels were actually reduced to a lower magnitudes than the microphone measurement but achieved a better result nonetheless.

Several recent studies have looked at the combined use of PIV and various acoustic analogies; however, they have almost entirely been limited to low Reynolds numbers and cavity or rod-airfoil problems. In general, the results shown were promising with Curle's analogy outperforming the Vortex Sound Theory when sharp corners are present (Koschatzky *et al.*, 2011b). Because the circulation control airfoil has a very important, sharp jet lip, Curle's analogy will be used for these investigations.

1.2 Unresolved Technical Issues

Proper orthogonal decomposition, stochastic estimation, and Kalman smoother methods are well known and widely used; however, their use in time-resolved velocity field estimation is limited. Further, the experimental work to this point estimating the pressure field have relied on time-resolved PIV while pairing of the velocity field estimation with the pressure estimation has gone untested. Only very recently have experiments been paired with acoustic analogies. Experiments that have been conducted using Curle's analogy have been focused on only two problems of cavity flow and rod-airfoil configurations and those studies have been limited to low Reynolds number ranges.

While circulation control acoustics have come a long way in recent times, inconsistencies between experiments and theory remain (Wetzel *et al.*, 2012). Obtaining the necessary flow parameters to estimate circulation control acoustics is difficult, even constant temperature anemometry systems have sensor sizes on the order of the friction velocity layer height. Inaccuracies in these measurements propagate through to the final result leading to improper conclusions. While phased acoustic arrays demonstrate source localization, their use with

this problem has been limited to conventional beamforming and very few test conditions.

1.3 Technical Approach

To address the increased acoustic noise generated by circulation control, experiments will be performed on a circulation control airfoil model (studied previously by Wetzel *et al.* (2012)) at high Reynolds numbers. Spatially-resolved velocity measurements will be taken at intervals that are synchronized with time-resolved unsteady surface pressure measurements. The surface pressure measurements will be obtained via a series of recessed electret sensors along the centerline of the models trailing edge while the velocities will be acquired from a two-component particle image velocimetry (PIV) system. The PIV laser will be aligned as closely as possible with the recessed electret sensors. Acoustic data will be acquired simultaneously with the PIV and unsteady pressure data.

The dynamic estimator will then be used to estimate the low-order velocity field at all pressure measurement times. In this way a low-order, time-resolved velocity field is obtained. Then, the pressure field is determined from an Eulerian perspective and Poisson's equation is solved to compute a spatially- and temporally-resolved surface pressure field from the existing velocity field. From the surface pressures, the far-field acoustic radiation is determined via Curle's acoustic analogy.

This method will first be tested and validated on the case of two-dimensional simulated flow around a circular cylinder at low a Reynolds number. Once validated, the method will be tested experimentally, first on a planar wall jet at a moderate Reynolds number, then on an elliptic circulation control airfoil at a high Reynolds number. The results of the experimental prediction will be compared to far-field acoustic data obtained in the Florida State Aeroacoustic Tunnel for validation. If successful this method will provide a means by which estimation of a far-field acoustic pressure can be obtained in closed wall wind tunnels. The acoustic data obtained for validation will also be investigated to gain understanding of the potential source mechanisms of circulation control noise and associated scaling laws.

CHAPTER 2

THEORY OF EMPLOYED METHODS

This chapter contains theoretical background surrounding the methodology used in the far-field pressure prediction. It starts by reviewing the velocity estimation, which employs proper orthogonal decomposition and stochastic estimation. It then discusses the Poisson solver and concludes with Curle's acoustic analogy.

2.1 Velocity Estimation Background

A discussion of the main methodologies utilized in solving for the conditioned time-resolved velocity field from spatially-resolved PIV (with some limit on spatial resolution) and a limited number of time-resolved unsteady surface pressure probe measurements is provided. A brief overview of the velocity estimation is presented in Figure 2.1.

2.1.1 Proper Orthogonal Decomposition

Application of the POD provides a means to produce a reduced-order approximation of a set of data while (in the case of velocity data) maximizing the energy maintained (Holmes *et al.*, 2012). $\mathbf{u}(\mathbf{x}_m, t_n)$ is a vector containing all fluctuating velocity components (u', v', w') at each point in space $(\mathbf{x}_m)$, $m = 1$ to M at time (t_n), $n = 1$ to N. In this definition, M is the number of spatial locations and N is the number of snapshots. This vector can now be decomposed into spatial (φ) and temporal (a) coefficients by (Sirovich, 1987; Aubry *et al.*, 1992),

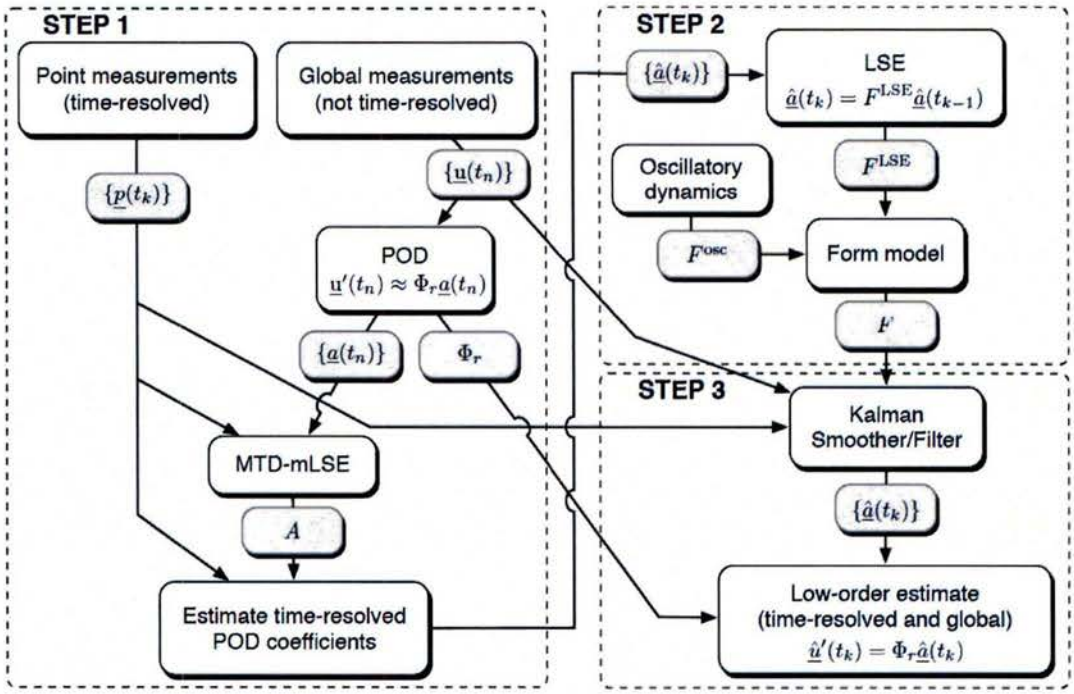

Figure 2.1: Overview of the velocity estimation procedure. (Used with permission from Griffin (2013).)

$$\mathbf{u}(\mathbf{x}_m, t_n) = \sum_{i=1}^{N} a_i(t_n)\varphi_i(\mathbf{x}_m). \tag{2.1.1}$$

In order to determine these coefficients the data matrix containing all spatial and temporal locations is given by:

$$X = \begin{bmatrix} \mathbf{u}(t_1) & \mathbf{u}(t_2) & \cdots & \mathbf{u}(t_n) \end{bmatrix},$$

where X is a real matrix of size kM by N, and k represents the number of velocity components per spatial location (i.e., 1 for hotwire measurements, 2 for 2-component PIV, 3 for stereo, tomographic, or plenoptic PIV).

There are two methods to compute the POD. The first method (the direct or the classical

method) involves solving the following eigenvalue problem (Lumley, 1967)

$$\int_x XX^T \varphi \mathrm{d}x = \lambda\varphi \tag{2.1.2}$$

where XX^T is the two-point correlation matrix in **space** with size kM by kM. Once solved, this method directly provides the POD spatial modes, φ (size kM by N), and the corresponding energy (eigenvalue) of each mode, λ. Since XX^T must be real and symmetric, the eigenvectors (or POD spatial modes φ) must be orthogonal,

$$< \varphi_i, \varphi_j >= \begin{cases} \varphi_i\varphi_j & \text{if } i = j. \\ 0 & \text{if } i \neq j. \end{cases} \tag{2.1.3}$$

The spatial modes are then normalized by λ,

$$\varphi = \frac{\varphi}{\lambda}, \tag{2.1.4}$$

to satisfy the orthonormal condition,

$$< \varphi_i, \varphi_j >= \begin{cases} 1 & \text{if } i = j. \\ 0 & \text{if } i \neq j. \end{cases} \tag{2.1.5}$$

With the normalized spatial POD modes and the original data, the POD temporal coefficients are obtained (Delville *et al.*, 1999),

$$a(t_n) = \frac{1}{M}\sum_{m=1}^{M} \mathbf{u}(x_m, t_n)\varphi(x_m). \tag{2.1.6}$$

The second method, known as the method of snapshots (Sirovich, 1987), requires the data to be ergodic in time. (Note that if the data are stationary or homogeneous in any spatial direction, a Fourier basis should be used first in that direction (Delville *et al.*, 1999)).

The method of snapshots relies on solving a similar equation to 2.1.2,

$$\int_t X^T X a dt = \lambda a \tag{2.1.7}$$

where $X^T X$ is the two-point correlation matrix in **time** with size N by N. Like the first method, the second method directly solves for the modal energy content, λ; however, instead of solving for the POD spatial modes, the temporal POD coefficients, a, are obtained. Using the temporal POD coefficients along with the original data set, the orthonormal POD spatial modes is obtained (Sirovich, 1987),

$$\varphi(x_m) = \frac{1}{N\lambda} \sum_{n=1}^{N} \mathbf{u}(x_m, t_n) a(t_n). \tag{2.1.8}$$

In order to account for the ortho-normalization of the spatial POD modes, the temporal POD coefficients are multiplied by λ such that,

$$a = a\lambda. \tag{2.1.9}$$

Once the POD modes and coefficients are obtained, the optimal reduced order approximation of the fluctuations, $\tilde{u}_n$ is calculated from

$$\tilde{u}(x_m, t_n) = \sum_{j=1}^{r} a_j(t_n) \varphi_j(x_m). \tag{2.1.10}$$

However, by applying POD in this way, homogeneities are ignored. Because a linear combination of the POD modes represents a low-order estimate of the velocity field, the POD retains the properties of the velocity field. Therefore, the boundary conditions and incompressibility of the flow are automatically satisfied (Sirovich, 1987). The difference between these two methods stems from the computational time required. Since the direct and snapshot methods require the solution of an kM-dimensional and N-dimensional eigenvalue problem, respectively, the direct method is more efficient when $kM < N$ and the snapshot

method is more efficient when $N < kM$. Additionally, the direct method allows one to handle flow symmetries and homogeneities where the POD reduces to Fourier analysis. In modern fluids applications, POD is generally applied via the method of snapshots because the spatial resolution is generally much better than the temporal resolution. For example, in the simulated flow-over-a-cylinder problem 1000 pairs of temporal snapshots are taken with 171 by 171 spatial locations (29241 total locations). Using the classical POD (on 2-component PIV) would rely on solving a 58482 by 58482 ($2M$ by $2M$) element eigenvalue problem while employing snapshot POD solves the same problem using only 1000 by 1000 (N by N) elements. An overview of the method of snapshots for a 2-velocity-component (u', v') is provided in figure 2.2. As shown in the figure, a singular value decomposition can be substituted for the eigenvalue problem with the same outcome. All POD performed for this document use the method of snapshots.

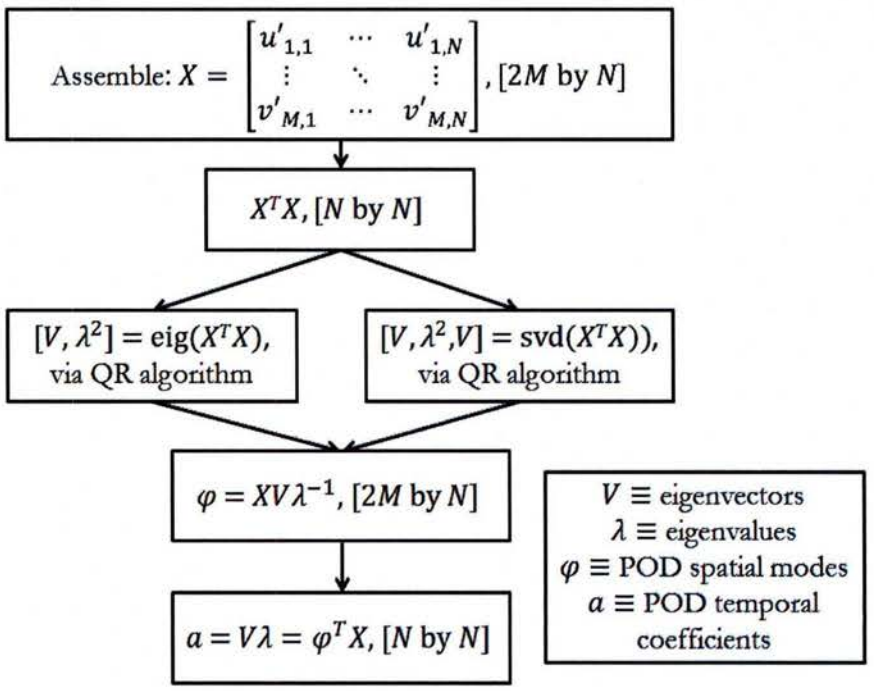

Figure 2.2: Overview of the Method of Snapshots applied to a 2-velocity-component dataset as processed in MATLAB.

2.1.2 Modified Stochastic Estimation

Stochastic estimation is a statistical estimation technique used to estimate a conditional average from unconditional data. Stochastic estimation uses a Taylor-series expansion to obtain a conditional average (Adrian & Moin, 1988)

$$\tilde{a}_i = \langle a_i | p_j \rangle = A_{ij} p_j + B_{ijk} p_j p_k + \ldots, \tag{2.1.11}$$

where a_i is the ith conditional measurement, $\tilde{[\cdot]}$ indicates an estimated quantity, p_j is the jth unconditional measurement, and $\langle \cdot \rangle$ denotes the expected value. In this document, a represents the POD coefficients and p indicates the fluctuating surface-pressure probe measurement. The coefficients of the Taylor series are determined by minimizing the mean square error of the estimation

$$E = \langle (\tilde{a}_i(t) - a_i(t))^2 \rangle. \tag{2.1.12}$$

Stochastic estimation employing the temporal POD coefficients, a, as the conditional variable is called "modified" stochastic estimation (Taylor & Glauser, 2004). Because the POD modes are ordered in such a way to optimally capture the energy of the low-order system, modified stochastic estimation provides a computationally efficient method to obtain an accurate low-order estimate of the full velocity field.

Modified stochastic estimation has been used by many sources in many applications. Taylor & Glauser (2004) used it a linear version, Murray & Ukeiley (2007) used a quadratic version, and Durgesh & Naughton (2010) used a linear version with multiple time delays. Each of these is discussed in detail in the following subsections.

Linear Stochastic Estimation. In linear stochastic estimation only the first term in equation 2.1.11 is retained, giving

$$\tilde{a}_i(t) = \sum_{j=1}^{N_p} A_{ij} p_j (t - \phi), \tag{2.1.13}$$

where N_p is the number of unconditional variables and ϕ represents a temporal shift allowing for a single lead or lag time between the conditional and unconditional variables. Incorporation of a constant time shift between the probes and the coefficients was suggested by Guezennec (1989) and Cole *et al.* (1992) to increase the correlation between the estimated value $\tilde{a}$ and probe measurement p, thereby reducing E. The linear coefficient is determined by the minimization of equation 2.1.12

$$\frac{\partial E}{\partial A_{ib}} = 2(A_{ij}p_j(t-\phi) - a_i(t))p_b(t-\phi), \tag{2.1.14}$$

which can be written as a set of linear equations,

$$\begin{aligned} A_{i,1}\overline{p_1(t-\phi)p_1(t-\phi)} + \cdots + A_{i,N}\overline{p_N(t-\phi)p_1(t-\phi)} &= \overline{a_i(t)p_1(t-\phi)} \\ &\vdots \\ A_{i,1}\overline{p_1(t-\phi)p_N(t-\phi)} + \cdots + A_{i,N}\overline{p_N(t-\phi)p_N(t-\phi)} &= \overline{a_i(t)p_N(t-\phi)}, \end{aligned} \tag{2.1.15}$$

where N is the number of probe measurements. $\overline{p_1(t-\phi)p_N(t-\phi)}$ represents a two-point correlation between a set of pressure measurements at the first and Nth probe locations with equal time lags. $\overline{a_i(t)p_N(t-\phi)}$ represents the correlation between the ith POD mode and the pressure signal at the first location with some time lag ϕ between them. This set of equations can be simplified into a matrix equation and solved for the linear coefficients as follows,

$$A_i = [\overline{PP}]^{-1}[\overline{a_iP}] \tag{2.1.16}$$

where A_i is size N by 1, $[\overline{a_iP}]$ represents the two-point correlation between the POD coefficients a and the pressure P of size N by 1, and $[\overline{PP}]$ represents the two-point correlation between the pressure probes of size N by N and are defined by,

$$[\overline{aP}] = \begin{bmatrix} \overline{a_i(t)p_1(t-\phi)} \\ \vdots \\ \overline{a_i(t)p_N(t-\phi)} \end{bmatrix}, [\overline{PP}] = \begin{bmatrix} \overline{p_1(t-\phi)p_1(t-\phi)} & \cdots & \overline{p_N(t-\phi)p_1(t-\phi)} \\ \vdots & \ddots & \vdots \\ \overline{p_1(t-\phi)p_N(t-\phi)} & \cdots & \overline{p_N(t-\phi)p_N(t-\phi)} \end{bmatrix}.$$

Multiple-Time-Delay LSE. Multiple-time delay mLSE (MTD-mLSE) can be used to increase correlations when the optimal time delay varies between probe measurements. MTD-mLSE also has the potential to reduce the effect of signal noise by increasing the number of data points used in the estimation. Ukeiley *et al.* (2008) used time delays in a strictly causal form, where Durgesh & Naughton (2010) used it in a non-causal manner. The following focuses on the non-causal version as it allows for increased accuracy, and real-time implementation is not desired.

Because multiple time delays are used in each estimate of the POD coefficient, equation 2.1.13 is re-written as follows

$$\tilde{a}_i(t) = \sum_{k=-m}^{m} \sum_{j=1}^{N} A_{ij}(\tau_k) p_j(t - \tau_k - \phi^*), \tag{2.1.17}$$

where $\tau_k = k\tau$, ϕ^* indicates the initial lead or lag time and m indicates the number of positive time delays being used. Because delays are generally used symmetrically, the total number of time delays used is $2m + 1$. For brevity we will set $t - \tau_{-k} = t_{-k}$. Therefore, the

equation set from equation 2.1.15 becomes

$$
\begin{aligned}
&A_{i,1}(\tau_{-m})\overline{p_1(t_{-m})p_1(t_{-m})} + \cdots + A_{i,1}(\tau_m)\overline{p_1(t_m)p_1(t_{-m})} + \ldots \\
&+A_{i,N}(\tau_{-m})\overline{p_1(t_{-m})p_1(t_{-m})} + \cdots + A_{i,N}(\tau_m)\overline{p_1(t_m)p_1(t_{-m})} \\
&= \overline{a_i(t)p_1(t_{-m})} \\
&\vdots \\
&A_{i,1}(\tau_{-m})\overline{p_1(t_{-m})p_1(t_m)} + \cdots + A_{i,1}(\tau_m)\overline{p_1(t_m)p_1(t_m)} + \ldots \\
&+A_{i,N}(\tau_{-m})\overline{p_N(t_{-m})p_1(t_m)} + \cdots + A_{i,N}(\tau_m)\overline{p_N(t_m)p_1(t_m)} \\
&= \overline{a_i(t)p_1(t_m)} \\
&\vdots \\
&A_{i,1}(\tau_{-m})\overline{p_1(t_{-m})p_N(t_{-m})} + \cdots + A_{i,1}(\tau_m)\overline{p_1(t_m)p_N(t_{-m})} + \ldots \\
&+A_{i,N}(\tau_{-m})\overline{p_N(t_{-m})p_N(t_{-m})} + \cdots + A_{i,N}(\tau_m)\overline{p_N(t_m)p_N(t_{-m})} \\
&= \overline{a_i(t)p_N(t_{-m})} \\
&\vdots \\
&A_{i,1}(\tau_{-m})\overline{p_1(t_{-m})p_N(t_m)} + \cdots + A_{i,1}(\tau_m)\overline{p_1(t_m)p_N(t_m)} + \ldots \\
&+A_{i,N}(\tau_{-m})\overline{p_N(t_{-m})p_N(t_m)} + \cdots + A_{i,N}(\tau_m)\overline{p_N(t_m)p_N(t_m)} \\
&= \overline{a_i(t)p_N(t_m)}
\end{aligned}
\tag{2.1.18}
$$

where $\overline{p_1(t_m)p_N(t_{-m})}$ represents a two-point correlation between a set of pressure measurements at the first and last locations with time lags of $m\tau$ and $-m\tau$, respectively, and $\overline{a_i(t)p_1(t_m)}$ represents the correlation between the ith POD mode and the pressure signal at the first location with a time lag $m\tau$. From these equations it is obvious that the equations are now expanded over both the number of probes and number of time delays. The solution to this equation set is given by solving equation 2.1.16; however, now, A_i, $[\overline{a_i P}]$, and $[\overline{PP}]$ are size $N(2m+1)$ by 1, $N(2m+1)$ by 1 and $N(2m+1)$ by $N(2m+1)$, respectively, now defined as,

$$A = \begin{bmatrix} A_{i,1}(\tau_{-m}) \\ \vdots \\ A_{i,1}(\tau_m) \\ \vdots \\ A_{i,N}(\tau_{-m}) \\ \vdots \\ A_{i,N}(\tau_m) \end{bmatrix}, \quad [\overline{aP}] = \begin{bmatrix} \overline{a_i(t)p_1(t_{-m})} \\ \vdots \\ \overline{a_i(t)p_1(t_m)} \\ \vdots \\ \overline{a_i(t)p_N(t_{-m})} \\ \vdots \\ \overline{a_i(t)p_N(t_m)} \end{bmatrix},$$

$$[\overline{PP}] = \begin{bmatrix} \overline{p_1(t_{-m})p_1(t_{-m})} & \cdots & \overline{p_1(t_m)p_1(t_{-m})} & \cdots & \overline{p_N(t_{-m})p_1(t_{-m})} & \cdots & \overline{p_N(t_m)p_1(t_{-m})} \\ \vdots & \ddots & \vdots & \ddots & \vdots & \ddots & \vdots \\ \overline{p_1(t_{-m})p_1(t_m)} & \cdots & \overline{p_1(t_m)p_1(t_m)} & \cdots & \overline{p_N(t_{-m})p_1(t_m)} & \cdots & \overline{p_N(t_m)p_1(t_m)} \\ \vdots & \ddots & \vdots & \ddots & \vdots & \ddots & \vdots \\ \overline{p_1(t_{-m})p_N(t_{-m})} & \cdots & \overline{p_1(t_m)p_N(t_{-m})} & \cdots & \overline{p_N(t_{-m})p_N(t_{-m})} & \cdots & \overline{p_N(t_m)p_N(t_{-m})} \\ \vdots & \ddots & \vdots & \ddots & \vdots & \ddots & \vdots \\ \overline{p_1(t_{-m})p_N(t_m)} & \cdots & \overline{p_1(t_m)p_N(t_m)} & \cdots & \overline{p_N(t_{-m})p_N(t_m)} & \cdots & \overline{p_N(t_m)p_N(t_m)} \end{bmatrix}.$$

There are now a total of $N(2m+1)$ equations that need to be simultaneously solved in order to determine the MTD-mLSE coefficients for each POD mode. Therefore, the cost of the MTD estimate is a significant increase in computation time and the use of non-causal data.

Quadratic Stochastic Estimation. For quadratic stochastic estimation the first two terms of the Taylor series (equation 2.1.11) are retained

$$\tilde{a}_i(t) = \sum_{j=1}^{N} A_{ij} p_j(t-\phi) + \sum_{l=1}^{N}\sum_{m=1}^{N} B_{ilm} p_l(t-\phi) p_m(t-\phi). \tag{2.1.19}$$

Minimizing the error requires taking the derivative with respect to A_{ib} and B_{icd} and setting the left hand side to zero, resulting in

$$\begin{aligned}\frac{\partial E}{\partial A_{ib}} = 2[&A_{ij}p_j(t-\phi) + B_{ilm}p_l(t-\phi)p_m(t-\phi) \\ &-a_i(t)]p_b(t-\phi) = 0,\end{aligned} \tag{2.1.20}$$

$$\begin{aligned}\frac{\partial E}{\partial B_{icd}} = 2[&A_{ij}p_j(t-\phi) + B_{ilm}p_l(t-\phi)p_m(t-\phi) \\ &-a_i(t)]p_c(t-\phi)p_d(t-\phi) = 0,\end{aligned} \tag{2.1.21}$$

which are written as the set of linear equations similar to those in equation 2.1.15 except they are solved for both the linear and quadratic coefficients and can be written in matrix form as

$$[AB] = [\overline{PP}]^{-1}[\overline{aP}],$$

where $[AB]$, $[\overline{aP}]$, and $[\overline{PP}]$ are size $N + N^2$ by 1, $N + N^2$ by 1, and $N + N^2$ by $N + N^2$ and defined by the following, letting $p_x = p_x(t-\phi)$ for brevity

$$A = \begin{bmatrix} A_{i,1}(\tau) \\ \vdots \\ A_{i,N} \\ \vdots \\ B_{i,1,1} \\ \vdots \\ B_{i,1,N} \\ \vdots \\ B_{i,N,N} \end{bmatrix}, [\overline{aP}] = \begin{bmatrix} \overline{a_i(t)p_1} \\ \vdots \\ \overline{a_i(t)p_N} \\ \vdots \\ \overline{a_i(t)p_1p_1} \\ \vdots \\ \overline{a_i(t)p_1p_N} \\ \vdots \\ \overline{a_i(t)p_Np_N} \end{bmatrix},$$

$$[\overline{PP}] = \begin{bmatrix} \overline{p_1p_1} & \cdots & \overline{p_1p_N} & \cdots & \overline{p_1p_1p_1} & \cdots & \overline{p_1p_1p_N} & \cdots & \overline{p_1p_Np_N} \\ \vdots & \ddots & \vdots & \ddots & \vdots & \ddots & \vdots & \ddots & \vdots \\ \overline{p_Np_1} & \cdots & \overline{p_Np_N} & \cdots & \overline{p_Np_1p_1} & \cdots & \overline{p_Np_1p_N} & \cdots & \overline{p_Np_Np_N} \\ \vdots & \ddots & \vdots & \ddots & \vdots & \ddots & \vdots & \ddots & \vdots \\ \overline{p_1p_1p_1} & \cdots & \overline{p_1p_1p_N} & \cdots & \overline{p_1p_1p_1p_1} & \cdots & \overline{p_1p_1p_1p_N} & \cdots & \overline{p_1p_1p_Np_N} \\ \vdots & \ddots & \vdots & \ddots & \vdots & \ddots & \vdots & \ddots & \vdots \\ \overline{p_1p_Np_1} & \cdots & \overline{p_1p_Np_N} & \cdots & \overline{p_1p_Np_1p_1} & \cdots & \overline{p_1p_Np_1p_N} & \cdots & \overline{p_1p_Np_Np_N} \\ \vdots & \ddots & \vdots & \ddots & \vdots & \ddots & \vdots & \ddots & \vdots \\ \overline{p_Np_Np_1} & \cdots & \overline{p_Np_Np_N} & \cdots & \overline{p_Np_Np_1p_1} & \cdots & \overline{p_Np_Np_1p_N} & \cdots & \overline{p_Np_Np_Np_N} \end{bmatrix}.$$

This system requires the simultaneous solution of $N(N+1)$ equations. Each of the estimated POD coefficients is then solved for by plugging the mQSE coefficients into equation 2.1.19. Clearly, MTD-mQSE would come at an even larger computational cost.

Method Cost Comparison for Two-Probe System. It is obvious that, due to the inclusion of higher-order terms, mQSE should have less error than mLSE for a single time delay. This may be especially true when estimating velocity based on a pressure measurement due to the quadratic dependence of pressure on velocity (Naguib *et al.*, 2001; Murray & Ukeiley, 2003). However, this accuracy comes at a cost. This additional expense is directly related to the number of terms within the matrix equations being solved. The matrix size for mLSE and mQSE with two probes are examined.

With two probes the $[\overline{PP}]$ matrix for mLSE becomes

$$[\overline{PP}]_{LSE} = \begin{bmatrix} \overline{p_1p_1} & \overline{p_1p_2} \\ \overline{p_2p_1} & \overline{p_2p_2} \end{bmatrix}.$$

However, with just two probes in mQSE, the $[\overline{PP}]$ matrix becomes

$$[\overline{PP}]_{QSE} = \begin{bmatrix} \overline{p_1p_1} & \overline{p_1p_2} & \overline{p_1p_1p_1} & \overline{p_1p_1p_2} & \overline{p_1p_2p_1} & \overline{p_1p_2p_2} \\ \overline{p_2p_1} & \overline{p_2p_2} & \overline{p_2p_1p_1} & \overline{p_2p_1p_2} & \overline{p_2p_2p_1} & \overline{p_2p_2p_2} \\ \overline{p_1p_1p_1} & \overline{p_1p_1p_2} & \overline{p_1p_1p_1p_1} & \overline{p_1p_1p_1p_2} & \overline{p_1p_1p_2p_1} & \overline{p_1p_1p_2p_2} \\ \overline{p_1p_2p_1} & \overline{p_1p_2p_2} & \overline{p_1p_2p_1p_1} & \overline{p_1p_2p_1p_2} & \overline{p_1p_2p_2p_1} & \overline{p_1p_2p_2p_2} \\ \overline{p_2p_1p_1} & \overline{p_2p_1p_2} & \overline{p_2p_1p_1p_1} & \overline{p_2p_1p_1p_2} & \overline{p_2p_1p_2p_1} & \overline{p_2p_1p_2p_2} \\ \overline{p_2p_2p_1} & \overline{p_2p_2p_2} & \overline{p_2p_2p_1p_1} & \overline{p_2p_2p_1p_2} & \overline{p_2p_2p_2p_1} & \overline{p_2p_2p_2p_2} \end{bmatrix}$$

Here we can see that the number of elements in mQSE (36) greatly outnumbers that of mLSE (4), even for a system with just two probes. We can extend this to compare MTD-mLSE to mQSE and we see that if $N > 2m$ then the cost of mQSE is greater and if $N < 2m$ then MTD-mLSE has a higher cost.

2.1.3 Model-Based Estimation

Stochastic estimation relies only on statistical relationships between a conditional and unconditional measurement; while this is desirable for its simplicity, it is not robust to noise. To reject noise in the velocity field estimation, model-based estimation techniques incorporate a model to improve the approximation. The model would ideally be based on the full Navier-Stokes equations, but this is presently unfeasible due to the associated computational cost. Instead, a model based on the estimated POD temporal coefficients is employed and improved by the measured POD coefficient data.

Kalman Filter and Smoother. The Kalman filter (Welch & Bishop, 1995) is a recursive predictor-corrector method. It is formulated by the following system of mathematical expressions.

$$x_k = Fx_{k-1} + m_k, \tag{2.1.22}$$

$$y_k = H_k x_k + n_k, \tag{2.1.23}$$

where x_k represents the state of the system at time k, F linearly maps the previous state, $k-1$ to the current state, k, m_k represents some process noise, y_k is a measured quantity, H_k denotes a measurement matrix, and n_k provides the sensor measurement noise. For this

discussion, the system state is represented by the estimated POD coefficients.

Equation 2.1.22 predicts the current state from the previous state, the process noise, and a system model (F). A natural choice for this reduced-order model (which should be linear for the standard Kalman filter) is POD because the modes are ordered in a manner such that the modes with the highest energy content occur first. The first r temporal coefficients are used to estimate the system model. From this, the accuracy of the model is based on the error of the original estimation of the POD coefficients and how well the model represents the system dynamics.

Equation 2.1.23 is the corrector phase of the two-step process. H_k is constructed based on the measurement method available at each time step. At time steps when a PIV measurement is available, H_k is set equal to the identity matrix so that the POD coefficients of that snapshot are used directly and not filtered. At times when only the time-resolved surface-pressure probe data are available, these data are used at each time step in the H_k matrix to help correct or weight the estimated POD coefficients such that n_k approximates the measurement noise.

A key assumption of the standard Kalman filter is that m_k and n_k are assumed to be zero mean, uncorrelated white noise with covariance matrices Q and R, respectively. The covariance matrices are user defined and are used to weight the accuracy of the sensor and model at each time. For example, if the sensor is known to be especially noisy, then the magnitude of R would be increased relative to Q so that the filter may rely more on the model than the noisy sensor. Alternatively, if the model is inaccurate, then R would be decreased relative to Q. For implementation on the PIV and probe-sensor estimation, the magnitude of R will be small at time steps with accurate full PIV data available and increased only when the pressure probe is relied upon. The values for Q and R for this study are discussed in the results section.

For implementation, the Kalman filter is first initialized ($k = 0$) with the stochastic-

estimated POD coefficients and P is defined as the covariance of the estimation as follows:

$$\hat{x}^+_{f,0} = E[\tilde{x}_0], \tag{2.1.24}$$

$$P^+_{f,0} = E[(\tilde{x}_0 - \hat{x}^+_{f,0})(\tilde{x}_0 - \hat{x}^+_{f,0})^T]. \tag{2.1.25}$$

Once the initial conditions are set, the equations are updated iteratively via the equation set for $k = 1, 2, \ldots, N_t$ (where N_t is the maximum number of times) from Simon (2006).

$$\begin{aligned} P^-_{f,k} &= F P^+_{f,k-1} F^T + Q_{k-1} \\ K_{f,k} &= P^-_{f,k} H_k^T ((K_k) P^-_{f,k} H_k^T + R_k)^{-1} \\ \hat{x}^-_{f,k} &= F \hat{x}^+_{f,k-1} \\ \hat{x}^+_{f,k} &= \hat{x}^-_{f,k} + K_{f,k}(m_k - H_k \hat{x}^-_{f,k}) \\ P^+_{f,k} &= (I - K_{f,k} H_k) P^-_{f,k} \end{aligned} \tag{2.1.26}$$

After the filter is used, a Kalman smoother variant (Rauch-Tung-Striebel [RTS] smoother) then performs a backward pass over the data. The smoothing step is initialized by the output of the filter as defined:

$$\begin{aligned} \hat{x}_{s,N_t} &= \hat{x}^+_{f,N_t} \\ \hat{P}_{s,N_t} &= \hat{P}^+_{f,N_t} \end{aligned} \tag{2.1.27}$$

Simon (2006) also defines the following set of smoother equations, which are iterated over values $k = N_t - 1, \ldots, 1, 0$.

$$\begin{aligned} K_{s,k} &= P^+_{f,k} F^T (P^-_{f,k+1})^{-1} \\ P_{s,k} &= P^+_{f,k} - K_{s,k}(P^-_{f,k+1} - P_{s,k+1}) K^T_{s,k} \\ \hat{x}_{s,k} &= \hat{x}^+_{f,k} + K_{s,k}(\hat{x}_{s,k+1} - \hat{x}^-_{f,k+1}) \end{aligned} \tag{2.1.28}$$

2.2 Pressure Field Calculation

This section discusses a method to calculate the temporally- and spatially-resolved pressure field from the previously estimated velocity field. The chosen method relies on an Eulerian approach to obtaining the pressure-gradient field because PIV data lends itself nicely to an Eulerian framework. It will also employ a Poisson solver as it has been shown to outperform the direct spatial integration (de Kat & van Oudheusden, 2010).

In order to obtain the pressure-gradient field, the Navier-Stokes equations are rearranged such that the pressure gradient stands alone on the left hand side. The general, three-dimensional momentum equation (in Eulerian form) then becomes

$$\frac{\partial p}{\partial x_i} = -\rho \left[\frac{\partial u_i}{\partial t} + u_j \frac{\partial u_i}{\partial x_j} - \nu \frac{\partial^2 u_i}{\partial x_j \partial x_j} \right]. \tag{2.2.1}$$

Because Curle's analogy is only dependent on fluctuating pressure, the above equation is separated into mean and fluctuating parts to obtain

$$\frac{\partial (P + p')}{\partial x_i} = -\rho \left[\frac{\partial (U_i + u_i')}{\partial t} + (U_j + u_j') \frac{\partial (U_i + u_i')}{\partial x_j} - \nu \frac{\partial^2 (U_i + u_i')}{\partial x_j \partial x_j} \right], \tag{2.2.2}$$

which can be expanded and simplified by removing the mean equation to obtain,

$$\frac{\partial p'}{\partial x_i} = -\rho \left[\frac{\partial (u_i')}{\partial t} + \frac{\partial (U_i u_j' + U_j u_i' + u_i' u_j' - \overline{u_i' u_j'})}{\partial x_j} - \nu \frac{\partial^2 u_i'}{\partial x_j \partial x_j} \right]. \tag{2.2.3}$$

The divergence of this equation, assuming incompressible flow and simplifying, offers a solvable form,

$$\frac{\partial^2 p'}{\partial x_i \partial x_i} = -\rho \left[\frac{\partial U_i}{\partial x_j} \frac{\partial u_j'}{\partial x_i} + \frac{\partial U_j}{\partial x_i} \frac{\partial u_i'}{\partial x_j} + \frac{\partial u_i'}{\partial x_j} \frac{\partial u_j'}{\partial x_i} - \frac{\partial^2 (\overline{u_i' u_j'})}{\partial x_j \partial x_i} \right], \tag{2.2.4}$$

where second-order central differences are used for the derivatives on the domain interior. Near the boundaries, ghost points (de Kat & van Oudheusden, 2012) along with forward and backward differences are employed for the derivative terms. To solve equation 2.2.4 a

standard five-point stencil is utilized and the system of equations generated are solved by Gaussian elimination. Some of the boundary conditions will rely on equation 2.2.3, to avoid error amplification the viscous term will be neglected (van Oudheusden, 2008) which gives,

$$\frac{\partial p'}{\partial x_i} = -\rho \left[\frac{\partial (u_i')}{\partial t} + \frac{\partial (U_i u_j' + U_j u_i' + u_i' u_j' - \overline{u_i' u_j'})}{\partial x_j} \right]. \tag{2.2.5}$$

2.3 Derivation of Curle's Analogy in the Time Domain

This section derives the general form of Curle's analogy in the time domain. The derivation follows from Goldstein (1976), Inoue & Hatakeyama (2002), and Gloerfelt *et al.* (2005).

2.3.1 The Acoustic Wave Equation

The general forced wave equation in space and time is given as:

$$\nabla^2 p(\mathbf{x}, t) - \frac{1}{c^2} \frac{\partial^2 p(\mathbf{x}, t)}{\partial t^2} = q(\mathbf{y}, t), \tag{2.3.1}$$

where c indicates the speed of sound and $p(\mathbf{x}, t)$ is fluctuating pressure as a function of space and time and $q(\mathbf{y}, t)$ is the source term. The source term for this document involves the Lighthill stress tensor, defined as (Lighthill, 1952),

$$T_{ij} = \rho u_i' u_j' + P_{ij} + c^2 \rho \delta_{ij}, \tag{2.3.2}$$

where u_i' defines the fluctuating velocity components, $P_{ij} = (p - p_0)\delta_{ij} - \sigma_{ij}$ is the compressive stress tensor, and ρ is density yielding,

$$q(\mathbf{y}, t) = -\frac{1}{c^2} \frac{\partial^2 T_{ij}}{\partial x_i \partial x_j}. \tag{2.3.3}$$

Lighthill (1952) shows that at low Mach numbers the stress tensor can be simplified to,

$$T_{ij} = \rho u_i u_j. \tag{2.3.4}$$

2.3.2 Green's Formulation

First, a finite volume $\mathbf{V}$ is defined. $\mathbf{V}$ is bound by the stationary surface Σ where p (or ρ) satisfies equation 2.3.1 outside of the volume. Σ is defined by the equation $f = 0$ where $f > 0$ inside and $f < 0$ outside of $\mathbf{V}$. This definition allows us to multiply equation 2.3.1 by the Heaviside function $\mathbf{H(f)}$, defined as (Duffy, 2001)

$$H(f) = \begin{cases} 1, & f < 0 \\ 0, & f > 0 \end{cases} \tag{2.3.5}$$

and maintain a form which is valid outside of $\mathbf{V}$, zero elsewhere, and therefore valid everywhere.

$$H(\nabla^2 p - \frac{1}{c^2}\frac{\partial^2 p}{\partial t^2}) = Hq \tag{2.3.6}$$

Employing the chain rule

$$\nabla^2 Hp = \nabla \cdot (p\nabla H + H\nabla p) \tag{2.3.7}$$

$$\nabla^2 Hp = \nabla \cdot (p\nabla H) + \nabla H \cdot \nabla p + H\nabla^2 p \tag{2.3.8}$$

Rearranging this equation and plugging in to 2.3.6, while noting that $\dfrac{\partial H}{\partial t} = 0$ since the surface is stationary, the following is obtained

$$\nabla^2 Hp - \frac{1}{c^2}\frac{\partial^2 p}{\partial t^2} Hp = Hq + \nabla H \cdot \nabla p + \nabla \cdot (p\nabla H) \tag{2.3.9}$$

It is known that some non-unique Green's function $G = G(\mathbf{x}, \mathbf{y}, t, t')$ will also satisfy

2.3.1 in the form:

$$\nabla^2 G - \frac{1}{c^2}\frac{\partial^2}{\partial t^2}G = \delta(t-t')\delta(\mathbf{x}-\mathbf{y}) \tag{2.3.10}$$

where this Green's function represents the result at $\mathbf{x}$ and t to some impulse at $\mathbf{y}$ at t'. Now the Green's function is convolved with the wave equation to solve for p

$$(\nabla^2 - \frac{1}{c^2}\frac{\partial^2}{\partial t^2})Hp * G = Hq * G + (\nabla H \cdot \nabla p + \nabla \cdot (p\nabla H)) * G, \tag{2.3.11}$$

where convolution is defined by:

$$h(t) * x(t) = \int_{-\infty}^{\infty} h(\tau)x(t-\tau)d\tau. \tag{2.3.12}$$

Employing the above definition to obtain,

$$\begin{aligned}\iiiint_{-\infty}^{\infty}(\nabla^2 - \frac{1}{c^2}\frac{\partial^2}{\partial t^2})HpGd\mathbf{y}dt' = \iiiint_{-\infty}^{\infty} HqGd\mathbf{y}dt' \\ + \iiiint_{-\infty}^{\infty}(\nabla H \cdot \nabla p + \nabla \cdot (p\nabla H))Gd\mathbf{y}dt'.\end{aligned} \tag{2.3.13}$$

The following relations become apparent from the definitions of the Green's function (equation 2.3.10) and Heaviside function (equation 2.3.5)

$$\iiiint_{-\infty}^{\infty}(\nabla^2 - \frac{1}{c^2}\frac{\partial^2}{\partial t^2})HpGd\mathbf{y}dt' = \iiiint_{-\infty}^{\infty}\delta(t-t')\delta(\mathbf{x}-\mathbf{y})Hpd\mathbf{y}dt' = p(\mathbf{x},t). \tag{2.3.14}$$

Since the Green's function must be causal and employing 2.3.5 once again,

$$\iiiint_{-\infty}^{\infty} HqGd\mathbf{y}dt' = \int_{-\infty}^{t}\iiint_{V} qGd\mathbf{y}dt'. \tag{2.3.15}$$

For the final term, the function is expanded such that G is included into the gradients and the chain rule is employed, this gives

$$\iiiint_{-\infty}^{\infty}(\nabla H \cdot \nabla p + \nabla \cdot (p\nabla H))Gd\mathbf{y}dt' = \int_{-\infty}^{t}\iiint_{-\infty}^{\infty}(G\nabla p - p\nabla G)\cdot\nabla H d\mathbf{y}dt'. \tag{2.3.16}$$

Finally, we obtain

$$p = \int_{-\infty}^{t} dt' \iiint_V qG d\mathbf{y} + \int_{-\infty}^{t} \iiint_{-\infty}^{\infty} (G\nabla p - p\nabla G) \cdot \nabla H d\mathbf{y} dt' \tag{2.3.17}$$

Using the fact that $\nabla H = \nabla f \delta(f)$ along with the definition of f such that $\nabla f/|\nabla f| = n_i$ the Green's formula in the time domain is achieved,

$$p = \int_{-\infty}^{t} \iiint_V qG d\mathbf{y} dt' + \int_{-\infty}^{t} \iint_\Sigma (G\frac{\partial p}{\partial x_i} - p\frac{\partial G}{\partial x_i}) n_i d\Sigma(\mathbf{y}) dt' \tag{2.3.18}$$

2.3.3 Free-Field Green's Function

The 2-D free-field Green function which is the solution to 2.3.10 in rectangular coordinates is given in Duffy (2001) as

$$G_0(\mathbf{x}, \mathbf{y}, t - t') = \frac{H(t - t' - |\mathbf{x} - \mathbf{y}|/c)}{2\pi\sqrt{(t - t')^2 - |\mathbf{x} - \mathbf{y}|^2/c^2}}. \tag{2.3.19}$$

The 3-D free-field Green function is given by Duffy (2001) as

$$G_0(\mathbf{x}, \mathbf{y}, t - t') = \frac{\delta(t - t' - |\mathbf{x} - \mathbf{y}|/c)}{4\pi|\mathbf{x} - \mathbf{y}|} \tag{2.3.20}$$

2.3.4 Generalized Curle's Analogy

Now that the Green's formulation and the Green's function have been defined the source term q is set to be Lighthill's stress tensor so equation 2.3.18 becomes

$$p = \int_{-\infty}^{t} \iiint_V (\frac{\partial^2 T_{ij}}{\partial x_i \partial x_j}) G_0 d\mathbf{y} dt' + \int_{-\infty}^{t} \iint_\Sigma (G_0 \frac{\partial p}{\partial x_i} - p\frac{\partial G_0}{\partial x_i}) n_i d\Sigma(\mathbf{y}) dt'. \tag{2.3.21}$$

Employing the chain rule on the volume term we can apply the differentiations to the Green's function by the following

$$\frac{\partial}{\partial x_i}\frac{\partial T_{ij} G_0}{\partial x_j} = \frac{\partial}{\partial x_j}\frac{\partial T_{ij} G_0}{\partial x_i}, \tag{2.3.22}$$

$$\frac{\partial}{\partial x_i}(T_{ij}\frac{\partial G_0}{\partial x_j} + G_0\frac{\partial T_{ij}}{\partial x_j}) = \frac{\partial}{\partial x_j}(T_{ij}\frac{\partial G_0}{\partial x_i} + G_0\frac{\partial T_{ij}}{\partial x_i}), \tag{2.3.23}$$

$$T_{ij}\frac{\partial^2 G_0}{\partial x_i \partial x_j} + \frac{\partial T_{ij}}{\partial x_i}\frac{\partial G_0}{\partial x_j} + \frac{\partial}{\partial x_i}(G_0\frac{\partial T_{ij}}{\partial x_j}) = G_0\frac{\partial^2 T_{ij}}{\partial x_i \partial x_j} + \frac{\partial T_{ij}}{\partial x_i}\frac{\partial G_0}{\partial x_j} + \frac{\partial}{\partial x_j}(T_{ij}\frac{\partial G_0}{\partial x_i}). \tag{2.3.24}$$

Simplifying the expression and solving for the familiar term from equation 2.3.21

$$G_0\frac{\partial^2 T_{ij}}{\partial x_i \partial x_j} = T_{ij}\frac{\partial^2 G_0}{\partial x_i \partial x_j} + \frac{\partial}{\partial x_i}(G_0\frac{\partial T_{ij}}{\partial x_j}) - \frac{\partial}{\partial x_j}(T_{ij}\frac{\partial G_0}{\partial x_i}). \tag{2.3.25}$$

This expression is then plugged into equation 2.3.21 to obtain

$$\begin{aligned} p = &\int_{-\infty}^{t}\iiint_V (T_{ij}\frac{\partial^2 G_0}{\partial x_i \partial x_j} + \frac{\partial}{\partial x_i}(G_0\frac{\partial T_{ij}}{\partial x_j}) - \frac{\partial}{\partial x_j}(T_{ij}\frac{\partial G_0}{\partial x_i}))d\mathbf{y}dt' \\ &+ \int_{-\infty}^{t}\iint_\Sigma (G_0\frac{\partial p}{\partial x_i} - p\frac{\partial G_0}{\partial x_i})n_i d\Sigma(\mathbf{y})dt'. \end{aligned} \tag{2.3.26}$$

And move the latter parts of the volume integral into a surface integral via divergence

$$\begin{aligned} p = &\int_{-\infty}^{t}\iiint_V (T_{ij}\frac{\partial^2 G_0}{\partial x_i \partial x_j})d\mathbf{y}dt' \\ &+ \int_{-\infty}^{t}\iint_\Sigma ((G_0\frac{\partial T_{ij}}{\partial x_j})n_i - (T_{ij}\frac{\partial G_0}{\partial x_i})n_j)d\Sigma(\mathbf{y})dt' \\ &+ \int_{-\infty}^{t}\iint_\Sigma (G_0\frac{\partial p}{\partial x_i} - p\frac{\partial G_0}{\partial x_i})n_i d\Sigma(\mathbf{y})dt'. \end{aligned} \tag{2.3.27}$$

Expanding T_{ij} into its full form (equation 2.3.2) in the surface integral terms, combining, and rearranging

$$\begin{aligned} p = &\int_{-\infty}^{t}\iiint_V (T_{ij}\frac{\partial^2 G_0}{\partial x_i \partial x_j})d\mathbf{y}dt' \\ &+ \int_{-\infty}^{t}\iint_\Sigma G_0\frac{\partial(\rho u_i u_j + P_{ij})}{\partial x_j}n_i d\Sigma(\mathbf{y})dt' \\ &- \int_{-\infty}^{t}\iint_\Sigma (\rho u_i u_j + P_{ij})\frac{\partial G_0}{\partial x_j}n_i d\Sigma(\mathbf{y})dt'. \end{aligned} \tag{2.3.28}$$

Conservation of momentum excluding external sources is employed to replace the second

term on the right hand side to obtain

$$\begin{aligned} p = &\int_{-\infty}^{t} \iiint_V (T_{ij} \frac{\partial^2 G_0}{\partial x_i \partial x_j}) d\mathbf{y} dt' \\ &+ \int_{-\infty}^{t} \iint_\Sigma G_0 \frac{\partial (\rho u_i)}{\partial t} n_i d\Sigma(\mathbf{y}) dt' \\ &- \int_{-\infty}^{t} \iint_\Sigma (\rho u_i u_j + P_{ij}) \frac{\partial G_0}{\partial x_j} n_i d\Sigma(\mathbf{y}) dt'. \end{aligned} \tag{2.3.29}$$

However, in the presence of a rigid body there must be no slip ($u_i = 0$) at the surface. The viscous stress terms are neglected. This simplifies equation 2.3.29 to

$$p = \int_{-\infty}^{t} \iiint_V (T_{ij} \frac{\partial^2 G_0}{\partial x_i \partial x_j}) d\mathbf{y} dt' - \int_{-\infty}^{t} \iint_\Sigma p_{ij} \frac{\partial G_0}{\partial x_j} n_i d\Sigma(\mathbf{y}) dt' \tag{2.3.30}$$

This is Curle's acoustic analogy (Curle, 1955) for a rigid body in a quiescent medium. The first term contains the quadrupole source contribution as shown by Lighthill (1952) and the second term provides the dipole source terms.

Given the Green function and Curle's acoustic analogy along with a velocity field and surface pressure field and using the form of Lighthill's stress tensor from equation 2.3.4, one can determine the acoustic field by taking the sum of the surface and volume integral such that the total acoustic pressure field is given by

$$p(\mathbf{x}, t) = \int_{-\infty}^{t} \iiint_V \rho u_i u_j \frac{\partial^2 G_0}{\partial x_i \partial x_j} d\mathbf{y} dt' - \int_{-\infty}^{t} \iint_\Sigma p_{ij} \frac{\partial G_0}{\partial x_j} n_i d\Sigma(\mathbf{y}) dt'. \tag{2.3.31}$$

2.3.5 2-D Curle's Analogy

Employing the Green function defined in equation 2.3.19 and recognizing $-p_{ij} n_j d\Sigma(\mathbf{y}) = f_i dL(\mathbf{y})$ the following is obtained

$$\begin{aligned} p(\mathbf{x}, t) = &\int_{-\infty}^{t} \iint_V \frac{\partial^2}{\partial x_i \partial x_j} \frac{\rho u_i u_j(\mathbf{y}, t')}{2\pi \sqrt{(t - t')^2 - |\mathbf{x} - \mathbf{y}|^2 / c^2}} d\mathbf{y} dt' \\ &- \int_{-\infty}^{t} \int_\Sigma \frac{\partial}{\partial x_i} \frac{f_i(\mathbf{y}, t')}{2\pi \sqrt{(t - t')^2 - |\mathbf{x} - \mathbf{y}|^2 / c^2}} d\Sigma \mathbf{y} dt', \end{aligned} \tag{2.3.32}$$

where $f_i = p_{ij}n_i$ is the pressure force exerted on the fluid in the i-direction by infinitesimal element $d\Sigma$. Assuming that the observer is either very far from the source or that the source is compact then $|\mathbf{x}-\mathbf{y}|=\mathbf{r}$. Employing retarded time $\tau = t - \mathbf{r}/c$ and using the chain rule to transfer spatial derivatives to time

$$\frac{\partial}{\partial x_i} = \frac{\partial}{\partial t'}\frac{\partial t'}{\partial x_i} = \left(-\frac{1}{c}\frac{x_i}{\mathbf{r}}\right)\frac{\partial}{\partial \tau},$$

and using the coordinate transform $t' = \tau + \tau'$,

$$\begin{aligned} p(\mathbf{x},t) =& \frac{x_i x_j}{2\pi c^2 \mathbf{r}^2}\int_{-\infty}^{0}\iint_V \frac{\partial^2}{\partial \tau^2}\frac{\rho u_i u_j(\mathbf{y},\tau+\tau')}{\sqrt{\tau'^2 - 2\mathbf{r}\tau'/c}}d\mathbf{y}d\tau' \\ &+ \frac{x_i}{2\pi c\mathbf{r}}\int_{-\infty}^{0}\int_\Sigma \frac{\partial}{\partial \tau}\frac{f_i(\mathbf{y},\tau+\tau')}{\sqrt{\tau'^2 - 2\mathbf{r}\tau'/c}}d\Sigma\mathbf{y}d\tau'. \end{aligned} \tag{2.3.33}$$

We now neglect the τ'^2 terms because "the integrals with respect to τ' are mainly contributed in the neighbourhood of $\tau' = 0$" (Inoue & Hatakeyama, 2002) and substitute back to t' to obtain the final full solution in two-dimensions

$$\begin{aligned} p(\mathbf{x},t) =& \frac{x_i x_j}{8^{1/2}\pi c^{3/2}\mathbf{r}^{5/2}}\int_{-\infty}^{\tau}\left[\frac{\partial^2}{\partial t'^2}\iint_V \rho u_i u_j(\mathbf{y},t')d\mathbf{y}\right]\frac{dt'}{\sqrt{\tau - t'}} \\ &+ \frac{x_i}{8^{1/2}\pi c^{1/2}\mathbf{r}^{3/2}}\int_{-\infty}^{\tau}\left[\frac{\partial}{\partial t'}\mathbf{F}_i(t')\right]\frac{dt'}{\sqrt{\tau - t'}} \end{aligned} \tag{2.3.34}$$

where $\mathbf{F}_i = \int_\Sigma p_{ij}n_i d\Sigma$ indicates the integrated pressure force in an axial direction.

The solution is then limited to low Mach numbers which allows the quadrupole term to be neglected.

$$p(\mathbf{x},t) = \frac{x_i}{8^{1/2}\pi c^{1/2}\mathbf{r}^{3/2}}\int_{-\infty}^{\tau}\left[\frac{\partial}{\partial t'}\mathbf{F}_i(t')\right]\frac{dt'}{\sqrt{\tau - t'}}. \tag{2.3.35}$$

This form has a singularity at the upper integration bound, which is handled by integration by parts, discussed in Appendix A. The final form (which will be employed in this paper) is obtained after the integration by parts as

$$p(\mathbf{x},t) = \frac{x_i}{8^{1/2}\pi c^{1/2}\mathbf{r}^{3/2}}\int_{-\infty}^{\tau}\left[2\frac{\partial^2}{\partial t^2}\mathbf{F}_i(t')\right]\sqrt{\tau - t'}dt' \tag{2.3.36}$$

This form assumes an infinite span due to the negative infinity lower integration bound. If a finite span is desired (as in this document) the lower bound is changed to $\tau - \tau_b$, where $\tau_b = t - \sqrt{\mathbf{r}^2 + (b/2)^2}/c$ and b indicates the span.

2.3.6 3-D Curle's Analogy

Employing the Green function defined in equation 2.3.20 along with equation 2.3.31 and, once again assuming low Mach number and a far-field observer, we obtain

$$p(\mathbf{x}, t) = \int_{-\infty}^{t} \frac{\partial}{\partial x_i} \frac{\delta(t - t' - \mathbf{r}/c)\mathbf{F}_i(t')}{4\pi\mathbf{r}} dt'. \tag{2.3.37}$$

Employing the delta functions sifting property and transferring the spatial derivative to temporal derivatives

$$p(\mathbf{x}, t) = \frac{x_i}{4\pi c\mathbf{r}^2} \frac{\partial}{\partial t}[\mathbf{F}_i(t - \mathbf{r}/c)], \tag{2.3.38}$$

where $\tau = t - \mathbf{r}/c$

2.3.7 Curle's Acoustic Analogy for a Plane Wall

The role of the pressure dipole in acoustic analogies has been the subject of some debate. It has been argued that the pressure dipole is purely an "equivalent" source, responsible for describing acoustic propagation rather than generation. In the case of an "infinite" plane wall Powell (1960) states that by the reflection principle, any surface dipole effect cancels out. This suggests "that the pressure exerted on a plane boundary are simply reflections of the quadrupole generators of the flow itself" (Powell, 1960). The pressure dipole then accounts for the enhancement of the quadrupole power due to reflection. While this may apply to the present case of a planer wall jet of sufficient downstream extent, it should be noted that for flows inhomogeneous in the direction of flow, diffraction about edges occurs and the role of the pressure dipole in that region changes. Therefore, for the simulated cylinder and the circulation control airfoil, it remains necessary to use Curle's acoustic analogy as presented in the previous section.

Powell addressed sound generation due to flow over a plane wall by formulating the problem as shown in figure 2.3. Here, a source region (V) partially encompasses a plane surface, S, with S_1 existing outside the source region and S_o existing within the source region. The method of reflections is then used to create a situation where an "image" source region is introduced such that the boundary conditions at S are met, with image variables denoted by the "prime" symbol and the point (X', Y') representing a point of observation.

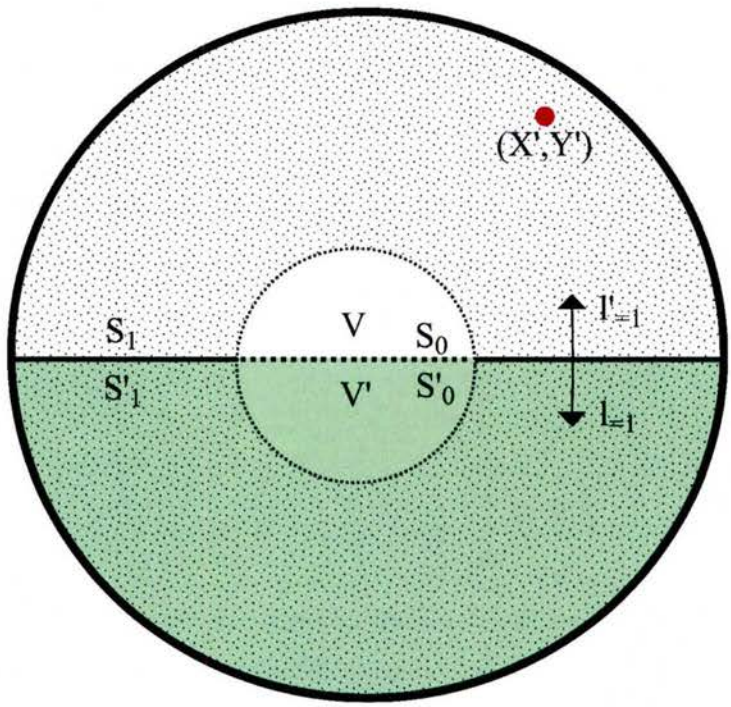

Figure 2.3: Plane wall with source field (V), image source field (V'), and example observation point at (X', Y'). The plane boundary has been divided into sections contained within the source region (S_o) and external from the source region (S_1).

For both the real source region and the image system, the assumptions used to derive Curle's acoustic analogy are valid and equations to described each region can be formulated as below. The systems have been defined in such a way that the pressure field outside of the real system is zero (equation 2.3.40),

$$4\pi(p-p_o) = \int_V \frac{1}{r}\frac{\partial^2 T_{ij}}{\partial x_i \partial x_j} dv + \int_{S_o} \frac{\partial}{\partial x_i}\frac{1}{r} l_j p_{ij} ds + \int_{S_1} \frac{\partial}{\partial x_i}\frac{1}{r} l_j p_{ij} ds, \tag{2.3.39}$$

$$0 = \int_{V'} \frac{1}{r}\frac{\partial^2 T_{ij}}{\partial x_i \partial x_j} dv + \int_{S_o'} \frac{\partial}{\partial x_i}\frac{1}{r} l_j p_{ij} ds + \int_{S_1'} \frac{\partial}{\partial x_i}\frac{1}{r} l_j p_{ij} ds. \tag{2.3.40}$$

Upon adding equations 2.3.39 and 2.3.40, it is apparent that any sources which radiate asymmetrically about the plane wall, will cancel out due to the corresponding, oppositely phased reflection sources. Therefore the pressure dipoles disappear, leaving only the volume quadrupoles of both the real and image fields as acoustic generation terms,

$$4\pi(p-p_o) = \int_{V+V'} \frac{1}{r}\frac{\partial^2 T_{ij}}{\partial x_i \partial x_j} dv. \tag{2.3.41}$$

In practical application, Powell (1960) found that is was useful to transfer the source distribution to the reflecting surface in a way that left the far-field radiation unaffected. Careful use of Taylor's expansion shows that point source radiation at a particular point may be represented by that identical source at a shifted location added with higher order sources at that shifted point to account for changes in the far-field. Therefore, if a source located a distance h above a plane is shifted down to the plane, with r representing the original absolute distance from source to observer and z representing the new absolute distance from source to observer, equation 2.3.42 can be formulated. In this equation R represents the far-field effect of a source,

$$F(r, t-\frac{r}{c_o}) = \sum_{n=0}^{\infty} \left(-h_k \frac{\partial}{\partial x_k}\right)^n F(z, t-\frac{z}{c_o}). \tag{2.3.42}$$

In the case of the quadrupole source of equation 2.3.41, this expansion is applied as shown below, with higher order terms neglected,

$$\frac{\partial^2}{\partial x_i \partial x_j}\frac{1}{z} T_{ij} dv + \frac{\partial^3}{\partial x_i \partial x_j \partial x_k}\frac{1}{z}\Big(-h_k T_{ij}\Big) dv + \ldots \tag{2.3.43}$$

These terms can then be substituted for the real and image system sources in equation

2.3.41. Before doing so however, it is helpful to divide the tensor T_{ij} into parts symmetric ($ST_{ij} = T_{11}, T_{22}, T_{33}, T_{23}, T_{32}$) about the plane and asymmetric ($AT_{ij} = T_{12}, T_{21}, T_{13}, T_{31}$) about the plane. For observer points in the far-field, the final equation arrived at by Powell (1960) takes the form shown below after substituting spatial derivatives for temporal derivatives,

$$4\pi(p - p_o) = \frac{z_i z_j}{z^3 c_o^2} \frac{\partial^2}{\partial t^2} \int_V 2ST_{ij} dv - \frac{z_i z_j z_k l_k}{z^4 c_o^3} \frac{\partial^3}{\partial t^3} \int_V 2hAT_{ij} dv. \tag{2.3.44}$$

It can be observed more clearly now that the effect of the surface is to double the acoustic generation from the symmetric portion of the stress tensor and to greatly reduce the asymmetric portion. Therefore the radiation field that results contains characteristics of a longitudinal quadrupole (due to the symmetric portion) and a lateral quadrupole (due to the asymmetric portion). This shows that the plane wall has a passive role, responsible for noise reflection instead of generation for the wall jet case.

CHAPTER 3

CYLINDER SIMULATION

3.1 Computational Setup

This section pertains to the setup of a simple computational test problem. A computational experiment is chosen because it provides a resolved data set in both space and time which can be used to evaluate the accuracy of the method. This problem will show both the potential applications of the current method, as well as show some limitations that may arise.

3.1.1 Problem Overview

Figure 3.1 shows an overview of the setup for the flow over a two-dimensional cylinder computation. For these computations, the Mach number is defined by $M = U_\infty/c_\infty$ where we let $c_\infty = 1$ such that $U_\infty = M$. The diameter of the cylinder is set to be unity. The Reynolds number (defined by $Re = U_\infty D/\nu_\infty$) for this section is chosen to be 150. This ensures that the simulation is fully two-dimensional, since it was shown experimentally by Cimbala *et al.* (1988) that three-dimensional effects start around a Reynolds number of 160.

3.1.2 Simulation Setup

A two-dimensional direct numerical simulation (DNS) is performed using CharLES from Cascade Technologies (Khalighi *et al.*, 2011). CharLES is an explicit compressible flow solver which employs a second order finite volume method in space and a third order Runge-Kutta

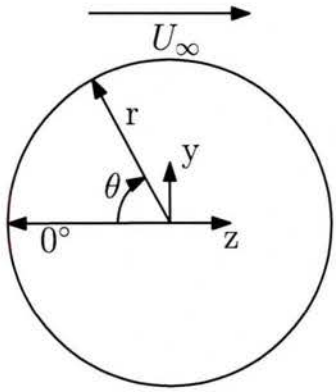

Figure 3.1: 2D cylinder in a uniform cross-flow. θ and r shown for reference.

scheme in time.

Grid Setup. In this simulation, an O-grid mesh with irregular spacing in the radial direction and regular spacing in the θ direction is employed. In the θ direction, the mesh is set such that $\Delta\theta = 0.725°$. In the radial direction, the grid is split into three regions, the boundary region, the data region, and the outer region. The grid as a whole is 496 by 769 grid points in the θ- and r-directions respectively. An overview of the setup and boundary conditions can be found in Figure 3.2 and the mesh is shown in Figure 3.3.

In the boundary region, grid spacing is set such that the small scales within the boundary layer are resolved. The boundary layer at this Reynolds number is $\delta \approx 0.08$ based on $\delta \approx 1/\sqrt{Re}$. The boundary region extends from the face of the cylinder at $r = 0.5$ to $r = 0.6$ in order to encompass the boundary layer. The spacing in this region is uniform in the radial direction with $\Delta r = 0.005$.

The data region is the region in which the majority of the pressure and velocity data are acquired (in addition to the boundary region). The data region extends out to $r = 150$ in all directions. In this region the spacing is allowed to vary from a match with the boundary region ($\Delta r = 0.005$ at $r_{boundary} = r_{data}$) up to the minimum spacing ($\Delta r = 0.6$) required for a second order solver in order to ensure acoustic propagation.

Outside of the data region is the outer region. This region is employed to allow for

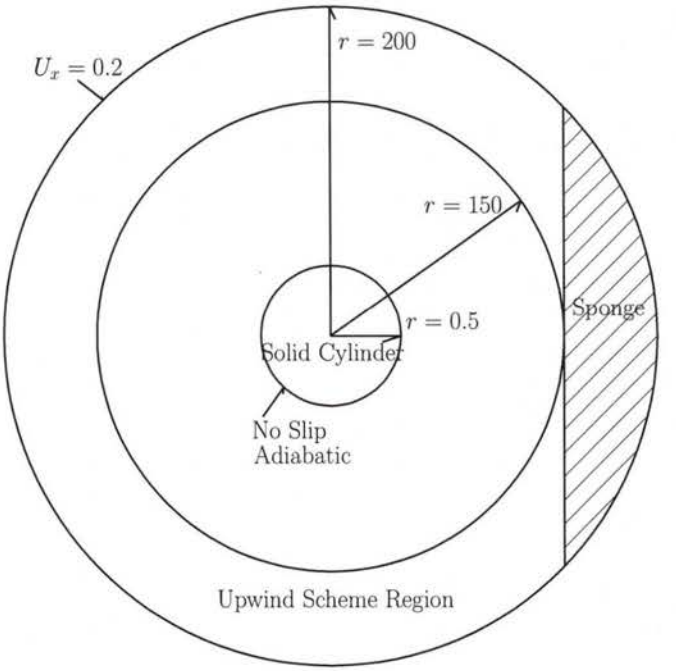

Figure 3.2: Overview of the 2D cylinder setup. Figure not to scale.

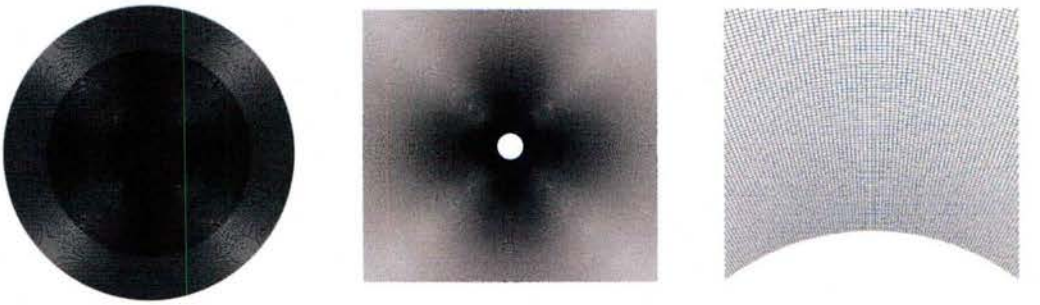

(a) View of full mesh (b) Zoomed in on cylinder (c) View of interior mesh

Figure 3.3: Several views of the mesh used in the simulation.

dissipation and prevent boundary reflection. In the outer region, the solver is changed to an upwind scheme in order to promote dissipation (see Khalighi *et al.* (2011) for more detail). In the area directly downstream of the cylinder (and within the outer region) a sponge region (Colonius *et al.*, 1997) is employed in order to introduce additional damping

in order to ensure the vortices which shed from the cylinder do not reflect. The spacing here matches the data region at $r_{data} = r_{outer}$ and grows geometrically outward to $r = 200$.

Initial and Boundary Conditions. An overview of the boundary conditions for this simulation is provided in Figure 3.2. On the cylinder face, $r = 0.5$, adiabatic and no-slip boundary conditions are used to impose a solid surface. At the outer boundary, $r = 200$, an in-flow/out-flow condition is maintained such that velocity in the flow direction, $U_z = 0.2$, velocity in the vertical direction, $U_y = 0$, pressure, $P_{ref} = 1/\gamma \approx 0.714$, and density, $\rho = 1$, are maintained constant. As discussed previously, the upwind scheme and sponge regions prevent reflections at the boundary.

The initial conditions are set to be the same as the parameters above for the outer boundary. Initially a small vortex is introduced just upstream from the cylinder in order break the symmetry and trigger the shedding instability. This vortex convects with the flow and dissipates as it moves. Data gathering occurs only after the vortex has convected fully out of the domain of the simulation.

3.2 Results and Discussion

This chapter discusses a computational solution to flow over a circular cylinder. This model problem is studied in order to better understand each step of the proposed methodology before moving onto the more complex flowfield involved in the wall jet and circulation control airfoil experiments. It begins by discussing the aerodynamic forces and near-field flow phenomena, then the pressure and velocity fields. It then examines the proper orthogonal decomposition and linear stochastic estimation and concludes with a discussion of the Poisson estimated near-field pressure and the Curle's analogy estimate of the far-field acoustics.

3.2.1 Aerodynamic Forces and Near-Field Flow

Figure 3.4 provides a time series of the forces acting on the cylinder in the form of coefficient of lift (C_l), coefficient of drag (C_d), and mean coefficient of pressure (C_p). The pressure coefficient curve contains the expected features from laminar flow over a two-dimensional cylinder at low Reynolds number. The stagnation point occurs at zero degrees and pressure drops until the flow separates at approximately 85 degrees. The profile here compares well with that in Inoue & Hatakeyama (2002).

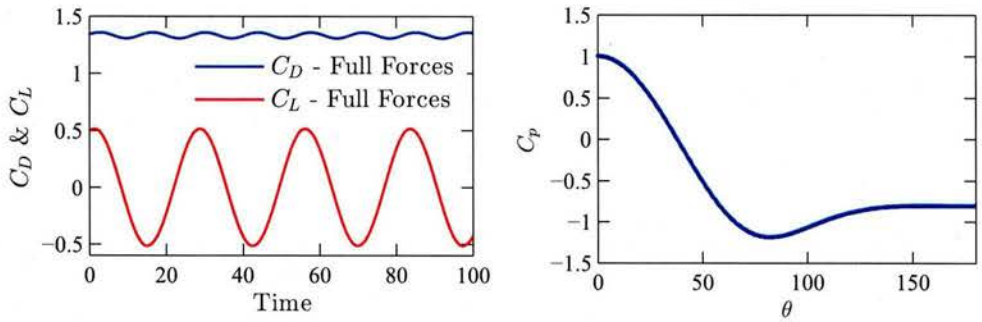

Figure 3.4: Aerodynamic forces on the cylinder. (a) contains the full force coefficients of lift and drag versus dimensionless convective time and (b) contains the coefficient of pressure from the cylinder surface versus θ.

The mean value of C_d is 1.33 with fluctuations about the mean of approximately 0.027 which matches the 0.026 found by Inoue & Hatakeyama (2002) well. The amplitude of the coefficient of lift is 0.52, which matches exactly the value found in Inoue & Hatakeyama (2002) and closely matches the value of 0.48 and 0.55 found by Kwon & Choi (1996) for Reynolds numbers of 140 and 160, respectively. Since the mean force does not matter in generating pressure fluctuations from a dipole source, we will expect the acoustic fluctuations due to the lift force to be much greater than that due to the drag force. This hypothesis is confirmed later in this section.

Since Curle's analogy will be investigated at the end of this section, it is also useful to compare the full forces (viscous and pressure) to the surface pressure forces alone. Curle's

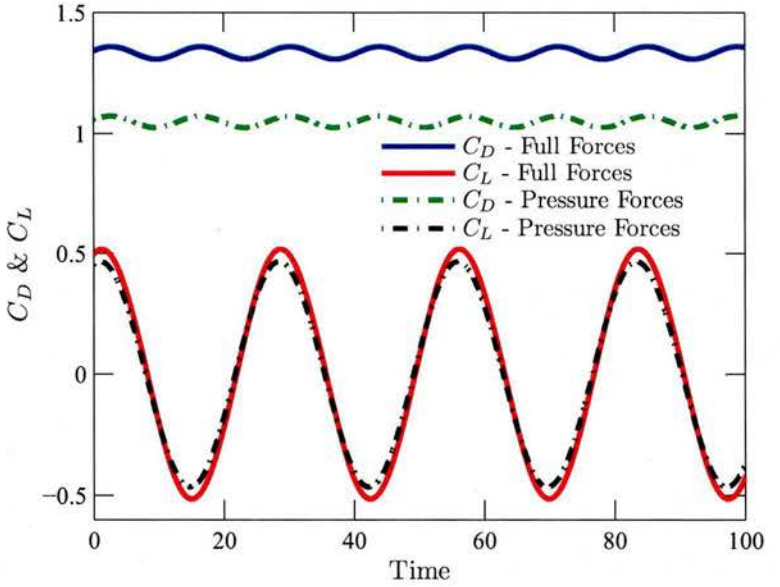

Figure 3.5: Comparison of full force and pressure force coefficient of lift and coefficient of drag.

analogy is typically utilized with only pressure forces since the viscous forces are difficult to measure. Figure 3.5 shows a time history of C_l and C_d for the full forces and the pressure forces. The first thing one notices is the significant reduction in the mean value of C_d down to 1.04 (or approximately a 22 percent decrease), which is expected due to the removal of the viscous forces. There is also a slight reduction in the amplitude of both the C_d and C_l lines. The new amplitudes are 0.025 and 0.47, respectively. We will see how these differences affect the outcome of the analogy later.

In figure 3.5 it is also shown that the period of lift and drag remain the same when comparing the full forces to the pressure forces. The period of lift oscillation is approximately 27.4 while the period of drag oscillation is roughly half that or 13.7 dimensionless convective time units. These periods indicate a Strouhal number (St) of 0.182 and 0.345, respectively. These estimates for St are confirmed by the first two peaks in figure 3.6. The lift Strouhal number matches very nicely with experimental data in Williamson (1989) who observed a St of 0.18 at the same Reynolds number as the current study.

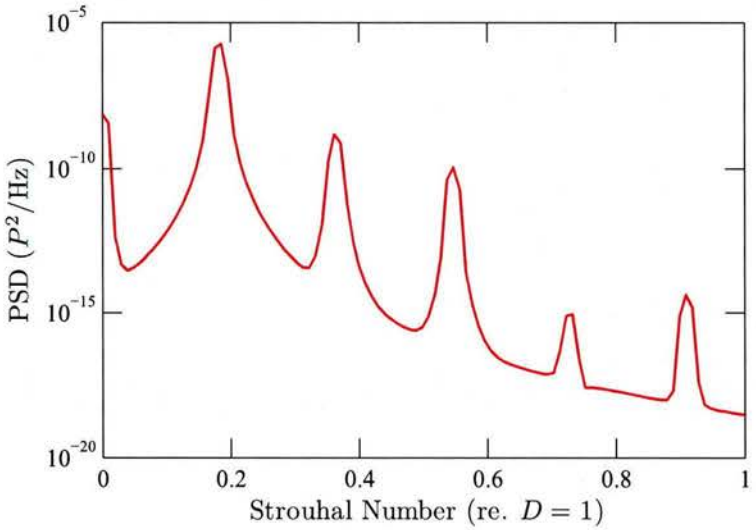

Figure 3.6: PSD versus Strouhal number. The first two peaks correspond to the lift and drag oscillations respectively; peaks after that contain higher harmonics.

3.2.2 Pressure Field

Figure 3.7 shows the total pressure field, P. In this figure, the positive pulses appear to propagate upstream while the negative pulses appear to propagate downstream. In order to gain an understanding of the pressure field, we will decompose the total pressure into the mean (steady) pressure and the fluctuating pressure by $P(\mathbf{x}, t) = \Delta P_{avg}(\mathbf{x}) + \Delta p'(\mathbf{x}, t)$.

Figure 3.8 shows the decomposed pressure field from the cylinder out to the far field. From this figure one can easily see that the reason for the appearance of different propagation angles is due to the mean pressure. When the mean pressure is removed from the total (figure 3.8 (c)) one can see that both positive and negative pressure fluctuations both propagate in the same direction and slightly upstream (due to the so-called Doppler effect, discussed later).

Figure 3.9 provides the total pressure, steady pressure, and fluctuating pressure for (a) an upstream location, (b) a downstream location, and (c) the angle of propagation of maximum pressure fluctuations. From this figure we can confirm that the maximum values of fluctuating pressure occur near the 78 degree line and decay in the positive and negative

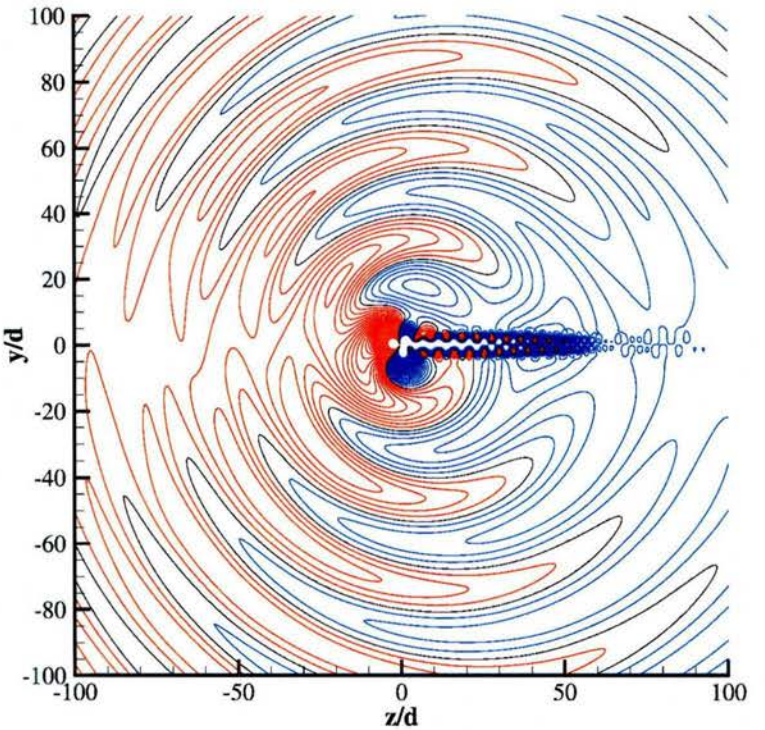

Figure 3.7: Total pressure field with Y and Z non-dimensionalized by the cylinder diameter. Contour levels for each are $-0.1M^{2.5}$ to $0.1M^{2.5}$ with steps of $0.0025M^{2.5}$ between contours (same levels used by Inoue & Hatakeyama (2002)). Orange indicates positive contours, blue indicates negative contours, and the black line indicates the zero contour.

azimuthal directions. These results match nicely with Inoue & Hatakeyama (2002) who found that the propagation angle is approximately 78.5°. Because Curle's analogy provides a representation of the far field pressure fluctuations, the discussion of the pressure field from this point on will be limited to the fluctuating pressure field ($\Delta p'$).

We can now decompose the fluctuating pressure field by a Fourier decomposition (Bendat & Piersol, 2010; Inoue & Hatakeyama, 2002):

$$\Delta p'(r,\theta,t) = \frac{a_0}{2} + a_1\cos(\theta) + b_1\sin(\theta) + a_2\cos(2\theta) + b_2\sin(2\theta) + \ldots \tag{3.2.1}$$

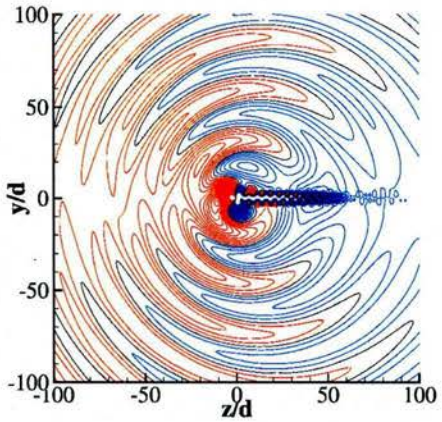

(a) Total pressure field

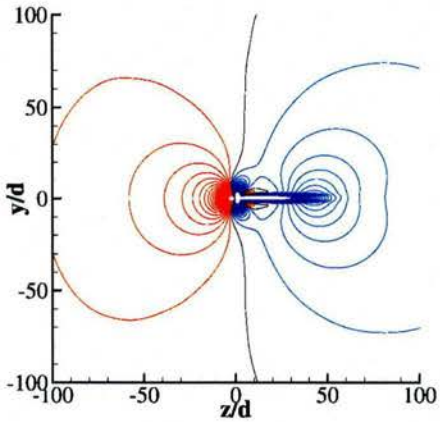

(b) Mean pressure field

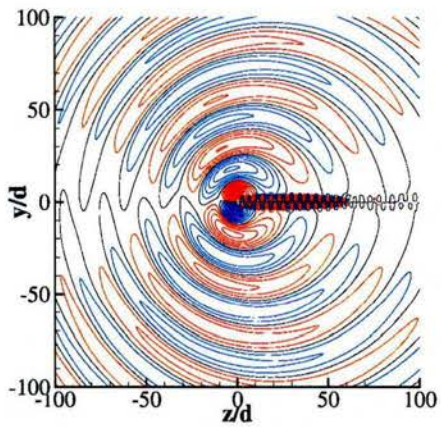

(c) Fluctuating pressure field

Figure 3.8: Pressure field decomposition. (a) shows the reference removed total pressure, (b) shows the mean pressure, and (c) shows the fluctuating pressure field. Contour levels are the same as Figure 3.7.

where the coefficients $a_0, a_1, b_1, ...$ are defined as follows

$$\begin{aligned} a_0 &= 1/\pi \int_0^{2\pi} \Delta p'(r,\theta,t) d\theta \\ a_n &= 1/\pi \int_0^{2\pi} \Delta p'(r,\theta,t) \cos(n\theta) d\theta \\ b_n &= 1/\pi \int_0^{2\pi} \Delta p'(r,\theta,t) \sin(n\theta) d\theta \end{aligned} \tag{3.2.2}$$

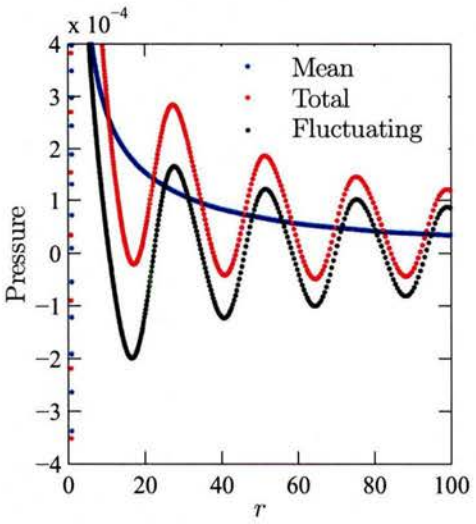

(a) Pressure versus radius at $\theta = 50°$

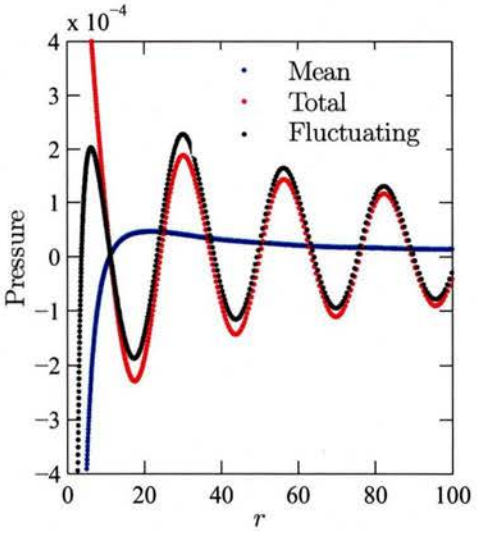

(b) Pressure versus radius at $\theta = 78°$

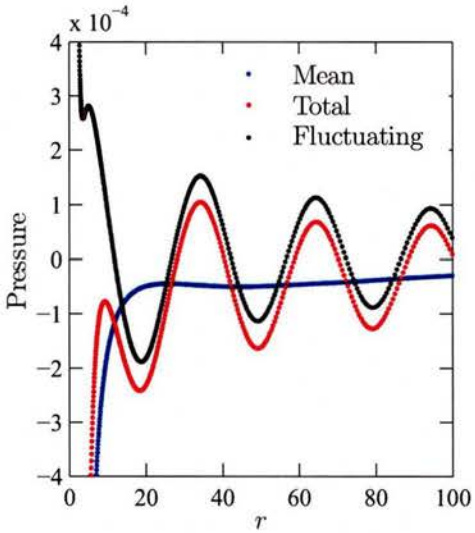

(c) Pressure versus radius at $\theta = 120°$

Figure 3.9: Pressure decomposition into mean, total, and fluctuating components at various theta values versus radius. (a) shows the $\theta = 50°$ line, (b) shows the $\theta = 78°$ line, and (c) shows the $\theta = 120°$ line.

The coefficients are especially useful as they define the contributions from the monopole (a_0), dipole, (a_1, b_1), and quadrupole (a_2, b_2) sources (Inoue & Hatakeyama, 2002). Figure 3.10 shows the contributions of the monopole, dipole, and quadrupole at $r = 75$ with respect

to the DNS result for fluctuating pressure at 90 degrees. This result seems to indicate that the dipole source is more prevalent than the other types, but is not the majority of the pressure signal. This result is due to the presence of the Doppler effect. When the Doppler effect is removed, the dipole is clearly the majority of the pressure in the far-field.

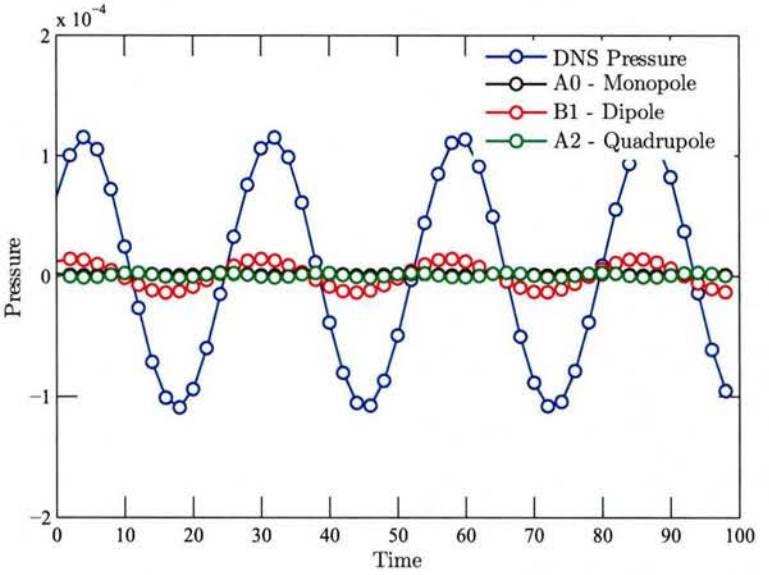

Figure 3.10: Fourier coefficients from pressure decomposition with the Doppler effect included, at $r = 75$ and $\theta = 90°$. The dipole dominates but still seems like a small portion of the pressure.

The Doppler Effect and the Doppler Removed Pressure Field. See appendix B for detailed derivation of the Doppler effect (also referred to as a Multi-pole expansion). In this context, the Doppler effect refers to the upstream propagation of pressure waves in the presence of a free-stream velocity. The primary result is the introduction of a fluctuation pressure in which the Doppler effect has been removed such that

$$\Delta p'(r,\theta,t) = \sum_{n=0}^{\infty} \Delta p_n^M(r',\theta,t) \left[\frac{r'}{r}\right]^n, \tag{3.2.3}$$

where $\Delta p_n^M(r',\theta,t)$ is the Doppler removed pressure fluctuations and $r' = r/(1 - M\cos\theta)$ as defined by Goldstein (1976). This result allows us to define the Doppler removed coefficients

similar to those in equation set 3.2.2,

$$\begin{aligned} a_0 &= 1/\pi \int_0^{2\pi} \Delta p^M(r', \theta, t) d\theta \\ a_n &= 1/\pi \int_0^{2\pi} \Delta p^M(r', \theta, t) \cos(n\theta) d\theta \\ b_n &= 1/\pi \int_0^{2\pi} \Delta p^M(r', \theta, t) \sin(n\theta) d\theta \end{aligned} \tag{3.2.4}$$

Figure 3.11 shows the results from equation set 3.2.4. With the Doppler effect removed, the

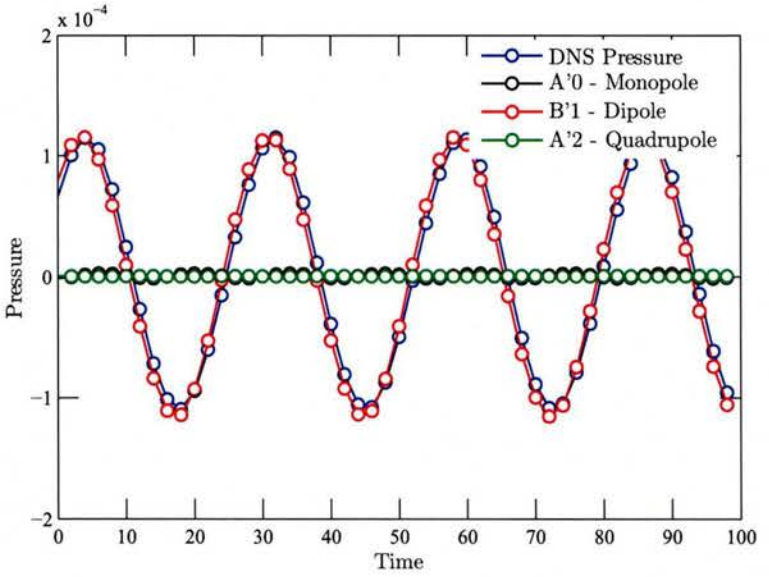

Figure 3.11: Fourier coefficients from pressure decomposition with the Doppler effect removed at $r = 75$ and $\theta = 90°$. The dipole clearly makes up the vast majority of the pressure signal.

dipole term matches the DNS pressure almost perfectly while the monopole and quadrupole terms remain almost non-existent. Because of the dominance of the dipole term we will make the assumption from here forward that $n = 1$ (where $n = 0$ and $n = 2$ would be the mono- and quadrupoles, respectively) or, stated another way,

$$\Delta p'(r, \theta, t) = \Delta p^M(r', \theta, t) \left[\frac{r'}{r}\right]. \tag{3.2.5}$$

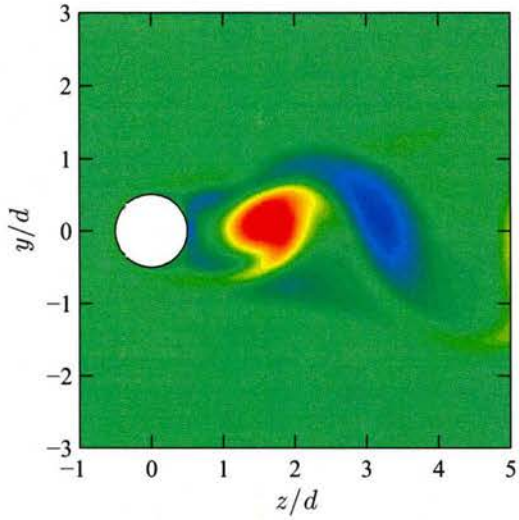

Figure 3.12: Instantaneous dimensionless fluctuating vorticity snapshot. Contour levels are from -1 to 1 with red being positive and blue negative.

3.2.3 Velocity Field Estimation

This section will discuss the estimation method involving proper orthogonal decomposition (POD), stochastic estimation (SE) and the Kalman filter/smoother to provide a low order estimation of the time resolved velocity field. Figure 3.12 shows a mean subtracted instantaneous vorticity field surrounding the cylinder body. At a Reynolds number of 150 we can see that the wake of the cylinder displays a Von Kármán vortex street. For the following, the data was downsampled in space in order to mimic the expected result from a PIV experiment. The domain is now limited to -3.2 to 3.2 diameters in the Y-direction and -1.2 to 5.2 diameters in the Z-direction with a resolution of 129 by 129 velocity vectors on an equally spaced Cartesian grid.

Proper Orthogonal Decomposition. As discussed in the theory section, POD provides the spatial distribution of energy in a field. Performing a POD analysis of the velocity field we see, from Figure 3.13, that over 95 percent of the total flow energy is contained in just the first two modes. The higher order modes are shown to contain significantly less energy and by the seventh mode, the energy contained is less than 0.05 percent per mode.

The first eight mode shapes are illustrated in figure 3.14. The highest energy modes can be seen to contain the largest coherent structures. We also note that these modes occur in pairs with similar structures and opposite phase.

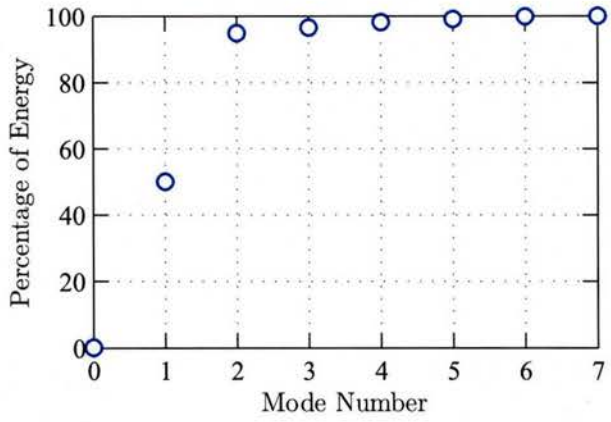

Figure 3.13: Percentage of energy contained in the first r modes.

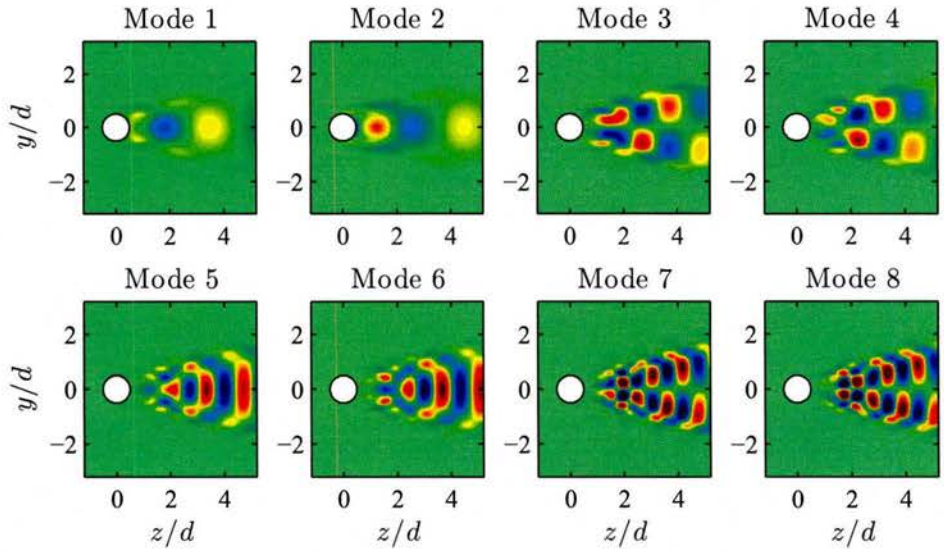

Figure 3.14: Spatial distribution of energy in POD modes one to eight.

While it might seem, based on energy, that two POD modes are sufficient for a good estimation of the flow field, it is shown in figure 3.15 that this is not the case. The figure

shows that in order to obtain a reasonable estimate of the fluctuating flow, it appears at least six modes are necessary. Figure 3.16 shows that reconstruction with more than six POD modes leads to diminishing returns. Therefore, the discussion that follows will focus on the first six POD modes.

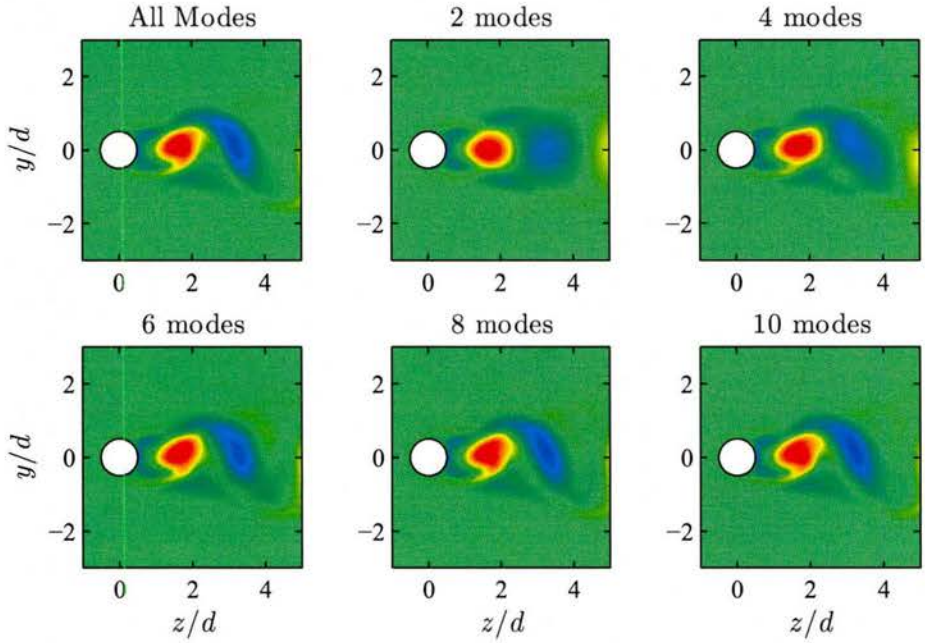

Figure 3.15: Reconstructed fluctuating dimensionless vorticity field based on an even number of POD modes from two to ten.

Modified Stochastic Estimation. As discussed previously, modified stochastic estimation (mSE) provides a means of estimating a time resolved set of POD modes given a non-time resolved POD data set and a time resolved probe signal. The probes used will be limited to unsteady surface pressure probes because this is the probe type used in all experimental work in this document. This section will provide discussion of several estimation cases. First, optimal pressure locations will be identified. Then the influence of the number of probes used will be investigated followed by a determination of an optimal initial time delay and number of time delays.

Since the proposed method does not require causality the non-causal version of the

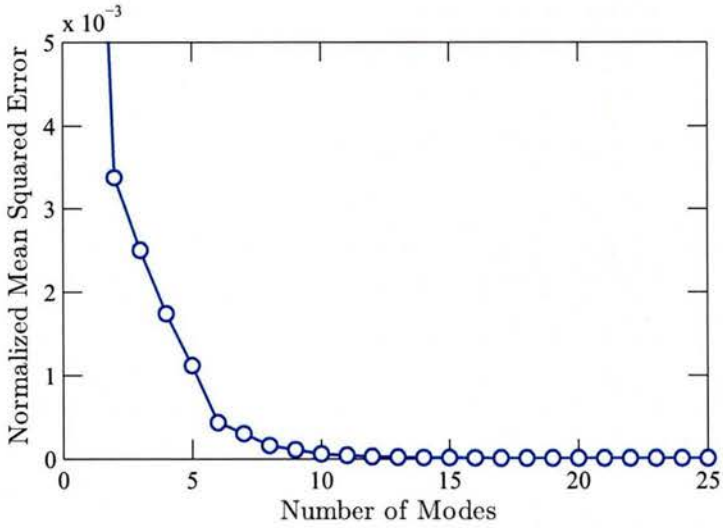

Figure 3.16: Mean squared error normalized by the maximum vorticity in the fluctuating vorticity reconstruction based on number of POD modes.

multi-time-delay mLSE (MTD-mLSE) will be employed. The MTD-mLSE method allows one to account for phase differences between the probe location and the field (Durgesh & Naughton, 2010). In order to use this method effectively a means of error estimation should first be defined. Tu *et al.* (2012) uses the following to estimate this error

$$e = \frac{\sum_{i=1}^{r}[\tilde{a}_i - a_i]^2}{\sum_{i=1}^{r}[a_i]^2} \tag{3.2.6}$$

where a and $\tilde{a}$ provide the known and estimated POD coefficient and r is the number of modes used in the estimation. This is chosen because it is a representation of the kinetic energy difference normalized by the energy captured by the same number of true POD coefficients (Tu *et al.*, 2012). The same error criterion will be used to compare to mQSE.

For all data in this section, PIV data is sampled such that there is approximately one sample per lift oscillation (and therefore does not satisfy the Nyquist condition), the surface pressure probes are sampled at a rate of 25 times that of the simulated PIV data. All estimates predict the first six POD modes for reasons discussed above. Measurement

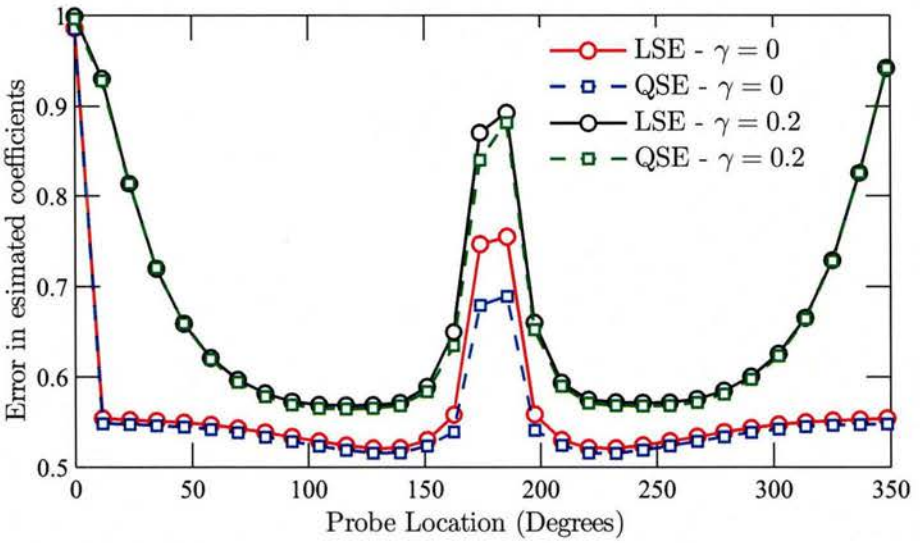

Figure 3.17: Error as a function of a single probe location for mLSE and mQSE for noise levels of $\gamma = 0$ and $\gamma = 0.2$.

noise (white) level is defined as (Tu *et al.*, 2012):

$$\gamma = \left(\frac{n'_{RMS}}{p'_{RMS}} \right)^2 \tag{3.2.7}$$

where p'_{RMS} is the RMS of the fluctuating pressure averaged over all the probes. Two levels of noise are considered, one with $\gamma = 0$ and another with $\gamma = 0.2$. Initially, the optimum pressure probe location for both mLSE (with no initial delay) and mQSE are determined and show in Figure 3.17 for both of the error levels. In this figure, the probe locations are spaced equally around the cylinder at 31 locations.

At the zero degree location, the figure shows that the error is large. This is likely due to the limited pressure fluctuations at this location. Figure 3.18 shows the (no-noise-added) root-mean-square (RMS) pressure versus location on the cylinder, from this it is noted that the areas of large RMS pressure are those locations with the best estimation. The added noise level is shown by the dashed red line. The noise clearly has a large effect on error in locations on the front end of the cylinder where pressure fluctuations are low. One can also

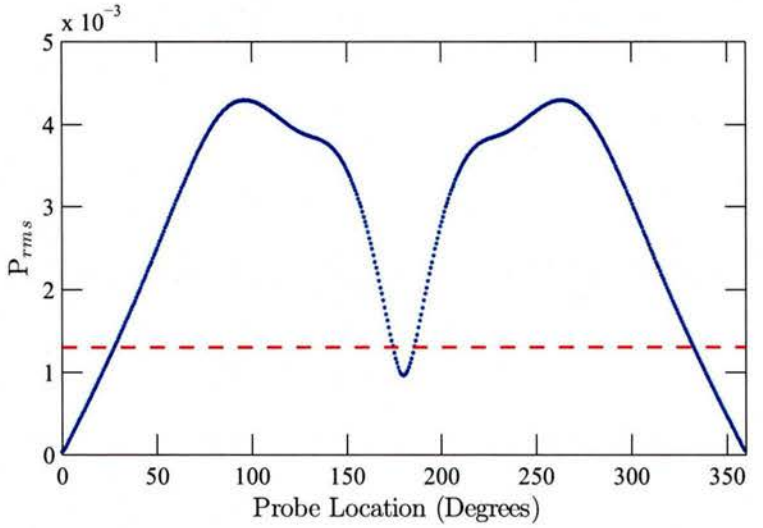

Figure 3.18: Root-mean-squared pressure with no noise added versus azimuthal location on the cylinder. The red dashed line indicates the added noise level.

see that the differences between the mLSE and mQSE are small with and without error, for this reason and the increased computational cost of mQSE, the remainder of the analysis is performed considering only mLSE.

The locations of the pressure probes for each case are shown in figure 3.19. Once the optimal probe positions are determined, the number of probes used in the estimation is investigated. Figure 3.20 shows the error relative to the number probes employed in the estimation for both the "clean" and noise added cases. With no added noise, the error starts high and quickly decreases to nearly zero; however, the noise added result shows a rather gradual decay of error with number of probes until about 14 probes when the error level asymptotes to approximately the added noise level of 0.2. Figure 3.21 shows the fluctuating vorticity field reconstruction for the no noise and noise added cases with 14 and 7 probes, respectively. Estimation without noise is clearly superior; however, it is unlikely to obtain experimental data as "clean" as CFD data so an additional method may be required to remove this noise. The Kalman filter and smoother discussed above is used to accomplish this feat.

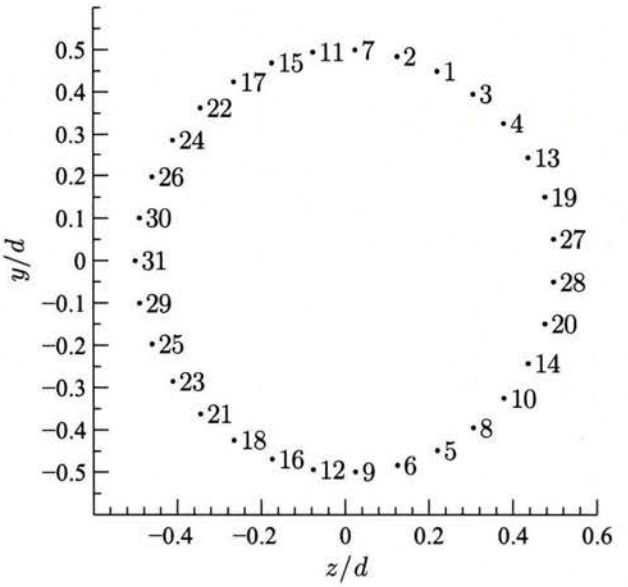

Figure 3.19: Locations of the pressure probes investigated for stochastic estimation. The number to the right of the marker indicates the relative error ranking with 1 being the optimal and 31 being the worst. 31 locations are considered with a constant $\Delta\theta$ between them.

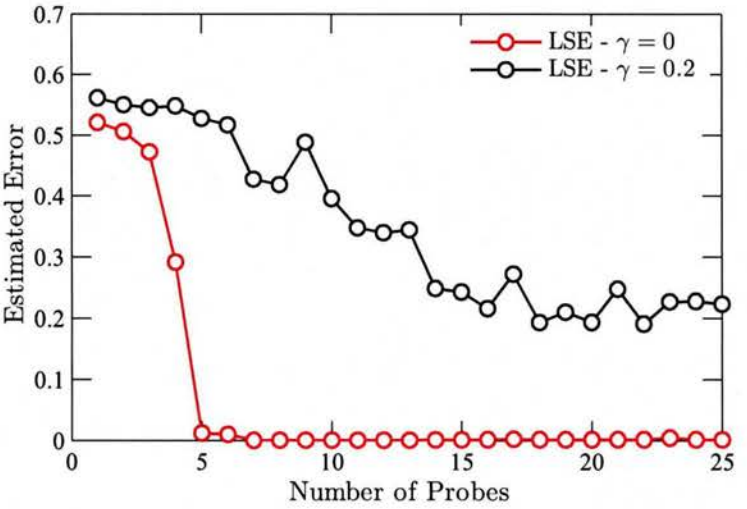

Figure 3.20: Error versus number of probes used in the estimation for the $\gamma = 0$ and $\gamma = 0.2$ cases. Probe locations shown in Figure 3.19

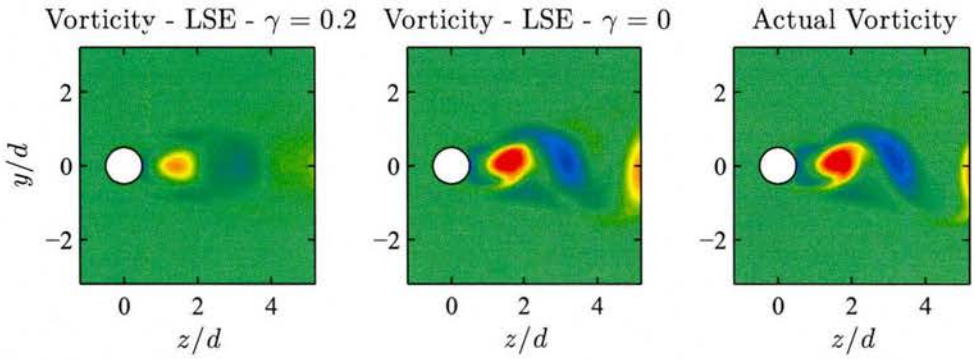

Figure 3.21: Comparison of LSE results with and without added noise. The with noise case uses 14 probes while the without noise case uses only 7.

Before moving to the Kalman filter, it should be noted that all these results assume only one time delay is used (and a zero delay at that). If an initial delay and multiple time delays are employed, the results may improve. For this discussion, the no noise case will be ignored, since its results are already quite impressive. An attempt to optimize the initial delay (ϕ in equation 2.1.13) and the number of delays (m in equation 2.1.17) for the single and 14 probe cases is shown in figure 3.22. This shows that a zero initial delay and a single time delay is the optimum for the 14 probe case, indicating that the (1) the correlation between the pressure probe location on the surface and the POD coefficients is maximum when they are taken at the same time and (2) that additional information gained by including multiple time delays actually decreases the correlation, likely due to increased presence of noise. For the case with just one probe, the best initial delay remains at zero. The optimal number of time delays moves to four, showing that more data in this case increases the correlation.

Kalman Filter and Smoother. From the previous section, it is clear that a method to reduce the effects of noise on the estimation is required if noise level in the probes is significant. The Kalman filter and smoother can help in this venture. This work will focus on use of the full filter/smoother model, as this methodology is will not be used in a causal manner, which is the primary reason to limit oneself to the filter.

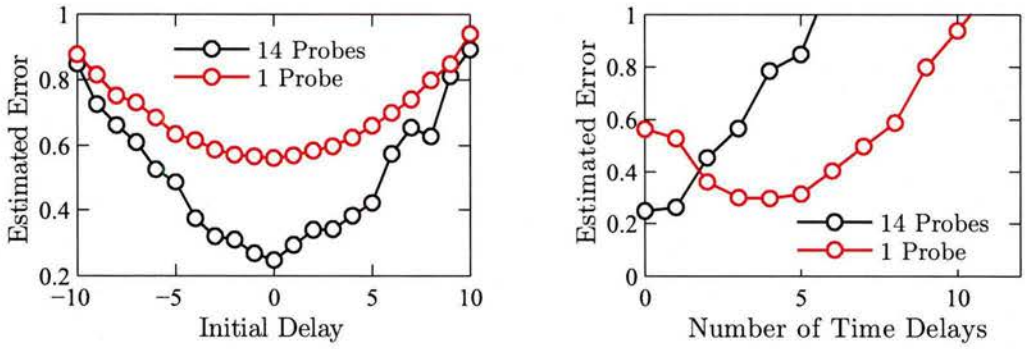

Figure 3.22: Error versus (a) initial delay and (b) number of delays for the single and 14 probe cases with noise added ($\gamma = 0.2$). Probe locations provided in Figure 3.19. The minimum point on these plots shows the optimal point for each case.

As defined above (eq. 2.1.22), the state variable, x_k is the POD coefficients, a, for the first six modes. The measured quantity, y_k, (eq. 2.1.23) is the probe measurement, which will be either the single probe or the 14 probes discussed above. The setup of the system model and measurement matrices (F and H_k) follow closely with that of Tu *et al.* (2012). The system model is chosen such that the first two states are estimated by the model of a standard second order oscillator, given by:

$$F_{osc} = \begin{bmatrix} 0 & -\omega \\ \omega & 0 \end{bmatrix}, \tag{3.2.8}$$

where ω is the nondimensional shedding frequency of the cylinder. The model for the remaining four states is estimated by employing the LSE estimated POD coefficients such that:

$$F_{LSE} = \frac{[a_j^n]}{[a_{j-1}^n]}, \tag{3.2.9}$$

where a_j^n is the matrix containing the first n modes (six in this case) at time j. The matrix a_j^n spans the full, time-resolved POD coefficient matrix, less the final temporal location. Likewise, the matrix a_{j-1}^n spans the time-resolved POD coefficient matrix from the second

temporal location to the end. Once this matrix is obtained, the first two states are replaced by F_{osc}, therefore,

$$F = \begin{bmatrix} F_{osc} & 0 \\ 0 & F_{LSE} \end{bmatrix}. \tag{3.2.10}$$

At times when the full PIV snapshot is available, the measurement matrix is simply the identity matrix, thus allowing the known POD modes to be accessed. At all other times, the measurement matrix is determined by solving

$$H = \frac{[p]}{[a]} \tag{3.2.11}$$

where p is the probe measurement matrix and a is the full matrix of POD coefficients for the first six modes. The system model is generated based on the clean data set and held constant throughout testing while the measurement matrix is allowed to vary based on the given (noisy or clean) probe input. The noise matrices, Q and R, are chosen such that the process noise, Q, is always the identity matrix and the measurement noise, R, is made small ($10^{-10}I$) when the PIV snapshot is accessed, and large ($10^{4}I$) at all other times.

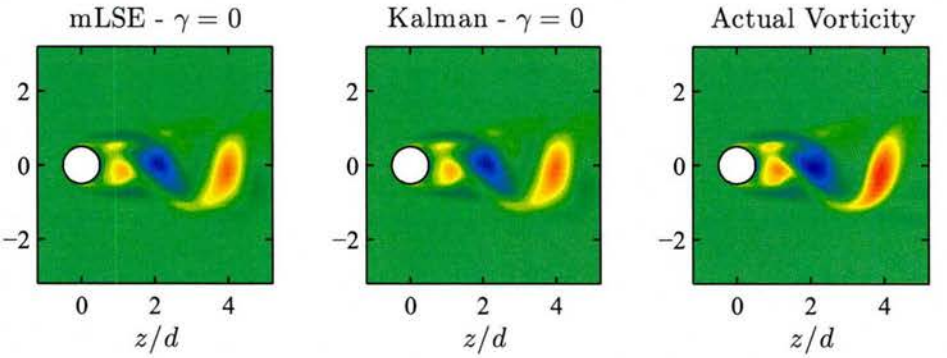

Figure 3.23: Vorticity field comparison of mLSE with no added noise, 14 probe case to the Kalman filter and smoother results.

The filter and smoother are first applied to the well-estimated no noise case with 14 probes, Figure 3.23 shows the result. Clearly the Kalman filter does not offer much im-

provement for this case since the mLSE already matches the actual field well. Next, the cases with additional noise and either 14 probes or one probe is considered. Figures 3.24 and 3.25 shows that the LSE estimation degrades heavily (also shown above), but the Kalman results are nearly identical. This suggests that the smoother/filter setup is robust to noise.

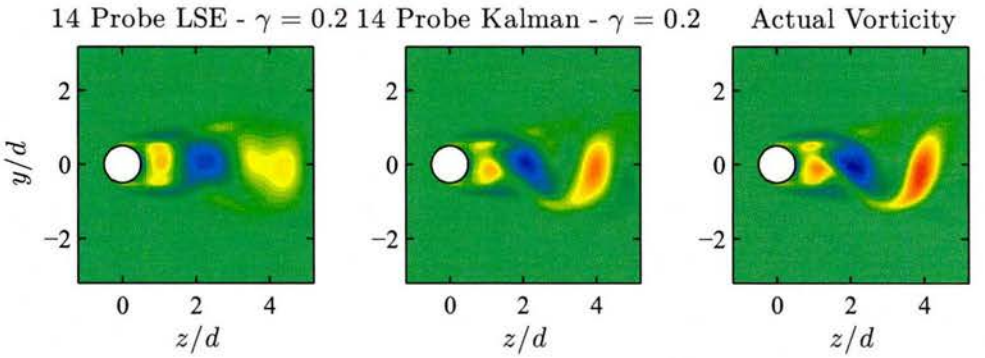

Figure 3.24: Vorticity field comparison of mLSE with added noise to the Kalman filter and smoother results employing 14 probes. Probe locations as shown in 3.19.

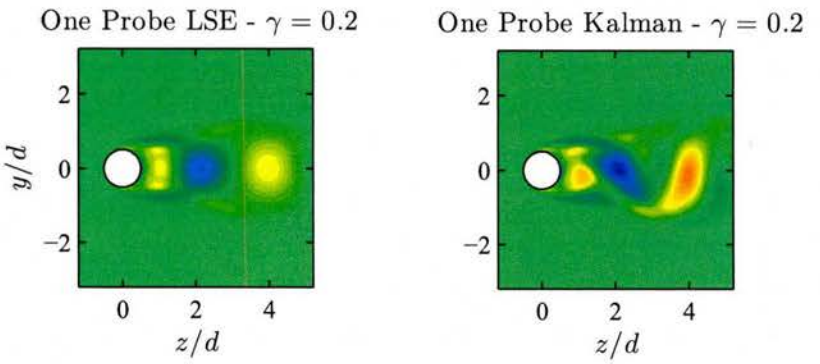

Figure 3.25: Vorticity field comparison of mLSE with added noise to the Kalman filter and smoother results employing one probe. Probe locations as shown in 3.19.

If, however, the *model* is created based on the oscillator and the noisy mLSE, with the same parameters defined above, there is little gain in accuracy and the results degrade to the mLSE estimate at temporal locations when a PIV snapshot is not available. These results are shown in Figure 3.26. Thus, the importance of a good model is shown.

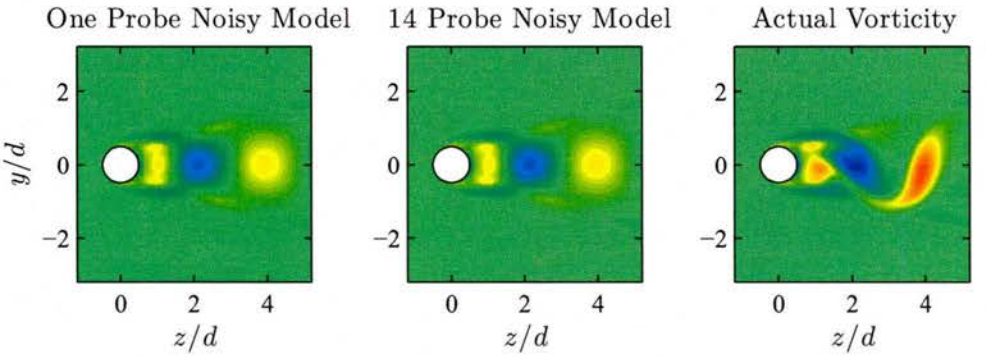

Figure 3.26: Vorticity field comparison of a noisy model Kalman filter estimated with one and 14 probes. Probe locations as shown in 3.19.

3.2.4 Poisson's Solver

The derivation of the Poisson solver can be found in section 2.2 above. The boundary conditions employed in this analysis are Neumann boundary conditions based on equation 2.2.5 for the outer edges, this is also the condition for cylinder locations with no known pressure. At cylinder locations with a pressure probe, a Dirichlet condition is used. The number and location of the probes was determined from the analysis above for the optimal probe locations for the velocity field estimation; either 7 or 14 probes locations were employed for the no noise and noise added cases, respectively.

Figure 3.27 shows the pressure field at two different times, one when a vortex is passing the downstream boundary and another when one is not. The pressure field estimation suffers greatly near the downstream boundary whenever a vortex passes through it; however, figure 3.28 shows that the surface pressure field does not seem heavily affected by the vortex passage. Since the surface pressure field is the primary thrust of this estimation it will be the focus of the remainder of the section. It should be noted that all lift and drag coefficients shown are calculated neglecting any influence from viscous forces.

Three cases were examined, the first used the velocity field from the DNS solution along with the no-noise-added pressure probes. The second employed the fields from the (Kalman smoother) velocity estimation (with the clean model and noisy probes) with noiseless pres-

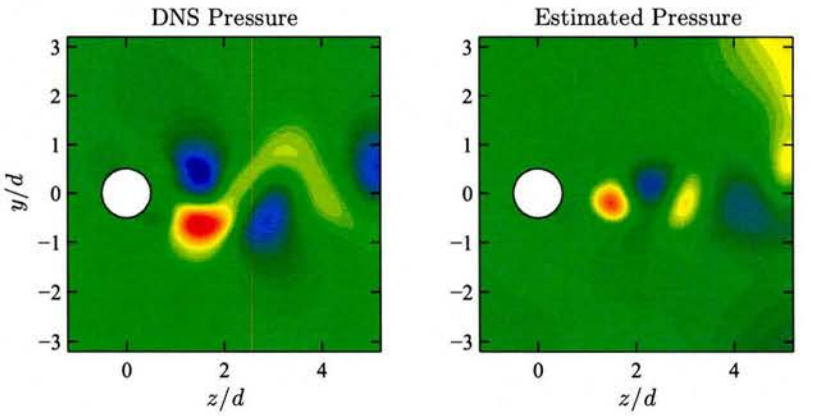

(a) No vortex passing the downstream boundary

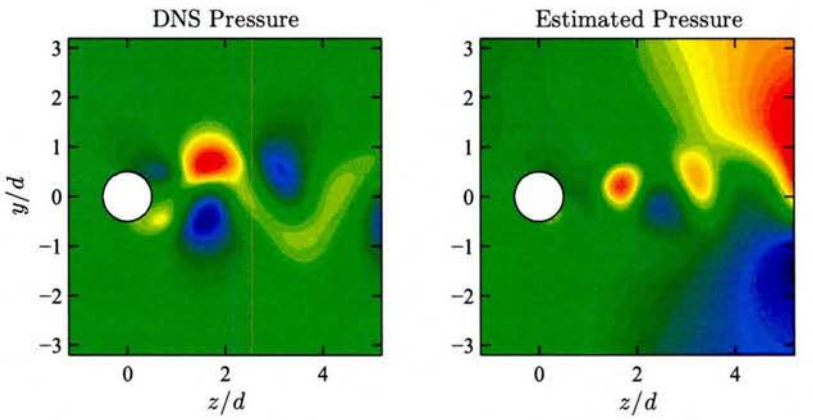

(b) Vortex passing the downstream boundary

Figure 3.27: Pressure field from the Poisson solver using the DNS velocity fields.

sure probes as the Dirichlet boundary conditions. Finally, the same estimated velocity fields were employed but now the boundary condition pressure probes contained added noise. The surface pressure forces estimated from the Poisson analysis are plotted against the full (DNS) surface pressure forces in 3.29. The Poisson estimates have a slightly lower amplitude than the DNS pressure forces in all cases for the lift coefficient and marginally higher for the coefficient of drag. These small differences are likely due to the effects of

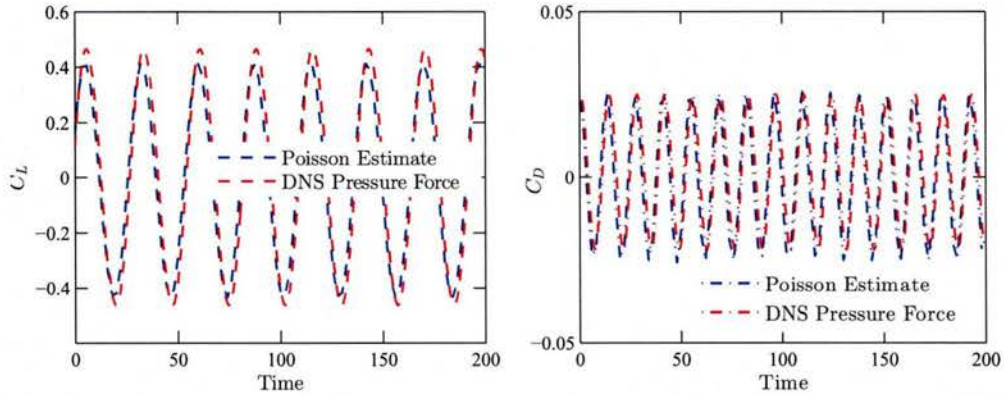

(a) Coefficient of lift

(b) Coefficient of drag

Figure 3.28: Coefficients of (a) lift and (b) drag for the pressure force from the DNS and Poisson estimated pressure force from DNS velocity fields.

the downstream boundary when a vortex is passing. The Poisson estimate of lift and drag employing the DNS and the Kalman estimated velocity fields are nearly identical with the exception that the Kalman fields are more resolved in time. The noise on the probes clearly affects the drag force much more substantially than the lift force, though this is likely due to the respective magnitude of the forces.

From these results it is observed that, even though the pressure field is greatly influenced by vorticies passing the outlet boundary, this change does not have a large effect on the surface pressures. This is an important result as PIV viewing fields are typically quite limited. It is also shown that noise in the probes has a large effect when the magnitudes of the forces are low but become less prevalent as the forces increase.

3.2.5 Curle's Analogy

This section will discuss a number of results related to the application of Curle's acoustic analogy. Throughout this section, the 2D form of Curle's analogy will be used with the

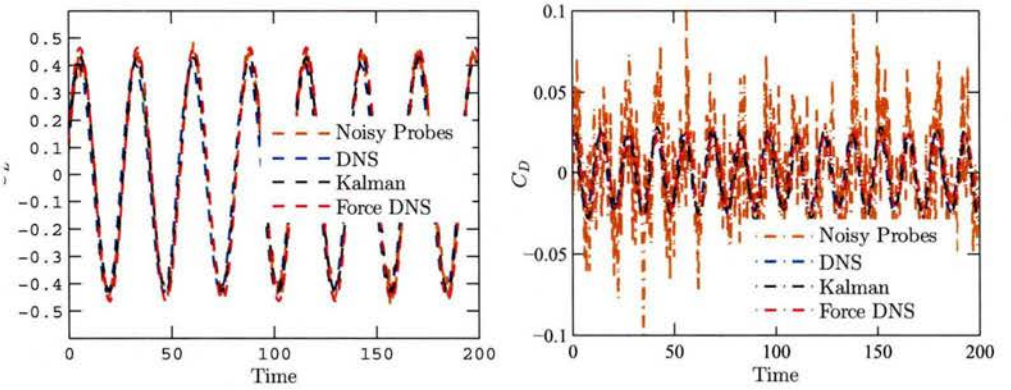

(a) Coefficient of lift

(b) Coefficient of drag

Figure 3.29: Coefficients of (a) lift and (b) drag for the pressure force from the DNS and Poisson estimated pressure force from the DNS velocity fields and the estimated velocity fields with and without noise added to the probes.

singularity removed (as discussed in Appendix A), restated here for clarity

$$p(\mathbf{x},t) = -\frac{x_i}{2^{1/2}\pi c^{1/2}\mathbf{r}'^{3/2}} \int_{-\infty}^{\tau} \left[\frac{\partial^2}{\partial t'^2}\mathbf{F}_i(\mathbf{r}',t')\right] \sqrt{\tau - t'}dt' \tag{3.2.12}$$

This portion begins by offering a discussion of the results of Curle's analogy employing the full forces obtained from the simulation and comparing these results to the DNS far-field pressure results. Once this is complete, these results are compared to those which rely on progressively less information. A second comparison is made by excluding the viscous forces. Finally, the full estimation method is performed, estimating the velocity field from POD/LSE/Kalman smoother then estimating the surface pressures using a Poisson solver and finally employing Curle's analogy. For brevity, time series and spectral plots are only shown at $r = 75, \theta = 80°$; however, other positions will be discussed where appropriate.

Full Force Result. Figure 3.30 shows the contributions to the pressure field from the lift and drag dipole as estimated by Curle's analogy. The orange lines indicate positive pressure contours, the blue represent negative pressure contours and the black line shows the zero contour. It should be noted that the lift contours are an order of magnitude larger than

the drag contours. From this figure, it is clear that the lift contribution to the pressure field dominates the drag contribution, this is expected as the amplitude of the lift fluctuation is significantly larger than for drag. It should also be noted that the lift and drag dipoles propagate in the 90° and 0° directions respectively.

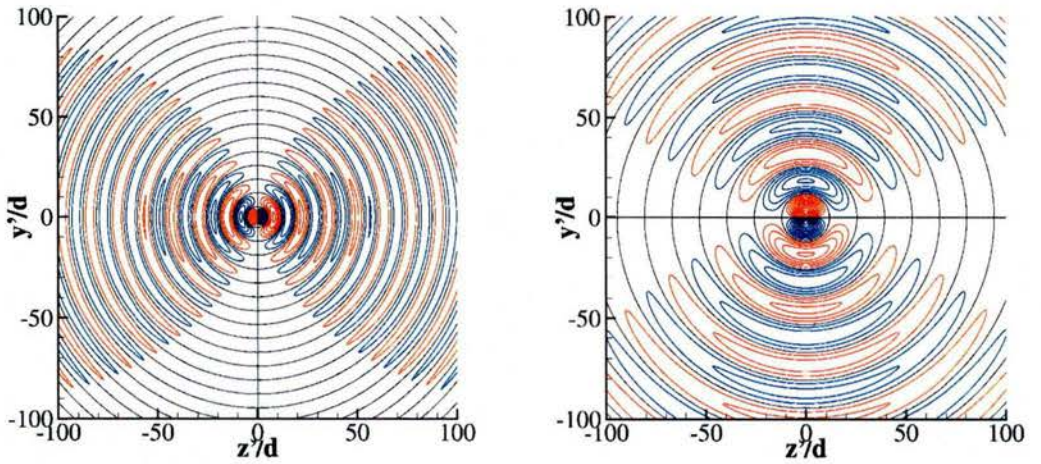

(a) Drag dipole

(b) Lift dipole

Figure 3.30: Results of Curle's analogy showing the (a) drag and (b) lift dipoles separately. The contour levels are from $-0.01M^{2.5}$ to $0.01M^{2.5}$ with steps of $0.00025M^{2.5}$ for the drag dipole and $-0.1M^{2.5}$ to $0.1M^{2.5}$ with steps of $0.0025M^{2.5}$ for the lift dipole. Orange indicates positive contours, blue indicates negative, and the black line is the zero contour.

The form of Curle's analogy used in eq. 3.2.12 does not account for the Doppler effect. In order to include the Doppler effect the following relations (from Appendix B) for a dipole source are applied (Inoue & Hatakeyama, 2002)

$$r' = r/(1 - M\cos\theta) \tag{3.2.13}$$

$$c = c_\theta/(1 - M\cos\theta) \tag{3.2.14}$$

$$p(r', t) = p(r, t)(1 - M\cos\theta) \tag{3.2.15}$$

where the left hand side of each of the above are the Doppler removed frame. Substituting

these values into equation 3.2.12 the form of Curle's analogy with the Doppler effect included is obtained

$$p(\mathbf{x},t) = -\frac{x_i}{2^{1/2}\pi c_\theta^{1/2}\mathbf{r}^{3/2}} \int_{-\infty}^{\tau} \left[\frac{\partial^2}{\partial t'^2}\mathbf{F}_i(\mathbf{r},t')\right] \sqrt{\tau - t'}dt' \tag{3.2.16}$$

while noting that the retarded time is now taken on the original coordinate system as $\tau = t - r/c_\theta$.

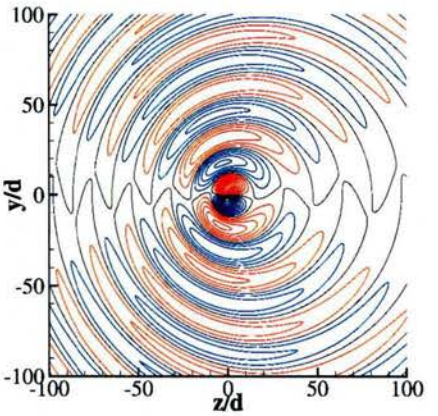

(a) Curle's Analogy with Doppler Effect Included

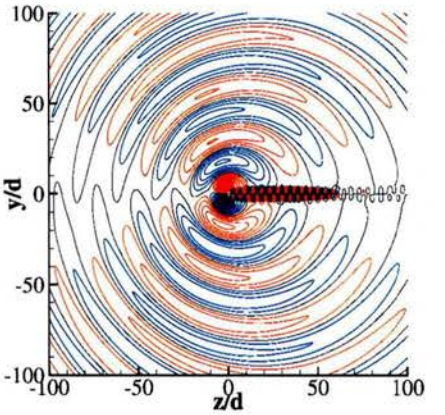

(b) Pressure Fluctuations

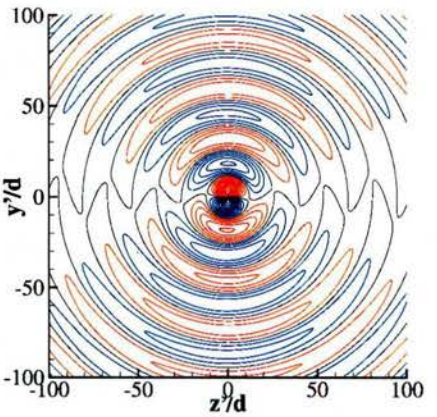

(c) Curle's Analogy

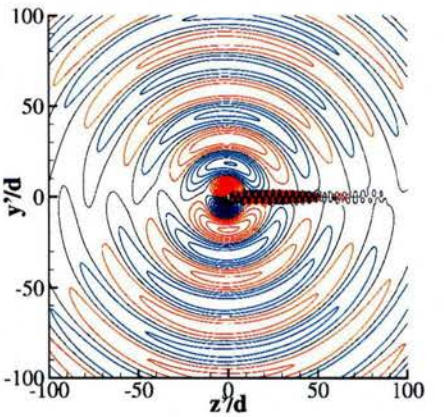

(d) Doppler Effect Removed Pressure Fluctuations

Figure 3.31: Comparison of Curle's analogy to DNS results for both (a),(b) Doppler effect included and (c),(d) Doppler effect removed.

Figure 3.31 shows a comparison of the Curle's analogy results to the DNS results for both the Doppler effect included and the Doppler removed cases at an instant in time. Figure 3.31 (a) and (c) show the Curle's analogy result using the full forces with and without the Doppler effect, respectively. Figure 3.31 (b) and (d) show the true pressure field with and without the Doppler effect, respectively. It is clear that the propagation angle is the same from the DNS to Curle's analogy result in both cases. Now that we know the full fields match well qualitatively we look into the spectral content and time series data.

Figure 3.32 shows both the spectral and time series data for the DNS pressure field versus the 2D Curle's analogy result at $r = 75, \theta = 80°$. The time series data matches well between the analogy and the DNS result. The spectral results both contain the same peak frequency levels. For this case, Curle's analogy predicts the first peak well while the second peak is under predicted by approximately half an order of magnitude. However, at other locations in the field, the second peak is over-predicted compared to the DNS pressure. The spectral harmonics remain intact and the broadband noise levels are higher in the analogy than in the DNS result.

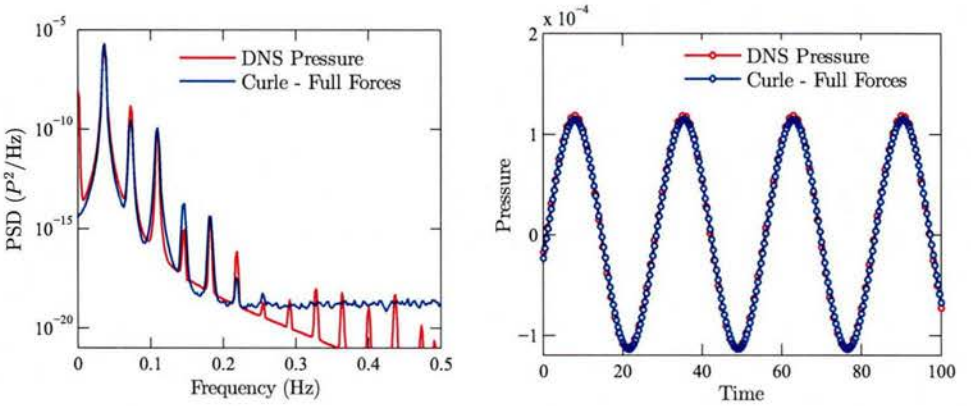

(a) Spectra at 80 Degrees

(b) Time Series at 80 Degrees

Figure 3.32: (a) Spectral and (b) time series data comparison between Curle's analogy employing the DNS full forces and DNS pressure at $r = 75, \theta = 80°$.

Pressure Forces Only. When viscous forces are neglected, a reduction of levels estimated by Curle's analogy is expected since it is proportional to the fluctuating forces. Figure 3.33 shows the results from the analogy when only surface pressure forces are employed at the same location as figure 3.32. Clearly this expectation is correct and that there is a noticeable difference in the amplitude of the time series fluctuations. However, even at this low Reynolds number the spectral results are still quite good with a difference in the first peak of only about 1.5 dB. As Reynolds number increases this difference may decrease due to the reduced relative dependence on viscous forces.

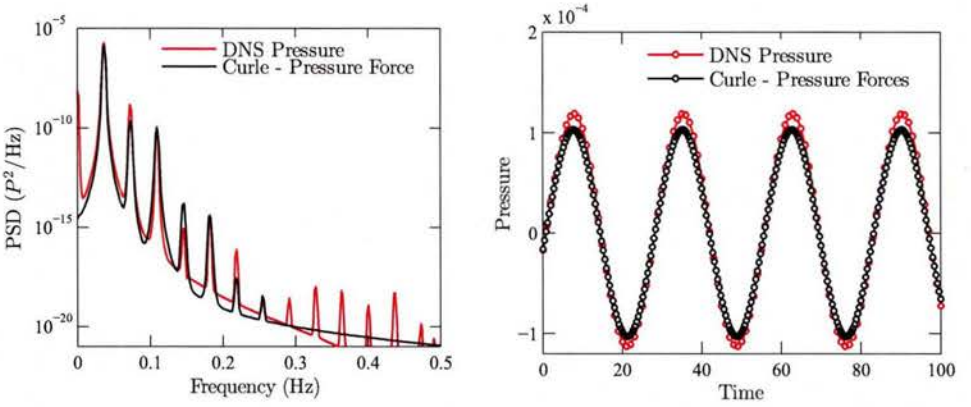

(a) Spectra at 80 Degrees

(b) Time Series at 80 Degrees

Figure 3.33: (a) Spectral and (b) time series data comparison between Curle's analogy using the DNS pressure forces and DNS pressure results at $r = 75, \theta = 80°$.

Poisson Estimated Pressure Forces. Applying Curle's analogy to the force results obtained the Poisson equation employing the DNS velocity field, figure 3.34 is obtained. Here, the Poisson estimate is compared directly to the pressure forces. While the Poisson estimate shows a slight decline in magnitude from the DNS pressure forces, the shape of the time series and frequency of the peaks continue to match well. In the spectral results, the broadband levels seem much higher, but this is likely due to the extremely low number of samples usable from the full DNS field (approximately 400) so the spectral uncertainty is quite large. As will be shown shortly, the broadband levels when the Kalman estimated

velocity fields are employed is much lower. It should also be noted that the sampling frequency of the DNS result is 0.5 Hz.

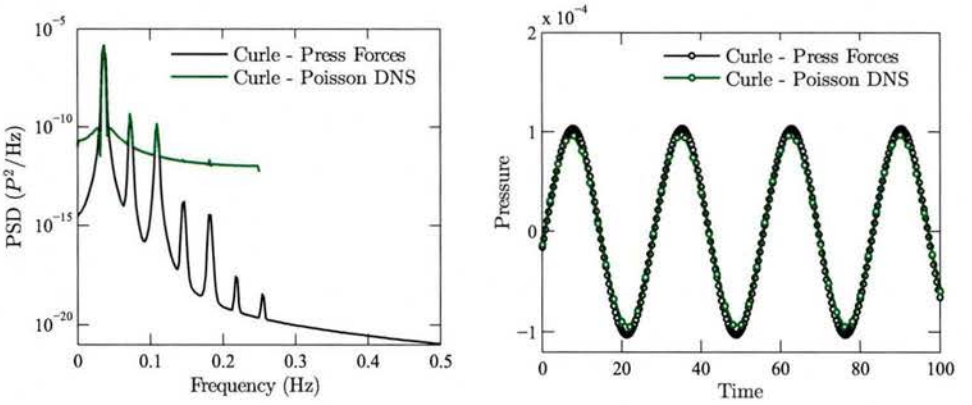

(a) Spectra at 80 Degrees

(b) Time Series at 80 Degrees

Figure 3.34: (a) Spectral and (b) time series data comparison between Curle's analogy using the pressure forces and the Poisson estimate from the DNS velocity fields at $r = 75, \theta = 80°$.

Full Estimation Method. The final step in the process was to estimate the velocity fields used as the input to the Poisson solver. This was done using a combination of POD, mSE, and a Kalman smoother as discussed above. First, the no-noise-added case was examined, shown in figure 3.35. The time series shows nearly identical magnitude and shape (in a time resolved version manner) as the case with velocity fields from DNS. The peaks in the spectra are once again nearly identical while the noise is quite a bit more pronounced than in the pressure force only estimation. When the noisy estimated velocity fields are employed along with the no noise pressure probes as boundary conditions, the spectra and time series are identical.

However, if the noisy pressure probes are used as the boundary conditions in the Poisson solver, the estimated pressure signal also becomes noisy as shown in figure 3.36. This suggests the importance of the cylinder boundary conditions on the final estimation and shows that significant noise levels in the pressure probes must be avoided. While the broadband component of the spectra are higher, the first two peaks remain well estimated.

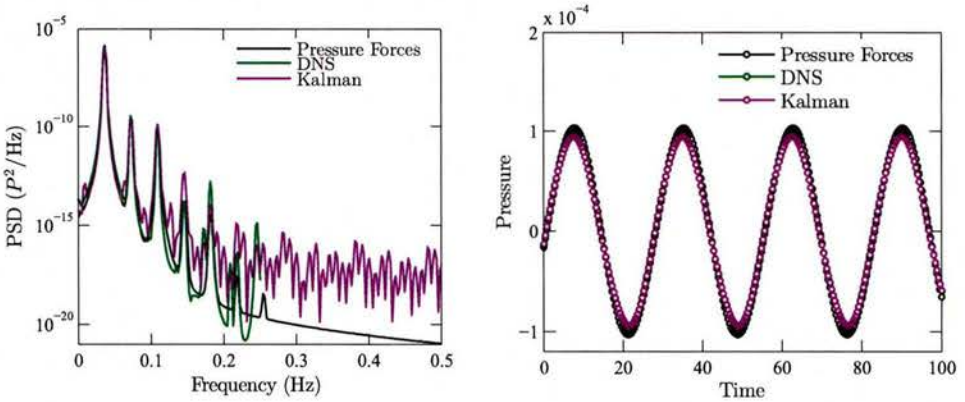

(a) Spectra at 80 Degrees (b) Time Series at 80 Degrees

Figure 3.35: (a) Spectral and (b) time series data comparison between Curle's analogy using the pressure forces and the Poisson estimate from the DNS and Kalman smoother estimated velocity fields at $r = 75, \theta = 80°$.

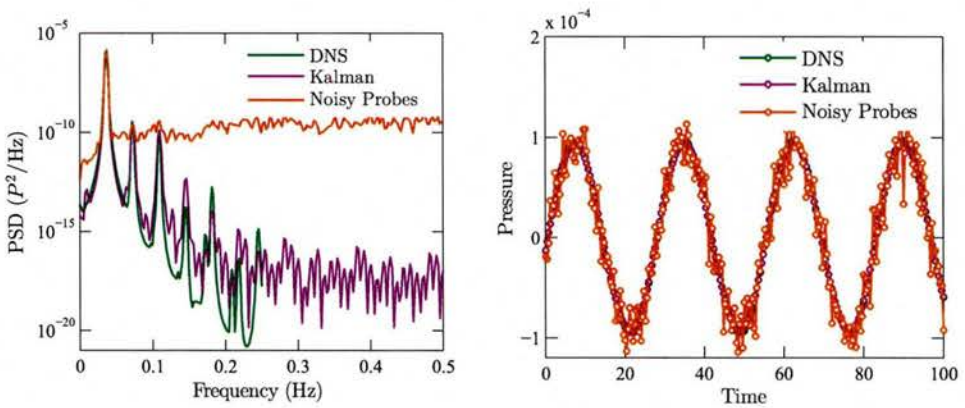

(a) Spectra at 80 Degrees (b) Time Series at 80 Degrees

Figure 3.36: (a) Spectral and (b) time series data comparison between Curle's analogy using the Poisson estimate from the DNS and Kalman smoother estimated velocity fields with and without "noisy probe boundary conditions" at $r = 75, \theta = 80°$.

CHAPTER 4

WALL JET EXPERIMENTS

The following chapter will discusses the experiments and results relating to the planar, turbulent wall jet which has served as a canonical, test bed for the previously discussed methods. In this intermediate study, spatially-resolved velocity field measurements are acquired using PIV. Synchronously, discrete but temporally-resolved surface pressure measurements are obtained using surface mounted, electret pressure transducers. To further elucidate certain flow characteristics and validate the PIV measurements, discrete, temporally-resolved velocity measurements are also obtained using hotwire anemometry. The PIV, surface pressure, and hotwire anemometry measurements of the turbulent wall jet will be presented before addressing the calculation of the velocity and pressure source terms for use in the proposed acoustic analogy. The estimation of temporally-resolved velocity fields will be presented along with the POD decomposition of the velocity fields and an investigation of the pressure/velocity cross-correlations. Finally, estimates of the far-field acoustics by Curle's acoustic analogy will be compared to direct measurements of the far-field acoustics.

4.1 Experimental Setup

The experiment performed to acquire the data analyzed in the study of the turbulent wall jet was conducted in a turbulent wall jet wind tunnel at the University of Florida, consisting of an Aerolab open-jet wind tunnel connected to a blower powered by a 1/2 horsepower DC motor. The flow passes through a honeycomb and several screens and is

contracted through an area ratio of 3:1 before reaching an exit nozzle that further reduces the flow area from a square of 165 mm (6.5 in) to a rectangular jet exit of aspect ratio (AR) eight, with a slot height of 19 mm (0.75 in) and a slot width of 152 mm (6 in). This configuration allows for jet exit velocities of up to 32 m/s. The planar jet exits smoothly onto a 0.61 m (24 in) by 0.91 m (36 in) sheet of optically clear acrylic. Flush mounted along the center-line of the sheet are 5 Panasonic WM-61A electret pressure transducers evenly spaced on centers at 12.7 mm (0.5 in), with the first pressure transducer residing 50 mm from the exit of the jet nozzle. Figure 4.1 shows a schematic of the streamwise locations of the surface pressure transducers relative to the nozzle exit, the location of the pulsed laser sheet used for PIV, the location of the PIV cameras, and flow visualization of the jet emanating from the nozzle. As shown, the planar laser sheet is offset from the pressure transducers as to not influence the membranes on their surface. An example of the PIV domain studied in this work can be seen in figure 4.2. While this particular image is not ideal for PIV due to its non-uniform and very dense dispersion of seed, the "flow visualization" gives a reference for the turbulent motion of the shear layer.

4.2 Discrete, Temporally Resolved Measurements

Vital to the proposed estimation techniques in this work, is the ability to measure the temporally-resolved surface pressure coincident with the PIV field of view. This is accomplished using five, Panasonic WM-61A electret pressure transducers that exhibit sensitivities in the range of 32 ± 3 mV/Pa and are able to capture frequencies up to 20 kHz. Data from the pressure transducers are recorded with an NI PXI-4472 8-Channel Dynamic Signal Acquisition Module housed in a NI PXI-1033 chassis. The electrets are calibrated using a Brül & Kjær acoustic calibrator, which produces a tone of 94 dB SPL at a frequency of 1000 Hz. Synchronization of the PIV snapshots and surface pressure measurements is ensured using software to monitor the various signals. When the PIV system is ready to take an image, a signal is sent from the host computer to the pulsed laser and PIV camera. As

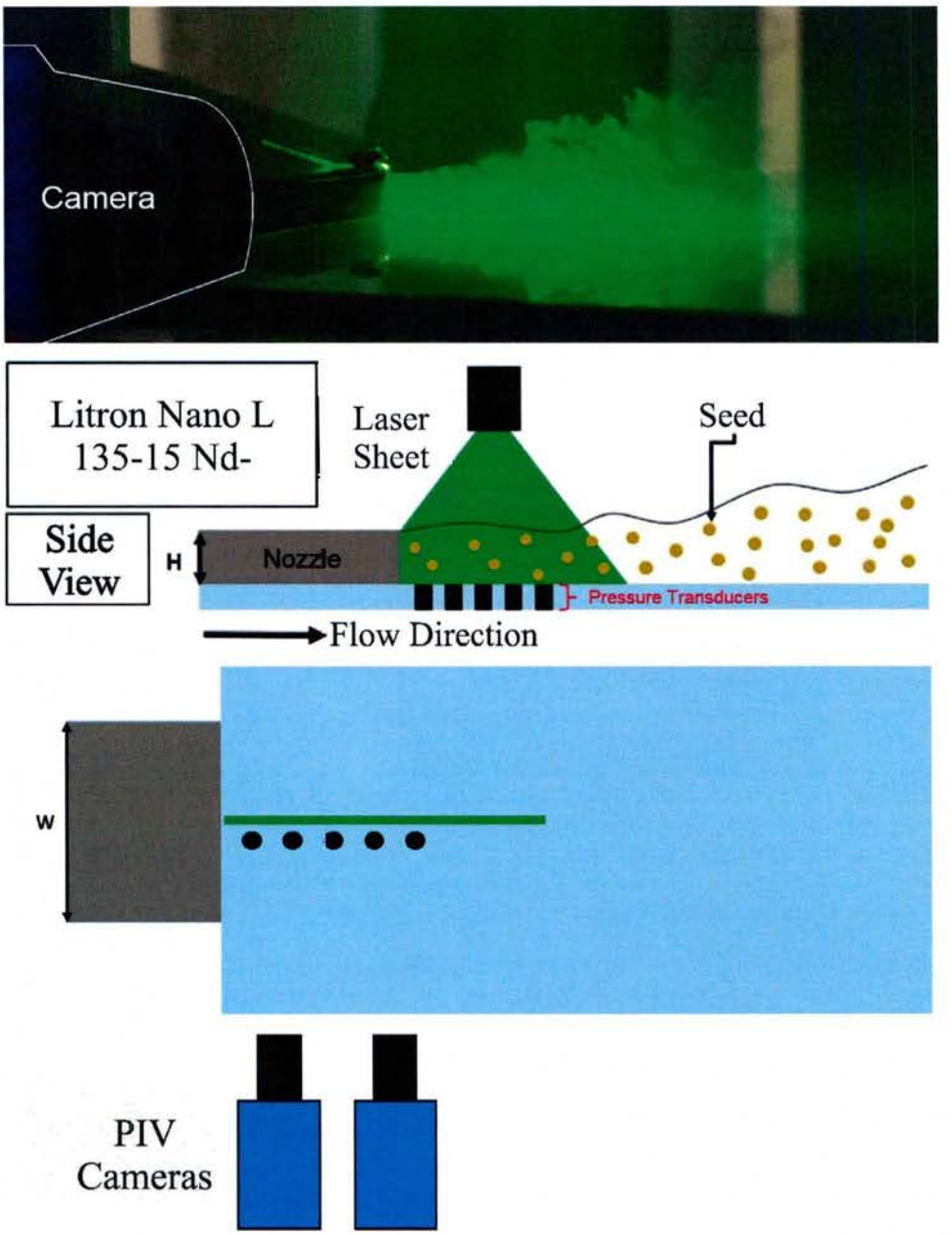

Figure 4.1: The relative placement of the surface mounted pressure transducers and PIV setup are depicted in this figure. A flow visualization of the turbulent wall jet flow, which is the basis of this study, is also shown as a physical reference.

shown in figure 4.3, the camera begins its exposure and the laser fires before the exposure closes. If the signal that triggers the laser to fire is also sent to a program controlling the

Figure 4.2: Raw PIV image showing the defining characteristics of the turbulent wall jet. Images such as this provide good flow visualization; however, from a PIV standpoint, a more uniform and less dense seeding is desirable.

electret pressure acquisition, this signal serves to synchronize the events. In the present study, pressure measurements at a given time are temporarily stored and replaced once a certain number of new measurements are received. When the laser trigger is received, pressure measurements, both coincident with the trigger and a certain time before and after the trigger, are stored permanently. This allows for analysis involving lagged-time correlations in post-processing. To ensure synchronization, a photo-diode is placed near the laser sheet to independently record each firing of the laser. The resulting photo-diode signal is then compared to the recorded triggering signal to ensure that any inherent delay in the system, which will be apparent between these two signals, is much smaller than the time scales of interest in the flow and the exposure time of the cameras.

While the data acquisition discussed above is all that is required for the estimation method proposed in this work, additional information can be gleaned by measuring the temporally-resolved velocity at discrete locations. This is accomplished through the use of hotwire anemometry. Hotwire anemometry operates on the principle relating the thermal loss of a heated resistance sensor to the convective effects of the flow being measured. These convective effects can be due to temperature, pressure, density, and velocity changes in the flow. If the dominant of these factors is velocity, however, then the velocity of the flow can

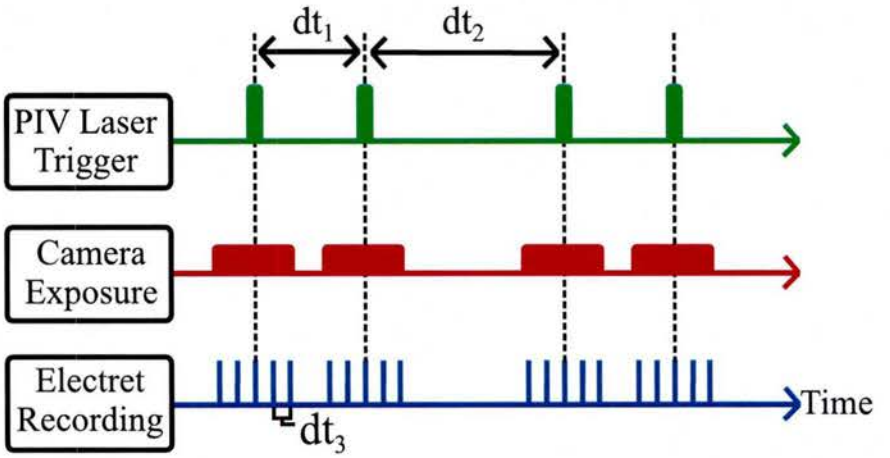

Figure 4.3: The synchronization diagram shown in this figure depicts the relative timing involved with the various signals in this experiment. Dt_1 represents the time between successive PIV images used to create the vector field at a given time, Dt_2 represents the time between successive vector fields or the frequency at which the velocity field is measured, and Dt_3 represents the inverse of the frequency at which the pressure transducers are recorded.

be measured directly by relation to the heat loss of the sensor.

The system used in this work is a constant-temperature anemometer system (CTA). A CTA system consists of a Wheatstone bridge and a servo amplifier, an example is shown in figure 4.4. The bridge consists of the sensing probe and other known resistances and compensation networks aimed at eliminating the effects of cabling, etc. When a change in the flow velocity occurs, the temperature of the senor is affected, changing the resistance and thus the voltage difference, and the bridge is thrown out of balance. The bridge operating voltage is then changed to compensate and bring the sensor back to its original temperature. If the gain of the servo is high enough, this response is rapid, increasing the frequency response of the system. To increase the sensitivity of a hotwire sensor, it is desirable to increase the operating temperature of the probe. There is an upper limit to this however, as thermal changes of the probe supports can influence measurements if a certain temperature is exceeded. In addition, it is beneficial to decrease the size of the sensor wire to reduce the area over which the measurement is averaged, and to decrease the time in which it takes for the probe to respond to thermal changes. The measurements obtained in

this study employed a Dantec Dynamics bridge and a platinum-coated, Tungsten hotwire probe. Calibration of the hotwire system is accomplished by measuring flow of a known velocity at various different speeds. Once enough speeds are obtained, a polynomial is fit to relate the measured voltage change necessary to balance the bridge at each flow speed.

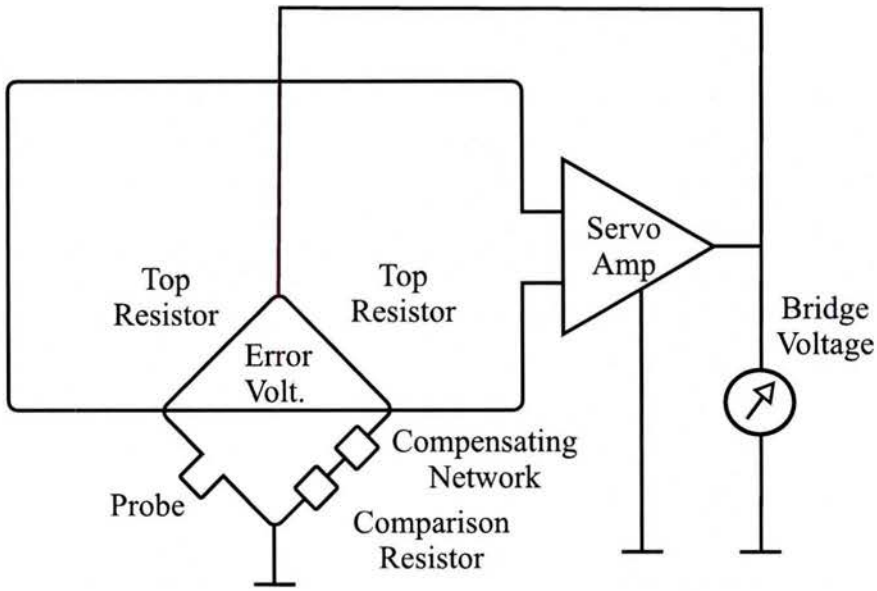

Figure 4.4: CTA Wheatstone bridge circuit example used in the hotwire setup.

4.3 Wall Jet Flow Characterization

As previously stated, two-dimensional PIV snapshots are acquired synchronously with surface pressure measurements along the center-line of the turbulent wall jet. 2400 PIV snapshots are acquired at a sampling frequency of 12 Hz, with "windows" of surface pressure measurements centered around PIV snapshots recorded at a rate of 32,160 Hz. The nozzle exit velocity for this experiment is set to 21 m/s for a Reynold's number based on nozzle height of 25,500.

4.3.1 PIV Measurements

The mean and root mean square (RMS) fluctuations of the wall jet in the streamwise and wall normal directions, normalized by the nozzle exit velocity U_∞, are depicted in figures 4.5 and 4.6. The streamwise mean velocity, shown in figure 4.5 A, clearly shows the potential core of the jet, boundary layer development, and shear layer growth characteristic of the turbulent wall jet. The wall normal mean velocity, shown in figure 4.6 A, is small due to the fact that the wall normal motion is almost entirely of fluctuating positive and negative value. The RMS fluctuations in both the wall normal (figure 4.6 B) and streamwise directions (figure 4.5 B), highlight the turbulent motion concentrated at the interface between the wall jet and ambient fluid, where turbulent mixing with ambient air causes growth of the shear layer. The RMS fluctuations in the wall normal direction appear in a wider "band" than those in the streamwise direction and appear to be of slightly higher intensity along the center of the shear layer.

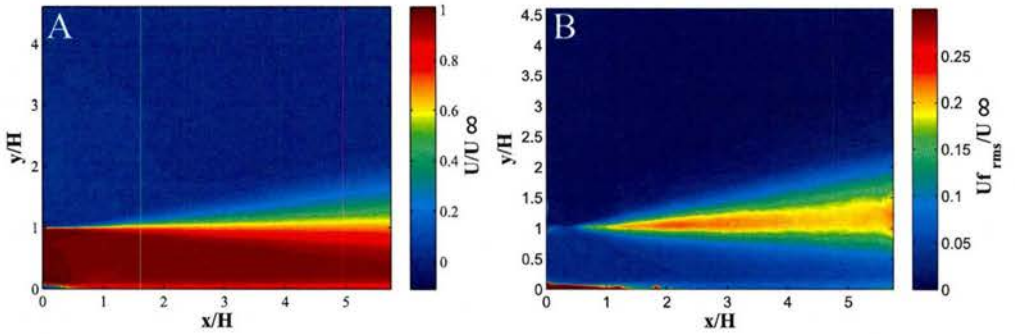

Figure 4.5: (A) Mean streamwise velocity profile and (B) RMS fluctuations, obtained using the entire PIV data-set and normalized by the nozzle exit velocity.

As two-component PIV data is used throughout this study, it is important to understand the effects of this two-dimensional assumption. In the present study, the PIV imaging plane extends downstream only a relatively short distance. Center-line velocity profiles obtained by Hall & Ewing (2007) and Grissom (2007) show that, as velocity profiles are analyzed further downstream, the shape broadens and can be collapsed by normalizing with the

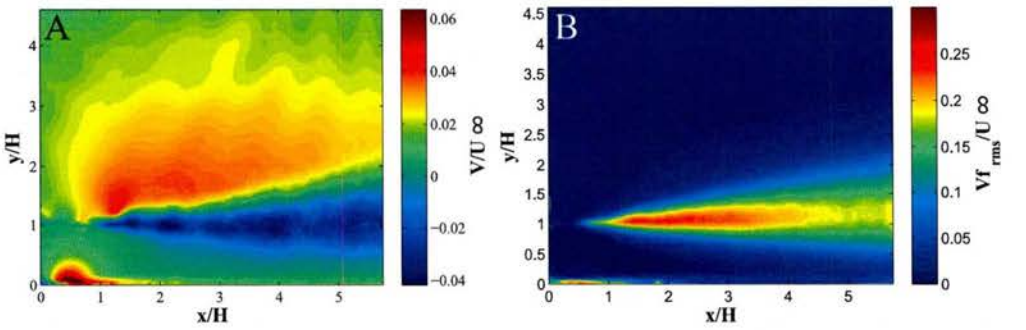

Figure 4.6: (A) Mean wall normal velocity profile and (B) RMS fluctuations, normalized by the nozzle exit velocity.

maximum in-plane velocity , U_m , and the half-height of its location, $y_{1/2}$. Figure 4.7 shows velocity profiles at various streamwise locations within the PIV field that have been normalized using these parameters.

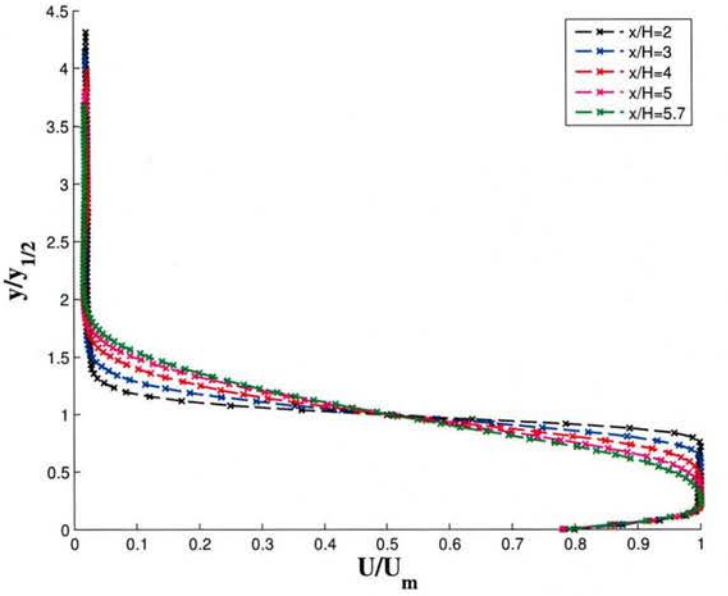

Figure 4.7: Center-line velocity profiles obtained at various streamwise locations and normalized by the maximum in plane velocity and half-height of its location.

It can be seen that the velocity profiles at $x/H = 2$, $x/H = 3$ and, $x/H = 4$ pass through the potential core due to the blunt shape of the velocity profile. At the two locations furthest

downstream, however, the profile begins to collapse, but does not completely collapse, suggesting that the flow is still transitioning to the fully-developed, self-similar downstream region. By this, it can be argued that three-dimensional effects are expected to be minimal, as the majority of the studied field has not evolved enough to feel the effects of the spanwise mixing. This is further reinforced when looking at the RMS velocity profiles shown in figure 4.8. Here it is shown that fluctuations near the wall are much smaller than those in the shear layer, consistent with two-dimensional jet development (Hall & Ewing, 2007), as the outer layer has not grown to overwhelmingly influence the inner layer.

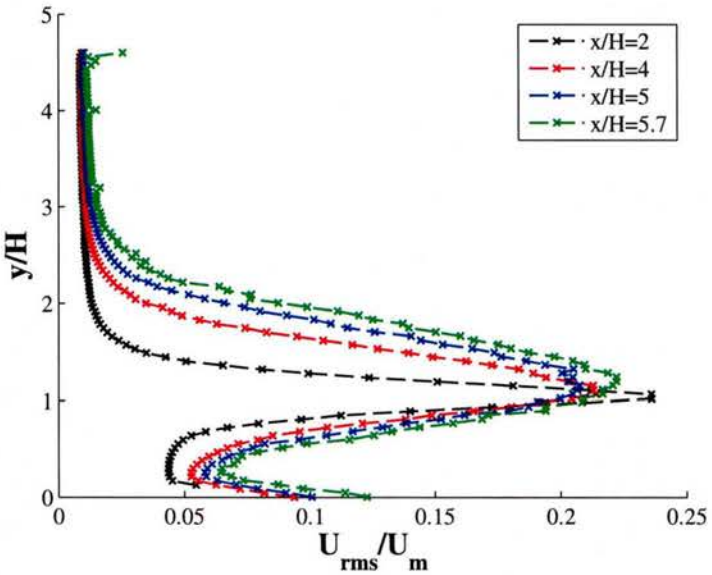

Figure 4.8: RMS fluctuation profiles at streamwise locations, normalized by the maximum in plane velocity and nozzle exit height.

Another way of evaluating this, is by calculating the growth rate of the jet (based on the upper location of half the maximum in plane velocity) due to the distinct difference between vertical growth of two-dimensional and three-dimensional wall jets. In general, two-dimensional wall jets are characterized by a wide aspect ratio, on the order of AR=20, and possess a vertical growth rate of about 0.073 (Launder & Rodi, 1983), with a growth rate low as 0.064 being recorded in work by Sigalla (1958). The vertical growth rate measured

in the current experiment (AR=8) is 0.051, as shown in figure 4.9, which matches that found by Hall & Ewing (2007) in their work investigating "moderate" aspect ratio wall jets, including an AR=8 wall jet at a Reynold's number based on height of 89,600. This low growth rate is indicative of a three-dimensional wall jet, which means that past the breakdown of the potential core and into the self-similar downstream region, mixing on all sides of the jet work to create large spanwise motion. As previously stated, the short length of the PIV domain being utilized helps to reduce the influence of out of plane motion on the current data set. Further investigations on the two-dimensionality of the current wall jet will be presented in the final dissertation for this work, including spanwise measurements of the velocity field to study uniformity.

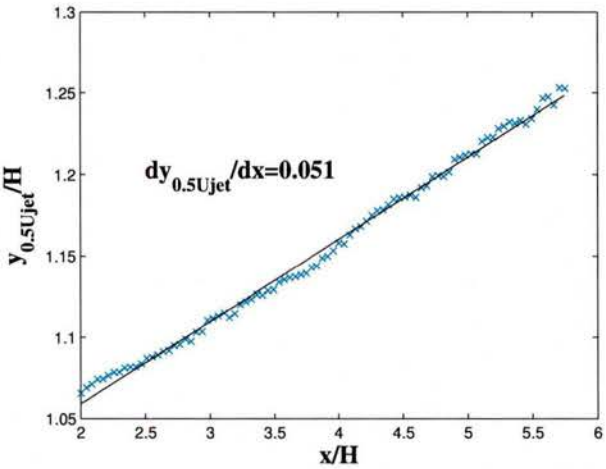

Figure 4.9: The growth rate of the wall jet defined by the streamwise change in location of the upper height of half the maximum in plane velocity.

Instantaneous snapshots of the fluctuating velocity field can be used to analyze the underlying structure of the wall jet shear layer. Figure 4.10 show snapshots of the the streamwise and wall normal PIV velocity fields. In both images, the Kelvin-Helmholtz instability responsible for the vortical motion in the shear layer is evidenced by the alternating pairs of positive and negative velocity regions. This instability is due to the large velocity shear between the jet and ambient fluid, which is susceptible to perturbations, giving rise

to the rolling up of the interface between the ambient and the jet.

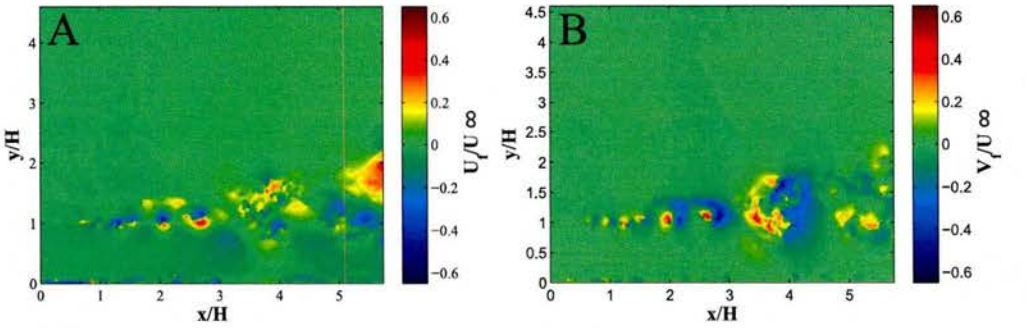

Figure 4.10: (A) Instantaneous streamwise and (B) wall normal velocity snapshot.

To further elucidate the turbulent structure present in the shear layer, the velocity field can be viewed in a Galilean or inertial frame of reference (Adrian *et al.*, 2000). This decomposition aims to uncover the turbulent structure or eddy by subtracting a velocity consistent with that at which the center of the eddy is translating in the flow. As seen in equation 4.3.1, the convection velocity chosen for this flow was 60% of the jet exit velocity. Once this is accomplished, eddies that are translating near to the chosen convection velocity appear as circular shapes, as shown in figure 4.11. The highlighted region in this figure shows a series of structures that are initially small, but grow in size as they convect downstream. Toward the end of the image, it can be seen that the well defined circular structure is broken down by turbulent mixing.

$$u_G = U - 0.6U_\infty \tag{4.3.1}$$

This turbulent mixing is also responsible for entrainment of the jet, which draws additional mass from the ambient region above the jet. This can be demonstrated by calculating the transport of momentum or momentum flux due to inertial forces in the shear layer. Figure 4.12 shows the momentum flux in the wall normal direction (defined by equation 4.3.2). The momentum flux is large in the region where the turbulent eddies are initially formed, but is reduced downstream as mixing smooths the velocity gradient between the jet and

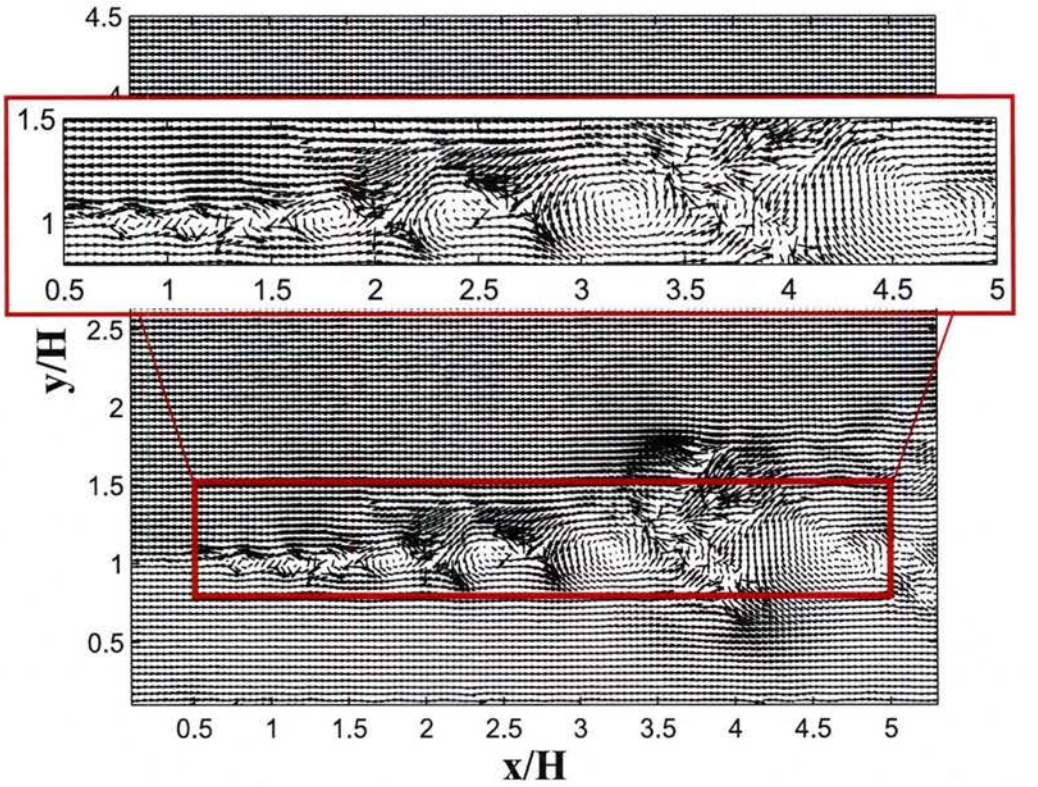

Figure 4.11: Velocity vectors viewed in a Galilean reference frame. Here 60% of the nozzle exit velocity has been subtracted from the streamwise velocity field to essentially "freeze" the turbulent eddies.

the ambient.

$$MF = \frac{\rho \vec{V} V}{A} \tag{4.3.2}$$

4.3.2 Temporally-Resolved Measurements

In this work, temporally-resolved measurements of surface pressure and velocity at discrete locations are obtained in addition to the spatially-resolved PIV measurements. This allows for spectral analysis of these quantities. The power spectral density of the surface pressure measured at each of the five streamwise pressure transducers is plotted against

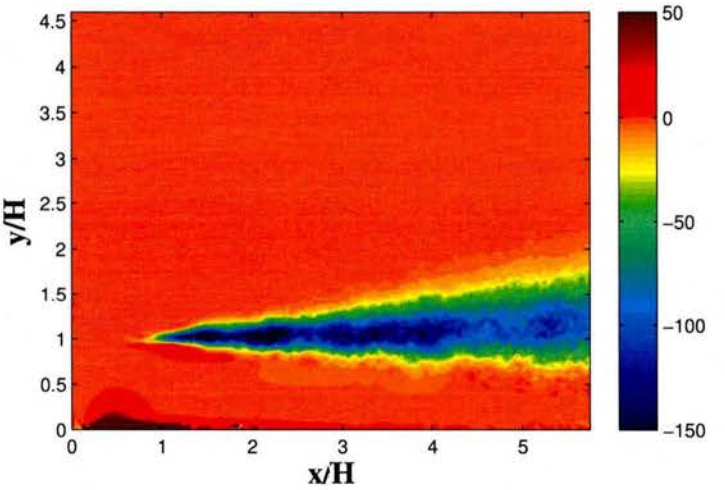

Figure 4.12: Wall normal momentum flux, indicating the flow is entraining fluid at the shear layer from the ambient.

Strouhal number in figure 4.13. Here, the Strouhal number is based on the nozzle exit velocity and height. In addition, a -7/3 reference is plotted representing the spectral roll-off of fluctuating pressure in shear flows (e.g., George *et al.* (1984)). The spectra, save for the

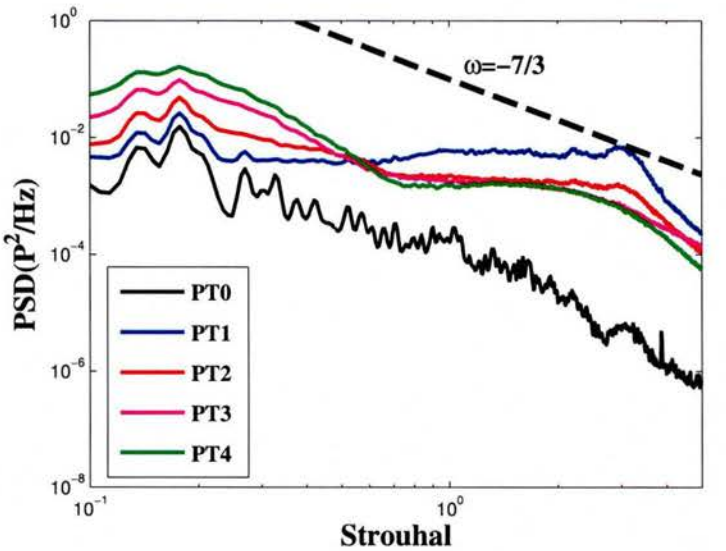

Figure 4.13: Surface pressure spectra versus Strouhal number for the five streamwise pressure transducers. $St = hf/U$

first location, possess broad peaks centered around a Strouhal of 0.2 and secondary peaks at a Strouhal number of 4. The roll-off of the pressure spectrum becomes steeper for pressure locations further downstream, but even the farthest downstream location is somewhat bi-modal. This suggests that, while the footprint of the turbulent outer layer of the wall jet is felt at the wall, interactions with the inner, wall region of the jet are still intermittent and the flow has not become self-similar.

Figure 4.14 displays the power spectral density of the hotwire measurements at several streamwise locations in the core and the shear layer/lip-line of the wall jet. The core displays a broadband signal in probes nearer to the nozzle exit, but, as the probes are traversed downstream a peak emerges and the spectra roll off at a reduced rate. Velocity spectra in the shear layer show a different behavior. For the two probes located nearest to the nozzle exit, distinct peaks appear at Strouhal numbers of 0.7 and 1, indicative of the initial vortices being formed by the shear layer instability. Further downstream, as these vortices are distorted and acted upon by inertial forces, the velocity spectrum smooths out, with a peak around a Strouhal number of 0.2. The spectra at these downstream locations match well with the familiar -5/3 law for turbulent velocity spectra, indicating the outer layer is approaching a fully-developed state.

4.4 Temporally Resolved Velocity Field Estimation Results

The ability to estimate a set of temporally-resolved velocity field estimates using the methods outlined previously is critical to the estimation of the far-field acoustics using Curle's analogy. As stochastic estimation is the chosen method to accomplish this in this study, it is vital that there exists a correlation between the velocity field and surface pressure that is accurately represented in the measurements. To verify this, cross-correlations between the PIV velocity snapshots and the surface pressure measurements were compared to cross-correlations between hotwire anemometry measurements of the velocity and surface pressure measurements. The advantage of using hotwire anemometry is that a high

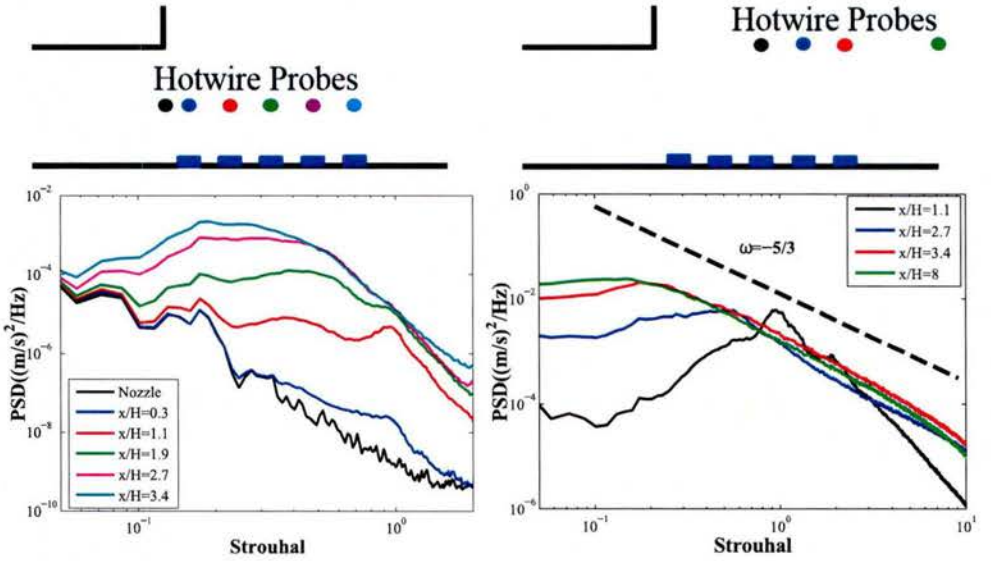

Figure 4.14: Location and power spectral density of velocity at various streamwise locations in both the core and shear layer of the wall jet.

signal-to-noise ratio (SNR), temporally-resolved signal is obtained, as opposed to the limited frequency range over which PIV measurements are obtained.

4.4.1 Velocity-Pressure Correlations

The cross-correlation coefficient between each surface pressure transducer and velocity measurements from both hotwire and PIV at a location in the shear layer of $x/H = 3.4$ appear in figure 4.15. Here, the non-dimensional time lag is plotted on the x-axis and is scaled by the nozzle exit velocity and height. For the pressure transducer at $x/H = 3.4$ it is shown that the correlation coefficient is at a maximum with zero lag, indicating that the velocity and surface pressure are being influenced by a common factor. Correlation also exists between the selected velocity location and the other surface pressure transducers, with the value of the correlation decreasing the farther away the probes become. The correlation at $x/H = 2.7$ is maximized at approximately $\tau^* = 1$, which corresponds to a convection velocity of approximately $0.60U_e$, the same value used in the Galilean frame of reference to identify turbulent eddies in figure 4.3.1. Similar correlations are obtained using PIV, albeit

with more inherent noise due to the increased uncertainty of PIV relative to hotwire. The fact that spatial correlation exists throughout the domain provides a basis for using the POD temporal coefficients as the conditional variable in the stochastic estimation with the surface pressure employed as unconditional variables.

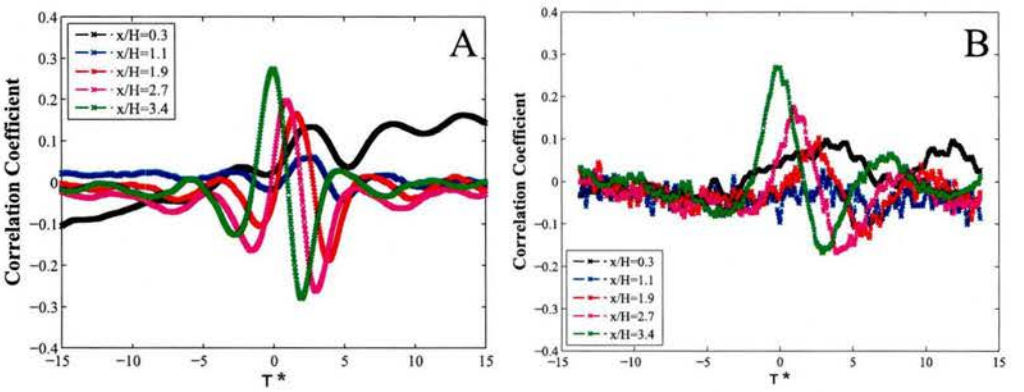

Figure 4.15: Cross-correlation coefficient between velocity and surface pressure for a location at $x/H = 3.4$ in the shear layer using both (A) hotwire and (B) PIV measurements.

4.4.2 POD of Velocity Field

In the proposed multi-time delay stochastic estimation, it was stated that POD expansion coefficients would be estimated from the surface pressure to produce reconstructed estimates of the velocity field. The results of snapshot POD applied to the PIV data set are shown below, with figure 4.16 displaying energy convergence of the kinetic energy contained in each additional POD mode. It can be observed that the lowest mode contains approximately 7% of the kinetic energy. The small energy content of even the lowest modes could be due to the competing effects of attempting to characterize both the inner layer and the outer layer structures in the orthogonal set. To support this, the set of calculated POD modes can also be searched for modes possessing evidence of energetic structures located in the boundary layer of the flow. As these structures represent a small portion of the kinetic energy in the entire flow they would be among the higher POD modes. Several higher order modes that show evidence of structure in the boundary layer are identified in this study,

but due to the increased uncertainty near the boundary it could not be determined that these are not artifacts of noise.

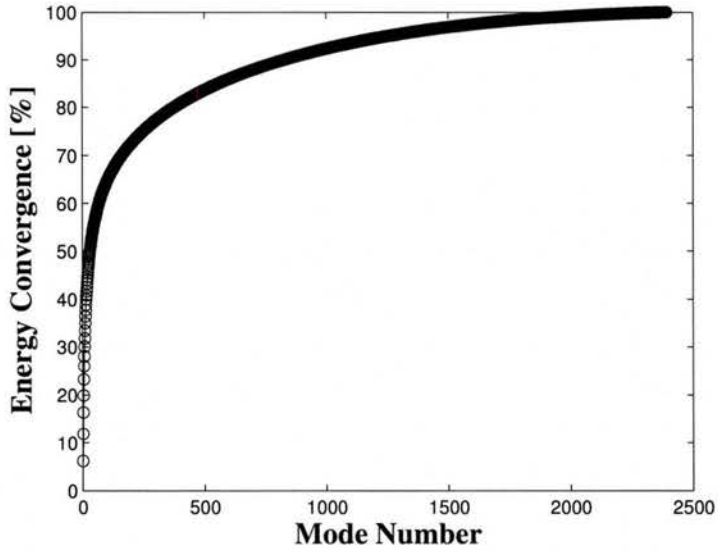

Figure 4.16: Energy convergence of modes resulting from POD.

Figure 4.17 shows the first four wall normal POD modes which highlight the alternating regions of positive and negative kinetic energy associated with vertical motion in the shear layer. The largest regions of kinetic energy are in the first mode, with subsequently higher modes decreasing in relative spatial extent and, at times, alternating phase with subsequent modes. This is consistent with the passage of turbulent eddies identified earlier in this chapter, which tended to grow in spatial extent as they convected downstream.

In the same way that velocity/surface pressure correlations were presented in the previous section, cross-correlation coefficients between the temporally varying, POD expansion coefficients and the surface pressure measurements are shown in figure 4.18. In the first four modes, it is apparent that correlation between expansion coefficients and surface pressure exists. Comparing the first two modes, the highest magnitude of the correlation coefficients (sub-figures (A) and (B)) are of similar value, but there is a distinct switching in location of positive and negative correlation peaks. In addition, there exists a noticeable phase shift

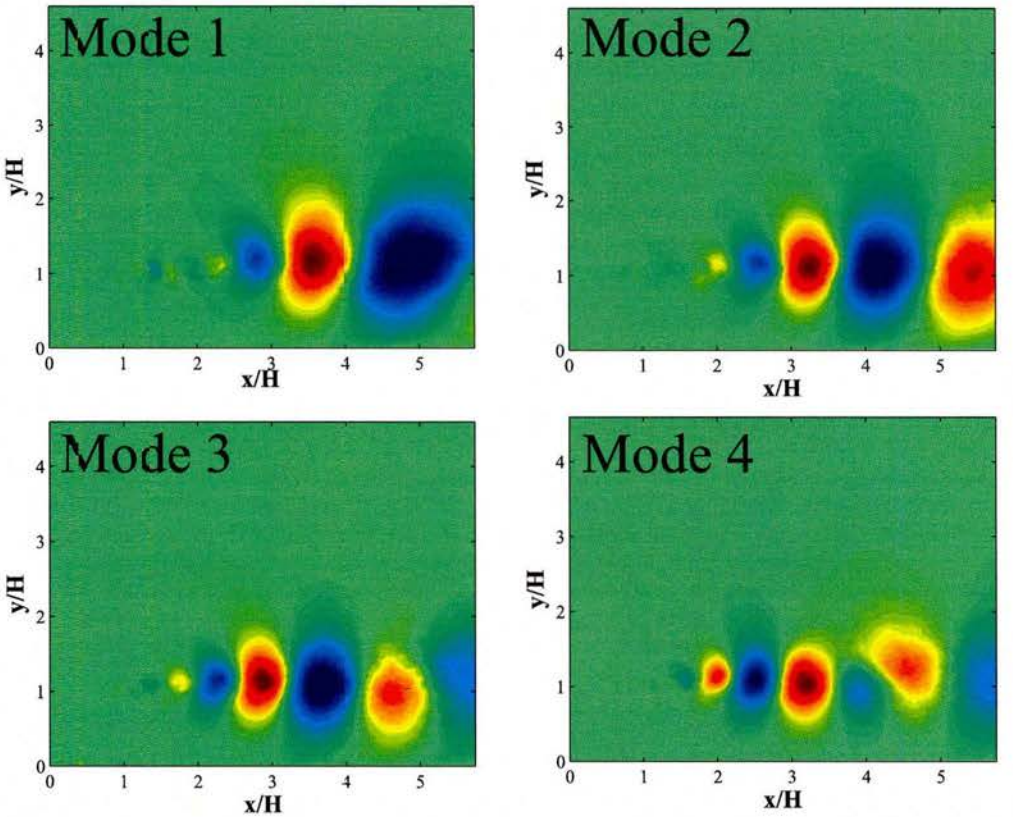

Figure 4.17: Figure (A)-(D) depict the first four wall normal POD modes.

of the temporal location of the maximum correlation. Comparing the third mode to the second (sub-figures (C) and (B)) it appears as though similar phasing exists between the correlations with decreased amplitude. Considering the fourth mode (sub-figure (D)) it is shown that the location of positive and negative correlation peaks is again switched. When considered with the spatial eigenfunctions in figure 4.17, the features described would seem to suggest that the lowest modes defined by the POD have the most interaction with the wall surface. As the modes become smaller in spatial extent, their footprint on the wall pressure decreases. In addition the phase shift of the correlation peaks between similar pairs and switching of positive and negative peaks would hint at the convection of these energetic structures. While the correlations involving only the first four modes are shown here, the characteristics described persist throughout the higher modes, with decreasing

magnitude of the correlation until they disappear into noise.

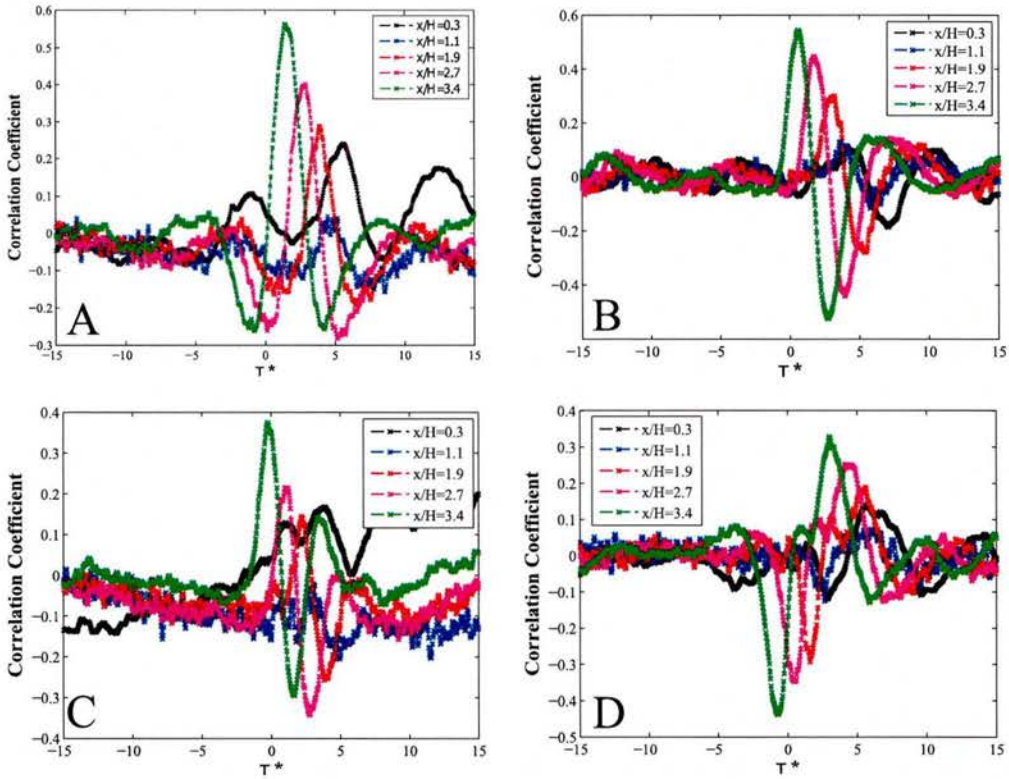

Figure 4.18: Cross-correlation coefficients between POD expansion coefficients and the surface pressure measurements for the first four POD modes, labeled (A) through (D) respectively.

To isolate when the correlation between a POD mode and the surface pressure loses its significance, the magnitude of the largest correlation coefficient over all time lags is plotted in figure 4.19 A. Here it is shown that the magnitude of the correlations drops off significantly after the first 12 modes, but remains above 0.1 for a large number of modes thereafter. The low correlation representative of a higher order mode at the chosen limit is shown in figure 4.19 B. In this work, it is found that by limiting the minimum correlation coefficient between POD expansion coefficient and surface pressure transducer to 0.1, the first 110 POD modes are retained. This set of modes captures approximately 70% of the kinetic energy in the velocity fluctuations.

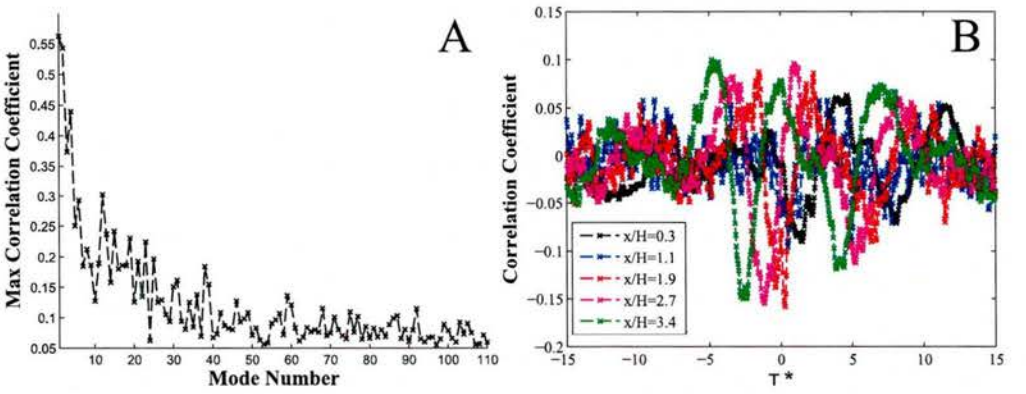

Figure 4.19: (A) Magnitudes of the maximum correlation coefficient regardless of time lag plotted against increasing POD mode number and (B) expansion coefficient/surface pressure cross-correlations for POD mode 110, showing the reduced magnitude of the correlation peak.

4.4.3 Estimation of Velocity Field

The results of the stochastic estimation described previously are shown below. Figures 4.20 and 4.21 display comparisons of the RMS fluctuations as measured by PIV (A), as calculated by reconstructing the velocity field based on the subset of the (110) modes used in the estimation technique, and as calculated by the estimation technique (C).

A consistent feature in both figures is that the estimates under-predict the fluctuations in the shear layer. This can be attributed to the relatively low correlation between some of the POD modes and the surface pressure used in the estimation. The truncated POD reconstruction captures less of the total kinetic energy than the PIV, by definition. The wall normal fluctuations appear to be more accurately represented than the streamwise fluctuations, where both under-represent the size of the shear layer. The estimate of the streamwise fluctuations is approximately 25% lower than the measured value throughout most of the shear layer.

Figure 4.22 shows an instantaneous PIV snapshot compared to both the POD reconstruction of the snapshot and an mLSE estimate of that snapshot. Similar regions of positive and negative vertical motion appear in the shear layer of all three fields; however, smaller-

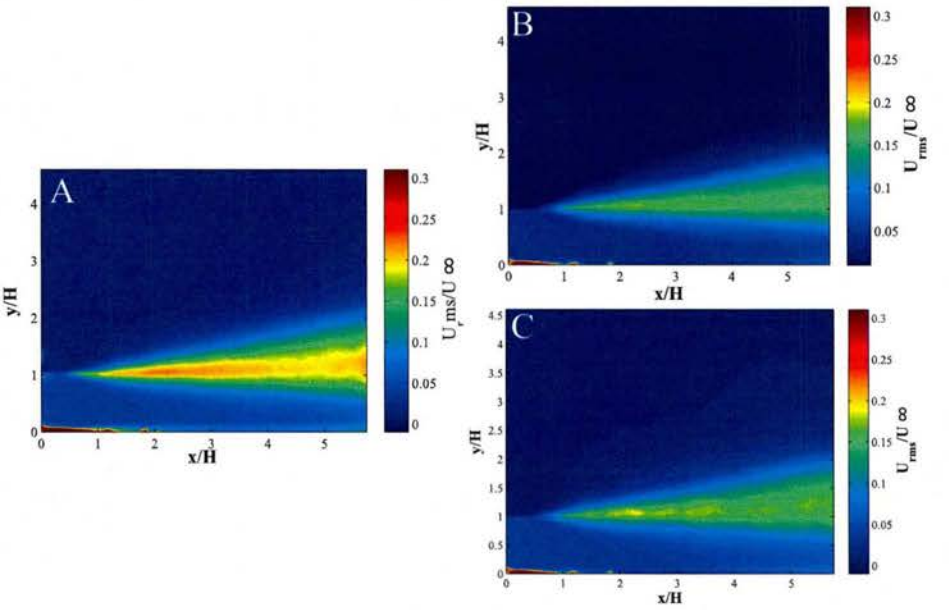

Figure 4.20: Comparison between the streamwise RMS fluctuations (A) measured by PIV, (B) reconstructed from the first 110 POD modes, and (C) estimated by stochastic estimation.

scale features are not as well captured by the estimate. The direct POD reconstruction, on the other hand, incorporates the correct scaling by POD expansion coefficient for all the modes used, allowing for resolution of finer details. While it is expected that the estimate should match within reason, as the pressure data at this instant are used to calibrate the stochastic estimation coefficients, estimates of the snapshots using entirely new pressure data follows similar trends. It should be noted however, that at times, the expected convection of turbulent structures through the shear layer, is instead shown as "pulsing" of phase shifted structures.

The power spectral density of the estimated velocity at a location in the shear layer of $x/H = 3.4$ is compared to similar hotwire measurements taken in the shear layer (as shown in figure 4.23). The estimated velocity set was obtained using pressure measurements obtained at 32,160 Hz. Due to the limited length of data however, only four averages of the spectra were obtained. This may explain the large high frequency noise as well as a large

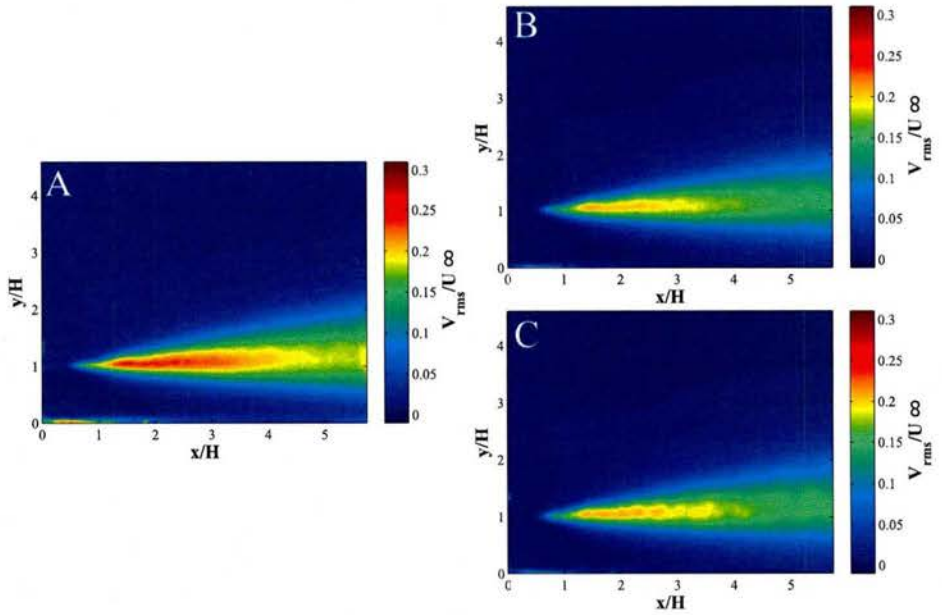

Figure 4.21: Comparison between the wall normal RMS fluctuations (A) measured by PIV, (B) reconstructed from the first 110 POD modes, and (C) estimated by stochastic estimation.

low frequency spike that appear. Of particular note is the early roll up of the estimated velocity spectra at a Strouhal number of 3. Overall, the trend of the spectra appears to follow the turbulent hotwire spectrum up to this frequency roll-off. This feature will be investigated in future work. For the final dissertation, a deeper investigation of the spectral properties of the velocity field estimates will be pursued.

4.5 Fluctuating Pressure Field Results

The following section presents the results of the Poisson solution for the hydrodynamic fluctuating pressure field. It should be noted, that the solver used in this work has been verified on the thoroughly studied problem of flow over a cylinder, as shown in the previous section and Nickels *et al.* (2014*a*). A snapshot of the fluctuating pressure field (calculated using the estimated velocity set) is shown in figure 4.24, where it is shown that alternating regions of high and low pressure appear in the shear layer in similar locations to the observed

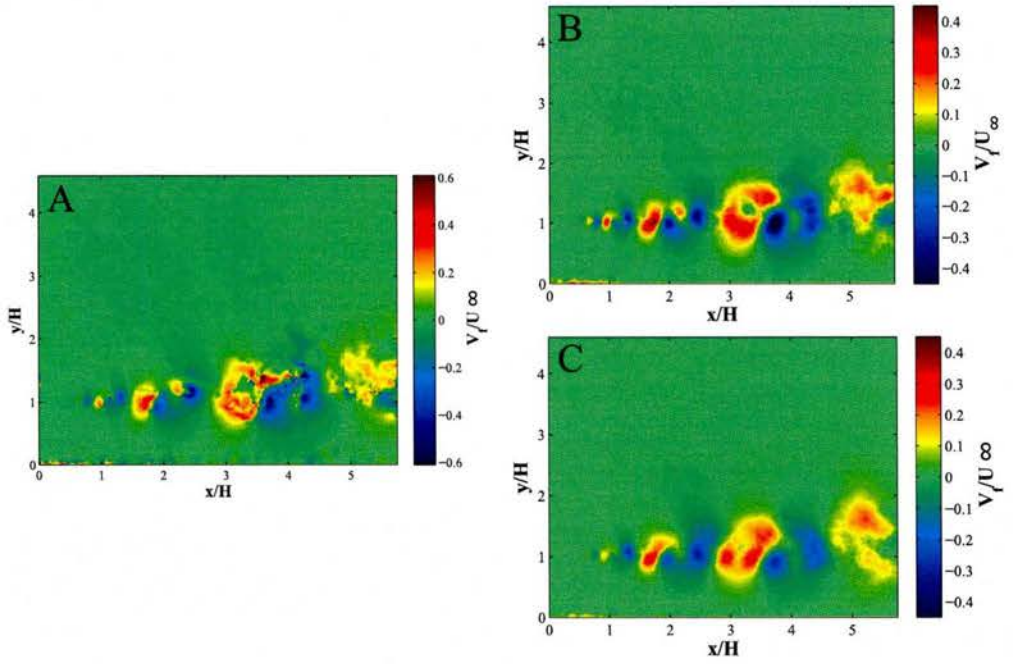

Figure 4.22: Comparison of (A) a measured PIV snapshot to (B) the POD reconstruction of that snapshot using 110 modes and (C) the estimate of that same snapshot using the proposed estimation technique.

vortex roll-ups. By integrating the surface pressure over the surface of the wall, the dipole source for Curle's acoustic analogy can be solved. It has been argued in this document that the appropriate acoustic analogy for the wall jet over a plane boundary is Powell's form of Curle's acoustic analogy; however, as a result, the pressure dipole is eliminated from the acoustic analogy.

4.6 Acoustic Analogy Results

The results of the acoustic analogies derived by Powell (1960) are shown in this section. Beginning with Curle's acoustic analogy in which only the pressure dipole is retained, figure 4.25 shows the acoustic pressure field. Here, the pressure field radiates as one-half of a dipole, with negligible preferred direction due to the low Mach number of the flow, and minimal acoustic pressure at very small angles with respect to the plane surface.

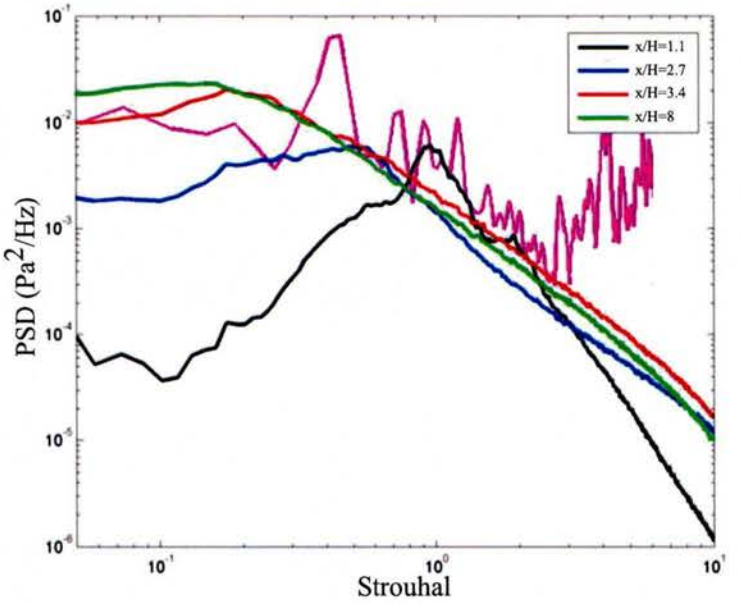

Figure 4.23: Estimated power spectral density of the estimated velocity field as compared to hotwire spectra at similar locations in the shear layer.

The acoustic pressure field estimated by Powell's formulation of Curle's acoustic analogy for a plane wall appears in figure 4.26. Here, a quadrupole radiation pattern is shown with the distinct near-field lateral quadrupole and far-field dipole-like shape. A major difference between this acoustic pressure field and the previously shown acoustic pressure field is the non-vanishing sound at small angles with respect to the plane wall. If an SPL field is created for this acoustic pressure field, referenced to 20 μ Pa, it can be observed that the levels appear to reside in the vicinity of 50 to 60 dB.

This is a reasonable match with direct measurements of the acoustic far-field at both 5 and 40 nozzle heights downstream of the nozzle exit shown in figure 4.28. The pressure dipole formulation of Curle's acoustic analogy on the other hand, over-predicts the direct measurements by up 15 dB. It should be noted, that the far-field acoustic measurements contain an unavoidable level of contamination from the lab environment. Due to this, it is expected that forthcoming estimates of the far-field acoustic spectra will be lower than those shown in figure 4.28, as they will not contain this contamination.

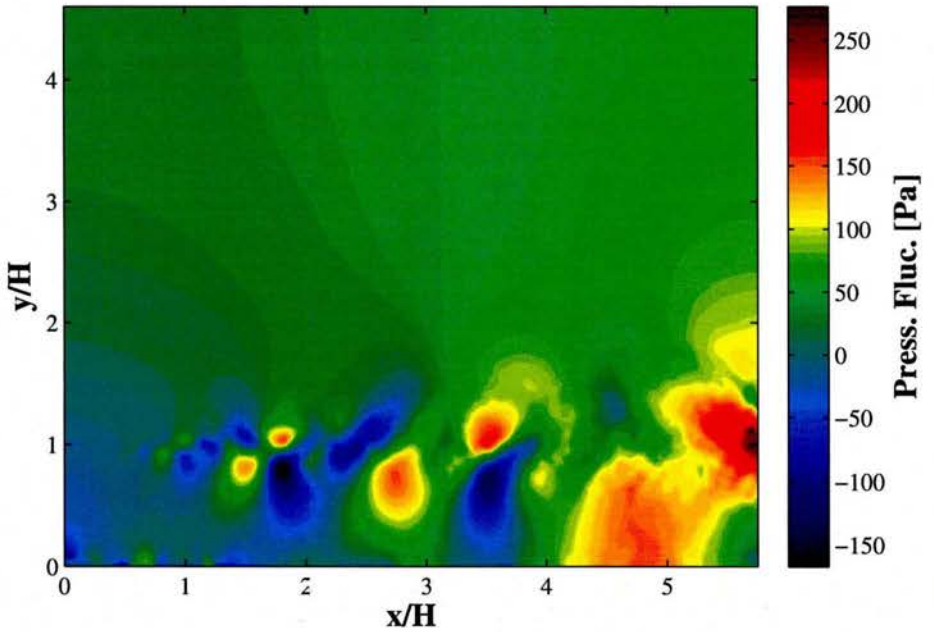

Figure 4.24: Instantaneous snapshot of the fluctuating pressure field as predicted by Poisson's equation.

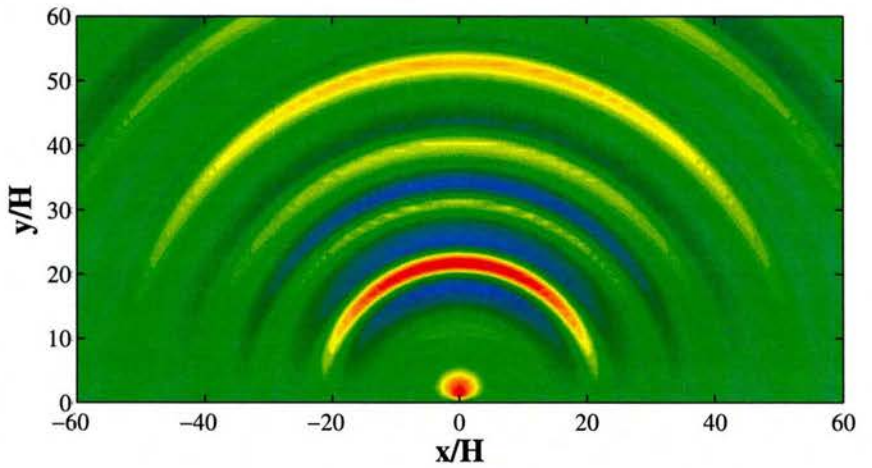

Figure 4.25: The acoustic pressure field predicted by Curle's acoustic analogy retaining only the pressure dipole formulation.

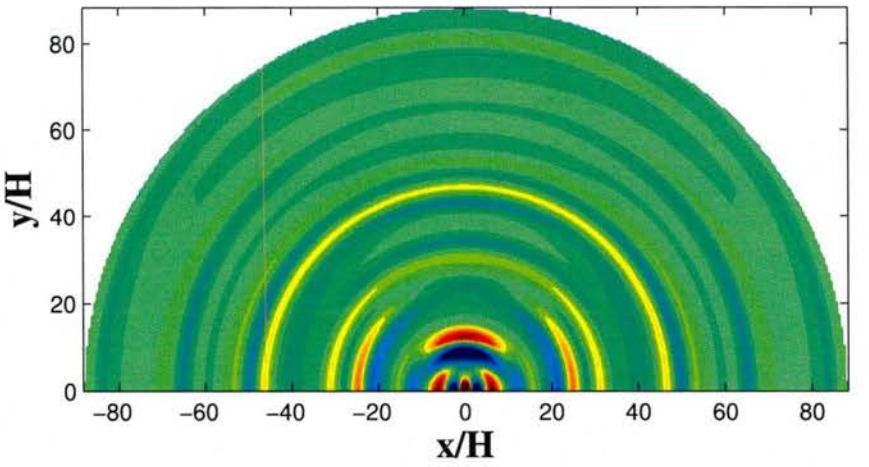

Figure 4.26: The acoustic pressure field predicted by Curle's acoustic analogy developed for a plane wall.

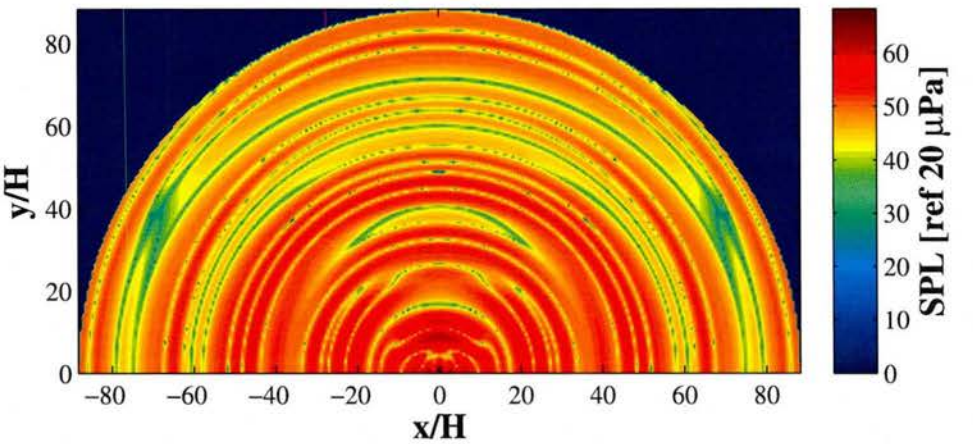

Figure 4.27: Sound pressure level field of the acoustic analogy developed by Powell's formulation of Curle's acoustic analogy.

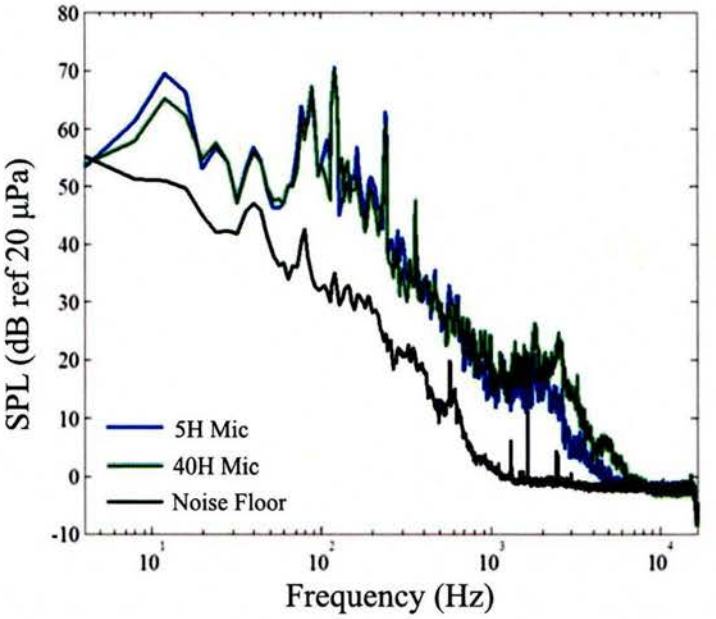

Figure 4.28: Measured far-field acoustics at both 5 and 40 nozzle heights downstream of the nozzle exit.

CHAPTER 5

CIRCULATION CONTROL EXPERIMENTS

5.1 Experimental Setup

5.1.1 Model Overview

The circulation control airfoil employed in these experiments is the one described by Wetzel (2011), whose design is based on the hydrofoil design of Rogers & Donnelly (2004), and is discussed here for completeness. The airfoil is two-dimensional and dual-slotted to allow for both upper and lower slot blowing; however, only the upper slot will be used in this work. The model is elliptical with a 20% thickness-to-chord ratio, no camber and a circular trailing edge, detailed in Figure 5.1. The airfoil has a chord of 0.521 m and a span of 0.914 m. The model was created in several pieces such that the interior and instrumentation are accessible; this design also allows for replacement of pieces for alternate configurations. The full drawing set of these assembly pieces can be found in Wetzel (2011), Appendix A. The trailing edge geometry is shown in Figure 5.2 where t_l indicates the lip thickness. The cylindrical trailing edge piece has three modular instrumentation rings which are outfitted with the instrumentation discussed in section 5.1.4.

The majority of the model was machined by Craig Johnson at the Illinois Institute of Technology entirely of aluminum. All the supports are 1018 steel while the air supply feeds were created in a selective laser sintering machine. The slot lips were machined by TMR Engineering in Micanopy, Florida.

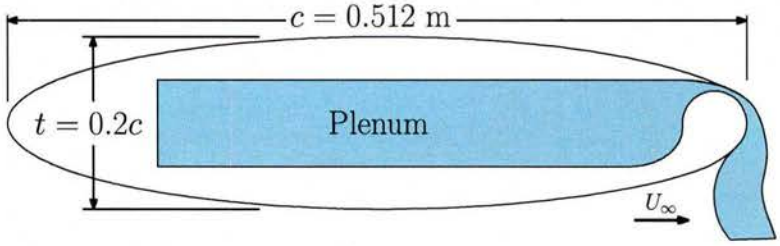

Figure 5.1: Sample single side blowing circulation control airfoil with geometric dimensions. (Adapted from Wetzel (2011))

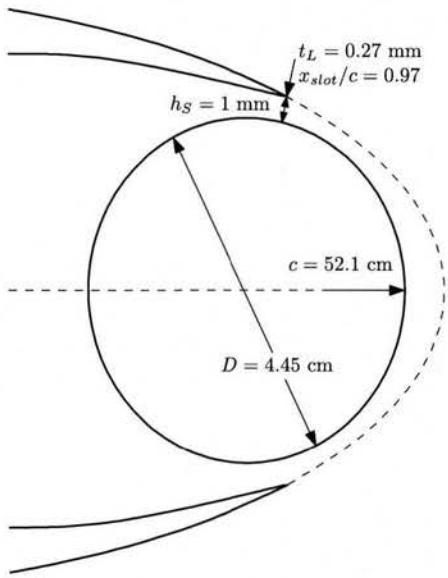

Figure 5.2: Trailing edge geometry. (Adapted from Wetzel (2011))

The interior of the model acts as a plenum and is split in two in order to separate the supply for the upper and lower blowing slots. The plenum is supplied from a dried, filtered, compressed air source external to the wind tunnel facility, which will be discussed later in this section 5.1.3. In order to set the height of the slot, eight sets of push-pull screws are placed on each side. All cases discussed have one slot height set to 1 mm (or $h/c = 0.0019$) while the other is closed and sealed with tape. The height of the slot is set by a shim material. Several measures are taken to reduce internal noise. First, the plenum is supplied from both spanwise ends of the model. This decreases plenum noise by reducing the flow

rate required by either side, thereby reducing the velocity of the flow entering the model and, by extension, the internal noise. This also helps to ensure flow uniformity and minimize flow speed within the plenum. Next, the flow encounters Poly-fil polyester filling to attenuate the noise from the incoming flow. At the mid-chord, strips of ERG Duocel Aluminum Foam (40, 20, and 10 pores per inch) are installed to reduce noise. A comparative study (Wetzel, 2011) finds that maximum noise reduction is achieved by placing these strips in series with the largest number of pores per inch in the most upstream position. The aluminum foam also helps to straighten the flow within the plenum. Finally, sheets of 2 mm thick foam are installed along the plenum walls to further decrease internal noise.

5.1.2 Florida State Aeroacoustic Tunnel

The Florida State Aeroacoustic Tunnel (FSAT) is an open-return wind tunnel with an open-jet test section. The wind tunnel is housed in an ISO 3745-certified 250 Hz anechoic room used to simulate an acoustic free-field. Air is pulled through the 0.91 m tall by 1.22 m wide by 3.05 m long test section by a 450-hp centrifugal blower connected to a jet collector via an acoustically lined diffuser. The tunnel is capable of producing free-stream velocities from 5 to 75 m/s with turbulence intensity levels below 0.12% and non-uniformity below 0.1% (Pascioni *et al.*, 2014). The anechoic room which houses the test section has dimensions of 2.7 m by 4.5 m by 4.8 m (height by width by length). Figure 5.3 provides an overview of the FSAT. The leading edge of the model is installed 13 cm downstream of the inlet exit at a zero degree geometric angle of attack. The upper and lower boundary layers are tripped with zig-zag turbulator tape placed at 18% chord (Wetzel, 2011). Throughout all testing the airfoil is bounded in the spanwise direction by sidewalls in order to ensure two-dimensional flow. The sidewalls are created from foam in order to minimize acoustic reflections on their surface. Further details regarding the FSAT can be found in Pascioni *et al.* (2014).

The FSAT is outfitted with instrumentation to provide important flow parameters such as temperature, free-stream pressure, and humidity. All data for the tunnel parameters are

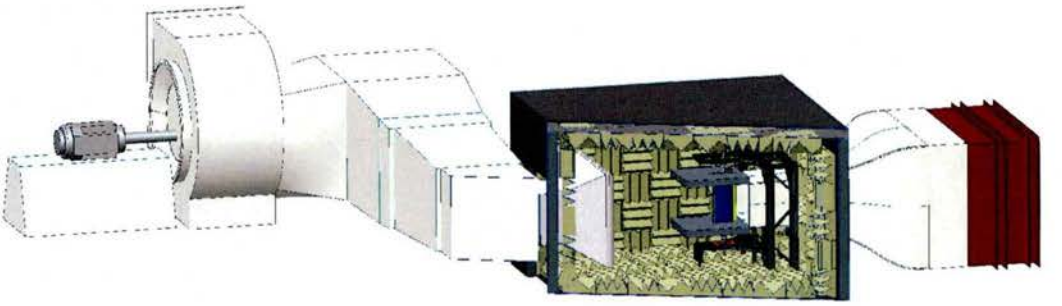

Figure 5.3: Overview of the FSAT facility. The foreground chamber wall is removed for illustration.

collected on a National Instruments cDAQ 9174 at 2 Hz. Temperature is acquired via four Omega RTD-805s and averaged to obtain the mean temperature of the flow. A Pitot-static probe is placed in the flow and connected to two Mensor 6115 digital pressure transducers (16 psia and 0.58 psig) to obtain free-stream static and dynamic pressure. The probe is retracted during testing to maximize flow uniformity and minimize background noise. Lastly, an Omega HX94V relative humidity sensor is used to acquire humidity information. Using these sensors, important fluid and free-stream flow parameters such as Reynolds numbers and momentum coefficient are obtained.

5.1.3 Compressed Air Delivery System

Compressed air is provided by three 560 SCFM, 209 hp compressors housed in a building isolated from the Florida State Aeroacoustic Tunnel (FSAT). The air is run through wet tanks to remove water then through desiccant driers and filters to ensure clean, dry air and fed into six 18.9 m^3 tanks. The peak tank pressure is 500 psi. Once the air is inside the building housing the FSAT the system is regulated down, by a 2 inch 95HP Air Regulator from Fisher, to 120 psig while maintaining a sufficient mass flow rate for all test conditions. This line is then split to run into the FSAT and into neighboring rooms so that static characterization and leak check can be performed between wind tunnel entries.

Within the FSAT, the air delivery system consists of a regulator, a Venturi meter, an

air filter equipped with an Omega PR-20 platinum RTD, and a Universal Silencer U5-1-1/2 straight-through acoustic silencer. The regulator serves to control the pressure in the plenum while the Venturi meter measures the mass-flow rate into the model, effectively setting and measuring the jet Reynolds number and momentum coefficient. The air filter removes contaminants and the silencer reduces the extraneous noise from the compressors. According to manufacturers specifications the silencers provide 30 dB sound pressure level attenuation from 500 Hz to 8 kHz. A relief valve is present to prevent over-pressurization of the plenum. Once the air leaves this system, it travels through flexible hosing 38 mm in diameter by 3.7 m long. From the hosing, the flow travels into the air supply feeds and exits into the plenum through a 50.8 mm^2 rectangular orifice into the model interior, which has been described in section 5.1.1. An overview of the full compressed air delivery system is provided in Figure 5.4.

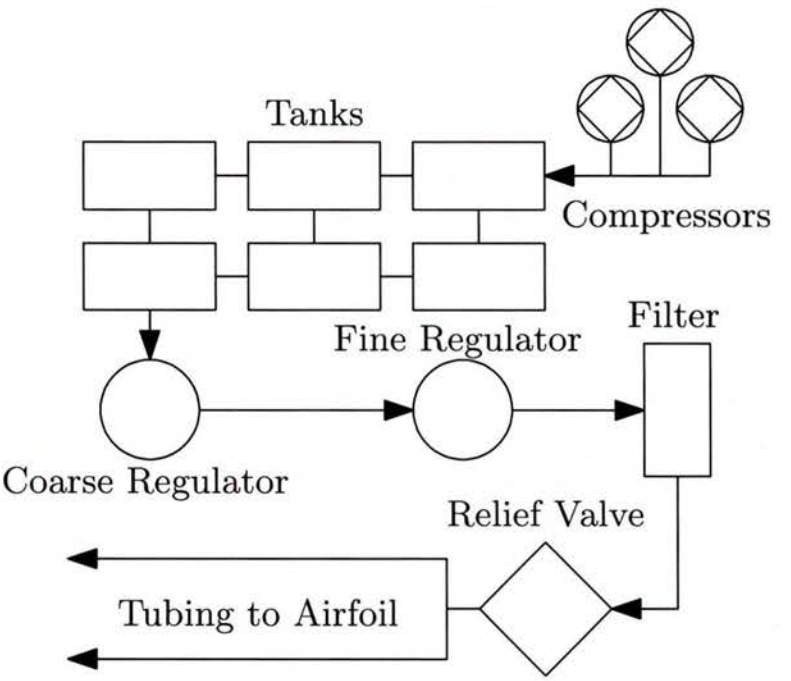

Figure 5.4: Overview of the compressed air delivery system.

5.1.4 Model Instrumentation

Steady Pressure. The midspan of the model is outfitted with 39 steady pressure ports with 0.71 mm diameter. Of these 39 ports, 30 are located in fixed positions along the body of the airfoil while 9 are contained on one of the instrumentation rings along the trailing edge. The chordwise locations of the steady pressure ports are provided in Table 5.1 (note that each chordwise position is represented on both the pressure and suction sides of the airfoil).

x/c Location
0
0.005
0.012
0.02
0.029
0.039
0.051
0.068
0.078
0.089
0.098
0.107
0.215
0.51
0.75
0.97
0.982
0.991
0.998
1

Table 5.1: Chordwise location of steady pressure taps. Each location represented on both the pressure and suction sides of the model.

Three 16-channel Esterline Pressure Systems pressure scanners (with ranges of 5, 1, and 0.36 psi) are used to acquire the steady pressure data. Each channel on the acquisition system is connected to a steady pressure port via 1 mm vinyl tubing. The remaining ports are used with the Venturi meters and the plenum pressure. The static pressure port

of the Pitot-static probe provides the reference pressure to the scanners. Along with the reference static pressure (p_∞), the dynamic pressure ($q_\infty = \frac{1}{2}\rho V^2$) from the Pitot-static probe is used to non-dimensionalize the pressure measurement to determine the coefficient of pressure (C_p) at each steady pressure port. Steady pressure data are acquired at 2 Hz for 60 seconds.

$$C_p = \frac{p - p_\infty}{q_\infty} \tag{5.1.1}$$

Unsteady Pressure. Unsteady pressure is acquired via transducers (WM-61a Panasonic Electret Microphones) located on an instrumentation ring positioned at the trailing edge of the model and centered in the spanwise direction. Details about the microphones can be found in Table 5.2. The upper range of linear operation for these microphones is 125 dB (re. 20 μ Pa). As such, they are not suitable as surface-mounted measurement devices because hydrodynamic fluctuations are generally considerably above 125 dB. Further, the sensor diameter (1/4 inch) is large compared to the trailing edge curvature. To circumvent these restrictions, a method of recessing the microphone from the flow behind a narrow pressure tube is employed (Bergh & Tidjeman, 1965; Zawodny *et al.*, 2016). These devices will be referred to as "recessed microphones" hereafter.

Microphone	Freq. Range	Uncertainty	Max Range	Nom. Sensitivity
WM-61a Panasonic	20 Hz - 16 kHz	±3 dB	125 dB	30 mV/Pa
G.R.A.S. Type 40BE	4 Hz - 80 kHz	±2 dB	168 dB	4 mV/Pa
B& K Type 4958	10 Hz - 20 kHz	±2 dB	140 dB	11 mV/Pa

Table 5.2: Microphone specifications.

Figure 5.5 shows a schematic of a typical recessed microphone used throughout this work. Upstream of the microphone and flush mounted to the surface of the model is a narrow tube. This tube allows the microphone to be recessed away from the surface, thereby lowering the effective pressure on the microphone diaphragm over a large frequency range. Downstream of the microphone is a four meter length of Tygon tubing. This tubing is utilized to

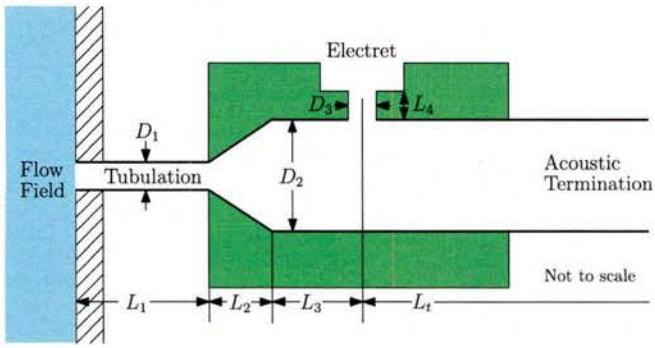

Figure 5.5: Schematic of recessed electret microphone (adapted from Zawodny (2013)).

Variable	Dimension
L_1	20.0 mm
D_1	0.4 mm
L_2	0.5 mm
D_2	3.0 mm
L_3	1.5 mm
D_3	2.0 mm
L_4	0.5 mm
L_t	4.0 m

Table 5.3: Dimensions for Fig 5.5

act as a gradual acoustic termination to reduce the reflections seen by the microphone. Further details regarding these devices can be found in Zawodny (2013). Because the data acquired from these devices provide lower amplitude pressure fluctuations, the signal must be transferred to the observation point at the surface through a transfer function. This is required to provide the correct (Dirichlet) boundary conditions for the Poisson solver discussed in section 2.2 and for stochastic estimation.

Before testing, the recessed electrets are calibrated to provide the frequency-dependent transfer function between the recessed location and the surface of the model. The calibration rig shown in figure 5.6 consists of a linear acoustic horn followed by a small (8.6 mm by 8.6 mm cross section by 50.8 mm in length) waveguide to ensure plane wave propagation. The linear acoustic horn serves to efficiently transition the tube from a 25.4 mm diameter circle (speaker diaphragm) to the 8.6 by 8.6 mm square cross section. The input into the speaker is a periodic white noise signal (from 250 Hz to 16 kHz), where the period of the signal is identical to the block length used in processing.

To obtain the transfer function between a surface and recessed microphone, a 2426H JBL speaker is placed at the location denoted A while a microphone is inserted at location B, hereafter referred to as the "side microphone." Next, a second microphone is brought to the surface at location C using the extension shown in figure 5.6b to ensure the microphone is equivalently mounted as if it were flush with the surface (referred to as the "surface

microphone"). Data is taken on each microphone then auto-spectra (Bendat & Piersol, 2010),

$$G_{bb} = \frac{2}{T} E[B^* B], \tag{5.1.2}$$

$$G_{cc} = \frac{2}{T} E[C^* C], \tag{5.1.3}$$

and cross-spectra,

$$G_{bc_1} = \frac{2}{T} E[B^* C_1], \tag{5.1.4}$$

(where B^* is the complex conjugate of the discrete Fourier transform of the side microphone output, C_1 is the discrete Fourier transform of the reference surface microphone output, and T is the length of the data) are taken from these signals. From these auto- and cross-spectra a transfer function is defined between the side and surface microphones by

$$H_{bc_1} = \frac{G_{bc_1}}{G_{bb}} \tag{5.1.5}$$

Then, the surface microphone and extension piece are removed and the calibration rig is brought flush (at location C) to the recessed microphone tube mounted in the model, defining a second transfer function using the identical input signal, H_{bc_2}. Finally, these two transfer functions are combined to obtain the transfer function between the surface microphone and the recessed microphone, defined as,

$$P_{c_1} = H_{c_2 c_1} P_{c_2} = \frac{H_{bc_2}}{H_{bc_1}} P_{c_2} = \frac{G_{bc_2}}{G_{bb}} \frac{G_{bb}}{G_{bc_1}} P_{c_2} = \frac{E[B^* C_2]}{E[B^* B]} \frac{E[B^* B]}{E[B^* C_1]} P_{c_2} = \frac{E[B^* C_2]}{E[B^* C_1]} P_{c_2} \tag{5.1.6}$$

where * denotes a complex conjugate, C_1 is the Discrete Fourier transform of the surface microphone signal and C_2 is the Discrete Fourier transform of the device under test signal, the recessed microphone. Thus, the original P_{c_2} is corrected to provide P_{c_1}, the equivalent unsteady pressure at the surface. Using an independent test case (i.e., a case not used to determine the transfer function), the rms error in reconstruction is estimated at approximately 2% of the actual rms value.

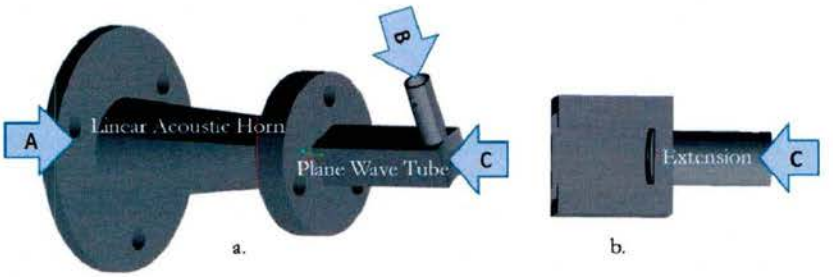

Figure 5.6: Calibration device for the recessed electrets, a.) shows the general overview while b.) shows the extension for comparison to surface mounted microphone. A indicates the speaker location, B indicates the side microphone location and C indicates the surface microphone (in b.) or the device under test (in a.)

5.1.5 Slot Characterization

The slot jet speed is obtained from isentropic relations between plenum and freestream pressures such that

$$U_{jet} = \sqrt{2RT_0\left(\frac{\gamma}{\gamma-1}\right)\left(1-\left(\frac{p_\infty}{p_0}\right)^{(\gamma-1)/\gamma}\right)} \tag{5.1.7}$$

assuming zero (or very small) velocity within the plenum (Wetzel, 2011). In Eq. (5.1.7), R is the ideal gas constant and γ is the ratio of specific heats, while the stagnation temperature, T_0, is measured by the RTD in the air delivery system, p_∞ is measured by the Pitot-static probe in the free-stream, and p_0 is measured by pressure scanners via a pressure tap from the plenum. The jet velocity is held constant throughout testing to within 5% of the intended value. Using the jet velocity U_j, the jet mass flow rate $\dot{m}$ (measured via two Venturi meters), the freestream dynamic pressure q_∞ and the model planform area S, the momentum coefficient is calculated as

$$C_\mu = \frac{\dot{m}U_j}{q_\infty S}. \tag{5.1.8}$$

Constant temperature hotwire anemometry is employed prior to wind tunnel testing in order to ensure uniform blowing over the span of the slot. The hotwire probes are approximately 5μm in diameter, 1.25 mm in length and consist of platinum plated tungsten

wires (type 55P11, from Dantec). The probes are calibrated via a Dantec Streamline free-jet calibrator from 10 to 110 m/s. The calibration data is used to determine the constants in King's power law (Bruun, 2001), which provides a relationship between voltage and flow speed. A Dantec StreamLine frame and CTA Module 90C10 are used to maintain a constant temperature over the probe during testing and calibration. All data are acquired on a National Instruments PXI-1042Q chassis on a PXI-4462 dynamic data acquisition card at 10 kHz.

The model is setup with the air delivery system discussed previously (section 5.1.3) and a three-axis Parker ACR9030 traverse is aligned to the blowing slot. A hotwire probe is then attached to the traverse. In order to account for small variations in slot velocity due to non-constant back pressure a stationary hotwire probe is placed at the center of the slot and used as a reference. The result of the uniformity tests are shown in Figure 5.7 for several different plenum pressures, corresponding to velocities of approximately 20, 40, 60, 80 and 100 m/s.

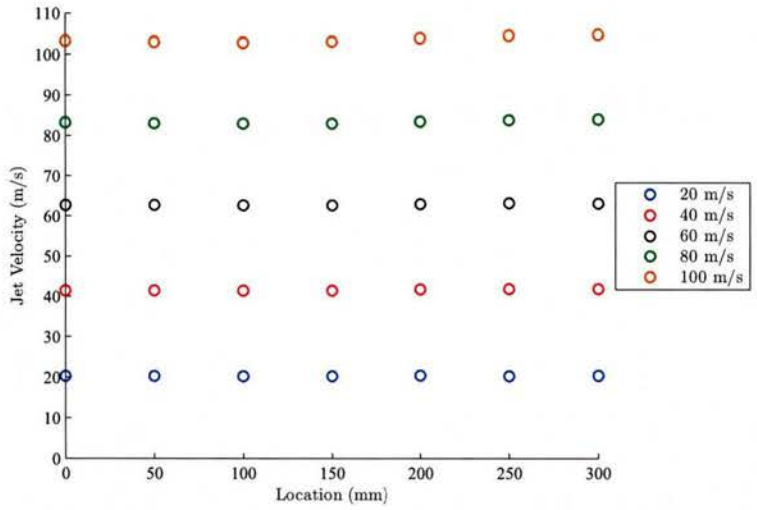

Figure 5.7: Uniformity test results across the middle 300 mm of the circulation control model.

5.1.6 Particle Image Velocimetry

Particle image velocimetry (PIV) is a non-intrusive technique by which spatially resolved velocity fields can be acquired. PIV involves seeding the flow with small particles and measuring the displacement of those particles from two "instantaneous" snapshots with a known temporal delay between them. Based on the distance these particles move over the given time, the local velocity is determined. A set of two images used to obtain each velocity field is called an image pair. Image pairs are acquired at a known rate.

To illuminate and "freeze" the particles in time, two high powered lasers are employed. These lasers are spatially equivalent but offset from one another temporally by a small, known time delay between snapshots. Each laser is passed through a series of optical lenses to first focus the light down to a thin line and then expand it into a thin sheet to illuminate the entire region of interest. For two-component (u and v velocity) PIV, a single high-resolution camera is placed outside of the flow field and normal to the plane of interest. The camera is controlled to obtain snapshots at the precise moment each laser is fired.

In order to determine the velocity field from a set of two images, each image is broken into smaller regions (known as interrogation windows). Spatial cross-correlation is then employed between the windows using fast Fourier transforms (FFT). This allows for the determination of the x and y components of velocity based on the displacement of all the particles within the window, instead of relying on following individual particles through the flow.

Experimental Setup. Two-component (u and v) PIV velocity fields are obtained using a 4-megapixel Imager ProX CCD camera. The region of interest for these tests is defined from slightly upstream of the slot jet to several inches downstream of the trailing edge (illustrated in figure 5.8). A Quantel Evengreen 200 mJ Nd:Yag laser is used as the light source, while LaVision software controls the timing and synchronization between the camera and laser. To minimize the effect of the PIV setup on the acoustic measurements (discussed in §5.1.7), the laser power supply and PIV acquisition computer are positioned

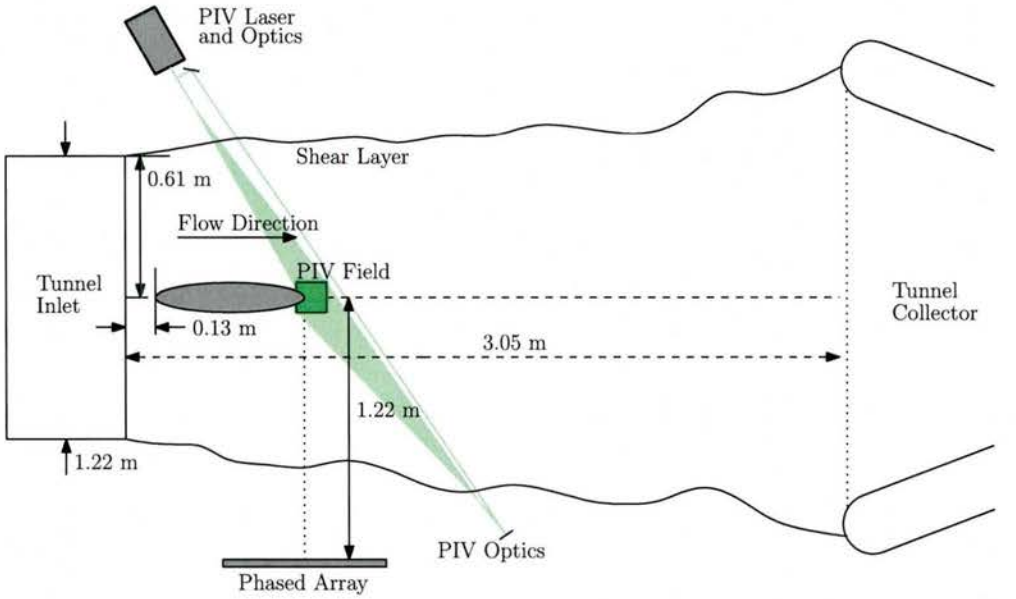

Figure 5.8: Schematic showing an overview of the tunnel including locations of the phased acoustic array and the PIV acquisition field. PIV power supply and all acquisition systems are located outside of the tunnel to remove their acoustic influence.

outside of the anechoic chamber. This requires the use of 10 meter cables for the laser head power, the laser cooling, and the camera relay. The length of these cables, camera RAM, and computer RAM limits the acquisition rate to a maximum of 1.5 Hz.

A 50/50 beamsplitter is used to illuminate both sides of the airfoil's trailing edge. To reduce the potential area for acoustic reflections and reduce losses in light intensity, a set of lenses and mirrors is set up on each side of the tunnel. An overview of this setup (along with the rest of the tunnel, instrumentation, and model) is shown in Figure 5.9 and is described presently. The laser head is setup on the far side of the tunnel (away from the phased acoustic array and shielded from the array by the model) along with the beamsplitter, a plane mirror (25.4 mm wide by 25.4 mm tall), a -15 mm focal length cylindrical lens (12.7 mm wide by 25.4 mm tall) and a 750 mm focal length spherical lens (25.4 mm diameter). The laser first encounters the beamsplitter, directing one beam toward the far-side lenses and the other to the mirror. The mirror then directs the beam across the test section to the near side (near to the array) of the chamber. Once on the near side, the beam encounters

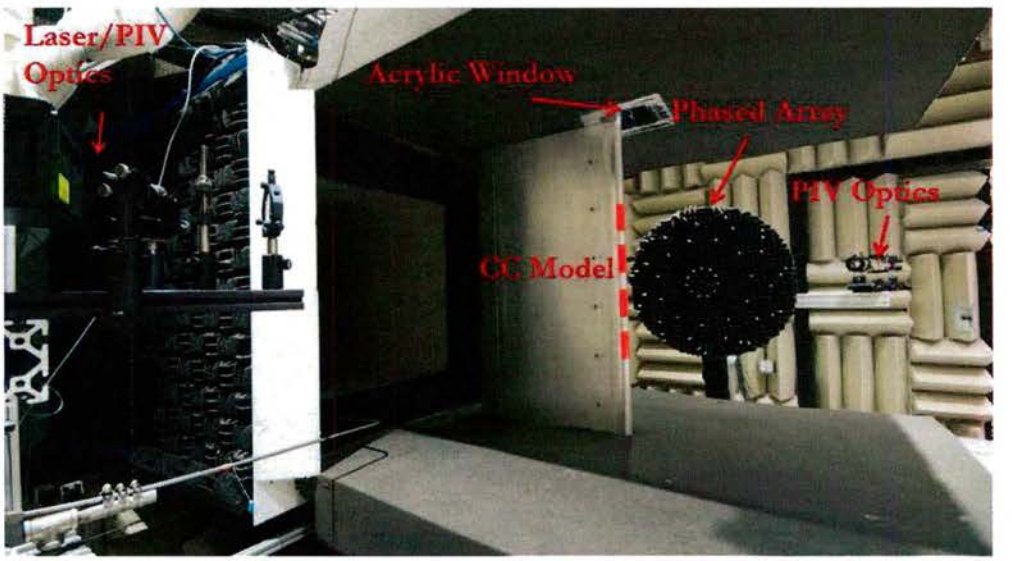

Figure 5.9: Overview of the FSAT with all instrumentation installed.

another planar mirror (25.4 mm diameter) along with a -20 mm cylindrical lens (25.4 mm wide by 50.8 mm tall) and a two-spherical-lens-assembly (each with 25.4 mm diameter) with an effective focal length of 1000 mm. The far side optics are shown in Figure 5.10a and the near side optics are in Figure 5.10b, with a list of optics found in Table 5.4. The total area illuminated by the light sheets and viewed by the camera is approximately 150 mm by 150 mm with a resolution of 0.150 mm per pixel. The light sheet is positioned (in a spanwise sense) as close to the unsteady pressure sensors as possible.

Optic Type	Location	Focal Length
50/50 Beamsplitter	Far-side	Planar
Cylindrical Lens	Far-side	-15 mm
Spherical Lens	Far-side	750 mm
Mirror	Far-side	Planar
Cylindrical Lens	Near-side	-20 mm
Spherical Lens	Near-side	-100 mm
Spherical Lens	Near-side	150 mm
Mirror	Near-side	Planar

Table 5.4: List of optics used for PIV testing.

A small area is cut out of the top foam sidewall and outfitted with an acrylic viewing

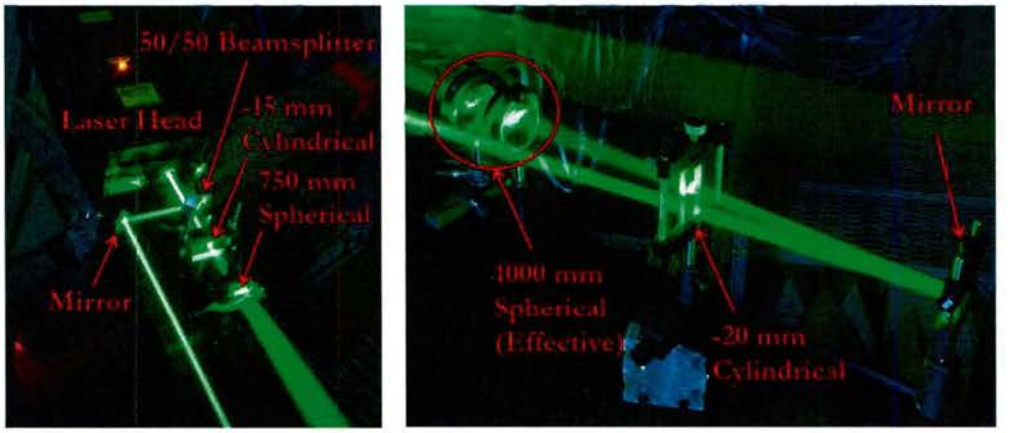

a. b.

Figure 5.10: Overview of the PIV optics setup on the a.) far and b.) near sides of the tunnel. A list of the optics is provided in Table 5.4.

window (as shown in Figure 5.9). This window allows the camera to be positioned directly above the region of interest and normal to the light sheet. Placing the camera normal to the light sheet reduces the effects of reflections on the images. To further reduce the effect of these reflections, which allows for reliable data acquisition close to the surface, 3M orange fluorescent marking tape (0.1 mm thick) is placed on the trailing edge of the model and a 532 nm bandpass filter is installed on the camera. When the (green, 532 nm) light encounters this tape, it fluoresces to a different wavelength and is filtered prior to reaching the camera's imaging sensor.

A six nozzle laskin atomizer (TSI 9307-6) is used to generate the particles that seed the flow. The particles are atomized olive oil approximately 1 μm in diameter (vendor specified). The seed is injected in the inlet of the tunnel before the contraction but after the conditioning screens. It is introduced into the flow by a custom rake which allows for control over the positioning of the seed within the flow and controls the seed density.

Image Processing. After acquisition, the 765 PIV image pairs are processed into vector fields in DaVis 8.2.2 by LaVision Inc. Before performing the spatial cross-correlation, several pre-processing steps are taken. Before the cross-correlation is performed, the min-

imum intensity field is removed from each location to reduce noise. A geometric mask is then used to remove areas occupied by the airfoil and an adaptive mask is used to remove areas of poor seeding.

The images are then processed to produce vector fields. For all cases included in this dissertation, the images are processed using five total cross-correlation passes. The first two passes are performed with 64 by 64 pixel interrogation windows with 50% overlap and no weighting function. The final three passes are performed with 24 by 24 pixel interrogation windows with 50% overlap. This provides a final spatial resolution of 0.906 mm per velocity vector. For these final passes an adaptive weighting function is used. Using the adaptive setting, the optimal weighting function is chosen by the software depending on the data within the window. Between each cross-correlation pass a universal outlier removal technique (Westerweel, 1993) is employed and interpolation is performed where data is missing.

After the final cross-correlation pass is performed, the universal outlier removal technique is employed again followed by multi-variate outlier detection (Griffin *et al.*, 2010). Finally, the vector fields are interpolated in regions with no data. In the proper orthogonal decomposition (POD), the mean is removed from each vector field. In regions with no data, this will result in an inaccurate, large (on the order of the mean) fluctuations which will lead to false POD modes. By interpolating these regions, the inaccurate fluctuations become zero and will have a reduced (undesirable) effect on the POD. It should be noted that if more than 20% of the vectors at any spatial location are interpolated, this area is considered to have no data and is ignored during all subsequent processing. Uncertainty in the PIV data are calculated in DaVis by the correlation statistics method (Wieneke, 2014).

5.1.7 Acoustic Measurements

The acoustic measurements taken throughout this study are based on both single microphone data and phased acoustic array methods. This section discusses single microphone and array beamforming techniques as well as the experimental setup, acquisition and pro-

cessing parameters.

Single microphone auto-spectrum can be obtained to view noise levels obtained over a frequency band of interest from a particular source region. However, since a single microphone simply provides the levels of all pressure incident on its diaphragm, it cannot distinguish between background noise and the acoustics of interest. It also cannot distinguish the location of acoustic sources. While considerably more complex, beamforming provides a method to obtain source locations and source field levels at the array center with background noise suppressed.

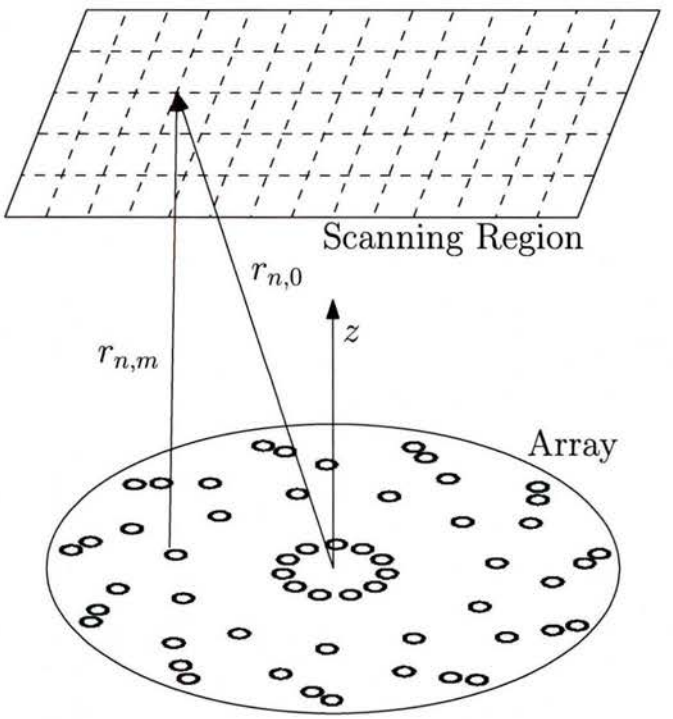

Figure 5.11: Schematic of the delay-and-sum beamforming setup (adapted from Yardibi *et al.* (2010*b*)).

Delay-And-Sum Beamforming. Beamforming is a method to determine acoustic source locations and amplitudes. Delay-and-sum (DAS) is the most straightforward form of beamforming. In order to understand DAS, consider a planar array consisting of M microphones directed at a scanning region of N scanning points as shown in Figure 5.11.

The distance from each microphone, m, to each scanning point, n, can be expressed as $r_{n,m}$. At each scanning point, there is assumed to be a point monopole source which is incoherent with every other source in the field. In the frequency domain, the strength of the source located at scanning point n can be estimated as (Dougherty, 2002),

$$Y_n = \frac{\hat{a}_n^H \hat{R} \hat{a}_n}{M^2}, \tag{5.1.9}$$

where $\hat{R}$ [size M by M] is the cross-spectral matrix (CSM) between each microphone, $(\cdot)^H$ indicates the Hermitian (or complex conjugate) transpose and $\hat{a}_n$ [size M by 1] is the so-called steering vector from scanning point n to all microphones. The steering vectors provide information about the distance the acoustic wave travels from the scanning location to each microphone, relative to the center of the microphone array. The steering vectors are given by

$$\hat{a}_n = \frac{1}{r_{n,0}} \begin{bmatrix} r_{n,1} \mathrm{e}^{-jkr_{n,1}} \\ r_{n,2} \mathrm{e}^{-jkr_{n,2}} \\ \vdots \\ r_{n,M} \mathrm{e}^{-jkr_{n,M}} \end{bmatrix} \tag{5.1.10}$$

where k is the acoustic wavenumber ($k = \frac{2\pi F}{c}$). Note that $r_{n,0}$ indicates the distance from the scanning point to the array center and is used to scale the levels to what a microphone located at the array center would measure. A different form of these steering vectors will be used later and are defined as,

$$\tilde{a}_n = r_{n,0} \begin{bmatrix} \frac{1}{r_{n,1}} \mathrm{e}^{-jkr_{n,1}} \\ \frac{1}{r_{n,2}} \mathrm{e}^{-jkr_{n,2}} \\ \vdots \\ \frac{1}{r_{n,M}} \mathrm{e}^{-jkr_{n,M}} \end{bmatrix} \tag{5.1.11}$$

One common issue with conventional beamforming is microphone self-noise. In order to remove this effect, diagonal removal is employed. Diagonal removal simply involves zeroing out the auto-spectral (diagonal) elements of $\hat{R}$, and,

$$Y_n = \frac{\hat{a}_n^H \hat{R}_{DR} \hat{a}_n}{M^2 - M}. \tag{5.1.12}$$

With Y_n computed at each scanning location, a so-called beammap (Y) is created which shows the acoustic field power associated with each source location in space. In DAS beamforming, the array's point spread function (PSF), which is the response of the array to a point source in space, is convolved with the true acoustic sources. Because of this the beammap is highly affected by the geometry of the array. Due to the dependence on the PSF, absolute levels in DAS beamforming are unreliable and source locations are imprecisely spread over several scanning locations. The geometry for the array employed in the current work is included in Figure 5.12.

In order to improve the results of conventional DAS beamforming, one must remove the effect of the array geometry. To accomplish this the Deconvolution Approach for Mapping Acoustic Sources (DAMAS) (Brooks & Humphreys, 2006) is employed.

DAMAS. DAMAS relies on solving the following equation:

$$Y = AX, \tag{5.1.13}$$

where Y is the conventional beamforming output [size N by 1], A is a matrix containing the array point spread function (PSF) at each scanning location [size N by N], and X is the unknown source field (as viewed by the array center) [size N by 1].

Based on Eq. (5.1.13) it is simple to see that using DAMAS involves three stages per frequency bin: 1.) Determine the DAS beamformer output at each scanning location (Y), 2.) Calculate the array point spread function (PSF) at each scanning location (A), 3.) Remove the effect of the array PSF from the conventional beammap using a non-

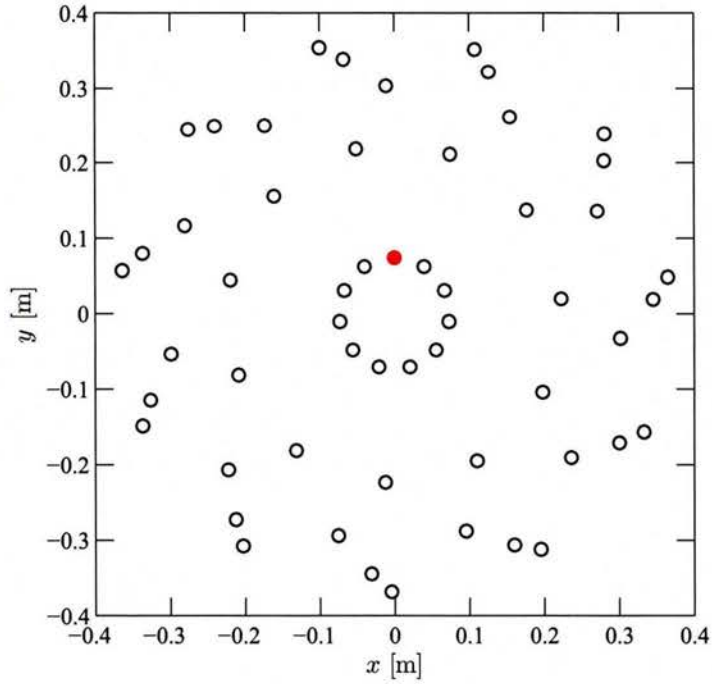

Figure 5.12: Array microphone locations. Array pattern is a reverse logarithmic spiral with center located at (0,0). Location marked by filled red circle is used as the single microphone measurement location.

negative Gauss-Seidel solver to solve a system of equations. The first of these steps has been discussed in the section above. The A-matrix is calculated in a similar manner to conventional beamforming. Instead of using the CSM, $\hat{R}$, generated by the source field, a synthetic CSM, $\hat{G}$, is generated from the propagation vectors. $\hat{G}$ is an M by M array with each element defined as,

$$\hat{G} = \tilde{a}_n \tilde{a}_n^H. \tag{5.1.14}$$

Employing $\hat{G}$ the equation for A becomes,

$$A = \frac{(\hat{a}_n)^H \hat{G} \hat{a}_n}{M^2}, \tag{5.1.15}$$

where M is the number of observers (microphones). For DAMAS (with no diagonal removal) this A-matrix is always real and always positive. If diagonal removal is employed the diagonal of matrix $\hat{G}$ is set to zero or,

$$\hat{G}_{DR} = \hat{G} - \text{diag}(\hat{G}). \tag{5.1.16}$$

A is also changed for diagonal removal in the same way as Y,

$$A = \frac{\hat{a}^H \hat{G}_{DR} \hat{a}}{M^2 - M}. \tag{5.1.17}$$

It should be noted that A may now have negative entries (Brooks & Humphreys, 2006).

Once the DAS beamforming output and the A-matrix are calculated Eq. (5.1.13) becomes the solution to a series of linear equations,

$$\begin{aligned} Y_1 &= A_{1,1}X_1 + A_{1,2}X_2 + \cdots + A_{1,N}X_N \\ Y_2 &= A_{2,1}X_1 + A_{2,2}X_2 + \cdots + A_{2,N}X_N \\ &\vdots \\ Y_N &= A_{N,1}X_1 + A_{N,2}X_2 + \cdots + A_{N,N}X_N. \end{aligned} \tag{5.1.18}$$

In order to solve these equations, a Gauss-Seidel solver is employed. The equations are iteratively solved by the following (Brooks & Humphreys, 2006),

$$X_n = Y_n - \left[\sum_{n'=1}^{n-1} A_{n,n'} X_{n'}^{(i)} + \sum_{n'=n+1}^{N} A_{n,n'} X_{n'}^{(i-1)} \right] \tag{5.1.19}$$

where N is the total number of scanning locations and i is the iteration number. For the first scanning point, $n = 1$, the first summation becomes zero while for the last scanning point, $n = N$, the second summation becomes zero. Each iteration consists of both a forward, $n = 1$ to $n = N$, pass followed by a backwards, $n = N$ to $n = 1$, pass. It was shown by Brooks & Humphreys (2006) that the choice for the initial condition of X_n can be chosen to be either zero or Y_n with little consequence on convergence time and result. Because

X_n must be positive for the solution to be valid physically, negative solutions are set to zero within the solver during the iteration process. A sample comparison between DAS and DAMAS results are shown in Figure 5.13 with source strength and locations provided in Table 5.5.

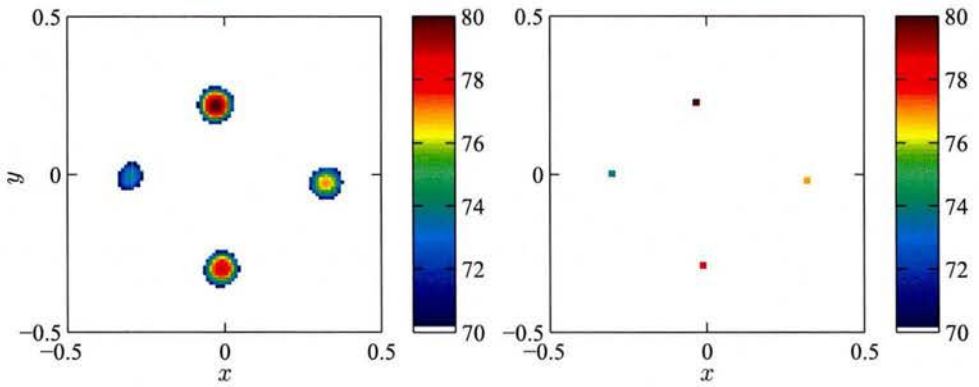

Figure 5.13: A sample comparison between DAS and DAMAS outputs. Field contains four sources of varying strength at 8 kHz. Source strength and locations provided in Table 5.5

Location (x,y) [cm]	Source Strength
(-29.3, 0)	74 dB
(-2.4, 22.5)	80 dB
(0, -29.3)	78.75 dB
(32.8, -2.4)	77 dB

Table 5.5: Source locations and strengths for Figure 5.13.

Phased Acoustic Array. The phased array employed during testing consists of 55 microphones as shown in Figure 5.12. The array was designed for a frequency range of 1 to 16 kHz with a constraint on maximum sidelobe level of 10 dB below the primary source. It is designed based on a reverse logarithmic spiral pattern as discussed in Underbrink (1995). The array has 11 arms with 5 microphones on each arm. A detailed list of microphones and locations can be found in Tables 5.6 and 5.7. The innermost ring of microphones is located at a radial distance of 7.4 cm while the outermost ring is placed at 36.8 cm from the center.

The 3-dB beamwidth of the array versus frequency is shown in Figure 5.14.

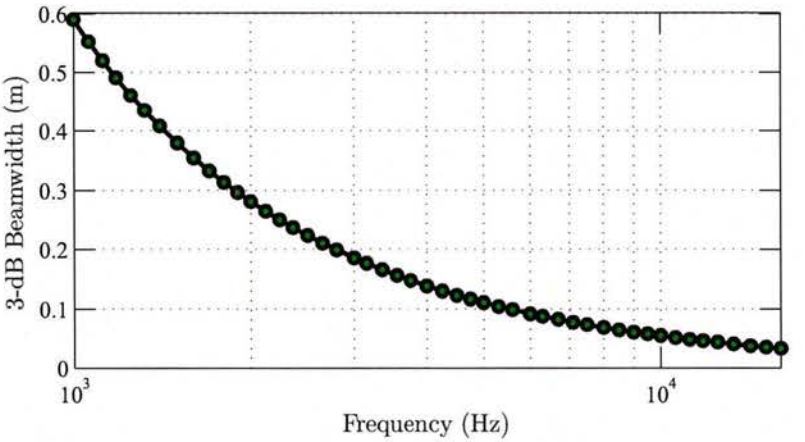

Figure 5.14: 3-dB beamwidth of the current phased acoustic array versus frequency at 1/12th ocatave band frequencies.

The array frame is made of 1 cm thick 6061 aluminum in order to compromise strength (to ensure accurate placement of the microphones) and weight (to ensure that the array was easily mountable in a variety of ways). A skeletal pattern is cut into the aluminum by a water jet machine to reduce the effective area. The microphones are then placed onto (0.3 meter long) mounting rods to move them away from the frame and further reduce the effect of reflections. Finally, the frame is covered in 7.6 cm acoustic wedge foam to mitigate any remaining reflections.

Experimental Setup. Figure 5.8 shows a schematic of the tunnel acoustic and PIV setups. The phased acoustic array is installed on the same side as the CC slot jet at a distance of 1.22 m from the centerline of the model and vertically centered at the airfoil midspan. In the streamwise direction, the center of the array is aligned to the trailing edge of the model. The array contains 12 quarter inch G.R.A.S. 40BE free-field microphones along with 43 1/4 inch Bruel and Kjær type 4958 microphones. All microphones are calibrated using a B& K 4231 Sound Calibrator which operates at a frequency of 1 kHz.

Acquisition	Mic Type	Serial Num.	X [cm]	Y [cm]	Sens. [mV/Pa]
Card 2 - Ch 1	G.R.A.S. 40BE	104822	0.00	7.37	4.41
Card 2 - Ch 2	G.R.A.S. 40BE	104821	3.98	6.20	3.65
Card 2 - Ch 3	G.R.A.S. 40BE	104823	6.70	3.06	2.84
Card 3 - Ch 0	G.R.A.S. 40BE	104819	7.29	-1.05	2.73
Card 3 - Ch 1	G.R.A.S. 40BE	104818	5.57	-4.82	2.82
Card 3 - Ch 2	G.R.A.S. 40BE	104824	2.08	-7.07	2.66
Card 3 - Ch 3	G.R.A.S. 40BE	107159	-2.08	-7.07	3.70
Card 4 - Ch 0	G.R.A.S. 40BE	104825	-5.57	-4.82	3.37
Card 4 - Ch 1	G.R.A.S. 40BE	104820	-7.29	-1.05	4.26
Card 4 - Ch 2	G.R.A.S. 40BE	104827	-6.70	3.06	2.54
Card 4 - Ch 3	G.R.A.S. 40BE	107168	-3.98	6.20	4.22
Card 5 - Ch 0	B & K 4958	2716755	7.49	21.10	12.03
Card 5 - Ch 1	B & K 4958	2716754	15.50	26.10	10.72
Card 5 - Ch 2	B & K 4958	2716752	12.67	32.18	9.73
Card 5 - Ch 3	B & K 4958	2716751	10.79	35.21	12.23
Card 6 - Ch 0	B & K 4958	2770483	17.70	13.70	13.11
Card 6 - Ch 1	B & K 4958	2770472	27.15	13.57	12.69
Card 6 - Ch 2	B & K 4958	2770480	28.05	20.22	11.33
Card 6 - Ch 3	B & K 4958	2770479	28.11	23.79	12.78
Card 7 - Ch 0	B & K 4958	2770470	22.30	1.95	12.57
Card 7 - Ch 1	B & K 4958	2770469	30.18	-3.26	12.80
Card 7 - Ch 2	B & K 4958	2770481	34.54	1.85	12.39
Card 7 - Ch 3	B & K 4958	2770478	36.51	4.81	13.42
Card 8 - Ch 0	B & K 4958	2770471	19.81	-10.41	12.72
Card 8 - Ch 1	B & K 4958	2770482	23.62	-19.06	11.62
Card 8 - Ch 2	B & K 4958	2716744	30.05	-17.12	9.41
Card 8 - Ch 3	B & K 4958	2716745	33.32	-15.69	10.65
Card 17 - Ch 1	B & K 4958	2716742	11.04	-19.47	10.88
Card 17 - Ch 2	B & K 4958	2716723	9.57	-28.81	11.33
Card 17 - Ch 3	B & K 4958	2716726	16.03	-30.65	12.19
Card 17 - Ch 4	B & K 4958	2716725	19.55	-31.21	11.05
Card 10 - Ch 0	B & K 4958	2716712	-1.24	-22.35	11.24
Card 10 - Ch 1	B & K 4958	2716730	-7.52	-29.41	11.31
Card 10 - Ch 2	B & K 4958	2716714	-3.09	-34.45	11.88
Card 10 - Ch 3	B & K 4958	2716739	-0.43	-36.83	13.09
Card 17 - Ch 11	G.R.A.S. 40BE	107163	-13.13	-18.13	4.01
Card 16 - Ch 0	B & K 4958	2716736	-22.23	-20.67	10.83

Table 5.6: Phased microphone array acquisition channels, microphone locations and microphone specifications. Part 1 of 2, continued in Table 5.7.

Acquisition	Mic Type	Serial Num.	X [cm]	Y [cm]	Sens. [mV/Pa]
Card 17 - Ch 12	B & K 4958	2716715	-21.22	-27.31	9.75
Card 17 - Ch 13	B & K 4958	2716716	-20.27	-30.75	10.06
Card 12 - Ch 0	B & K 4958	2716743	-20.84	-8.15	11.64
Card 12 - Ch 1	B & K 4958	2716731	-29.87	-5.37	11.29
Card 12 - Ch 2	B & K 4958	2770476	-32.62	-11.50	13.29
Card 12 - Ch 3	B & K 4958	2716732	-33.68	-14.91	12.31
Card 13 - Ch 0	B & K 4958	2770473	-21.94	4.41	13.97
Card 13 - Ch 1	B & K 4958	2716741	-28.04	11.63	9.41
Card 13 - Ch 2	B & K 4958	2716734	-33.66	7.96	10.62
Card 13 - Ch 3	B & K 4958	2770474	-36.39	5.67	13.09
Card 14 - Ch 0	B & K 4958	2716735	-16.08	15.57	10.15
Card 14 - Ch 1	B & K 4958	2710737	-17.30	24.94	10.43
Card 14 - Ch 2	B & K 4958	2770475	-24.01	24.89	13.72
Card 14 - Ch 3	B & K 4958	2770477	-27.55	24.44	12.79
Card 15 - Ch 0	B & K 4958	2716713	-5.11	21.79	10.97
Card 15 - Ch 1	B & K 4958	2716711	-1.06	30.34	10.80
Card 15 - Ch 2	B & K 4958	2716746	-6.74	33.92	10.72
Card 15 - Ch 3	B & K 4958	2716747	-9.96	35.46	10.99

Table 5.7: Phased microphone array acquisition channels, microphone locations and microphone specifications. Part 2 of 2, continued from Table 5.6.

5.1.8 Processing Parameters

PIV data are taken at 1.5 Hz using DaVis 8.2.2 from LaVision. The unsteady pressure and acoustic data are sampled at 32,768 Hz and anti-alias filtered using 24-bit PXI 4462 cards installed in an NI PXI-1045 chassis. Data are acquired for 510 seconds to maximize the temporal overlap between unsteady pressure and PIV data. The PIV and pressure data are aligned using the Q-switch signal from the PIV system, sampled at the same rate as the pressure data, the uncertainty in the timing is therefore $\pm 1/16384$ seconds. Unless otherwise noted, all spectral results are generated using a block size of 8192 samples resulting in a 4 Hz binwidth. The blocks are windowed via a Hanning window and overlapped by 75%, resulting in a 1.5% autospectral random uncertainty.

5.2 Experimental Results

This section will first discuss the measurements made during testing, including steady pressure, unsteady pressure, and a detailed discussion of the acoustics. Then, a discussion of the velocity field will be provided. Finally, the proposed methodology is carried out and issues that were in encountered will be covered.

5.3 Steady Pressure

Steady surface pressure are plotted for four momentum coefficients in Figure 5.15. The effect of blowing from the slot jet is quite apparent from the increasing suction with increased momentum coefficient. The suction peak which typically occurs in practice (Abramson, 1975) is notably absent. Wetzel (2011) shows that this is observed in open-jet facilities. The coefficient of pressure distribution matches well with work done previously by Wetzel *et al.* (2009). Due to the desire to obtain unsteady pressure, PIV, and acoustic data simultaneously, a closed test section is not an option for these tests.

5.4 Unsteady Pressure

Unsteady pressure is captured on three recessed devices discussed in section 5.1.4 above. The unsteady pressure transducers must be corrected to account for their recessed nature. In order to do this, a transfer function is determined for each device prior to testing. These FRFs are generated by the method discussed in section 5.1.4.

A representative transfer function for the recessed devices is shown in figure 5.16 along with the theoretical transfer function based on the geometry (calculated based on analysis in Zawodny (2013) and Zawodny *et al.* (2016)). Unfortunately, the resonance peak for these devices appears at a frequency of approximately 10 kHz. All unsteady pressure data are post-processed with a low-pass filtered (via an 8th order Chebyshev filter) and decimated at 8 kHz to remove the resonance effect. It should also be noted that the calibration procedure

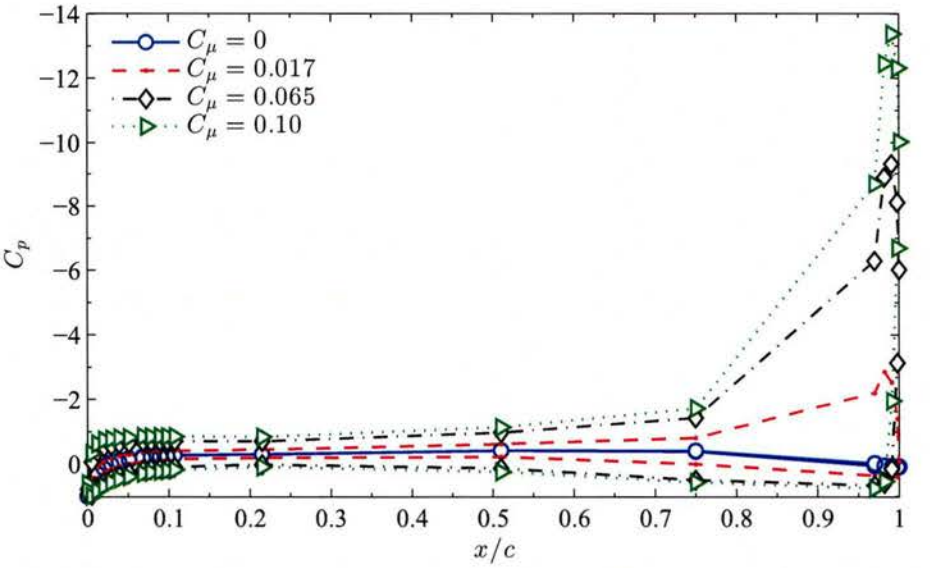

Figure 5.15: Coefficient of pressure distribution over the CC airfoil. Shown for four coefficients of momentum including (a)$C_\mu = 0$, (b)$C_\mu = 0.017$, (c)$C_\mu = 0.065$, and (d)$C_\mu = 0.10$.

shows good coherence between the device under test and the reference devices down to 60 Hz, below which the coherence drops rapidly. For this reason, the data is also digitally high-pass filtered at 60 Hz using a 4th-order Butterworth filter.

The transfer-function-corrected unsteady pressure for each of the three devices is shown in figure 5.17. Note that the pre-decimated data are shown to further reinforce the reasoning behind decimation, shown by the non-physical peak at approximately 10 kHz. The pertinent feature of these unsteady pressure data is that the jet clearly introduces a significant level of broadband fluctuations into the pressure measurements, shown by the increased broadband levels with increased C_μ. This result is consistent across all pressure transducers except low frequencies at P2. This may reduce the overall correlation between the pressure data and the velocity/POD fields. These data also provide insight into the separation location for each momentum coefficient. While the flow is separated at P2 and P3 for the no-blowing case and at P3 for the $C_\mu = 0.004$ case, the flow remains attached at all pressure sensors for momentum coefficients greater than $C_\mu = 0.004$.

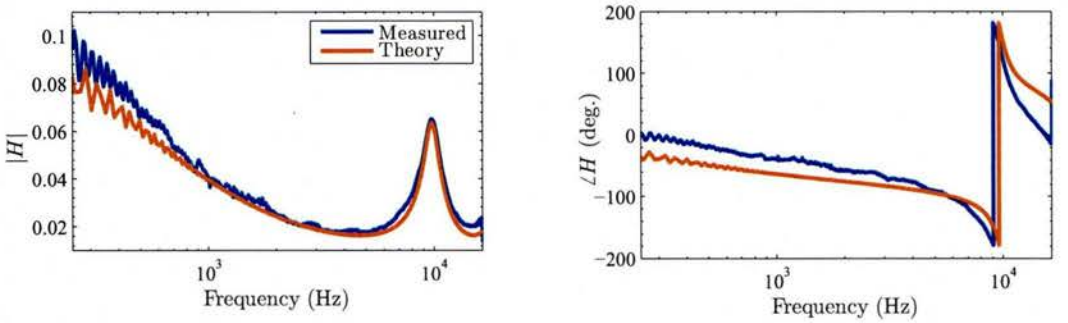

(a) Magnitude

(b) Phase

Figure 5.16: Frequency dependent transfer function for recessed device P1. Each device contains slight amplitude differences but the trends occur at the same frequency locations.

5.5 Acoustics

Acoustic measurements are made for five freestream Reynolds numbers from $Re_c = 0$ to 1.3 million, and up to six momentum coefficients from $C_\mu = 0$ to 0.10 (jet velocities up to 100 m/s, Mach 0.29). Higher momentum coefficients are omitted at the high tunnel speeds to avoid over-pressurization of the internal plenum. This section begins by discussing single microphone spectra. It shows operating conditions where single microphone measurements are insufficient due to tunnel background noise. Then, it discusses phased acoustic array beamforming results attempting to remove the effects of the background noise. Microphone data are acquired at 204,800 Hz for 30 seconds. Single microphone spectra are processed with 16 Hz binwidth employing a Hanning window with 75% overlap resulting in 3.2% autospectral random uncertainty. All spectral results in this document are scaled from a distance of 1.22 meters (distance from microphones to source) to a distance of 1 meter. A 2D shear layer correction (Amiet, 1975) is applied to all data obtained with the wind tunnel turned on.

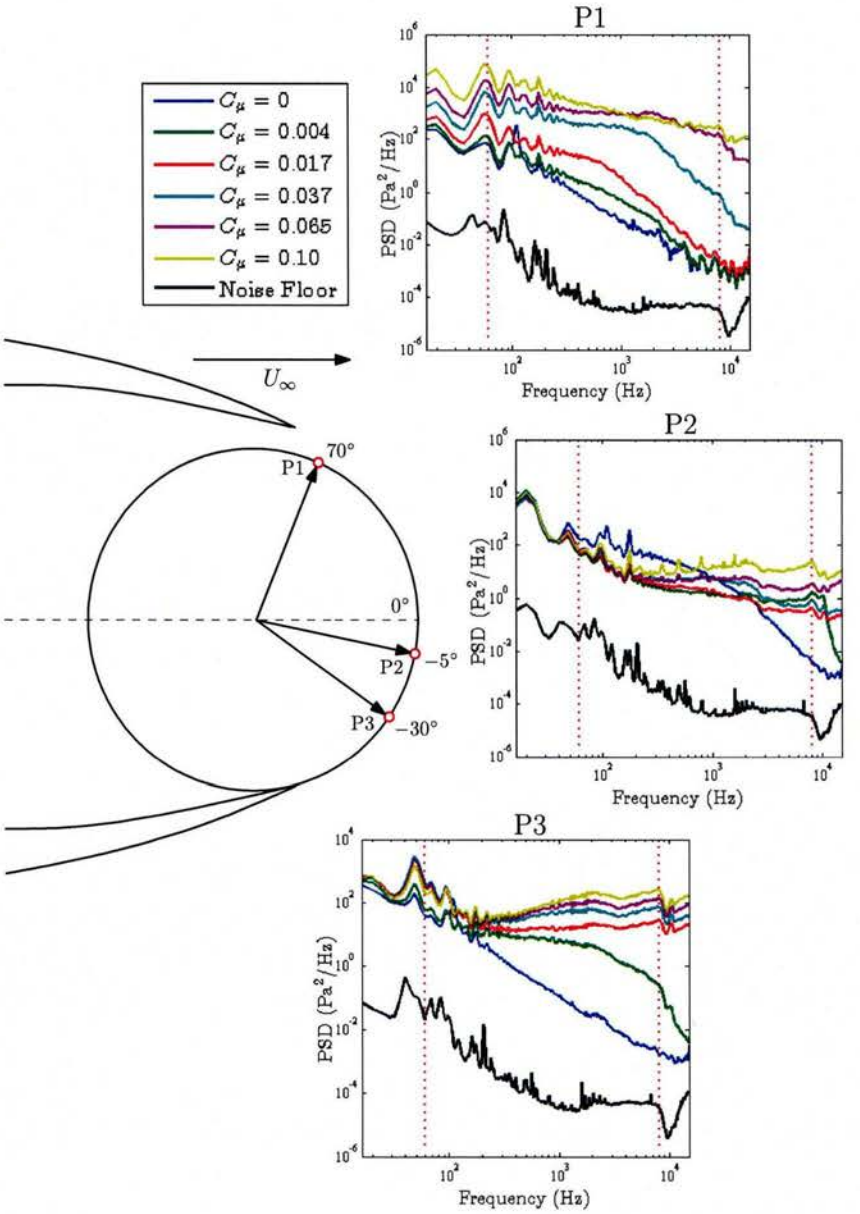

Figure 5.17: Transfer-function-corrected unsteady pressure data at each of the three locations employed during testing. Data shown for all momentum coefficients at a Reynolds number of 650,000 based on chord. Red vertical, dotted lines indicate the limits of the band-pass filter.

5.5.1 Single Microphone Results

Single microphone spectra are a powerful tool in quickly determining noise levels over a wide range of frequencies. For the purposes of this section, a frequency range from 100 Hz to 80 kHz is investigated. Note that the lower limit is below the anechoic chamber cut-on frequency (250 Hz) to show the shedding peak and the upper limit is set by the dynamic range of the microphone (location shown in figure 5.12). Each spectral plot is shown in sound pressure level per Hertz (SPL/Hz) and contains all blowing conditions as well as a microphone noise floor. The plots also contain a "no model" noise floor which is taken with the wind tunnel running (and sidewalls installed) but no model in the tunnel, estimating the facility's effective background noise floor.

Initially, tunnel off ($Re_c = 0$) acoustics are investigated. For this case, jet Reynolds number (Re_J, defined by slot height and jet velocity) is used instead of momentum coefficient due to the absence of a freestream. Results are shown in Figure 5.18. At the lowest jet Reynolds number, the noise generated from the model is below the noise floor of the microphone over a wide range of frequencies. For all jet Reynolds numbers, a peak occurs in the spectra from 500 to 900 Hz. While this peak is at a constant frequency, its levels increase with jet velocity. When compared to hotwire tests performed pre-test, this appears to be a Helmholtz resonance of the plenum. Also apparent in the spectra is a high frequency hump which broadens, increases in frequency, and increases in magnitude as jet Reynolds number increases. One can deduce that this spectral behavior is due to slot-jet interaction noise since it is the only source present due to the absence of the freestream.

Results from tests at several different chord Reynolds numbers and blowing conditions are considered next. These data are shown in Figures 5.19 - 5.22. For all cases at the no blowing condition ($C_\mu = 0$) the background noise is significant for all frequencies. It should be noted, that for all the no blowing cases, a peak in the spectra exists (below the tunnel's lowest anechoic frequency, an example of which is shown in Figure 5.22) which corresponds to bluff body shedding. For the lowest chord Reynolds number ($Re_c = 3.2e5$, Figure 5.19) the spectral levels for all blowing conditions are (at best) marginally above the tunnel and

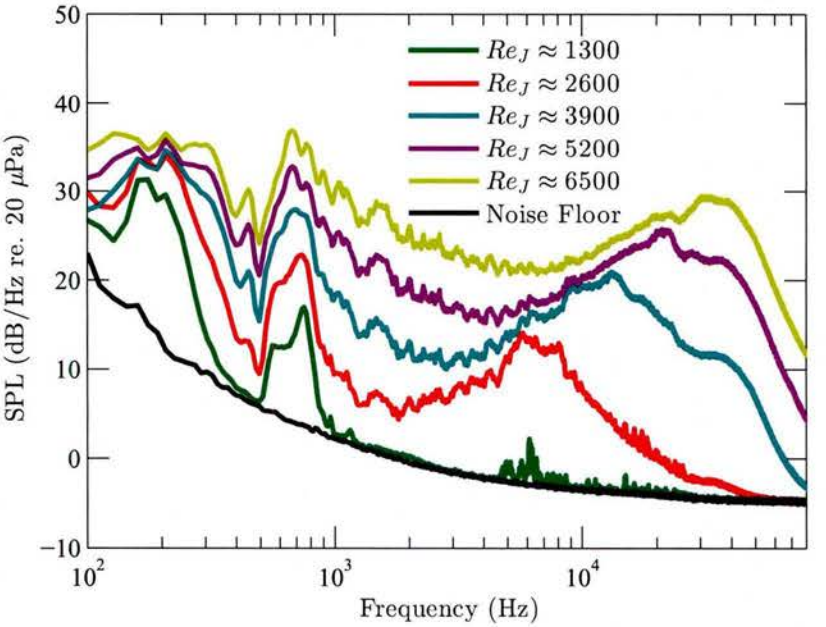

Figure 5.18: Spectral data from a single microphone above the trailing edge on the same side as the blowing slot at $Re_c = 0$.

microphone noise floors. At the highest chord Reynolds number ($Re_c = 1.3e6$, Figure 5.22) a similar trend is noted due to the inability to achieve significantly large momentum coefficients at this tunnel speed.

At the lowest blowing conditions for the other two chord Reynolds numbers ($Re_c = 6.5e5$ and $Re_c = 9.7e5$, Figures 5.20 and 5.21), the tunnel background noise remains a significant source of acoustics. However, unlike the previous cases, the higher momentum coefficient cases show significant noise being generated by the model. It is shown in Figures 5.20 and 5.21 that from middle to high frequencies, the noise increases with increasing coefficient of momentum. This suggests increased noise generated by the slot-jet interacting with the slot lip as well as higher passive slot noise (Howe, 2002). However, additional noise sources may be present.

Due to the significant levels of background noise shown in the single microphone spectra, another method will be investigated to obtain accurate model-generated-noise spectra. Two-

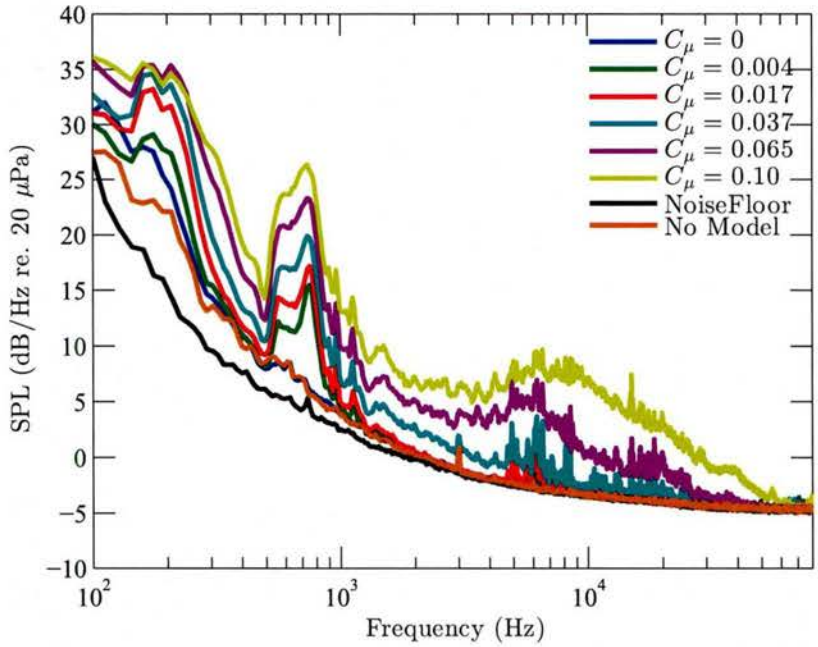

Figure 5.19: Spectral data from a single microphone above the trailing edge on the same side as the blowing slot at $Re_c = 3.2e5$.

and three-microphone methods were considered; however, the primary background noise is generated by the tunnel and these methods remove only incoherent noise. Therefore, phased acoustic array beamforming is used for this purpose.

5.5.2 Beamforming

Unlike single microphone measurements, a phased array allows for the identification of individual sources by digitally focusing all the microphones to a single point. By using the ability to focus on certain locations and summing up only the relevant components, spectral levels can be obtained which suppress background noise. Unfortunately, array design constraints and microphone bandwidth limit the frequency range over which beamforming is possible from approximately 1 to 16 kHz. Fortunately, this frequency range overlaps a large portion of the relevant single microphone data.

Due to its relative simplicity (and small computation time), delay-and-sum beamforming

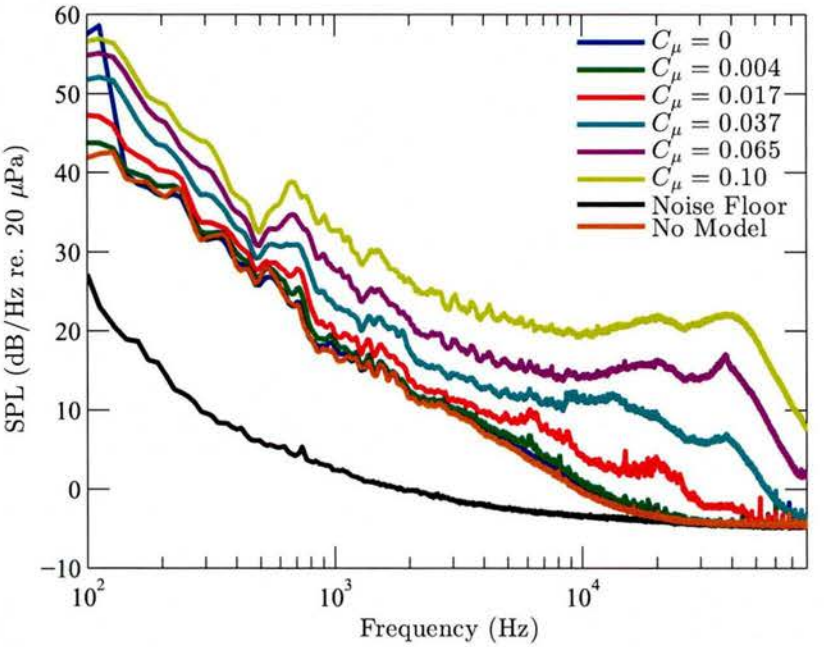

Figure 5.20: Spectral data from a single microphone above the trailing edge on the same side as the blowing slot at $Re_c = 6.5e5$.

(DAS) is investigated initially. The array point spread functions (PSF) for the frequencies discussed are shown in Figure 5.23, with the source located at the center span of the trailing edge. In this and all other beammaps in this document, the dotted lines on the left indicate the location of the collector and on the right indicate the inlet, the dashed lines on top and bottom indicate the sidewall locations and the solid vertical lines define the leading (right) and trailing (left) edges of the model, as shown in Figure 5.24. Flow goes from right to left in these beammaps.

Delay-and-Sum. Initially, three cases are investigated which provide a representative sample of the complexities associated with circulation control. These cases are 1.) zero freestream velocity (zero chord Reynolds number, $Re_c = 0$), 100 m/s jet velocity (6500 jet Reynolds number, $Re_J = 6500$), 2.) $Re_c = 6.5e5$, zero jet velocity (zero coefficient of momentum, $C_\mu = 0$), 3.) $Re_c = 6.5e5$, $C_\mu = 0.10$ (jet velocity approximately 5 times

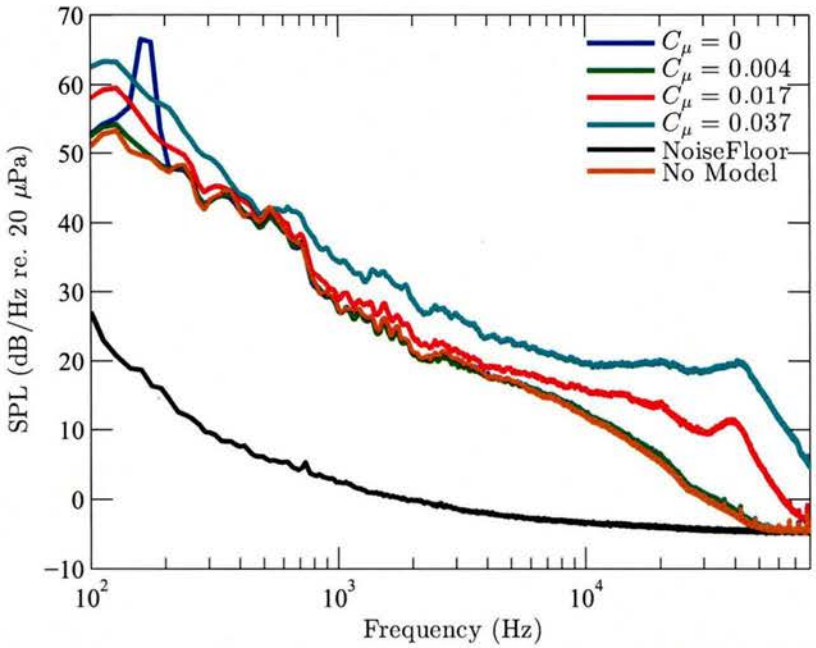

Figure 5.21: Spectral data from a single microphone above the trailing edge on the same side as the blowing slot at $Re_c = 9.7e5$.

freestream velocity). By studying the beammaps from these cases, insight into the sources, locations, and conditions for different external noise sources is observed. These data will then be used to determine accurate integration regions to acquire overall CC noise with external sources removed.

Figure 5.25 shows the DAS beammaps for frequencies of 1, 2, 4, 8, 12, and 16 kHz for the $Re_c = 0$, maximum blowing ($Re_J = 6500$) case. At the lowest frequency (1 kHz), the primary source of noise is centered around the model trailing edge, which could indicate curvature noise (Howe, 2002). At the middle frequencies of 2 and 4 kHz, the primary noise source is at the slot-jet exit (slightly upstream of the trailing edge); indicative of slot-jet interaction or passive slot noise (Howe, 2002). As the frequency increases, the sources move toward the sidewalls. This suggests jet/sidewall interaction becoming more influential as frequency increases.

Figure 5.26 shows DAS beammaps for the $Re_c = 6.5e5$, $C_\mu = 0$ case at the same

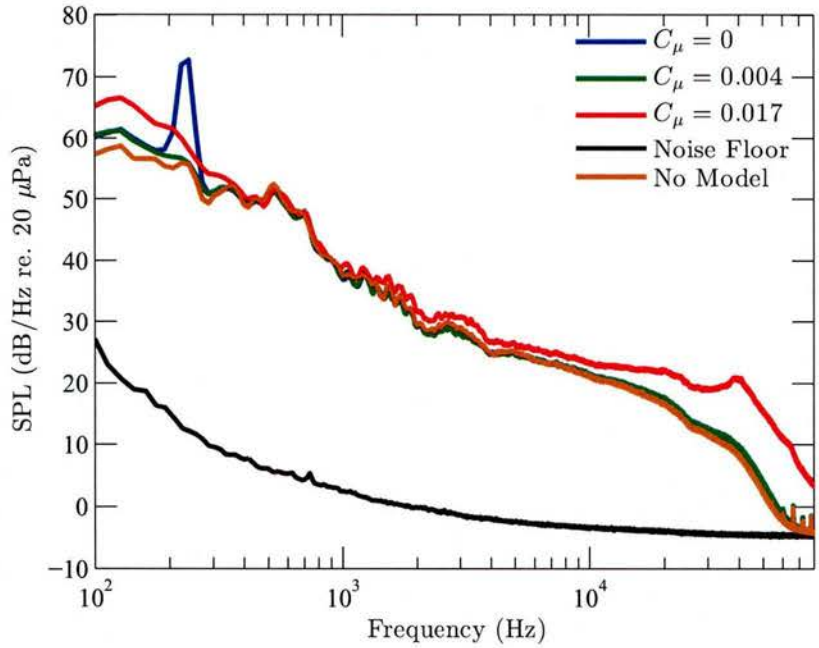

Figure 5.22: Spectral data from a single microphone above the trailing edge on the same side as the blowing slot at $Re_c = 1.3e6$.

frequencies. Here, the background noise is clearly significant at all frequencies. At the lowest frequency, the collector is the dominate noise source and appears as noise from the collector as well as reflected noise off the model which will be discussed later. At low frequencies (2, and 4 kHz) the noise generated from the collector continues to be the dominant noise source. As frequency increases (4 kHz and higher) the sidewall noise near the leading edge of the model becomes the dominant source. These beammaps confirm the result shown by the single microphone spectra discussed previously; the background noise appears to be the significant noise source over all relevant frequencies.

In order to further investigate the collector noise, a pulsed laser point source (Bahr *et al.*, 2015) is generated within the collector. This point source is used to determine reflection locations which occur due to noise generated at the source location. The beammaps for this test are shown in Figure 5.27. At 1 kHz, significant reflected noise appears near the model leading edge; this reflection also appears in the $Re_c = 6.5e5$, $C_\mu = 0$ case. If an integration

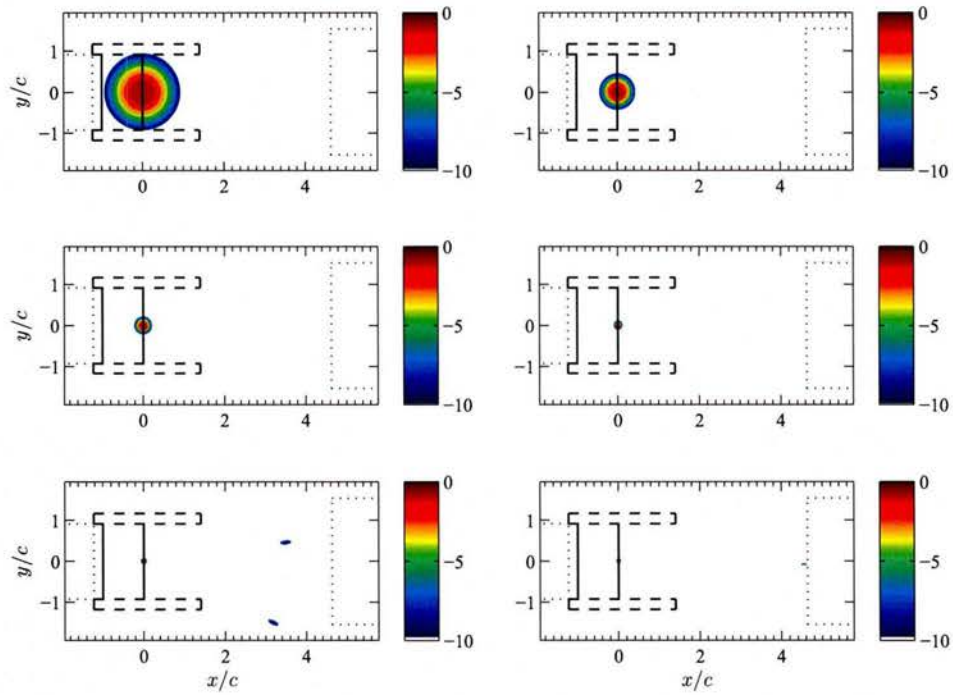

Figure 5.23: Theoretical point spread functions for the array pattern used during this study. From top left to bottom right 1 kHz, 2 kHz, 4 kHz, 8 kHz, 12 kHz, and 16 kHz.

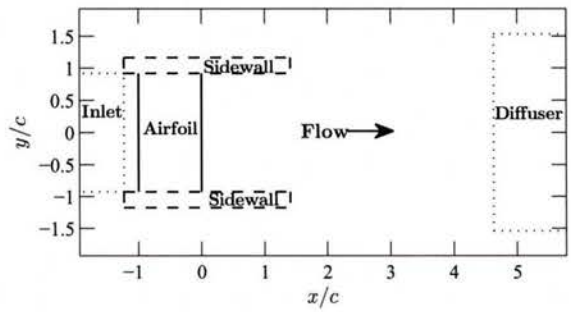

Figure 5.24: Schematic labeling relevant objects in beammaps.

region is chosen which includes the entire chordwise extent of the model, this noise is a significant contributor.

Finally, Figure 5.28 investigates the $Re_c = 6.5e5$, $C_\mu = 0.10$ case. The dominant noise source for all frequencies is the jet/sidewall interaction.

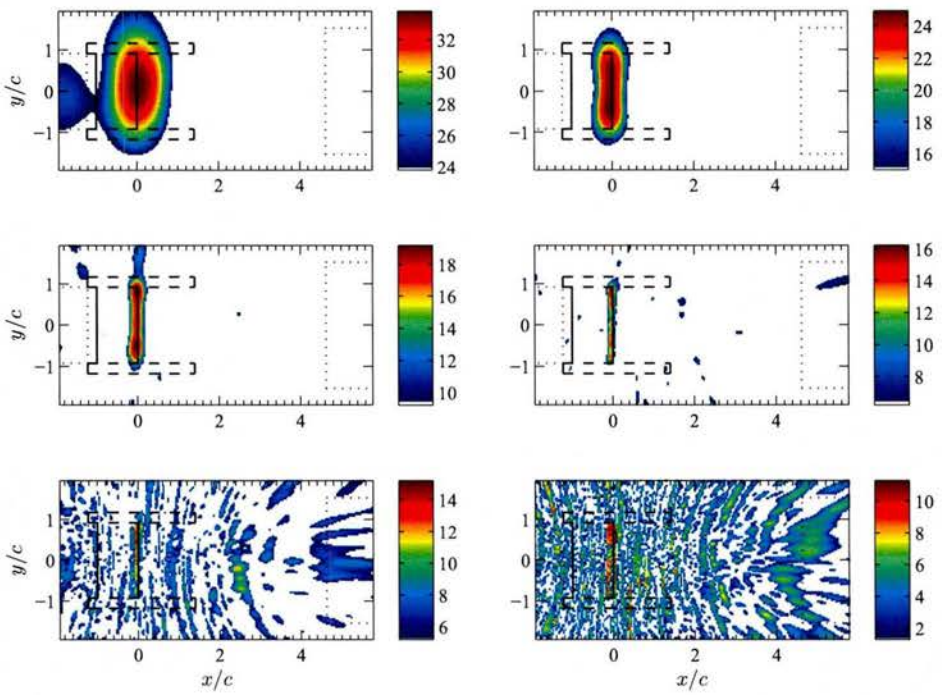

Figure 5.25: Beammaps for the $Re_c = 0$, $Re_J = 6500$ case. From top left to bottom right 1 kHz, 2 kHz, 4 kHz, 8 kHz, 12 kHz, and 16 kHz.

The three general sources of background noise are shown in these experiments, 1.) collector noise, 2.) sidewall noise (near the leading edge), and 3.) jet/sidewall interaction noise. To isolate the CC noise, a region which removes all of these external noise sources should be employed. In the streamwise direction one needs to include only the airfoil itself and regions slightly downstream (to include jet noise). By limiting the region in this manner the collector noise is removed. In the spanwise direction, the sidewall interaction noise must be excluded. At a frequency of 2 kHz, only the middle 0.44 m of the airfoil span is included. The integration region chosen based on these criteria (assuming an origin at center span on the model's trailing edge) is -1.2 to 0.4 chords (-0.6 to 0.2 m) in the streamwise direction and -0.25 to 0.25 spans (-0.22 to 0.22 m) in the spanwise direction. These results are then scaled to a unit meter span (from 0.44 meters) and a unit meter distance (at 90° from the

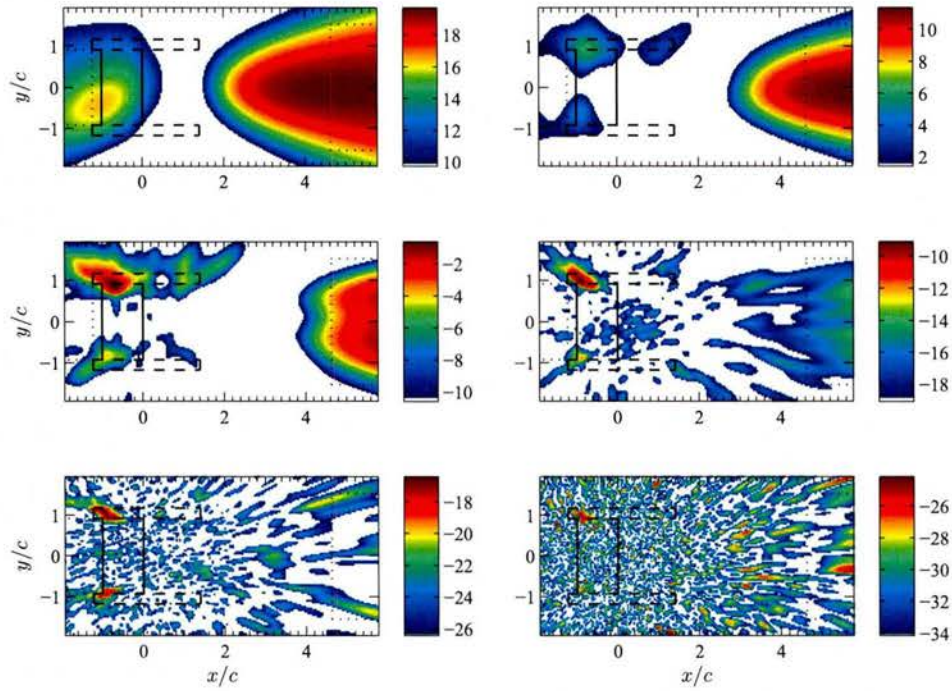

Figure 5.26: Beammaps for the $Re_c = 6.5e5$, $C_\mu = 0$, no blowing, case. From top left to bottom right 1 kHz, 2 kHz, 4 kHz, 8 kHz, 12 kHz, and 16 kHz.

chordwise and spanwise directions) in order to compare to the single microphone results. Integrated spectra for all DAS results are provided with shaded uncertainty bounds.

Uncertainty in the integrated DAS spectra is also estimated via 1000 iteration Monte-Carlo simulations (Yardibi *et al.*, 2010*a*). For these simulations the DAS beamformer is perturbed about: 1.) microphone position (x, y, and z coordinates by 1 cm), 2.) scanning plane height (2%), 3.) microphone sensitivity (10%), 4.) temperature (1%), and 5.) cross-spectral uncertainty.

Due to computational expense, spectra for the DAS cases (as well as the uncertainty) are gathered at 1/12th octave band centers instead of the 16 Hz resolution used in the single microphone spectra. The $Re_c = 3.2e5$ cases are not included for the beamforming cases due to non-physical behavior caused by their proximity to the microphone noise floor.

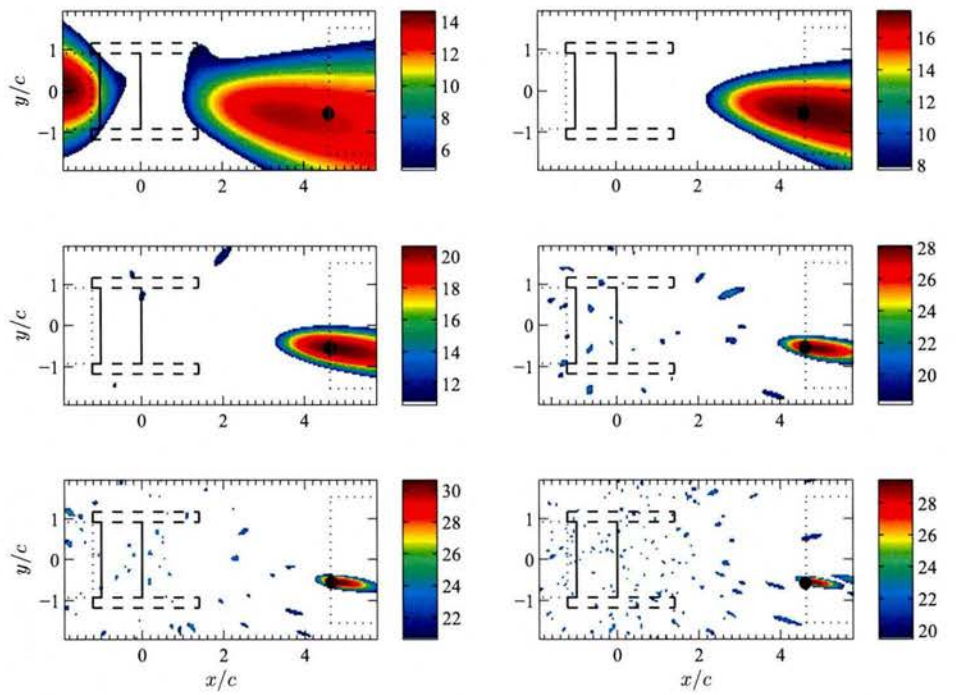

Figure 5.27: Beammaps for a laser point source located in the collector, below tunnel centerline. From top left to bottom right 1 kHz, 2 kHz, 4 kHz, 8 kHz, 12 kHz, and 16 kHz. Both tunnel and jet are off. Note that the location of the laser impulse is indicated by the black dot at the diffuser face.

The tunnel off ($Re_c = 0$) integrated spectra are compared to the single microphone result in Figure 5.29. Overall, the DAS results are several decibels lower than the single microphone due to the exclusion of extraneous sources. The shape of the spectra over this range of frequencies are quite similar for both data types, confirming that the conclusions drawn from the single microphone data for this case are indeed from the CC and not background noise.

Turning attention to those cases with considerably more background noise the $Re_c = 6.5e5$, $Re_c = 9.7e5$, and $Re_c = 1.3e6$ single microphone and DAS cases are compared in Figures 5.30, 5.31, and 5.32, respectively. In the $Re_c = 6.5e5$ cases a significant reduction in overall levels from the single microphone results are shown. At high frequencies the no

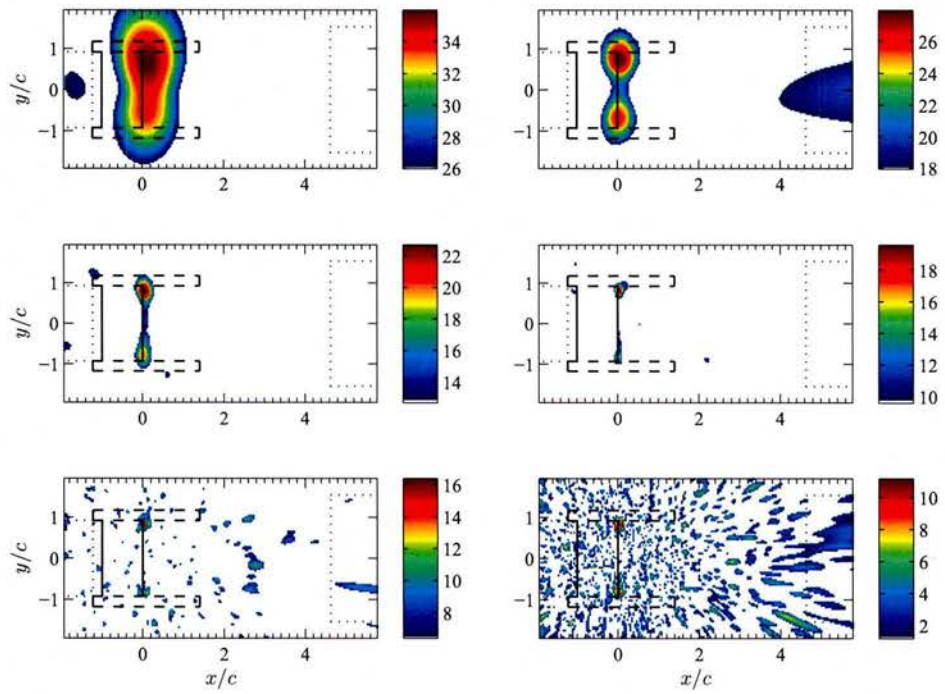

Figure 5.28: Beammaps for the $Re_c = 6.5e5$, $C_\mu = 0.10$ case. From top left to bottom right 1 kHz, 2 kHz, 4 kHz, 8 kHz, 12 kHz, and 16 kHz.

blowing and lowest blowing ($C_\mu = 0$ and $C_\mu = 0.004$, respectively) cases are still saturated by the wind tunnel background noise and show large uncertainty (in some areas even larger than the mean value). It is also shown that at low frequencies for the lower blowing conditions ($C_\mu = 0, C_\mu = 0.004$, and $C_\mu = 0.017$) the levels are quite similar. By using DAS, the higher blowing cases ($C_\mu = 0.037, C_\mu = 0.065$, and $C_\mu = 0.10$) are much more significantly differentiated from the background noise. It should also be noted (similar to the $Re_c = 0$ case) that the shape of the spectra vary little from the single microphone to the DAS results.

In the $Re_c = 9.7e5$ and $Re_c = 1.3e6$ cases (Figures 5.31 and 5.32) the changes from single microphone to DAS results are quite similar to those shown in the $Re_c = 6.5e5$ case. Once again, a significant decrease in overall levels for the DAS results is shown. For the

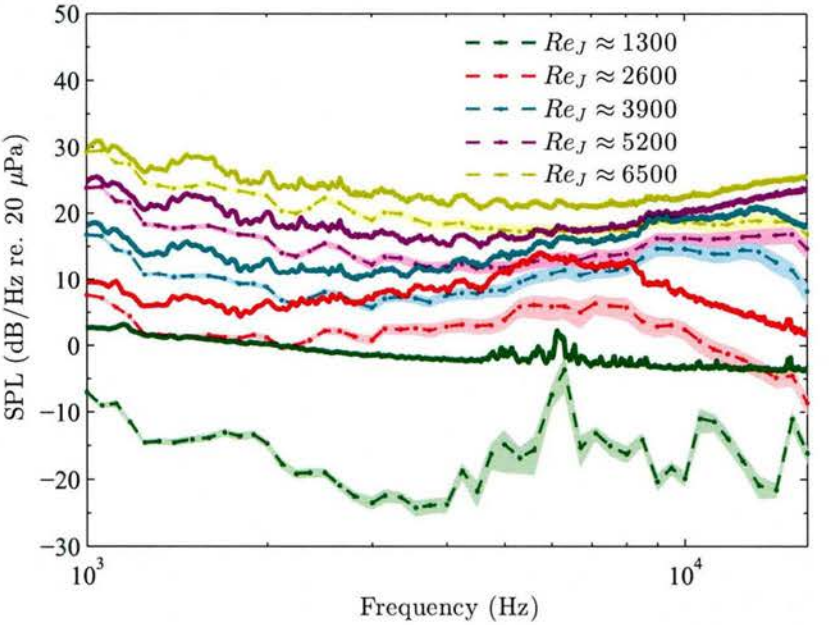

Figure 5.29: Spectral data from a single microphone (16 Hz binwidth, solid line with no markers) compared to DAS integrated spectra (1/12th octave bands centers, dashed lines with dot markers) with shading showing DAS 95% uncertainty based on 1000 iteration Monte Carlo simulations at $Re_c = 0$.

no and lowest blowing conditions ($C_\mu = 0$, and $C_\mu = 0.004$) the uncertainty is once again larger than the mean value at high frequencies and at low frequencies they converge due to the (unremovable) reflected noise. Unlike the $Re_c = 6.5e5$ case, the DAS removes enough background noise from the $C_\mu = 0.017$ case that it is significantly above the tunnel noise floor. For the higher blowing condition ($C_\mu = 0.037$) in the $Re_c = 9.7e5$ case it is again observed that, while the absolute levels are reduced, the shape of the spectra is unchanged.

Deconvolution Approach Mapping Acoustic Sources. DAMAS removes the influence of the point spread function from the DAS beamforming result. By doing so it can provide accurate source locations and levels. However, because DAMAS relies on solving an inverse problem (Brooks & Humphreys, 2006) care must be taken when choosing scanning region bounds, number of iterations, and grid resolution. Ideally, one would simply maximize each of these items. Unfortunately, this is not possible due to the computational

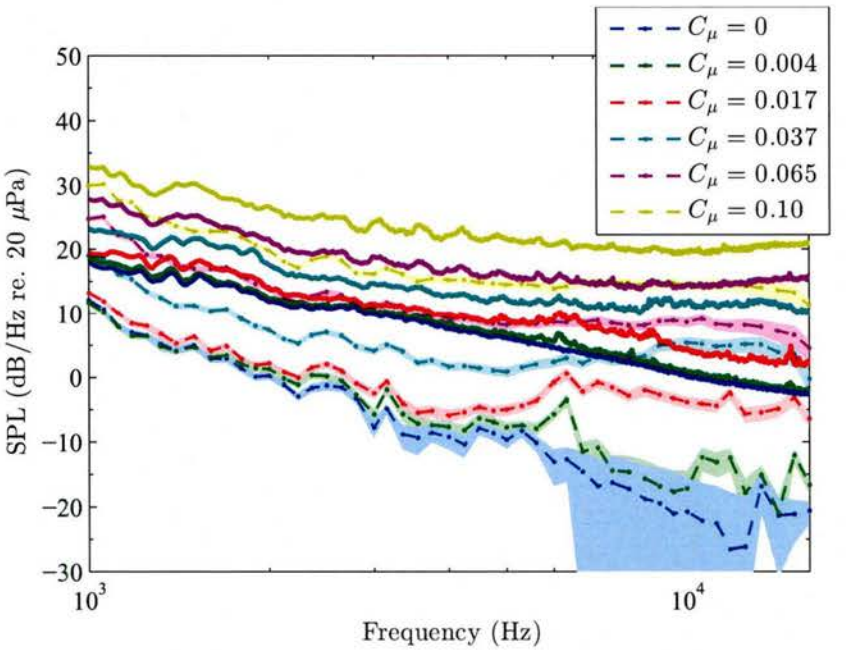

Figure 5.30: Spectral data from a single microphone (16 Hz binwidth, solid line with no markers) compared to DAS integrated spectra (1/12th octave band centers, dashed lines with dot markers) with shading showing DAS 95% uncertainty based on 1000 iteration Monte Carlo simulations at $Re_c = 6.5e5$.

expense associated with DAMAS.

Each of these parameters is studied from simulated acoustic fields and experimental results prior to processing. The grid resolution and scanning region bounds must be balanced with computational time to obtain integrated spectra in a reasonable time-frame. It is observed (in pre-processing) that a field spanning -2 to 6 chords (-1.0 to 3.1 m) in the streamwise direction and -1 to 1 spans (-0.9 to 0.9 m) in the spanwise direction is reasonable with a grid resolution of 20% of the 3dB beamwidth for frequencies below 6 kHz. Above 6 kHz, the region size and resolution (relative to the beamwidth) are reduced due to the decreasing beamwidth. For frequencies above 6 kHz, 30% of the beamwidth is used along with a scanning region from -1.5 to 1.5 chords (-0.75 to 0.75 m) in both the streamwise and spanwise directions. The scanning regions are chosen to be larger than the integration region because sources outside of the DAMAS solution are erroneously located on the edges

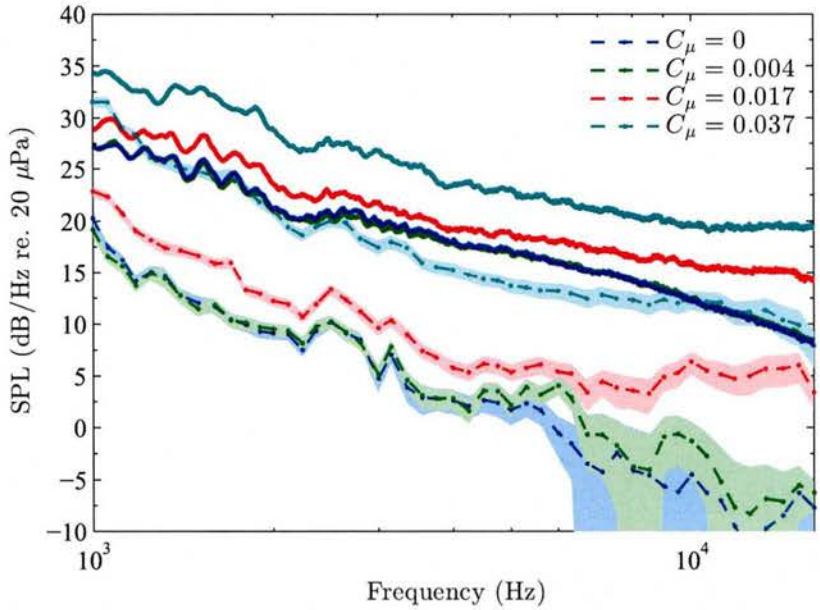

Figure 5.31: Spectral data from a single microphone (16 Hz binwidth, solid line with no markers) compared to DAS integrated spectra (1/12th octave band centers, dashed lines with dot markers) with shading showing DAS 95% uncertainty based on 1000 iteration Monte Carlo simulations at $Re_c = 9.7e5$. Single microphone noise floor shown in black.

of the region. Figure 5.33 shows the scanning region bounds for both instances. For the experimental cases studied, the results converge to a solution by 1000 iterations. While the scanning region is varied over the range of frequencies, the integration region for the spectra remains the same as in the DAS beamforming. Spectral results are, once again, scaled from 0.44 meter span to a unit meter span and from a 1.22 meter distance for a unit meter distance for comparison purposes.

Investigating the three cases discussed previously provides similar source locations. Figure 5.34 shows the $Re_c = 0$, $Re_J = 6500$ case using DAMAS. As shown in the DAS result, the primary source at 1 kHz occurs at the trailing edge of the model, suggesting curvature noise (Howe, 2002). The movement of the source upstream to the slot-jet exit at the middle frequencies is shown more clearly in DAMAS than it had been in DAS. Contrary to the DAS result, the high frequency noise does not appear to be located heavily near the sidewalls

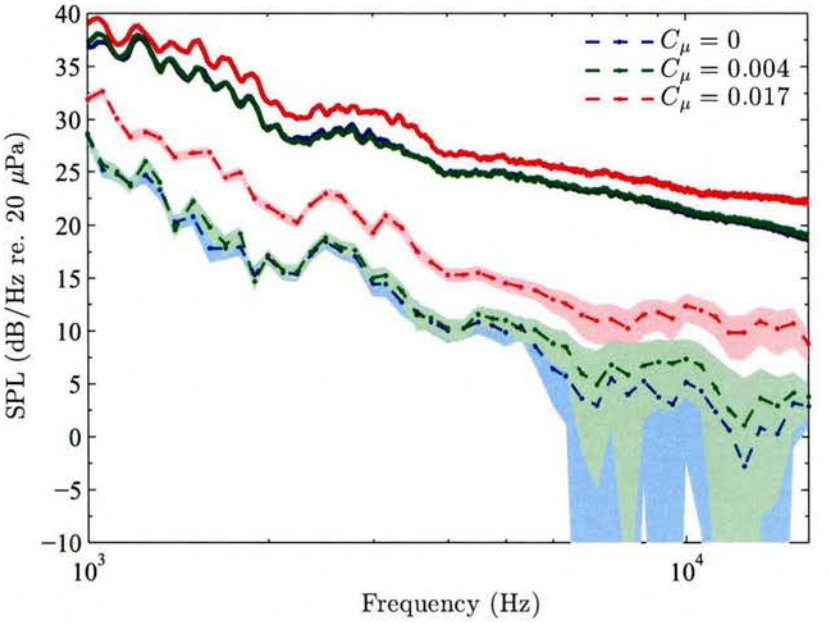

Figure 5.32: Spectral data from a single microphone (16 Hz binwidth, solid line with no markers) compared to DAS integrated spectra (1/12th octave band centers, dashed lines with dot markers) with shading showing DAS 95% uncertainty based on 1000 iteration Monte Carlo simulations at $Re_c = 1.3e6$. Single microphone noise floor shown in black.

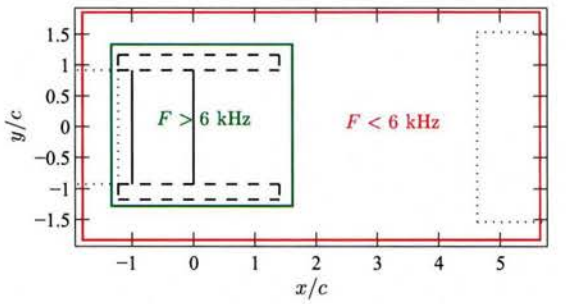

Figure 5.33: Schematic showing the scanning region bounds used in DAMAS for all frequency ranges.

and, instead, is distributed in a manner similar to the middle frequencies. This suggests that slot-jet interaction and passive slot noise are the dominant source for all but the lowest frequency (Howe, 2002).

Figure 5.35 shows DAMAS applied to the $Re_c = 6.5e5$, $C_\mu = 0$ case. At 1 kHz the

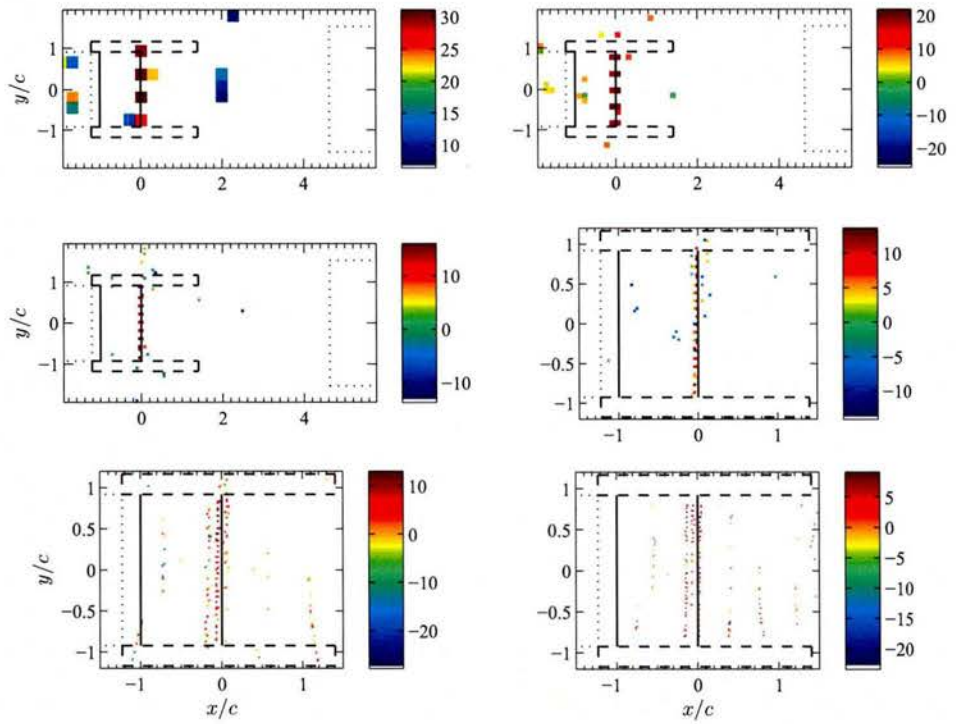

Figure 5.34: DAMAS beammaps for the $Re_c = 0$, $Re_J = 6500$ case. From top left to bottom right 1 kHz, 2 kHz, 4 kHz, 8 kHz, 12 kHz, and 16 kHz.

DAMAS result shows the same properties as the DAS; the primary noise source occurs at the collector with reflected noise near the leading edge of the airfoil. As frequency increases, the DAMAS result shows much more clearly that the primary source of noise is the sidewall near the model. While the DAS results at the highest frequencies show noise sources scattered throughout the domain, the DAMAS results remove these sidelobes and identify the dominant noise source as the sidewalls.

As shown in Figure 5.36 at the highest blowing condition, $C_\mu = 0.10$, the DAMAS result shows the same trends as the DAS, again with significantly reduced sidelobe noise at high frequencies. Unlike the $Re_c = 0$ case, the sources at 2 and 4 kHz do not move as far upstream. This difference can be attributed to the changing dominant noise source mechanism from slot-jet (Howe, 2002) in the case without a free-stream to jet-sidewall

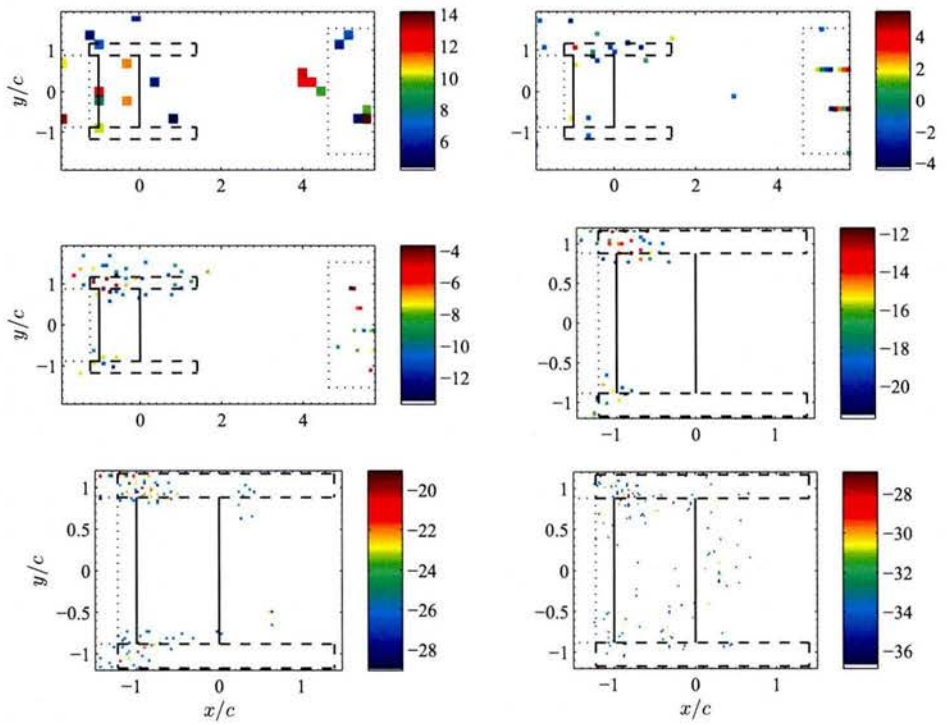

Figure 5.35: DAMAS beammaps for the $Re_c = 6.5e5$, $C_\mu = 0$ case. From top left to bottom right 1 kHz, 2 kHz, 4 kHz, 8 kHz, 12 kHz, and 16 kHz.

interaction in the $Re_c = 6.5e5$ case.

Comparing the DAMAS results to the DAS results suggests that DAMAS spectral results are likely to be more accurate than DAS, especially at higher frequencies, due to its exclusion of sidelobes. Figures 5.37, 5.38, 5.39, and 5.40 provide spectral comparisons between the DAMAS and DAS beamformer results for all free-stream Reynolds numbers and momentum coefficients.

In the $Re_c = 0$ cases (Figure 5.37) the DAS result shows slightly higher levels than DAMAS for moderate to high frequencies. The difference between DAS and DAMAS over these frequencies decreases with increasing momentum coefficient. This behavior is likely due to the tendency for the sidelobes to have a greater effect when the overall levels are lower.

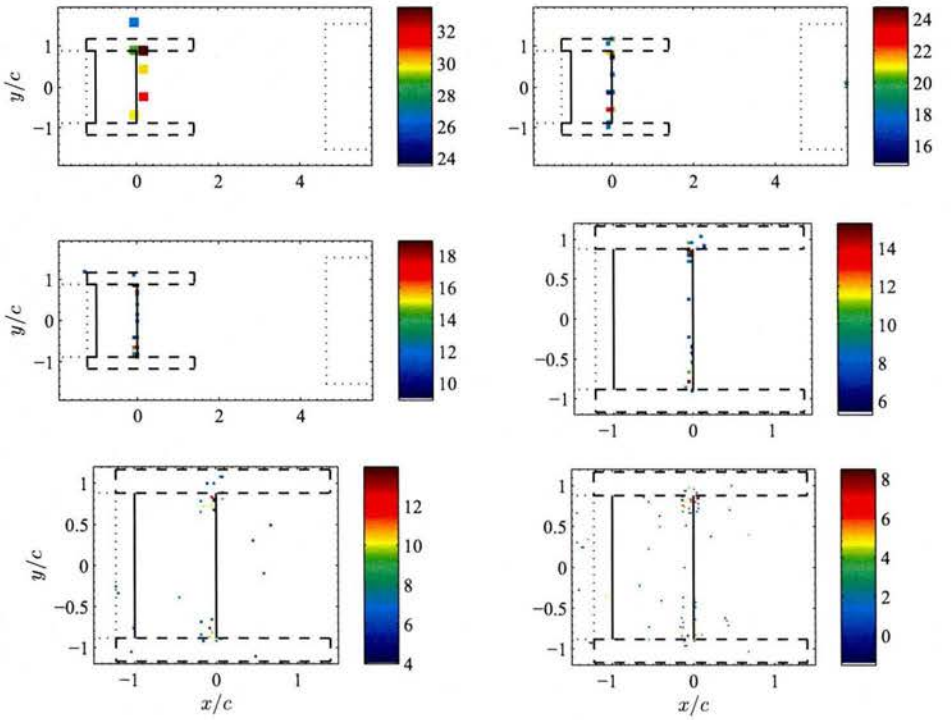

Figure 5.36: DAMAS beammaps for the $Re_c = 6.5e5$, $C_\mu = 0.10$ case. From top left to bottom right 1 kHz, 2 kHz, 4 kHz, 8 kHz, 12 kHz, and 16 kHz.

With the flow at prescribed Reynolds numbers (Figures 5.38, 5.39, and 5.40) several similarities to the DAS results are shown. The zero and lowest ($C_\mu = 0.004$) momentum coefficients remain contaminated by background noise. As with the DAS results, the DAMAS output removes enough external noise from the $C_\mu = 0.017, Re_c = 9.7e5$ and $Re_c = 1.3e6$ cases to distinguish them from the background (no model) noise (compared to the single microphone data). Also, like DAS, the background noise continues to be significant at low to middle frequencies in the $C_\mu = 0.017, Re_c = 6.5e5$ case. The trend noted in the $Re_c = 0$ cases continues with the DAMAS results being slightly lower than the DAS at high frequencies.

Even using DAMAS the spectral results show that the two lowest blowing conditions ($C_\mu = 0$ and $C_\mu = 0.004$) are not appreciably above the no model case for any of the free-

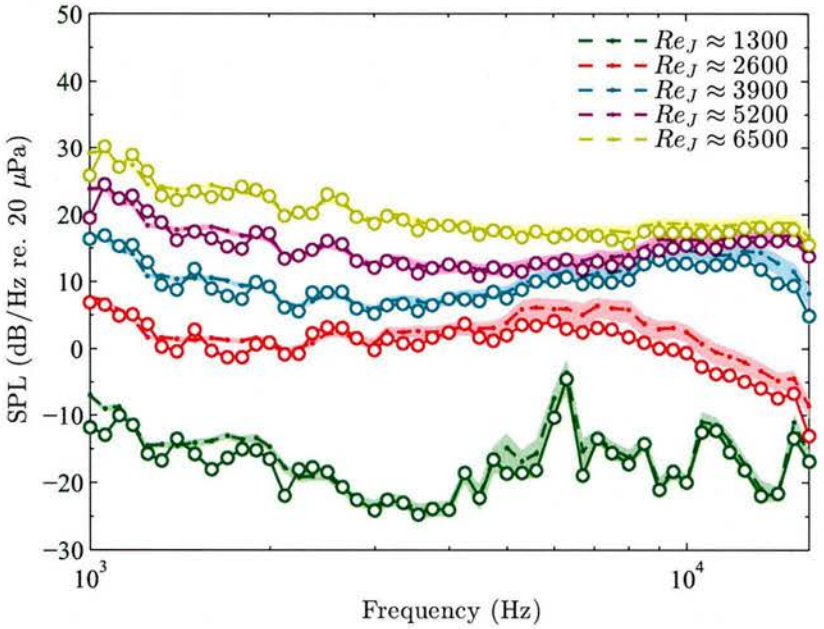

Figure 5.37: Spectral data from DAS (dashed lines with dot markers) and DAMAS (solid line with hollow markers) integrated spectra at 1/12th octave bands centers with shading showing DAS 95% uncertainty based on 1000 iteration Monte Carlo simulations at $Re_c = 0$.

stream Reynolds numbers. A scaling analysis is now performed on the suitable acoustic data.

5.5.3 Acoustic Comparison to NACA 0012

With all non-CC noise sources suppressed, the overall sound pressure levels (OASPL) from the CC experiments are compared to those of a NACA 0012 airfoil. NAFNoise (Moriarty, 2005) is employed to match the specific parameters of the CC airfoil experiment, namely, airfoil geometric parameters (chord, span, observer distance, and observer location), and free-stream flow parameters (density, velocity, Mach number, Reynolds number, and lift coefficient). Lift coefficient is matched by varying the angle of attack in the NACA 0012 estimate. In the estimate, boundary layer trips are placed at $0.2x/c$ on the upper and lower surfaces, corresponding to the locations given by Brooks *et al.* (1989). Within

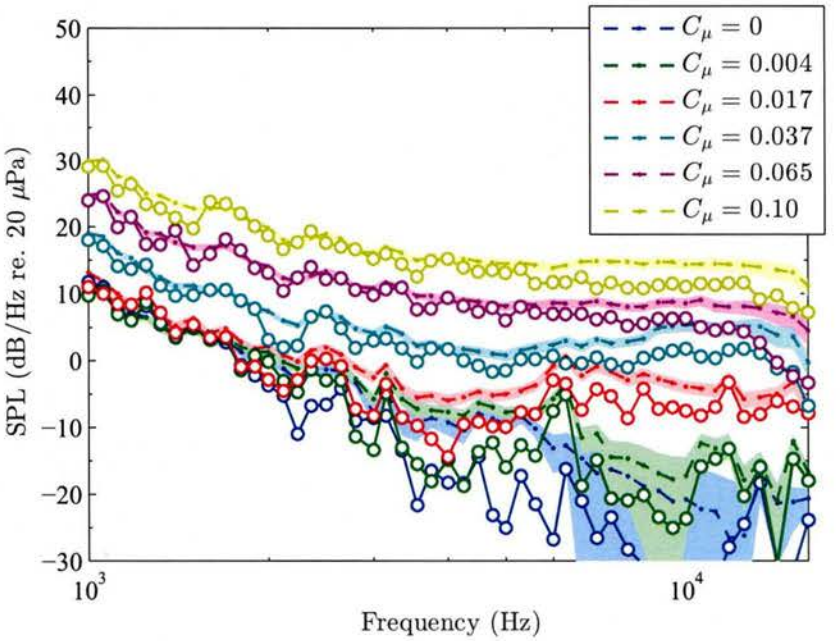

Figure 5.38: Spectral data from DAS (dashed lines with dot markers) and DAMAS (solid line with hollow markers) integrated spectra at 1/12th octave bands centers with shading showing DAS 95% uncertainty based on 1000 iteration Monte Carlo simulations at Re_c = 6.5e5.

NAFNoise, the boundary layer parameters are calculated using XFOIL (Drela, 1989) while the turbulent boundary layer noise is obtained by the method described in Moriarty & Migliore (2003). Turbulent inflow noise and trailing edge bluntness noise are neglected. The OASPL results over a frequency range of 1 to 16 kHz are compared in Table 5.8 for the simulated NACA 0012 and the measured CC noise (where Δ = CC Noise - NACA 0012 Noise).

Case	CC	NACA 0012	Δ dB
$\mathrm{Re}_c = 9.7e5, C_l = 0.72$	49 dB	46 dB	+3 dB
$\mathrm{Re}_c = 1.3e6, C_l = 0.76$	59 dB	57 dB	+2 dB
$\mathrm{Re}_c = 6.5e5, C_l = 1.26$	44 dB	36 dB	+8 dB
$\mathrm{Re}_c = 9.7e5, C_l = 1.32$	57 dB	46 dB	+11 dB

Table 5.8: OASPL comparison from the CC airfoil experiments to NACA 0012 airfoil estimates from NAFNoise. OASPL computed from 1 to 16 kHz.

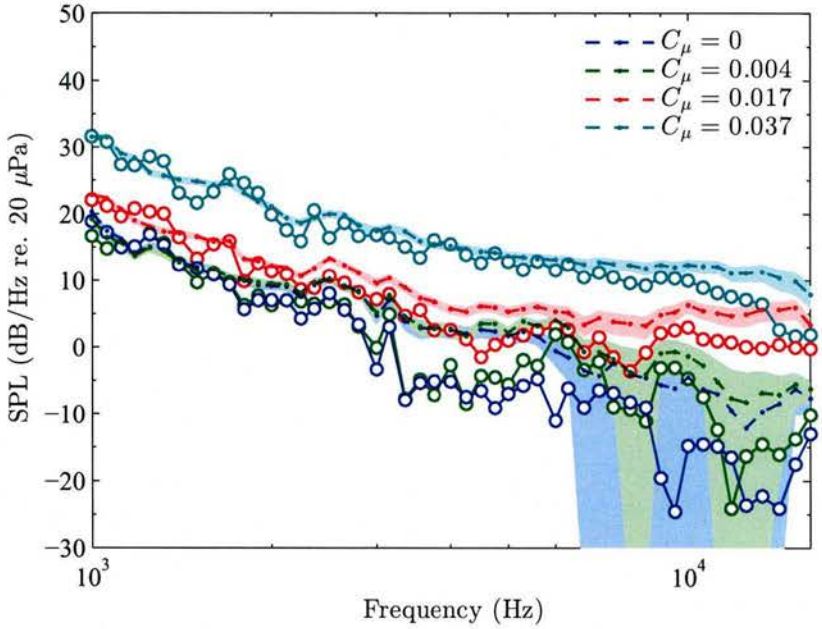

Figure 5.39: Spectral data from DAS (dashed lines with dot markers) and DAMAS (solid line with hollow markers) integrated spectra at 1/12th octave bands centers with shading showing DAS 95% uncertainty based on 1000 iteration Monte Carlo simulations at $Re_c = 9.7e5$.

The first two cases correspond to $C_\mu = 0.017$ for the CC or $\alpha \approx 6.5°$ for the NACA 0012 and the latter two $C_\mu = 0.037$ or $\alpha \approx 13.5°$, respectively . All other cases have either been ruled unsuitable within this document or would require angles of attack well above stall. As shown in table 5.8, CC noise is considerable when compared to a NACA 0012 at the same chord Reynolds number and lift coefficient. At the lower lift coefficients, the difference is somewhat small; however, as the lift coefficient increases, the CC noise is substantially higher that that generated by the NACA 0012. In spite of this increase in noise, CC remains an attractive option due to its ability to generate lift coefficients which are not achievable by symmetric airfoils (traditionally used in underwater applications to achieve positive or negative lift). However, this analysis shows this high lift comes at the expense of increased noise.

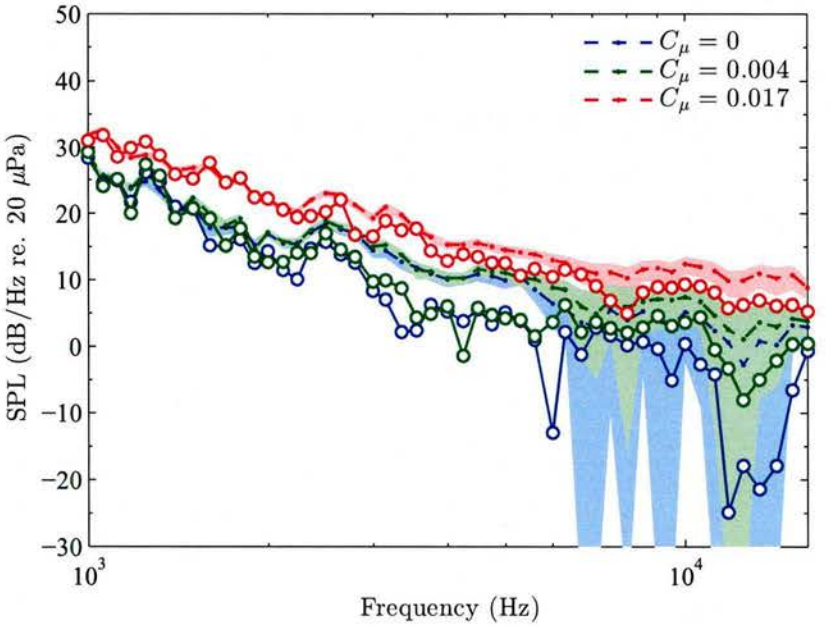

Figure 5.40: Spectral data from DAS (dashed lines with dot markers) and DAMAS (solid line with hollow markers) integrated spectra at 1/12th octave bands centers with shading showing DAS 95% uncertainty based on 1000 iteration Monte Carlo simulations at $Re_c = 1.3e6$.

5.5.4 Scaling Analysis

Using the DAMAS results discussed above, a Mach scaling analysis to identify possible acoustic source types is investigated. In order to scale the results, the following equation is employed,

$$SPL_S = 10\log\left[\Delta F\left(\frac{PSD}{P_{ref}^2}\right)\left(\frac{M_{ref}}{M}\right)^n\right], \tag{5.5.1}$$

where $P_{ref} = 20\mu$Pa, $M_{ref} = 0.1$ and n is the power of Mach number scaling. For scaling versus Helmholtz number ($He = 2\pi FD/c_0$), $\Delta F = c_0/2\pi D$, where c_0 is the speed of sound, F is frequency, and D is the trailing edge diameter. While scaling against Strouhal number ($St = FD/U_{jet}$), $\Delta F = U_{jet}/c$, where c is the airfoil chord. It should be noted that the following discussion applies only to the location discussed throughout this document (directly above the CC slot jet). In the event that a highly directive source exists, the

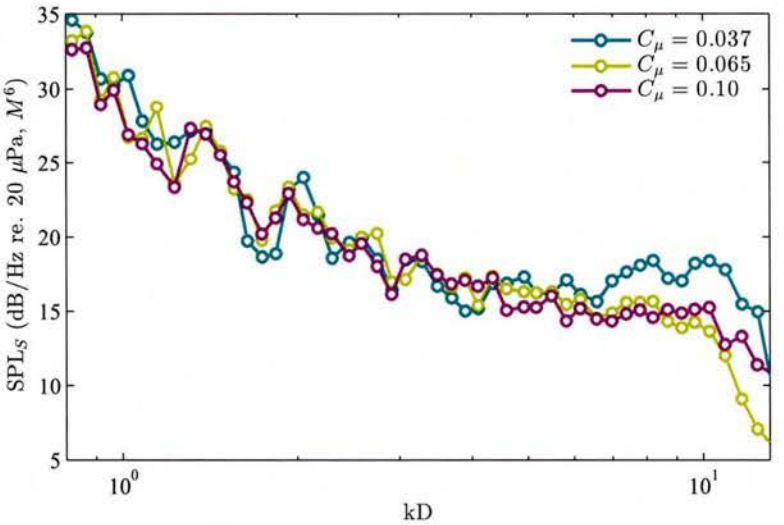

Figure 5.41: Spectral data from integrated DAMAS at 1/12th octave bands centers scaled by jet Mach number to the 6th power at $Re_c = 6.5e5$.

scaling may change with observer location.

First, the free-stream Reynolds number is held constant and the jet Mach number is used as a scaling parameter. Figure 5.41 shows that the spectra in the $Re_c = 6.5e5$ case collapses quite well with jet Mach number to the 6th power for low and intermediate Helmholtz numbers (kD, where k is the wavenumber). This is indicative that a dipole-like source dominates, which can represent either curvature noise or noise generated from turbulence interacting with the slot lip (Howe, 2002). Based on the scaling Helmholtz range and dominant source locations (discussed above), the low kD noise is likely generated by turbulence from the jet interacting with the curved trailing edge while the middle Helmholtz numbers come from the turbulence in the free-stream interacting with the slot lip (Howe, 2002). Interestingly, the highest kD noise does not scale well with any power of jet Mach number, suggesting a more complex phenomenon. The same (M^6) scaling is shown in Figure 5.42 for the $Re_c = 9.7e5$ case. Again, there is a reasonable collapse over low and middle Helmholtz numbers.

The $Re_c = 0$ case is investigated in Figure 5.43. For the zero free-stream case a significant

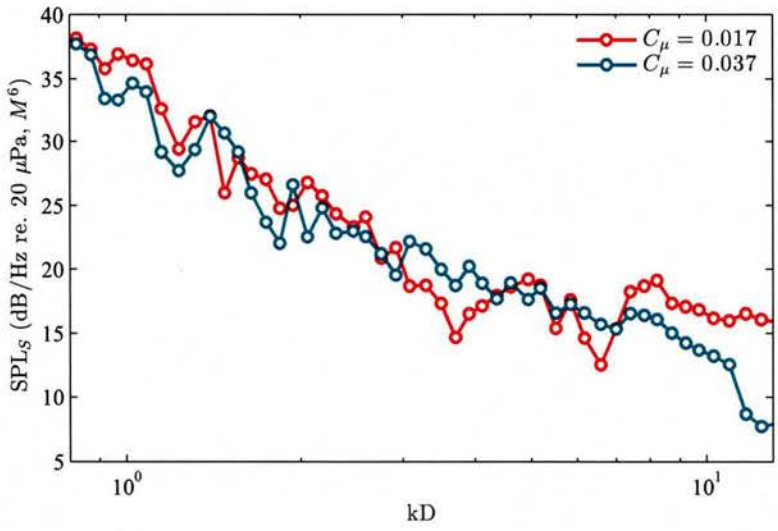

Figure 5.42: Spectral data from integrated DAMAS at 1/12th octave bands centers scaled by jet Mach number to the 6th power at $Re_c = 9.7e5$.

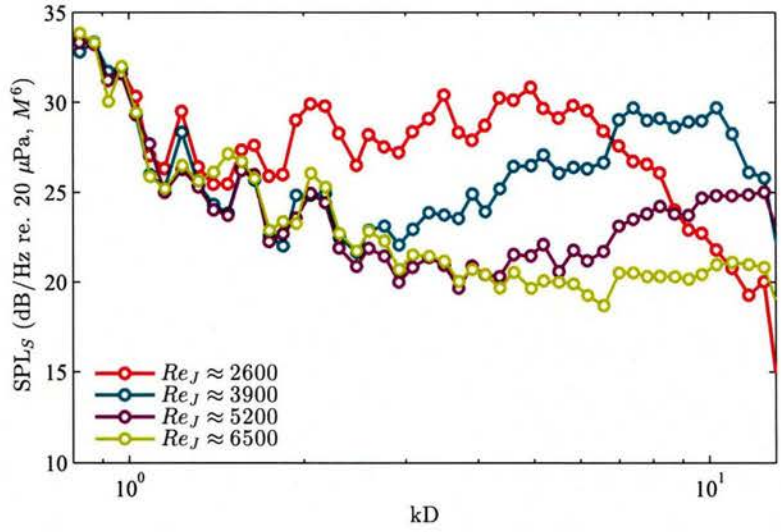

Figure 5.43: Spectral data from integrated DAMAS at 1/12th octave bands centers scaled by jet Mach number to the 6th power at $Re_c = 0$.

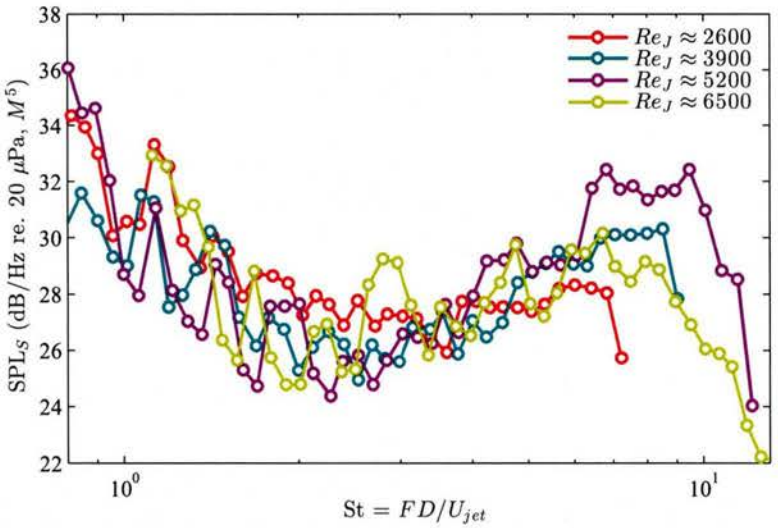

Figure 5.44: Spectral data from integrated DAMAS at 1/12th octave bands centers scaled by Strouhal number and jet Mach number to the 5th power at $Re_c = 0$.

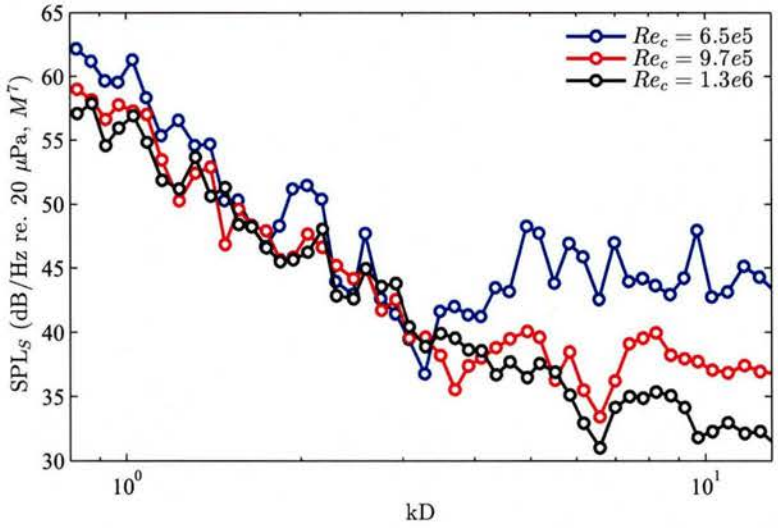

Figure 5.45: Spectral data from integrated DAMAS at 1/12th octave bands centers scaled by freestream Mach number to the 7th power with constant $C_\mu = 0.017$.

collapse continues to be obtained over the lowest Helmholtz numbers; however, unlike the previous cases, the middle kD range do not scale well. This change can be attributed to the lack of a free-stream; the noise generation mechanism (free-stream turbulence interacting with the slot lip) which scaled in the $Re_c = 6.5e5$ cases is no longer present. Instead, Figure 5.44 shows that over the middle range of Strouhal numbers, the spectra collapse reasonably well with jet Mach number to the 5th power. This further indicates a changing dominant acoustic generation mechanism for the middle Helmholtz/Strouhal numbers from the case with no jet to the cases with the jet active.

Finally, the momentum coefficient is held constant (implying a nearly constant jet to free-stream velocity ratio) and scaling is performed versus freestream Mach number. The result is shown for $C_\mu = 0.017$ in Figure 5.45. A reasonable collapse is achieved employing Mach scaling to the 7th power. The dominant noise production mechanism is a combination of dipole-like and quadrupole-like sources, suggesting significant noise generation from the interaction between the free-stream and the jet.

5.6 Methodology Overview

This section details the results at each stage of the proposed methodology. This section focuses on two sets of test conditions. Both cases are performed at a chord Reynolds number of 650,000 (corresponding to a free-stream velocity of approximately 20 m/s). The simple test case involves no blowing out of the CC slot ($C_\mu = 0$), while the more complex case employs the maximum momentum coefficient used during testing ($C_\mu = 0.10$ or slot velocity approximately 5 times the free-stream velocity). This section progresses in the same manner as §2; it starts with POD, explores the correlations between the surface pressure and the POD expansion coefficients, moves on to the mLSE and Kalman smoother, discusses the Poisson solution and concludes with Curle's analogy. All vorticity plots have been nondimensionalized by D/U_∞, where D is the diameter of the trailing edge and U_∞ is the freestream velocity. Turbulent kinetic energy ($TKE = 0.5(\overline{u'^2} + \overline{v'^2})$) and Reynolds stresses

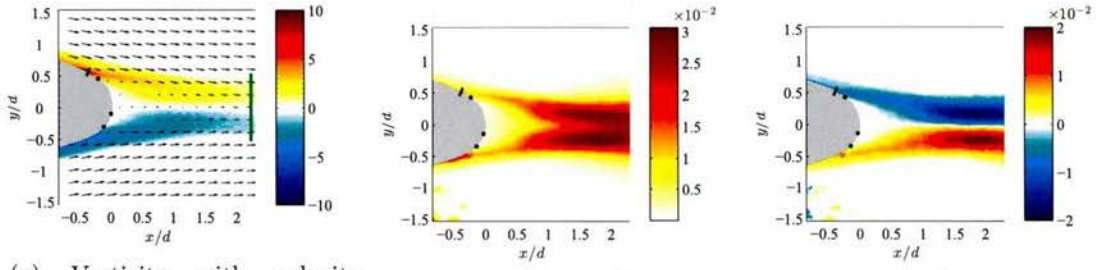

(a) Vorticity with velocity quiver

(b) TKE/U_∞^2

(c) $\overline{u'v'}/U_\infty^2$

Figure 5.46: Dimensionless mean-flow quantities (vorticity, velocity, TKE, Reynolds stress) for the $C_\mu = 0$ case. The solid black line indicates the slot lip location, dots indicate pressure sensor locations P1, P2, and P3 from top to bottom. The green line at the boundary indicates the region over which momentum flux is calculated for scaling of Kalman-smoother results discussed later. In the quiver plots of velocity, one out of every 10 vectors is shown for clarity.

are normalized by U_∞^2. Figures 5.46 and 5.47 show dimensionless mean-flow quantities for the two selected cases. In the $C_\mu = 0$ case we see that the dominant fluctuations occur downstream of the model in the region associated with the shed bluff-body vorticies. In the $C_\mu = 0.10$ case the dominant fluctuations are due to the presence of the jet and decay as the jet separates and moves away from the model. The solid black line indicates the slot lip location while the dots indicate pressure sensor locations P1, P2, and P3 from top to bottom.

5.6.1 POD Results

First, the POD is performed on the PIV data set comprised of 765 image pairs. Figure 5.48 shows the distribution of the energy in the POD modes for the no-blowing and $C_\mu = 0.10$ cases. The first four modes in the no-blowing case contain a much higher percentage (46%) of energy than those in the maximum-blowing case (22%). Mode shapes of vorticity (generated from the u and v POD modes) for the first eight POD spatial modes are illustrated in figures 5.49 and 5.50. In the $C_\mu = 0$ case, bluff body shedding is represented by the first two modes, while the third and fourth mode represent energy in the shear layer

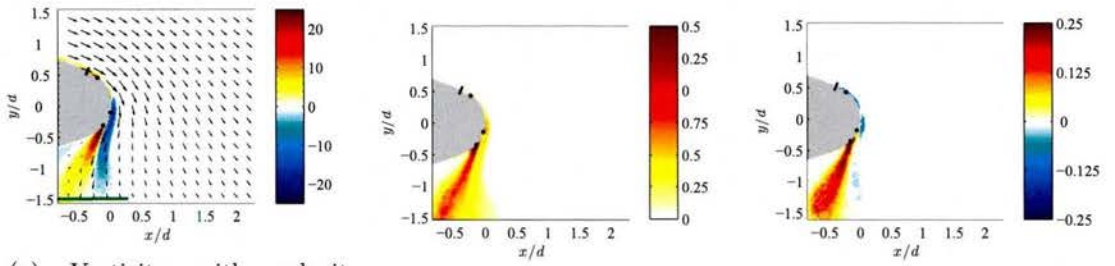

(a) Vorticity with velocity quiver

(b) TKE/U_∞^2

(c) $\overline{u'v'}/U_\infty^2$

Figure 5.47: Dimensionless mean-flow quantities (vorticity, velocity, TKE, shear component of Reynolds stress) for the $C_\mu = 0.10$ case. The solid black line indicates the slot lip location, dots indicate pressure sensor locations P1, P2, and P3 from top to bottom. The green line at the boundary indicates the region over which momentum flux is calculated for scaling of Kalman-smoother results discussed later. In the quiver plots of velocity, one out of every 10 vectors is shown for clarity.

from the upper and lower sides of the model. As mode number increases (and therefore modal percentage of energy decreases) the structures in the mode shapes become smaller, higher in spatial frequency, with a lower signal-to-noise ratio. This trend is repeated in the maximum-blowing case where the first two modes represent the shear layer and the spatial frequency increases with mode number.

One important consideration for the velocity estimation step is determining which POD modes to use for the reconstruction. This will be accomplished based on estimated uncertainty in the POD modes. To estimate the uncertainty, a 1000-iteration Monte-Carlo simulation is performed. The instantaneous velocity fluctuation (u' and v') snapshots used initially in the POD are perturbed by the PIV measurement uncertainty. PIV uncertainty is usually attributed to in-plane motion, out-of-plane motion, background (Gaussian) noise, out-of-focus seed and non-uniform seed density (Sciacchitano *et al.*, 2014) and is determined by the correlation statistics method (Wieneke, 2014) in DaVis. For the purposes of the simulation, the PIV uncertainty is estimated using independent Gaussian distributions for the perturbations defined by the DaVis (8.2.2) output (Wieneke, 2015). It should be noted that the mean-flow random uncertainty is not considered because the instantaneous fluctuating

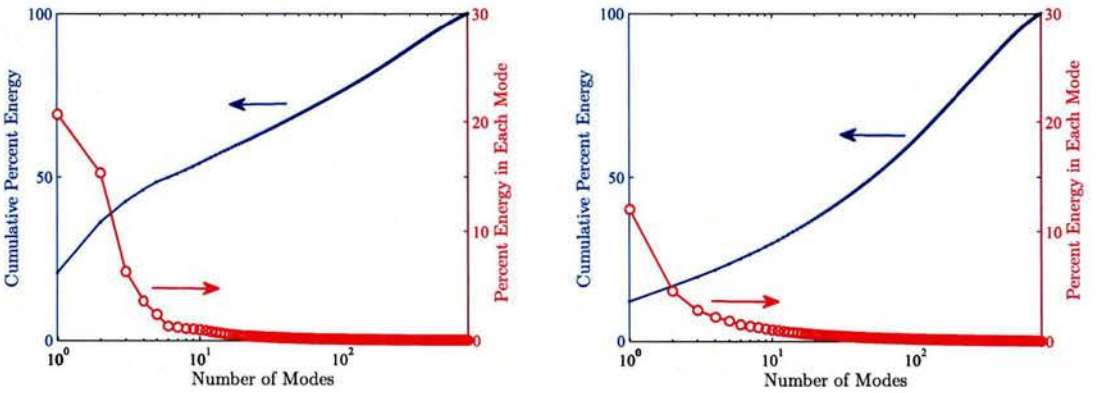

(a) $C_\mu = 0$ (b) $C_\mu = 0.10$

Figure 5.48: Percentage of energy contained in POD modes for the $C_\mu = 0$ and $C_\mu = 0.10$ cases, cumulatively and individually.

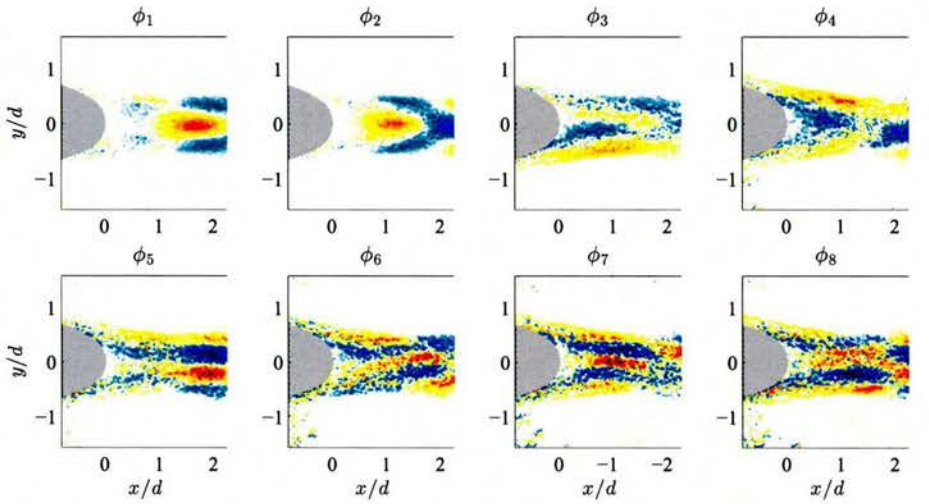

Figure 5.49: Vorticity mode shapes of the first eight POD modes for the $C_\mu = 0$ case.

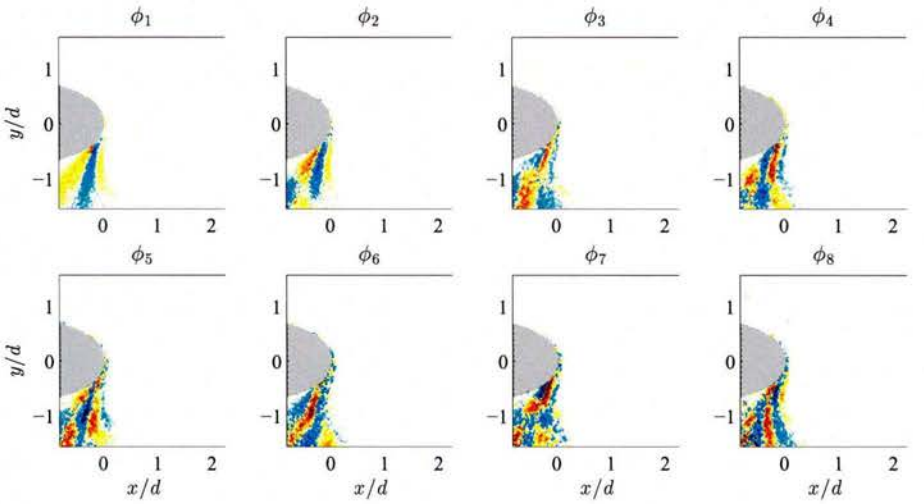

Figure 5.50: Vorticity mode shapes of the first eight POD modes for the $C_\mu = 0.10$ case.

velocity snapshots are used in the POD.

One issue encountered during the Monte-Carlo simulation is the ambiguity of the signs $(+/-)$ on the POD spatial modes and temporal coefficients. Because the reconstruction relies on multiplying the two together, the sign assigned to either is arbitrary, i.e. if the velocity at a certain time and location in space should be positive then the spatial mode at that location and the temporal coefficient at that time must both have the same sign. Either of these two outcomes is acceptable mathematically; however, this makes the standard deviation (and therefore uncertainty) of the spatial modes and temporal coefficients (over a large number of iterations) appear to be larger than in reality. To remove the effect of sign switching, the sign of the POD temporal coefficient for the first instance of each mode is designated by the first iteration. This sign is then enforced on all subsequent iterations. If the sign is switched, it is switched for the entire set of temporal coefficients for that mode *and* for the entire spatial mode shape for that mode. By applying this correction to both, the reconstruction has not been altered. The modified reconstruction is verified by comparing it to the standard version. Convergence of the simulation is observed at 1000 iterations.

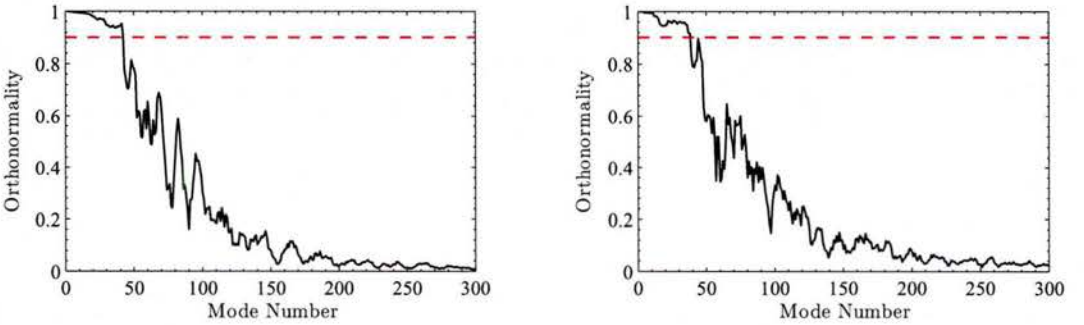

(a) $C_\mu = 0$ (b) $C_\mu = 0.10$

Figure 5.51: Orthonormality of the Monte-Carlo mean and unperturbed POD mode shapes. Orthonormality greater than 0.9 results in the mode being selected for use. The dashed red line indicates the 0.9 cutoff.

The mean of the 1000 iteration simulations are then compared to the initial unperturbed modes. To see how well the mean of the perturbed modes match the unperturbed modes, the orthonormality requirement of POD is tested. The inner product is taken between mode n from the unperturbed set and mode n from the Monte-Carlo mean from $n = 1$ to 765 and the results are shown in figure 5.51 for the no- and maximum-blowing cases. 42 modes for the no-blowing and 38 modes for the maximum-blowing cases are observed to be nearly identical (orthogonality greater than 0.9) which indicates that they are relatively unaffected by the velocity uncertainty. Therefore only these modes are considered in the reconstruction.

The 42- and 38-mode reconstructions are shown in figure 5.52. The no-blowing, 42-mode reconstruction contains 66% of the total energy, and the maximum-blowing, 38-mode reconstruction contains 42% of the total energy. The low-order reconstructions tend to retain the large-scale vorticity while filtering the small-scale contributions. With a defined set of POD modes, POD coefficients, and unsteady pressure signals, the analysis moves to the time-resolved velocity estimation.

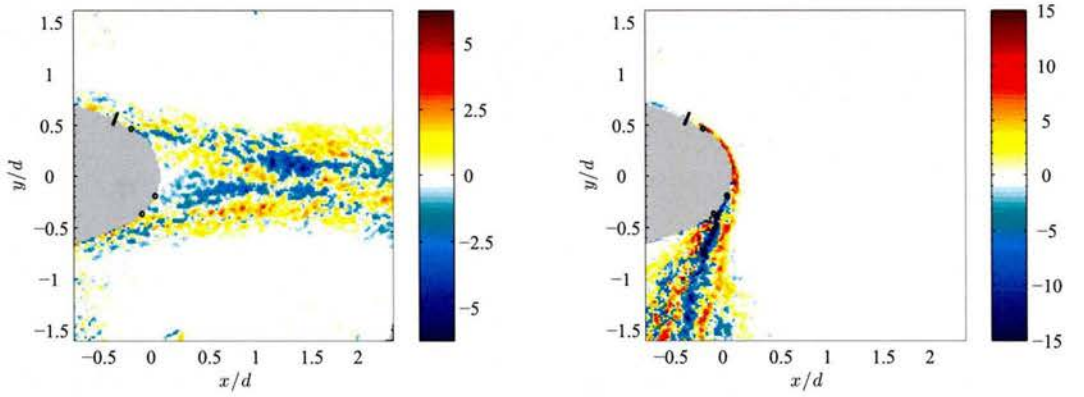

(a) $C_\mu = 0$ - 42 Modes

(b) $C_\mu = 0.10$ - 38 Modes

Figure 5.52: POD reconstructed instantaneous vorticity fields for the $C_\mu = 0$ and $C_\mu = 0.10$ cases employing 42 and 38 modes, respectively. The solid black line indicates the slot lip location, dots indicate pressure sensor locations P1, P2, and P3 from top to bottom.

5.6.2 Pressure to Velocity/POD Coefficient Correlation

Estimating the velocity via the modified stochastic estimation relies on a significant correlation between the POD coefficients and the pressure signals. Figure 5.53(a) shows the correlation (at the optimal time delay, determined below in figure 5.56) between POD temporal coefficients and pressure data for the no-blowing case. The first two POD modes are shown to have significant correlation with the pressure data; however, all other correlations are well below 0.2. Examining the $C_\mu = 0.10$ case (figure 5.53(b)) maximum correlation coefficients of less than 0.12 are obtained.

To understand the outcome of the correlation analysis above, the correlation between vorticity field and surface-pressure sensors is investigated. Figure 5.54 shows the correlation between vorticity and pressure for each transducer at the optimal time delay. A clear, strong correlation is obtained for all three transducers in the wake corresponding to bluff body shedding (and bear a striking resemblance to POD modes 1 and 2). The prominence of these modes in the velocity field suggests that the shedding behavior should be well estimated.

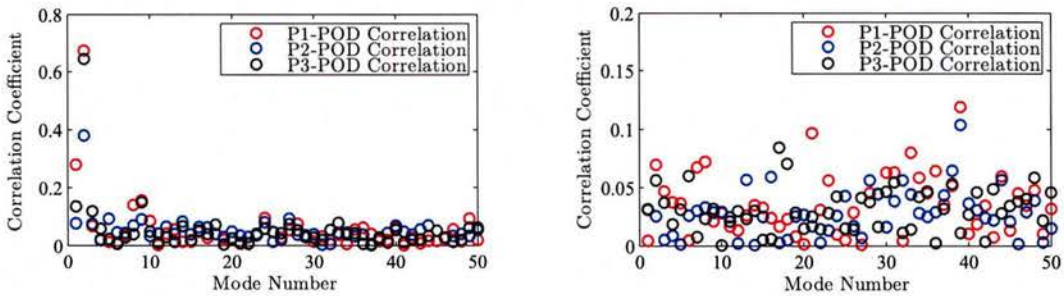

(a) $C_\mu = 0$ (b) $C_\mu = 0.10$

Figure 5.53: Correlation coefficient between POD temporal coefficients and pressure data for (a) $C_\mu = 0$ and (b) $C_\mu = 0.10$.

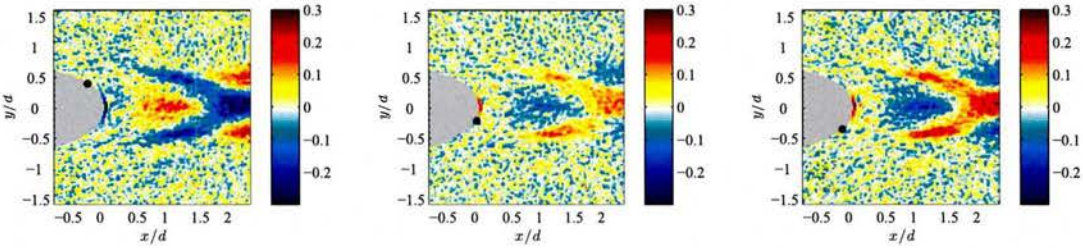

(a) $P1$ (b) $P2$ (c) $P3$

Figure 5.54: Correlation coefficient between vorticity field and pressure data at the optimal time delay (0) for (a) P1, (b) P2, and (c) P3 for the no-blowing case. The dot indicates the location of the pressure probe.

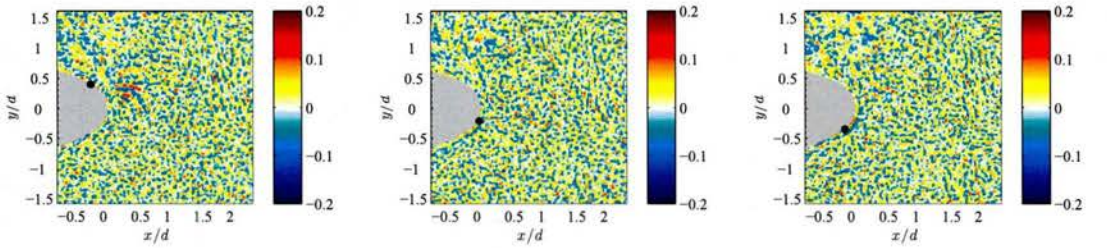

(a) $P1$ (b) $P2$ (c) $P3$

Figure 5.55: Correlation coefficient between vorticity field and pressure data at the optimal time delay (0) for (a) P1, (b) P2, and (c) P3 for the maximum-blowing case. The dot indicates the location of the pressure probe.

For the $C_\mu = 0.10$ case, correlation between the vorticity field and pressure are shown in figure 5.55. The correlation field for each of the three pressure probes shows no structure with significant correlation. For this case, the pressure transducers likely have significant correlation only with the turbulent boundary layer in which they are embedded, which is not resolved by the PIV measurements. Due to the low correlation levels, poor estimates of the velocity field (aside from the shedding peak present in the $C_\mu = 0$ case) are expected from the mLSE. However, the effects of poor mLSE estimate on the proposed method is not immediately clear from the present results. As such, an attempt to use the method continues.

5.6.3 Time Resolved Velocity Field - Stochastic Estimation

To obtain an initial estimate of the time-resolved velocity, mLSE is performed. To make the best use of the mLSE it is first important to determine the optimal initial delay as well as the optimal number of delays in equation 2.1.17 (Durgesh & Naughton, 2010). A difference metric (using the kinetic energy of the difference between the measured and estimated fields normalized by the measured kinetic energy) is defined (Tu *et al.*, 2012) to

determine the most accurate number and initial delays,

$$e = \frac{\sum_{i=1}^{r}[\tilde{a}_i - a_i]^2}{\sum_{i=1}^{r}[a_i]^2}, \tag{5.6.1}$$

where a and $\tilde{a}$ are the known and estimated coefficients, respectively, for n POD modes. Figure 5.56 shows the difference in the estimated coefficients versus chosen initial delay, ϕ^*,

$$\phi^* = \frac{\tau U}{D}, \tag{5.6.2}$$

where U for the no-blowing case is the freestream velocity (20 m/s) and jet velocity (100 m/s) for the blowing case and D is the cylinder diameter (45 mm) for both cases.

The frequency of oscillation in the no-blowing case corresponds to the bluff-body shedding frequency. This, along with the large POD-to-pressure correlation, implies the bluff-body shedding modes (POD modes 1 and 2) are likely to be well represented in the estimation. For both cases an initial time delay of zero, i.e., with the PIV snapshot and the pressure signal occurring simultaneously, is optimal. Next, the use of multiple time delays is investigated. Figure 5.57 shows the difference in the estimated coefficients versus the maximum number of delays (m from equation 2.1.17) where each τ^* starts with the optimal value of ϕ^* and expands to include additional delays by increasing m. A single time delay is optimal, indicating additional data in time degrades the correlation between the pressure and POD coefficients, presumably due to the rapid increase in number of unknown parameters with the number of time delays used.

A velocity-field reconstruction (at the same instant in time as figure 5.52) is shown in figure 5.58. The field is, as expected, observed to have considerably lower amplitude than the true POD reconstruction. This is due to the relatively low levels of correlation between the pressure and the POD coefficients. In the no-blowing case the vorticity field appears very similar to the first and second POD modes, while the $C_\mu = 0.10$ case appears to be some combination of the POD modes. Although the reconstructed vorticity fields appear generally similar to the reduced-order vorticity fields, when these fields are advanced in time

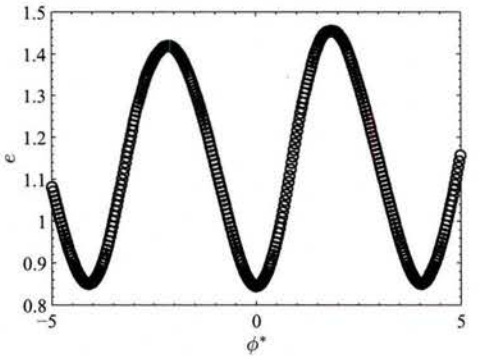

(a) $C_\mu = 0$ - 42 Modes

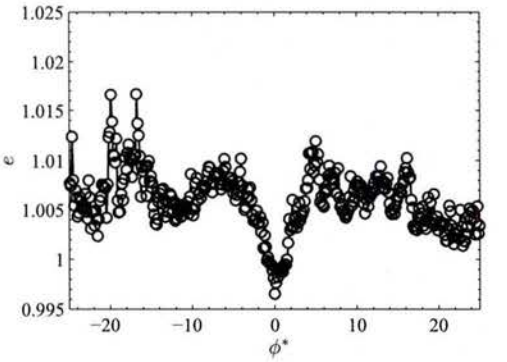

(b) $C_\mu = 0.10$ - 38 Modes

Figure 5.56: Difference in the estimated POD coefficients with various initial time delays, ϕ^*.

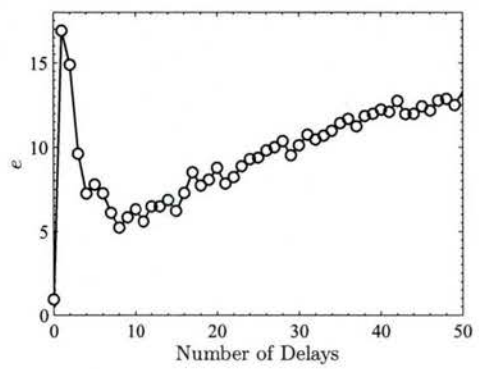

(a) $C_\mu = 0$ - 42 Modes

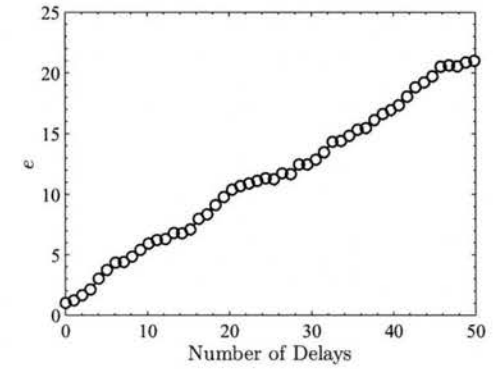

(b) $C_\mu = 0.10$ - 38 Modes

Figure 5.57: Difference in the estimated POD coefficients with various numbers of maximum time delays (m from equation 2.1.17). Each location along the independent axis contains that value of $m\tau^*$ as well as all those below that value.

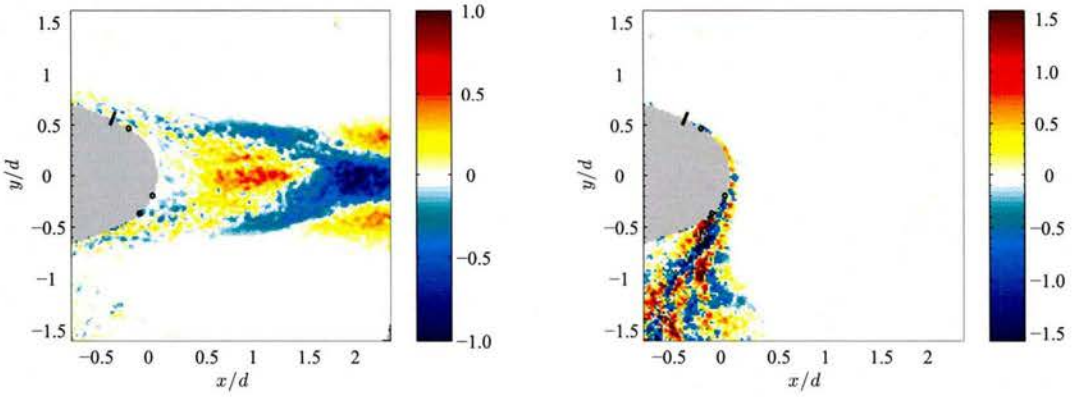

(a) $C_\mu = 0$ - 42 Modes

(b) $C_\mu = 0.10$ - 38 Modes

Figure 5.58: POD-mLSE reconstructed instantaneous vorticity fields for the $C_\mu = 0$ and $C_\mu = 0.10$ cases employing 42 and 38 modes, respectively, estimated from mLSE. The solid black line indicates the slot lip location, dots indicate pressure sensor locations P1, P2, and P3 from top to bottom.

the structures representing the POD modes appear to strengthen and decay rather than convecting. In figure 5.59, the RMS value of the estimated and measured POD coefficients for each mode are shown. This illustrates the (relative) dominance of the first two POD modes in the no-blowing case and the minimal impact (compared to the measurement) of all other modes in both cases. With the velocity field now estimated in a temporally and spatially resolved sense, the Kalman smoother is used to improve the stochastic estimate.

5.6.4 Time Resolved Velocity Field - Kalman Smoother

The system model (for equation 2.1.22) is generated by using the estimated POD temporal coefficients such that,

$$F = \frac{[a_j^r]}{[a_{j-1}^r]}, \tag{5.6.3}$$

where a_j^r is the matrix of size r by $N_t - 1$ containing the r POD modes used in the estimate at times spanning the full time history N_t, less the first temporal location. Likewise, a_{j-1}^n of size r by $N_t - 1$ contains the employed POD modes but spanning the full time history

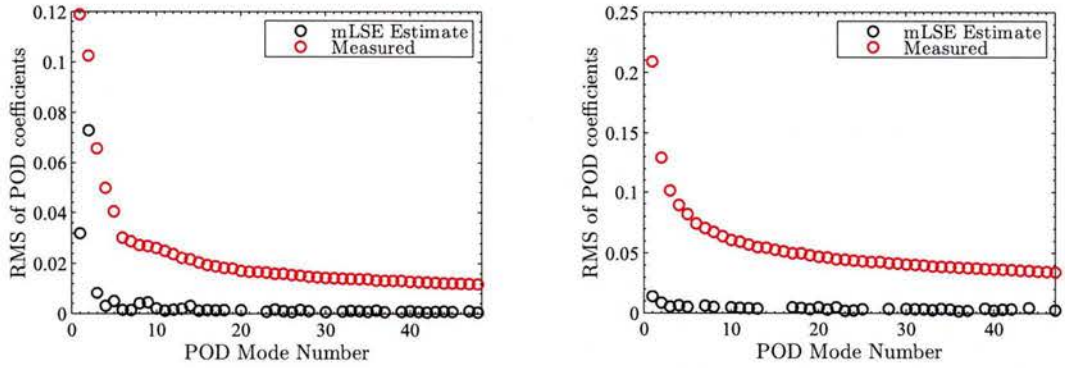

(a) $C_\mu = 0$ - 42 Modes

(b) $C_\mu = 0.10$ - 38 Modes

Figure 5.59: RMS value of the estimated and measured POD temporal coefficients versus POD mode number for the $C_\mu = 0$ and $C_\mu = 0.10$ cases.

save the *final* temporal location. Here, F is solved by using a pseudo-inverse.

The measurement matrix, H_k, (equation 2.1.23) is defined differently based on the type of data available at time k. At temporal locations when a PIV snapshot is available, the measurement matrix is the identity matrix, I, which allows the known POD modes to be accessed directly. At times when PIV is not available,

$$H = \frac{[p]}{[a]} \tag{5.6.4}$$

where p is the pressure probe data matrix of size N_p (number of probes) by N_t and a is the matrix size r by N_t of POD coefficients. This allows y_k to be the surface-pressure probe data. The noise covariance matricies, Q and R are chosen such that the process noise Q is the identity matrix at all times. It is chosen as such because the model does not change with respect to time. Conversely, R is made small (10^{-8}) when a PIV snapshot with known POD modes is available because this is the best available information and is assumed to be essentially correct. At times when only pressure data are available, R is set using the difference metric (discussed above) to estimate the noise (which result in typical values on the order of 10^2). It should be noted that the result is quite insensitive to changes in Q and

R such that they could be changed by more than an order of magnitude with only small changes to the result.

This implementation of the Kalman smoother improves the POD reduced-order estimation of the velocity field at times when PIV data are available. This is expected because the mLSE only estimates the portion of the field that is well correlated with the pressure data while the Kalman smoother directly accesses the POD temporal coefficients. At these times, the estimates are very similar to the true POD reduced order velocity fields as shown comparing figures 5.52 and 5.61. The estimates at PIV locations are greatly improved from those obtained by the mLSE; however, as the estimates get further in time from the PIV data, the estimates gradually degrade towards those of the mLSE analysis.

To mimic the original POD reduced-order flow field more accurately, the average momentum flux across the boundary in the primary flow direction is matched between the Kalman-smoother result and POD reduced-order snapshots. In the $C_\mu = 0$ case, the momentum flux (in the primary flow direction) is defined by (Schlichting, 1979),

$$J_x = \int_A \rho u_x (U_\infty - u_x) dA, \tag{5.6.5}$$

where u_x is the velocity in the x-direction and the integral is defined over the wake region from $y/d = -0.6$ to 0.6 at $x/d = -2.2$ (denoted by the green line in figure 5.46). The momentum flux (in the primary flow direction) is defined by (Schlichting, 1979),

$$J_y = \int_A \rho u_y u_y dA, \tag{5.6.6}$$

for the $C_\mu = 0.10$ case. Here, u_y is the velocity in the y-direction and the integral is evaluated from $x/d = -0.8$ to 0.3 at $y/d = -1.5$ (denoted by the green line in figure 5.47). Histograms of the results for both cases from the POD reduced-order snapshots are provided in figure 5.60 and show approximate normal distributions. These histograms show that the momentum flux in the primary flow direction at the boundary in the POD reduced-order snapshots is approximately invariant in time. The Kalman-smoothed, reduced-order velocity fields in

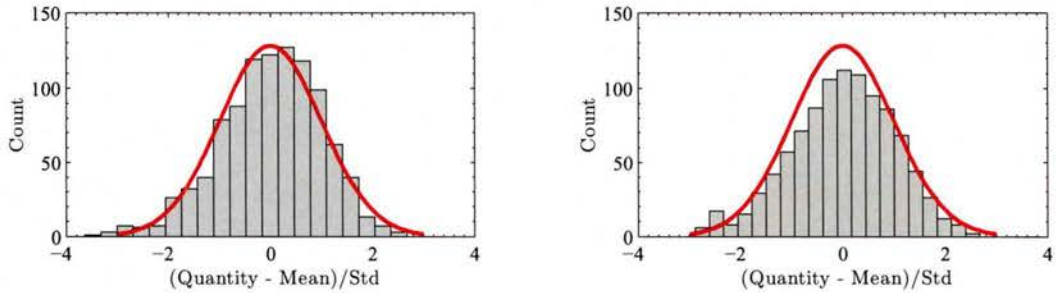

(a) $C_\mu = 0$ (b) $C_\mu = 0.10$

Figure 5.60: Histograms of momentum flux less the mean, normalized by the standard deviation for the $C_\mu = 0$ and $C_\mu = 0.10$ cases. Momentum flux is taken in the primary flow direction over the region where the fluctuating flow leaves the field (downstream for the $C_\mu = 0$ case, below the model for the $C_\mu = 0.10$ case). Red line denotes a normal distribution. Skewness and Kurtosis are 0.28 and 2.80 for the $C_\mu = 0$ case, 0.38 and 2.17 for the $C_\mu = 0.10$ case.

figure 5.61 are scaled up by 4.4% and 15.1% for the no-blowing and maximum-blowing cases, respectively, to match these average values and more accurately reproduce the original POD reduced-order flow field.

5.6.5 Pressure Field - Poisson Solver

With the time-resolved velocity field estimated, the methodology moves on to determining the associated fluctuating pressure field at each temporal location. The boundary conditions chosen for the solution to Poisson's equations are generally of the Neumann type. At each boundary (top, bottom, left, right, and airfoil surface) the Neumann condition is obtained by rearranging the momentum equation, provided in 2.2.5. The notable exception is at locations where unsteady pressure is obtained directly where Dirichlet conditions are imposed instead. The Poisson domain and boundary conditions are indicated in figure 5.62. The blue line indicates the domain exterior as well as the Neumann boundary condition locations and the red dots indicate the 3 locations where Dirichlet boundary conditions are used.

As discussed in Koschatzky *et al.* (2011a), the other primary concerns regarding the

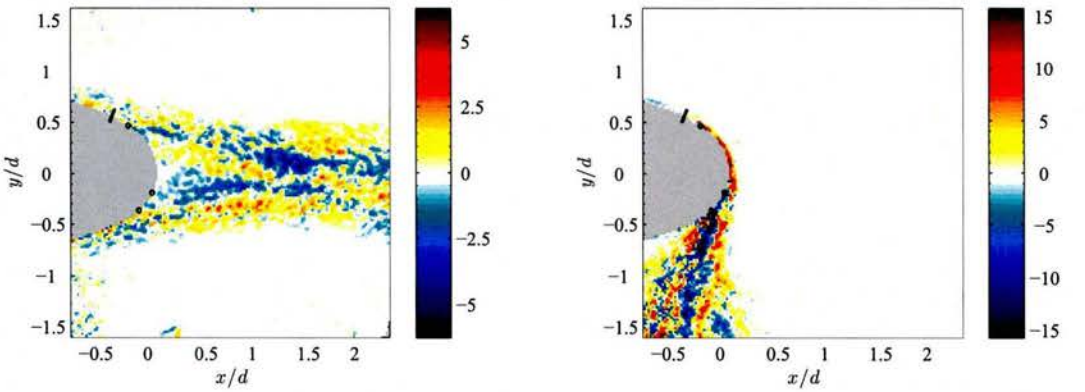

(a) $C_\mu = 0$ - 42 Modes

(b) $C_\mu = 0.10$ - 38 Modes

Figure 5.61: Kalman-smoothed, POD-mLSE-reconstructed instantaneous vorticity field for the $C_\mu = 0$ and $C_\mu = 0.10$ cases. The solid black line indicates the slot lip location, dots indicate pressure sensor locations P1, P2, and P3 from top to bottom.

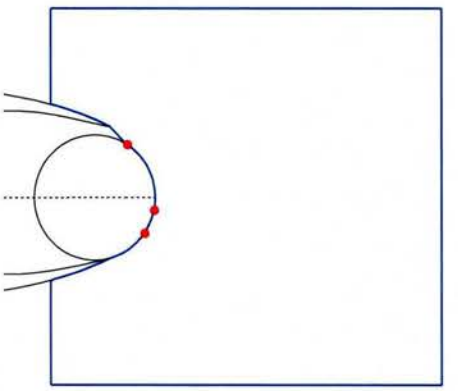

Figure 5.62: Poisson domain and boundary conditions. Blue indicates the exterior edge of the domain as well as locations with Neumann boundary conditions. Red indicates locations with Dirichlet boundary conditions.

Poisson solver involve the size of the domain and the spatial resolution. Using PIV, there is an inherent trade-off between domain size and resolution. It has been shown that placing a boundary too near to the surface of interest can affect the force estimates due to the passage of flow structures across the boundary (Nickels *et al.*, 2014*b*). To combat this, the domain is maximized so the surface forces are negligibly affected by this effect, this allows for resolution of all but the smallest structures. Due to the limited resolution, the boundary layer is not resolved in these tests. While the presence of the sidewalls reduces the flow in the spanwise direction, gradients of fluctuating velocity in this direct are still expected. Because the data only contain two components of velocity, there is also some additional error associated with the missing third component.

The pressure field shown in figure 5.63 is at the same temporal location as the velocity fields presented previously (figure 5.61). In the no-blowing case, pairs of alternating high and low pressure regions appear in the wake of the model which are generated by the bluff body shedding of the model. It is also interesting to note the effect the unsteady pressure probes have on the field. The $C_\mu = 0.10$ case shows a region of negative pressure fluctuations occurring over the top side (slightly upstream of the known pressure P1) followed by a region of alternating pressure fluctuation in the jet. The effect of the known unsteady pressure data on the flow remains apparent at locations P2 and P3.

To extract the surface forces from the fluctuating pressure field, the surface locations are assigned an angle based on the geometry of the model. Using these angles, lift and drag forces are estimated from the pressure distributions. The fluctuating coefficient of lift and drag time series are shown for both cases in figure 5.64. Due to limited computational resources, one second (16384 temporal locations) is estimated. In each case the fluctuating coefficient of drag is larger than that of lift; however, this relative difference is greatly increased with the introduction of blowing. The maximum C_μ case also contains higher frequency content than the no-blowing case due to the introduction of significant turbulence from the jet. Using the fluctuating forces along with Curle's analogy, the acoustic spectrum is estimated next.

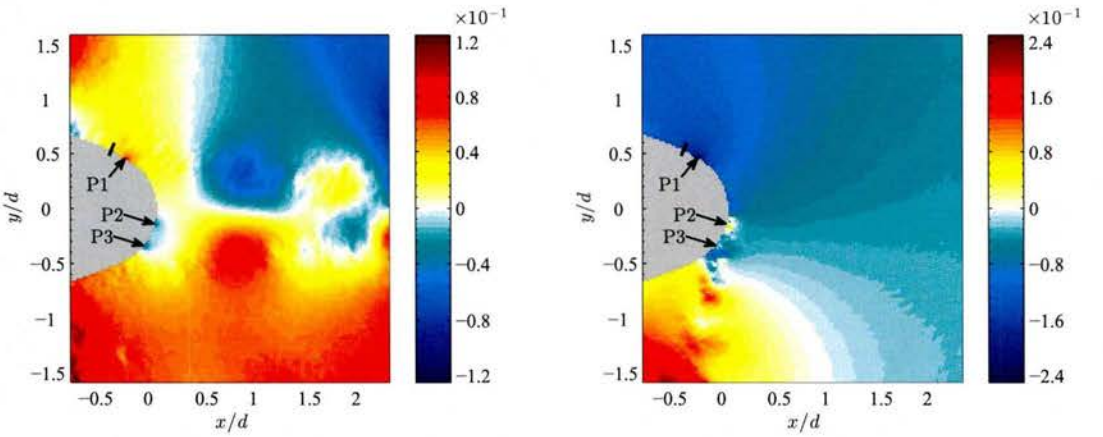

(a) $C_\mu = 0$ (b) $C_\mu = 0.10$

Figure 5.63: Instantaneous Poisson estimated pressure field employing Kalman smoothed POD-mLSE reconstructed instantaneous velocity field along with all three unsteady pressure probes. Color scale shows pressure non-dimensionalized by free-stream dynamic pressure. Solid black line indicates the location of the slot lip.

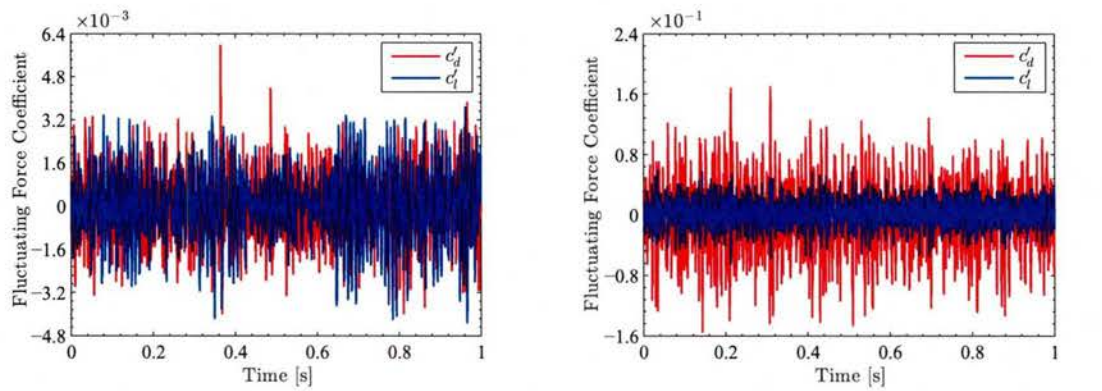

(a) $C_\mu = 0$ (b) $C_\mu = 0.10$

Figure 5.64: Time series of the estimated fluctuating coefficients of lift and drag on the trailing edge of the CC model.

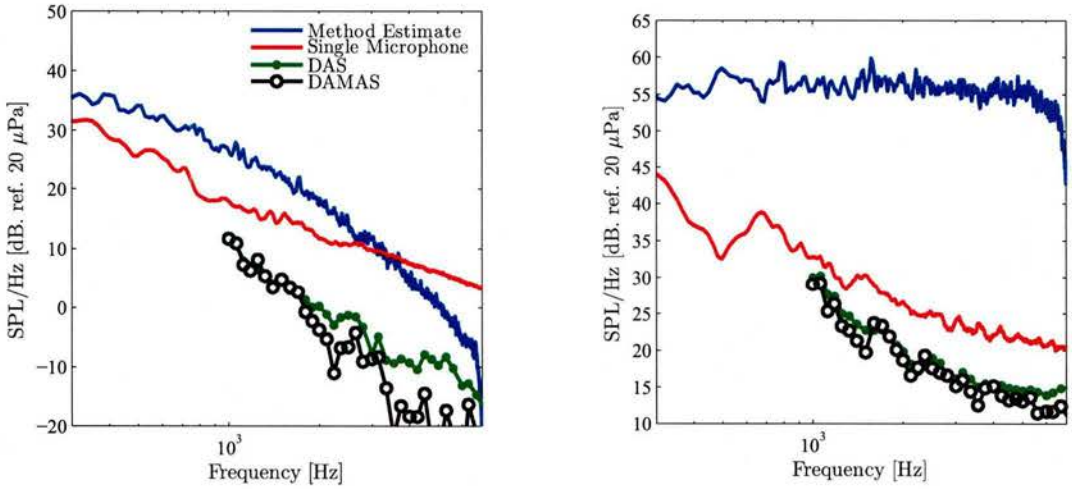

(a) $C_\mu = 0$ (b) $C_\mu = 0.10$

Figure 5.65: SPL comparison for the method estimate, single microphone data, DAS, and DAMAS. Details regarding the DAS and DAMAS results provided in Reger *et al.* (2016).

5.6.6 Acoustic Spectra - Curle's Analogy

The estimated acoustic spectra are compared to the single microphone, DAS, and DAMAS results (Reger *et al.*, 2016) in figure 5.65. All data are scaled to a unit meter span and unit meter observer distance with the observer located directly above the trailing edge mid span. Note that the acquisition and sampling parameters used to generate these spectra are not identical. The measured (single microphone) and estimated acoustic spectra are sampled as discussed in 5.1.8; however, due to the limited number of samples obtained from the Poisson solver, the estimated acoustic spectra has a larger autospectral uncertainty of 17.6% (as opposed to 1.5% for the measured data). Also due to limited computational resources, DAS and DAMAS are obtained (in a narrowband sense) at 1/12th octave center frequencies. All data provided are given in dB/Hz. The no-blowing case estimate ranges from 0-10 dB different than the single microphone data over the frequency range of interest. In the maximum-blowing case a significant level shift of 10-35 dB from the measured acoustic signal to the estimate is observed.

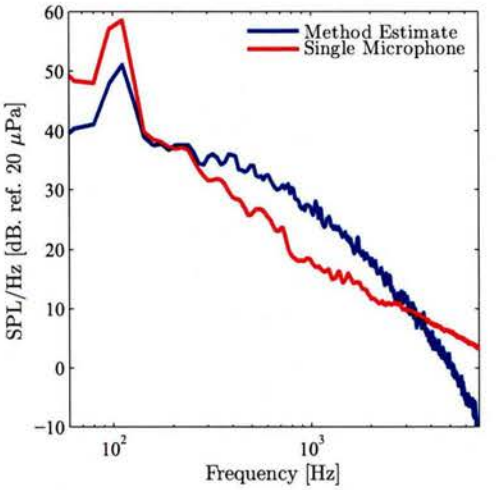

Figure 5.66: Plot of SPL per Hz versus frequency comparison for the method estimate, single microphone data, DAS, and DAMAS. Plotted below the anechoic rating of the tunnel to show bluff body shedding peak.

In the case without blowing from the slot jet, bluff-body shedding is exhibited at a frequency below the anechoic cutoff frequency (250 Hz) of the tunnel. Figure 5.66 shows the spectra from a single microphone as well as the estimate. The bluff-body shedding peak is underestimated by about 6 dB. The shedding is the only significant peak observed in the spectra. The shedding is picked up by the POD as the first and second modes, which (as shown in figure 5.59) are estimated at much higher amplitudes than any other modes in the mLSE. This leads to the velocity and pressure fields representing the structure significantly, while all other structures are less well represented and not well estimated.

CHAPTER 6

CONCLUSIONS AND FUTURE WORK

6.1 Conclusions

In this work, far-field acoustic prediction tools were developed and tested. First, the relevant methods involved in the prediction were described and discussed. These methods include proper orthogonal decomposition (POD), stochastic estimation, Kalman smoother, Poisson's equation, and Curle's analogy. The prediction began by breaking a spatially- (but not temporally-) resolved velocity field into modes, ordered by energy content, by use of POD. Some number of the coefficients from these modes were used in multi-time-delay modified linear stochastic estimation (MTD-mLSE) with a set of temporally- (but not spatially-) resolved probe measurements to obtain an estimate of a set of time-resolved POD coefficients. The stochastic estimate of the POD temporal coefficients and PIV data were then used along with a Kalman smoother to improve the performance of the estimator. This new set of POD coefficients were then used to determine a low-order estimate of the time-resolved velocity field. The estimated velocity field was then used along with the Poisson solver to estimate the time-resolved pressure field. From these fields, the surface pressure forces were extracted and used with Curle's analogy to estimate the far-field pressure.

A direct numerical simulation (DNS) was performed in CharLES from Cascade Technologies. Two-dimensional flow over a circular cylinder at a Reynolds number of 150 was investigated. This model problem was chosen in order to develop and validate the esti-

mation methodology. Results were shown for various modal reconstructions from proper orthogonal decomposition (POD). While two modes contained a vast majority of the energy, the error in the low-order vorticity field did not begin to asymptote to a minimum value until roughly six modes. Based on the first six modes, the non-time-resolved POD coefficients were used along with time-resolved pressure probes to estimate time-resolved velocity fields via several different methods. Modified linear stochastic estimation (mLSE) and modified quadratic stochastic estimation (mQSE) performed very similarly which leads to the use of mLSE due to the increased computational cost associated with mQSE. When no noise was added to the data, the mLSE performs quite well when the number of probes exceeds 4; however, when noise was added to the data, even with 14 probes, the mLSE did not perform well. A model for use in the Kalman filter/smoother was developed based on a second-order oscillator and the mLSE result. When the no-noise-added mLSE was used in the model, the Kalman smoother performed well even when just a single probe measurement was employed; however, when the noisy mLSE was chosen for the model, the performance degraded significantly.

Using the DNS and Kalman smoother velocity fields, a Poisson solver was employed to determine the temporally- and spatially-resolved surface pressure field. While the external pressure field suffered from a small domain size, (chosen to be representative of that obtained using PIV) the surface pressure field performed well. When noisy pressure probe data were employed as boundary conditions, the estimated coefficient of drag was significantly different than the DNS result, illustrating the effect of error propagation through the Poisson solver. Curle's analogy was then utilized. First, a comparison from the Curle's analogy using the full forces to the DNS solution was obtained. This showed good agreement in both magnitude and frequency content. The viscous forces were removed and a decrease in magnitude was shown (as expected), but the frequency content continued to match well. Next, the Poisson-estimated surface pressure forces were compared to the DNS result. A slight decrease in magnitude is observed and noise, which propagated into the Poisson solution, presented itself in the acoustic pressure field.

After testing the proposed analysis methods on a numerical problem, a turbulent wall jet flow was analyzed using PIV, unsteady surface pressure, and hotwire anemometry measurements. Past studies employing acoustic analogies have shown that accurate estimates of far-field acoustics can be calculated provided that the appropriate source terms can be sufficiently resolved. To this end, correlation between surface pressure measurements and PIV velocity fields were shown to exist, such that sensor-based estimation could be employed to estimate temporally-resolved velocity fields. In addition, it was shown that Poisson's equation for pressure fluctuations could be solved using the time-resolved velocity set to estimate any surface pressure forces that may be pertinent to the generation of acoustics. The snapshot POD decomposition of the flow field revealed correlation between the most energetic modes of the flow and the surface pressure measurements, but as the physical extent of the POD modes decreased, correlation values were reduced. This resulted in only a limited subset of the turbulent kinetic energy being retained for the estimation methods and included the possibility of removing less energetic velocity fluctuations that are important to far-field acoustic generation.

With this toolset developed and validated, experiments were performed on an elliptic circulation control (CC) airfoil within an open-jet, open-circuit wind tunnel housed in an anechoic chamber. A 55-microphone phased acoustic array was employed to measure the noise generated from the airfoil. Previous experimental studies regarding the acoustics of circulation control airfoils were limited to primarily single microphone results with some delay-and-sum (DAS) beamforming at limited free-stream velocities, chord Reynolds numbers (Re_c) and momentum coefficients. This study investigated the acoustics with single microphone and DAS as well as the so-call deconvolution approach to mapping acoustic sources (DAMAS) beamforming due to significant background noise in the single microphone measurements. Data were acquired at five Re_c ranging from 0 to 1.3e6 and six momentum coefficients (C_μ) from 0 to 0.10 for a fixed slot height of 1 mm.

The single microphone data showed that the spectral noise levels were only significantly above the tunnel background noise when the jet velocities were large compared to the free-

stream. At the lowest non-zero Re_c the CC acoustics were also shown to be insignificant compared to background noise. DAS beamforming was then used to distinguish the sources of CC noise from background noise in the measurement. The background was shown to be primarily comprised of tunnel collector noise and CC-sidewall interaction noise while the CC noise was primarily generated by slot-jet interaction. The DAS levels were integrated in space to remove the primary extraneous noise components, which allows the sources of interest to be revealed in the acoustic spectra. In the DAS results, sidelobes were clearly present, especially at high frequencies. DAMAS was then used to remove the effect of the array point-spread-function. Due to the presence of the sidelobes, the DAS also tended to overestimate the levels at middle to high frequencies. Even with erroneous noise sources removed, the overall sound pressure level remained above that of a traditional airfoil (NACA0012) at the same geometric and flow conditions.

A scaling analysis was performed on the DAMAS spectra. With a constant free-stream Reynolds number, the acoustic pressure scaled well against jet Mach number to the 6th power at low and intermediate Helmholtz numbers (kd). When the free-stream was removed, the jet Mach number to the 6th power scaling remained for low, but not moderate, Helmholtz numbers. This suggested that Howe's curvature noise remains the dominant source at low Helmholtz numbers for all cases; however, the passive slot noise (Howe, 2002) (which relies on free-stream turbulence interacting with the slot lip) depends explicitly on having a significant free-stream to dominate. Finally, reasonable collapse was achieved with a free-stream Mach scaling to the 7th power if the coefficient of momentum was held constant. This suggested that interaction of the free-stream with the jet produced significant acoustic pressure.

The method to predict far field acoustics was then utilized to determine its efficacy with experimental measurements. PIV and unsteady pressure data were acquired simultaneously with the far-field acoustic data. PIV was measured in a spatially- but not temporally-resolved manner while unsteady pressure was time resolved but not resolved in space. The method employed on the simulation data was then tested on the experimental data. Two

cases were investigated with $C_\mu = 0$ and $C_\mu = 0.10$. The former is dominated by bluff body shedding, while the latter contains a more complex flow field. In the case with no blowing ($C_\mu = 0$) the far-field acoustic prediction was accurate with the single microphone measurement to within 0-10 dB (15 dB versus the DAMAS integrated spectra) for the frequency range of interest. The measured and estimated spectra were broadband in nature; however, each contains a dominant shedding peak at low frequencies. The shedding peak was under-estimated by approximately 6 dB by the prediction method. The measured and estimated spectra for the $C_\mu = 0.10$ case were also broadband in nature; however, the prediction over-estimates the noise level significantly and differ from measurements by as much as 35 dB. The poor prediction was primarily attributed to lack of significant correlation between the POD temporal coefficients and the unsteady pressure signals. Suggestions for improvement of the proposed method and future work are offered in the following.

6.2 Research Impact

A method to predict far-field noise from low cost near field quantities was developed. The method was first validated on low Reynolds number simulation data for flow over a circular cylinder. In the absence of added noise, the estimated spectrum matched the measured spectrum well. When a significant level of additional noise was introduced into the pressure signal the broadband portion of the spectra was over-estimated while the primary lift and drag peaks remained well estimated.

The method was then tested on a moderate Reynolds number wall jet and high Reynolds number flow over an elliptic circulation control airfoil. The results with the method employing experimental data were considerably degraded from those using the simulated data. In the circulation control no-blowing case (the less complex flow field), the shedding peak from the model was obtained but at a decreased level compared to the measurement. The broadband levels were estimated to within 0-10 dB of the single microphone measurement. In the case with slot-jet blowing, the results were poor. This experimental test provided

insight into requirements/limitations of the method:

1.) The domain must be large enough such that no strong fluctuations cross the boundaries. This issue was shown in the simulation estimate. When the domain is not sufficiently large, structures passing over boundaries cause the Poisson solution to be adversely affected. Experimentally, a sufficiently large domain is difficult to obtain with the resolution required to resolve small structures in a high Reynolds number flow.

2.) A large correlation must exist between the conditional and unconditional measurements. In the context of this document, this means that the POD temporal coefficients must be well correlated with the pressure measurements. In the simulated data, the correlation was large for all modes. For the no blowing case, a correlation was present for the first two modes (corresponding to bluff body shedding). Poor correlation existed in the case with slot-jet blowing.

3.) Because the probe data are used at multiple stages in the method, probe noise has a large effect on the ultimate outcome. As shown in the simulated estimate, when random noise is added to the probe the result of the prediction degrades considerably. This is also the case with "noise" introduced by the turbulence in the jet, which causes the correlation discussed above to weaken.

Phased array acoustic data were acquired. Single microphone data were shown to be significantly contaminated with background noise. Conventional and advanced beamforming techniques were employed in order to remove the noise. Removing the background noise allowed for accurate measurement of the noise directly associated with circulation control. It was shown that low and middle frequency noise (generated by trailing edge curvature and turbulence in the free-stream interacting with the slot lip, respectively) scale with jet Mach number to the 6th power.

6.3 Future Work

This work showed that the proposed method to estimate far-field noise worked well on the low Reynolds number, simulated data and performed poorly as the flow became more complex. This suggests that an intermediate test case should be attempted to gain a better understanding of the conditions and requirements necessary for successful implementation and its limitations. To gain further insight into the method as it relates to circulation control noise, time-resolved velocity measurements should be acquired. This would allow for better understand of the performance of the Poisson solver and Curle's analogy stages of the estimation.

A large number of time-resolved velocity fields would also open up the potential to look at the data in new ways to better understand the dominant acoustic sources. For example, Henning *et al.* (2008) shows that, given a large (much more than 5000) number of synchronous velocity and acoustic pressure measurements, correlation can be obtained to show which structures in the velocity field are associated with the far-field noise. Another is example is given by Berger *et al.* (2014) where the POD modes are correlated with the acoustic far-field in order to identify the "loud modes" which may not contain significant kinetic energy but have a significant effect on the acoustic pressure. Once the "loud modes" are identified, they could be used in the method to estimate their contribution to the overall noise.

The DAMAS investigation identified jet-sidewall interaction noise to be a significant contributor to noise over a wide range of frequencies. While this may be due to the porous nature of the sidewall, it is worth investigating whether this source is significant in real-world applications. As such, acoustic investigation of a circulation control wing-fuselage model (or a full sail model) is important to see if the 3D effects dominate the 2D effects. Additionally, with the background noise suppressed, noise reduction modifications to the slot lip and the trailing edge can be investigated. Finally, an acoustic study comparing steady to unsteady actuation may be of interest.

APPENDIX A

2D CURLE'S ANALOGY SINGULARITY

The 2D form of Curle's analogy 2.3.35 has a singularity at the upper integration limit. In order to avoid this singularity, we have chosen to use integration by parts in the following manner

$$\int udv = uv - \int vdu \tag{A.0.1}$$

where we let:

$$u = F'(t') \tag{A.0.2}$$

$$dv = \frac{dt'}{\sqrt{\tau - t'}} \tag{A.0.3}$$

$$du = F''(t')dt' \tag{A.0.4}$$

$$v = 2\sqrt{\tau - t'} \tag{A.0.5}$$

Plugging in to A.0.1 we can solve for the integral in 2.3.35 without the singularity

$$\int_{-\infty}^{\tau} F'(t')\frac{dt'}{\sqrt{\tau - t'}} = 2F'(t')\sqrt{\tau - t'}\Big|_{-\infty}^{\tau} - \int_{-\infty}^{\tau} 2F''(t')\sqrt{\tau - t'}dt' \tag{A.0.6}$$

If we expand out the first term on the right hand side of the equation we see that

$$2F'(t')\sqrt{\tau - t'}\Big|_{-\infty}^{\tau} = (2F'(\tau)\sqrt{\tau - \tau}) - (2F'(-\infty)\sqrt{\tau + \infty}) \tag{A.0.7}$$

$$= 0 \tag{A.0.8}$$

because of the free-field assumption we know that there are no reflections and therefore do not expect what happened at $-\infty$ to have any effect on the field. So the integral goes from

$$\int_{-\infty}^{\tau} F'(t')\frac{dt'}{\sqrt{\tau - t'}} = -\int_{-\infty}^{\tau} 2F''(t')\sqrt{\tau - t'}dt' \tag{A.0.9}$$

APPENDIX B

THE DOPPLER EFFECT

In this section the Doppler effect (also known as a multipole expansion) for a multi-polar source (i.e. monopole, dipole, quadrupole). The derivation follows from Howe (1998) and Inoue & Hatakeyama (2002). Start by defining $q(\mathbf{x},t)$ as the source term in the wave equation (2.3.1) as,

$$\nabla^2 p(\mathbf{x},t) - \frac{1}{c^2}\frac{\partial^2 p(\mathbf{x},t)}{\partial t^2} = q(\mathbf{x},t)$$

And let the source be acoustically compact, which allows the solution to be a superposition of all the point multi-poles. Howe (1998) identifies that the source may then be replaced by the multi-pole expansion

$$q(\mathbf{x},t) = \sum_{n=0}^{\infty}\left[\frac{(-1)^n}{n!}\int y_i y_j y_k \cdots q(\mathbf{y},t)d\mathbf{y}\right]\frac{\partial^n \delta(\mathbf{x})}{\partial x_i \partial x_j \partial x_k \cdots} \tag{B.0.1}$$

The term in brackets is replaced by

$$S^n_{ijk\ldots}(t) = \frac{(-1)^n}{n!}\int y_i y_j y_k \cdots q(\mathbf{y},t)d\mathbf{y}$$

for brevity. We can now solve the wave equation for $p(\mathbf{x},t)$ by convolving 2.3.12 the Green's function G with the source term such that

$$p(\mathbf{x},t) = \iint_{-\infty}^{\infty} q(\mathbf{y},t)G(\mathbf{x}-\mathbf{y},t-t')d\mathbf{y}dt' \approx \sum_{n=0}^{\infty} p_n(\mathbf{x},t) \tag{B.0.2}$$

where the n in p_n describes the order of the multipole (i.e. mono-, di-, quadru- are $n = 0, 1, 2$ respectively) and p_n is given by using the delta function to evaluate the derivative over $\mathbf{y}$,

$$p_n(\mathbf{x}, t) = \frac{\partial^n}{\partial x_i \partial x_j \partial x_k \cdots} \int_{-\infty}^{\infty} S_{ijk\cdots}(t') G(\mathbf{x}, t - t') dt' \tag{B.0.3}$$

Continuing on the 2D Green's function will be used as in Inoue & Hatakeyama (2002), the derivation using the 3D Green's function can be found in Howe (1998). The 2-D free-field Green's function is given in 2.3.19 and repeated here for convenience

$$G_0(\mathbf{x}, \mathbf{y}, t - t') = \frac{H(t - t' - |\mathbf{x} - \mathbf{y}|/c)}{2\pi\sqrt{(t - t')^2 - |\mathbf{x} - \mathbf{y}|^2/c^2}}$$

Plugging in the Green's function p_n becomes

$$p_n(\mathbf{x}, t) = \frac{\partial^n}{\partial x_i \partial x_j \partial x_k \cdots} \int_{-\infty}^{\infty} S_{ijk\cdots}(t') \frac{H(t - t' - |\mathbf{x} - \mathbf{y}|/c)}{2\pi\sqrt{(t - t')^2 - |\mathbf{x} - \mathbf{y}|^2/c^2}} dt' \tag{B.0.4}$$

We now perform a transform from t' to τ' such that $-\tau' = t - t' - r/c$ where $r' = |\mathbf{x} - \mathbf{y}|$, therefore our (Doppler effect included) p_n^D is written as

$$p_n^D(r, t) = \frac{\partial^n}{\partial x_i \partial x_j \partial x_k \cdots} \int_{-\infty}^{\infty} \frac{S_{ijk\cdots}(\tau' + (t - r'/c)) H(\tau')}{2\pi\sqrt{\tau'^2 - 2(r'/c)\tau'}} d\tau' \tag{B.0.5}$$

Applying the Heaviside function condition of causality

$$p_n^D(r, t) = \frac{\partial^n}{\partial x_i \partial x_j \partial x_k \cdots} \int_{-\infty}^{0} \frac{S_{ijk\cdots}(\tau' + (t - r/c))}{2\pi\sqrt{\tau'^2 - 2(r/c)\tau'}} d\tau' \tag{B.0.6}$$

Since the integral grows most quickly near $\tau' = 0$ we can let τ'^2 be neglected. Now, we define the retarded time as $\tau = t - r'/c$ so the equation above can be rewritten as

$$p_n^D(r, t) = \frac{\partial^n}{\partial x_i \partial x_j \partial x_k \cdots} \frac{c^{1/2}}{2\pi * (2r)^{1/2}} \int_{-\infty}^{0} \frac{S_{ijk\cdots}(\tau' + \tau)}{\sqrt{-\tau'}} d\tau' \tag{B.0.7}$$

Transferring the differentiation from space to retarded time by

$$\frac{\partial \tau}{\partial x_i} = -\frac{r'_i}{cr'(1 - M\cos\theta)} \tag{B.0.8}$$

where θ is the angle between the free stream velocity and the vector pointing from the source to the observer. Using the above relation we obtain

$$p_n^D(r,t) = \frac{(-1)^n r_i r_j r_k \cdots}{c^n r'^n (1 - M\cos\theta)^n} \frac{c^{1/2}}{2\pi * (2r)^{1/2}} \int_{-\infty}^{0} \frac{S_{ijk\ldots}(\tau' + \tau)}{\sqrt{-\tau'}} d\tau' \tag{B.0.9}$$

Comparing this result to the result if $M = 0$ we obtain the transform from the Doppler shifted pressure $p_n^D(r,t)$ to the Doppler effect removed pressure $p_n(r',t)$ such that

$$p_n^D(r,t) = \frac{p_n(r',t)}{(1 - M\cos\theta)^n} \tag{B.0.10}$$

where $r \approx r'(1 - M\cos\theta)$ and for our case (of an almost purely dipole source) $n = 1$.

BIBLIOGRAPHY

ABRAMSON, J. 1975 Two-dimensional subsonic wind tunnel evaluation of a 20-percent-thick circulation control airfoil. In *Tech. Rep.*.

ADRIAN, R. J. 1977 On the role of conditional averages in turbulence theory. *Turbulence in liquids* pp. 323–332.

ADRIAN, R. J. 1979 Conditional eddies in isotropic turbulence. *Physics of Fluids* **22**.

ADRIAN, R. J., CHRISTENSEN, K. T. & LIU, Z.-C. 2000 Analysis and interpretation of instantaneous turbulent velocity fields. *Experiments in Fluids* **29** (3), 275–290.

ADRIAN, R. J. & MOIN, P. 1988 Stochastic estimation of organized turbulent structure: homogeneous shear flow. *Journal of Fluid Mechanics* **190**, 531.

AMIET, R. 1975 Correction of open jet wind tunnel measurements for shear layer refraction. In *2nd Aeroacoustics Conference*.

AUBRY, N., GUYONNET, R. & LIMA, R. 1992 Spatio-temporal symmetries and bifurcations via biorthogonal decompositions. *Journal of Nonlinear Science* **2**, 183–215.

AUBRY, N., HOLMES, P., LUMLEY, J. L. & STONE, E. 1988 The dynamics of coherent structures in the wall region of a turbulent boundary layer. *Journal of Fluid Mechanics* **192**, 115–173.

BAHR, C., ZAWODNY, N. S., BERTOLUCCI, B., JIAN, L., SHEPLAK, M., CATTAFESTA, L. N. & LI, J. 2015 A plasma-based non-intrusive point source for aocustic beamforming applications. *Journal of Sound and Vibration* .

BAUR, T. & KONGETER, J. 1999 PIV with high temporal resolution for the determination of local pressure reductions from coherent turbulent phenomena. *3rd International Workshop on Particle Image Velocimetry* pp. 101–106.

BENDAT, J. S. & PIERSOL, A. G. 2010 *Random Data Analysis and Measurement Procedures*, 4th edn. Wiley. Pp. 387-414.

BERGER, Z. P., BERRY, M. G., SHEA, P. R., GLAUSER, M. N., KAN, P. LEWALLE, J., RUSCHER, C. J. & GOGINENI, S. 2014 Investigation of Loud Mode in a High-Speed Jet to. In *76th AIAA Theoretical Fluid Mechanics Conference*.

BERGH, H. & TIDJEMAN, H. 1965 Theoretical and experimental results for the dynamic response of pressure measuring systems. *NLR - TR F* pp. 1–21.

BERKOOZ, G., HOLMES, P. & LUMLEY, J. L. 1993 The proper orthogonal decomposition in the analysis of turbulent flows. *Annual Review Fluid Mechanics* **25**, 539–575.

BERTON, E., MARESCA, C. & FAVIER, D. 2004 A new experimental method for determining local airloads on rotor blades in forward flight. *Experiments in Fluids* **37**, 455–457.

BONNET, J. P., COLE, D. R., DELVILLE, J., GLAUSER, M. N. & UKEILEY, L. S. 1994 Stochastic estimation and proper orthgonal decomposition: Complementary techniques for identifying structure. *Experiments in Fluids* **17**, 307–314.

BROOKS, T. F. & HUMPHREYS, W. M. 2006 A deconvolution approach for the mapping of acoustic sources (DAMAS) determined from phased microphone arrays. *Journal of Sound and Vibration* **330**, 375–409.

BROOKS, T. F., POPE, D. S. & MARCOLINI, M. A. 1989 Airfoil Self-Noise and Prediction. In *NASA Reference Publication 1218*.

BRUUN, H. H. 2001 *Hot-Wire Anemometry, Principles and Signal Analysis*. Oxford University Press.

CHARONKO, J. J., KING, C. V., L., S. B. & VLACHOS, P. P. 2010 Assessment of pressure field calculations from particle image velocimetry measurements. *Measurement Science and Technology* **21**, 105401.

CHASE, D. M. 1980 Modeling the wavevector-frequency spectrum of turbulent boundary layer wall pressure. *Journal of Sound and Vibration* **33**, 29–67.

CHRISTENSEN, K. T. & ADRIAN, R. J. 2002 Measurement of instantaneous Eulerian accerlation fields by particle-image accelerometry: Method and accuracy. *Experiments in Fluids* **33**, 759–769.

CIMBALA, J. M., NAGIB, H. M. & ROSHKO, A. 1988 Large structure in the far wakes of two-dimensional bluff bodies. *Journal of Fluid Mechanics* **190**, 265–298.

CITRINITI, J. 2012 *Experimental investigation into the dynamics of the axisymmetric mixing layer utilizing the Proper Orthogonal Decomposition*. Dissertation, State University of New York at Buffalo.

COANDA, H. 1938 Propelling device.

COLE, D. R., GLAUSER, M. N. & GUEZENNEC, Y. G. 1992 An application of the stochastic estimation to the jet mixing layer. *Physics of Fluids: Fluids Dynamics* **4**, 192.

COLONIUS, T., LELE, S. K. & MOIN, P. 1997 Sound generation in a mixing layer. *Journal of Fluid Mechanics* **330**, 375–409.

CURLE, N. 1955 The influence of solid boundaries upon aerodynamic sound. *Proceedings of the Royal Society of London* **231**, 233–253.

DELVILLE, J., BELLIN, S. & BONNET, J. P. 1989 Use of the proper orthgonal decomposition in a plane turbulent mixing layer. *Turbulence and Coherent Structures* pp. 75–90.

DELVILLE, J., UKEILEY, L., CORDIER, L., BONNET, J. P. & GLAUSER, M. 1999 Examination of large-scale structures in a turbulent plane mixing layer. Part 1. Proper orthogonal decomposition. *Journal of Fluid Mechanics* pp. 91–122.

DOUGHERTY, R. P. 2002 *Aeroacoustic Measurements*, 4th edn. Springer-Verlag.

DRELA, M. 1989 XFOIL: An Analysis and Design System for Low Reynolds Number Airfoils. *Low Reynolds Number Aerodynamics* .

DUFFY, D. G. 2001 *Green's Functions with Applications*. Chapman and Hall/CRC. Pp. 75-101.

DURGESH, V. & NAUGHTON, J. W. 2010 Multi-time-delay LSE-POD complementary approach applied to unsteady high-Reynolds-number near wake flow. *Experiments in Fluids* **49**, 571–583.

EWING, D. & CITRINITI, J. 1999 Examination of a LSE/POD complementary technique using single and multi-time information in the axisymmetric shear layer. *Proceedings of the IUTAM Symposium on simulation and identification of organized structures in flows* pp. 375–384.

FUJISAWA, N., TANAHASHI, S. & SRINIVAS, K. 2005 Evaluation of pressure field and fluid forces on a circular cylinder with and without rotational oscillation using velocity data from PIV measurement. *Measurement Science and Technology* **16**, 989–996.

GEORGE, W. K., BEUTHER, P. D. & ARNDT, R. E. 1984 Pressure spectra in Turbuelent free shear flowd. *J. Fluid Mech* **148**, 155–191.

GLAUSER, M. N. & GEORGE, W. K. 1987 An orthogonal decomposition of the axisymmetric jet mixing layer utilizing cross-wire measurements. *Proceedings, Sixth Symposium on Turbulent Shear Flow* pp. 10.1.1–10.1.6.

GLOERFELT, X., PÉROT, F., BAILLY, C. & JUVÉ, D. 2005 Flow-induced cylinder noise formulated as a diffraction problem for low Mach numbers. *Journal of Sound and Vibration* **287**, 129–151.

GOLDSTEIN, M. E. 1976 *Aeroacoustics*. McGraw-Hill. Pp. 113-116.

GOODY, M. C. 2004 Empirical spectral model of surface pressure fluctuations. *AIAA Journal* **42**, 1788–1794.

GORDEYEV, S. 1999 *Investigation of coherent structure in the similarity region of the planar turbulent jet using POD and wavelet analysis*. Dissertation, University of Notre Dame.

GRESHO, P. M. & SANI, R. L. 1987 On pressure boundary conditions for incompressible Navier-Stokes equations. *International Journal for Numerical Methods in Fluids* **7**, 1111–1145.

GRIFFIN, J., SCHULTZ, T., HOLMAN, R., UKEILEY, L. & CATTAFESTA, L. 2010 Application of multivariate outlier detection to fluid velocity measurements. *Experiments in Fluids* **49**, 305–317.

GRIFFIN, J. C. 2013 *On the control of a canonical separated flow*. Ph.D. Dissertation, University of Florida.

GRISSOM, D. L. 2007 *A Study of Sound Generated by a Turbulent Wall Jet Flow Over Rough Surfaces*. Dissertation, Virginia Tech University.

GUEZENNEC, Y. G. 1989 Stochastic estimation of coherent structures in turbulent boundary layers. *Physics of Fluids: Fluids Dynamics* **1**, 1054.

GURKA, R., LIBERZON, A., HEFETZ, D., RUBINSTEIN, D. & SHAVIT, U. 1999 Computation of pressure distribution using PIV velocity data. *Proceedings of the 3rd International Workshop PIV* pp. 671–676.

HAIGERMOSER, C. 2009 Application of an acoustic analogy by PIV data from rectangular cavity flows. *Experiments in Fluids* **47**, 145–157.

HALL, J. W. & EWING, D. 2007 Three-Dimensional Turbulent Wall Jets Issuing from Moderate-Aspect-Ratio Rectangular Channels. *AIAA Journal* **45** (6), 1177–1186.

HENNING, A., KAEPERNICK, K., EHRENFRIED, K., KOOP, L. & DILLMANN, A. 2008 Investigation of aeroacoustic noise generation by simultaneous particle image velocimetry and microphone measurements. *Experiments in Fluids* **45**, 1073–1085.

HOLMES, P., LUMLEY, J. L., BERKOOZ, G. & ROWLEY, C. W. 2012 *Turbulence, Coherent Structures, Dynamical Systems and Symmetry*. Cambridge University Press.

HOWE, M. S. 1975 Contributions to the theory of aerodynamic sound, with application to excess jet noise and the theory of the flute. *Journal of Fluid Mechanics* **71**, 625–673.

HOWE, M. S. 1998 *Acoustics of Fluid-Structure Interactions*. Cambridge University Press.

HOWE, M. S. 2002 Noise generated by a Coanda wall jet circulation control device. *Journal of Sound and Vibration* **249**, 679–700.

INOUE, O. & HATAKEYAMA, N. 2002 Sound generation by a two-dimensional circular cylinder in a uniform field. *Journal of Fluid Mechanics* **471**, 285–314.

JAKOBSEN, M. L., DEWHIRST, T. P. & GREATED, C. A. 1997 Particle image velocimetry for predictions of acceleration fields and force within fluid flows. *Measurement Science and Technology* **8**, 1502–1516.

JENSEN, A. & PEDERSEN, G. K. 2004 Optimization of acceleration measurements using PIV. *Measurement Science and Technology* **15**, 2275–2283.

JOSLIN, R. D. 2005 Circulation control: Issues for naval applications. In *Proceedings of the 2004 NASA/ONR Circulation Control Workshop*.

DE KAT, R. & VAN OUDHEUSDEN, B. W. 2010 Instantaneous planar pressure from PIV: Analytic and experimental test-cases. *15th International Symposium on Applications of Laser Techniques to Fluid Mechanics* .

DE KAT, R. & VAN OUDHEUSDEN, B. W. 2012 Instantaneous planar pressure determination from PIV in turbulent flow. *Experiments in Fluids* **52**, 1089–1106.

KHALIGHI, Y., HAM, F., MOIN, P., LELE, S. K., SCHLINKER, R., REBA, R. & SIMONICH, J. 2011 Noise presdiction of pressure-mismatched hets used unstructured large eddy simulation. In *Proceedings of ASME Turbo Expo*.

KOSCHATZKY, V., MOORE, P. D., WESTERWEEL, J., SCARANO, F. & BOERSMA, B. J. 2011a High speed PIV applied to aerodynamic noise investigation. *Experiments in Fluids* **50**, 863–876.

KOSCHATZKY, V., OVERMARS, E. F. J., BOERSMA, B. J. & WESTERWEEL, J. 2012 Comparison of planar PIV and tomographic PIV for aeroacoustcs. *16th International Symposium on Applications of Laser Techniques to Fluid Mechanics* .

KOSCHATZKY, V., WESTERWEEL, J. & BOERSMA, B. J. 2011b A study on the application of two different acoustic analogies to experimental PIV data. *Physics of Fluids* **23**, 065112.

KWON, K. & CHOI, H. 1996 Control of laminar vortex shedding behind a circular cylinder using splitter plates. *Physics of Fluids* **8**, 479–486.

LARSSON, J., DAVIDSON, L., OLSSON, M. & ERIKSSON, L. E. 2004 Aeroacoustic investigation of an open cavity at low mach number. *AIAA Journal* **42**.

LAUNDER, B. & RODI, W. 1983 The turbulent wall jet measurements and modeling. *Annual Review of Fluid Mechanics* .

LIGHTHILL, M. J. 1952 On sound generated aerodynamically: I. General theory. *Proceedings of the Royal Society of London* **221**, 564–587.

LIN, J. C. & ROCKWELL, D. 1996 Force identification by vorticity fields: Techniques based on flow imaging. *Journal of Fluids and Structures* **10**, 663–668.

LIU, X. & KATZ, J. 2004 Measurement of pressure distribution by integrating the material acceleration. *2004 ASME Heat Transfer/Fluids Engineering Summer Conference* .

LIU, X. & KATZ, J. 2006 Instantaneous pressure and material acceleration measurements using a four-exposure PIV system. *Experiments in Fluids* **41**, 227–240.

LIU, X. & KATZ, J. 2011 Time resolved measurements of the pressure field generated by vortex-corner interactions in a cavity shear layer. *Proceedings of ASME-JSME-KSME Joint Fluids Engineering Conference 2011* .

LOEVE, M. 1955 *Probability Ttheory*. D. van Nostrand.

LORENZONI, V., MOORE, P., SCARANO, F. & TUINSTRA, M. 2009 Aeroacoustic analysis of a rod-airfoil flow by means of time-resolved PIV. *Proceedings of the 15th AIAA/CEAS Aeroacoustics Conference* .

LORENZONI, V., TUINSTRA, M. & SCARANO, F. 2012 On the use of time-resolved particle image velocimetry for the investigation of rod-airfoil aeroacoustcs. *Jounral of Sound and Vibration* **331**, 5012–5027.

LORENZONI, V., VIOLATO, D. & SCARANO, F. 2010 Aeroacoustic analysis of a rod-airfoil flow by means of time-resolved PIV. *Proceedings of the 16th AIAA/CEAS Aeroacoustics Conference* .

LUMLEY, J. L. 1967 The structure of inhomogeneous turbulent flows. *Atmospheric, Turbulence, and Radio Wave Propagation* pp. 166–178.

MOORE, P., LORENZONI, V. & SCARANO, F. 2011 Two techniques for PIV- based aeroacoustic prediction and their application to a rod-airfoil experiment. *Experiments in Fluids* **50**, 877–885.

MORIARTY, P. 2005 Nafnoise user guide. In *National Wind Technology Center*.

MORIARTY, P. & MIGLIORE, P. 2003 Semi-empirical aeracoustic prediction code for wind turbines. In *NREL/TP-500-34478, National Wind Technology Center*.

MOSHER, M. 1983 Acoustics of rotors utilizing circulation control. *Journal of Aircraft* **20**, 946–952.

MUNRO, S. E., AHUJA, K. K. & ENGLAR, R. J. 2001 Noise reduction through circulation control. *AIAA* .

MURAI, Y., NAKADA, T., SUZUKI, T. & TAMAMOTO, F. 2007 Particle tracking velocimetry applied to estimate the pressure field around a Savonius turbine. *Measurement Science and Technology* **18**, 2491–2503.

MURRAY, N. E. & UKEILEY, L. S. 2003 Estimation of the flowfield from surface pressure measurements in an open cavity. *AIAA Journal* **41**, 969–972.

MURRAY, N. E. & UKEILEY, L. S. 2007 Modified quadratic stochastic estimation of resonating subsonic cavity flow. *Journal of Turbulence* **7**, 1–29.

NAGUIB, A. M., WARK, C. E. & JUCKENHOFEL, O. 2001 Stochastic estimation and flow sources associated with surface pressure events in a turbulent boundary layer. *Physics of Fluids* **13**, 2611–2626.

NICKELS, A., UKEILEY, L., REGER, R. & CATTAFESTA, L. 2014*a* A Method for Estimating Surface Pressure Forces and Far-Field Acoustics. In *AIAA 6.2014-3340*, pp. 1–15.

NICKELS, A., UKEILEY, L., REGER, R. & CATTAFESTA, L. 2014*b* A Method for Estimating Surface Pressure Forces and Far-Field Acoustics. In *76th AIAA Theoretical Fluid Mechanics Conference*.

NOCA, F., SHIELS, D. & JEON, D. 1997 Measuring instantaneous fluid dynamic forces on bodies, using only velocity fields and their derivatives. *Journal of Fluids and Structures* **11**, 345–350.

NOCA, F., SHIELS, D. & JEON, D. 1999 A comparison of methods for evaluating time-dependent fluid dynamic forces on bodies, using only velocity fields and their derivatives. *Journal of Fluids and Structures* **13**, 551–578.

NOVAK, C. J. & CORNELIUS, K. C. 1986 An LDV investigation of a circulation control airfoil flowfield. *AIAA* .

NOVAK, C. J., CORNELIUS, K. C. & ROADS, R. K. 1987 Experimental investigation of the circular wall jet on a circulation control airfoil. *AIAA* .

VAN OUDHEUSDEN, B. W. 2008 Principles and application of velocimetry-based planar pressure imaging in compressible flows with shocks. *Experiments in Fluids* **45**, 657–674.

VAN OUDHEUSDEN, B. W. 2013 PIV-based pressure measurements. *Measurement Science and Technology* **24**, 032001.

VAN OUDHEUSDEN, B. W., SCARANO, F. & CASIMIRI, E. W. F. 2006 Non-intrusive load characterizaion of an airfoil using PIV. *Experiments in Fluids* **40**, 988–992.

PASCIONI, K., REGER, R., EDSTRAND, A. & CATTAFESTA, L. 2014 Characterization of an Aeroacoustic Wind Tunnel Facility. In *43rd International Congress of Noise Control Engineering*.

POWELL, A. 1960 Aerodynamic noise and the plane boundary. *The journal of the Acoustical Society of America* **564** (1136), 982–990.

POWELL, A. 1964 Theory of vortex sound. *Journal of the Acoustical Society of America* **36**, 177–195.

REGER, R., NICKELS, A., UKEILEY, L. & CATTAFESTA, L. 2016 On the Acosutics of Circulation Control Airfoil. *Journal of Sound and Vibration* Submitted to JSV.

ROGERS, E. O. & DONNELLY, M. J. 2004 Characteristics of a dual-slotted circulation control wing of low aspect ratio intended for naval hydrodynamic applications. *AIAA* .

SALIKUDDIN, M., BROWN, W. H. & AHUJA, K. K. 1987 Noise from a circulation control wing with upper surface blowing. *Journal of Aircraft* **24**, 55–64.

SCHLICHTING, H. 1979 *Boundary-Layer Theory*, 7th edn. McGraw-Hill. Pp. 729-757.

SCHRODER, A., HERR, M., LAUKE, T. & DIERKSHEIDE, U. 2006 A study on trailing edge noise structures using high-speed particle image velocimetry. *Notes on Numerical Fluid Mechanics and Multidisciplinary Design* **92**, 373–380.

SCHWABE, M. 1935 ber druckermittlung in der nichtstationren ebenen strmung. *Ingenieur-Archiv* **6**, 34–50.

SCIACCHITANO, A., NEAL, D. R., SMITH, B. L., WARNER, S. O., VLACHOS, P. P., WIENEKE, B. & SCARANO, F. 2014 Collaborative framework for PIV uncertainty quantification: comparative assessment of methods. In *17th International Symposium on Application of Laser Techniques to Fluid Mechanics.*

SEINER, J. M. & PONTON, M. K. 1999 Jet noise measurements using PIV. *5th AIAA/CEAS Aeroacoustics Conference* .

SHANNON, D. & MORRIS, S. 2008 Experimental investigation of slotted circulation control airfoil acoustics. *AIAA* .

SIGALLA, A. 1958 Measurements of skin friction in a plane turbulent wall jet. *Journal of the Royal Aeronautical Society* **62** (579), 873.

SIMON, D. 2006 *Optimal State Estimation: Kalman, H Infinity, and Nonlinear Approaches.* John Wiley and Sons.

SIROVICH, L. 1987 Turbulence and the dynamics of coherent structures. part 1: Coherent structures. *Quarterly of Applied Mathematics* **45**, 561–571.

SLOMSKI, J. F. 2009 Reducing vortex shedding sound from a trailing edge above a wall jet. *AIAA* .

SRIDHAR, G. & KATZ, J. 1995 PIV-based pressure measurements. *Physics of Fluids* **7**, 389–399.

STRATTON, J. A. 1941 *Electromagnetic Theory.* John Wiley I& Sons.

TAYLOR, J. A. & GLAUSER, M. 2004 Towards practical flow sensing and control via POD and LSE based low-dimensional tools. *Journal of Fluids Engineering* **126**, 337–345.

TINNEY, C. E., COIFFET, F., DELVILLE, J., HALL, A. M., JORDAN, P. & GLAUSER, M. N. 2006 On spectral linear stochastic estimation. *Experiments in Fluids* **41**, 763–775.

TU, J., ROWLEY, C. W., GRIFFIN, J. & CATTAFESTA, L. N. 2012 Integration of non-time-resolved piv and time-resolved velocity point sensors for dynamic estimation of time-resolved velocity fields. In *AIAA Aerospace Sciences Meeting*.

TUNG, T. C. & ADRIAN, R. J. 1980 Higher order estimates of conditional eddies in isotropic turbulence. *Physics of Fluids* **23**, 1469–1470.

UDA, T., NISHIKAWA, A., SOMEYA, S. & IIDA, A. 2011 Prediction of aeroacoustic sound using the flow field obtained by time-resolved particle image velocimetry. *Measurement Science and Technology* **22**, 075402.

UKEILEY, L., CORDIER, L., DELVILLE, J., GLAUSER, M. & BONNET, J. P. 2001 Examination of large-scale structures in a turbulent plane mixing layer. Part 2. Dynamical systems model. *Journal of Fluid Mechanics* pp. 67–108.

UKEILEY, L., MURRAY, N. E., SONG, Q. & CATTAFESTA, L. 2008 Dynamic surface pressure based estimation for flow control. In *IUTAM Symposium on Flow Control and MEMS*.

UNAL, M. F., LIN, J. C. & ROCKWELL, D. 1997 Force identification by PIV imaging: A momentum-based approach. *Journal of Fluids and Structures* **11**, 965–971.

UNDERBRINK, J. R. 1995 *Practical Considerations in focused array design for passive broadband source mapping applications*. Master's Thesis, Pennsylvania State University.

VIOLATO, D., BRYON, K., MOORE, P. & SCARANO, F. 2010 Application of Powell's analogy for the prediction of vortex-pairing sound in a low-Mach number jet based on tim-

resolved planar and tomographic PIV. *Proceedings of the 16th AIAA/CEAS Aeroacoustics Conference* .

VIOLATO, D., MOORE, P. & SCARANO, F. 2011 Lagrangian and Eulerian pressure field evaulation of rod-airfoil flow from time-resolved tomographic PIV. *Experiments in Fluids* **50**, 1057–1070.

WELCH, G. & BISHOP, G. 1995 An introduction to the kalman filter.

WESTERWEEL, J. 1993 *Digital particle image velocimetry - theory and application.* Dissertation, Delft University.

WETZEL, D., LIU, F., ROSENBERG, B. & CATTAFESTA, L. 2009 Acoustic Characteristics of a Circulation Control Airfoil. In *15th AIAA/CEAS Aeroacoustics Conference.*

WETZEL, D. A. 2011 *An experimental investigation of circulation control acoustics.* Dissertation, University of Florida.

WETZEL, D. A., LIU, F. & CATTAFESTA, L. 2012 A theoretical and experimental study of broadband circulation control noise. In *AIAA/CEAS Aeroacoustics Conference.*

WIENEKE, B. 2014 Generic a-posteriori uncertainty quantification for PIV vector fields by correlation statistics. In *17th International Symposium on Application of Laser Techniques to Fluid Mechanics.*

WIENEKE, B. 2015 PIV uncertainty quantification from correlation statistics. *Measurement Science Technology* **26**.

WILLIAMS, R. M. & CHEESEMAN, I. C. 1978 Potential acoustic benefits of circulation control rotors. *NASA. Langley Research Center Helicopter Acoustics* **2**, 149–179.

WILLIAMSON, C. H. K. 1989 Oblique and parallel modes of vortex shedding in the wake of a circular cylinder at low Reynolds numbers. *Journal of Fluid Mechanics* **206**, 579–627.

YARDIBI, T., BAHR, C., ZAWODNY, N. S., LIU, F., CATTAFESTA, L. N. & LI, J. 2010*a* Uncertainty analysis of the standard delay-and-sum beamformer and array calibration. *Journal of Sound and Vibration* **329**, 2654–2682.

YARDIBI, T., ZAWODNY, N. S., BAHR, C., LIU, F., CATTAFESTA, L. N. & LI, J. 2010*b* Comparison of microphone array processing techniques for aeroacoustics measurements. *International Journal of Aeroacoustics* **9**, 732–762.

ZAWODNY, N., LIU, F. & CATTAFESTA, L. 2016 Transfer matrix modeling of a recessed microphone for unsteady surface pressure measurements. *Applied Acoustics 2015* Submitted to Applied Acoustics 2015.

ZAWODNY, N. S. 2013 *Aeroacoustic Characterization of Scaled Canonical Nose Landing Gear Configurations*. Dissertation, University of Florida.